Flow control using optical sensors

Nicolas Gautier

Ecole doctorale: Sciences mécaniques, acoustique, électronique & robotique (UPMC)
ESPCI, Laboratoire PMMH

Flow control using optical sensors

(Contrôle d'écoulement par capteurs optiques)

Nicolas Gautier

Thèse de doctorat de Physique

Dirigée par Jean-Luc Aider

Jury

Dr. François Lusseyran	(Rapporteur)	LIMSI
Dr. Denis Sipp	(Rapporteur)	ONERA
Dr. Philippe Guibert	(Examinateur)	UPMC
Dr. Azeddine Kourta	(Examinateur)	PRISME
Dr. Bernd Noack	(Examinateur)	PPRIME
Dr. Jean-Luc Aider	(Directeur de thèse)	PMMH

0.1 Abstract

Flow control using optical sensors is experimentally investigated. Real-time computation of flow velocity fields is implemented. This novel approach featuring a camera for acquisition and a graphic processor unit (GPU) for processing is presented and detailed. Its validity with regards to speed and precision is investigated. A comprehensive guide to software and hardware optimization is given. We demonstrate that online computation of velocity fields is not only achievable but offers advantages over traditional particle image velocimetry (PIV) setups. It shows great promise not only for flow control but for parametric studies and prototyping also.
A hydrodynamic channel is used in all experiments, featuring a backward facing step for separated flow control. Jets are used to provide actuation. A comprehensive parametric study is effected to determine the effects of upstream jet injection. It is shown upstream injection can be very effective at reducing recirculation, corroborating results from the literature.

Both open and closed loop control methods are investigated using this setup. Basic control is introduced to ascertain the effectiveness of this optical setup. The recirculation region created in the backward-facing step flow is computed in the vertical symmetry plane and the horizontal plane. We show that the size of this region can be successfully manipulated through set-point adaptive control and gradient based methods.
A physically driven control approach is introduced. Previous works have shown successful reduction recirculation reduction can be achieved by periodic actuation at the natural Kelvin-Helmholtz frequency of the shear layer. A method based on vortex detection is introduced to determine this frequency, which is used in a closed loop to ensure the flow is always adequately actuated. Thus showing how recirculation reduction can be achieved through simple and elegant means using optical sensors.
Next a feed-forward approach based on ARMAX models is implemented. It was successfully used in simulations to prevent amplification of upstream disturbances by the backward-facing step shear layer. We show how such an approach can be successful in an experimental setting.
Higher Reynolds number flows exhibit non-linear behavior which can be difficult to model in a satisfactory manner thus a new approach was attempted dubbed machine learning control and based on genetic programming. A number of random control laws are implemented and rated according to a given cost function. The laws that perform best are bred, mutated or copied to yield a second generation. The process carries on iteratively until cost is minimized. This approach can give surprising insights into effective control laws.

0.2 Résumé

Le contrôle d'écoulement en utilisant des capteurs optiques est étudié dans un contexte expérimental. Le calcul de champs de vitesses en temps réel en utilisant une caméra pour l'acquisition et une carte graphique pour le calcul est détaillé. La validité de l'approche en terme de rapidité et de précision est étudiée. Un guide complet pour l'optimisation logicielle et matérielle est donné. Nous démontrons que le calcul dynamique de champs de vitesse est non seulement possible mais plus facile à gérer que l'utilisation d'un appareillage (PIV)

classique.
Un canal hydrodynamique est utilisé pour toutes les expériences. Celui-ci comporte une marche descendante pour le contrôle d' écoulements décollés. Les actionneurs sont des jets. Dans le cas de la marche descendante une étude paramétrique approfondie est faite pour qualifier les effets d'une injection en amont des jets, celle-ci étant traditionnellement effectuée à l'arrête de la marche.

Plusieurs méthodes de contrôle sont étudiées. Un algorithme de contrôle basique de type PID est mis en place pour démontrer la viabilité du contrôle d'écoulement en boucle fermée par capteurs optiques. La zone de recirculation située derrière la marche est calculée en temps réel dans un plan vertical et horizontal. La taille de cette région est manipulée avec succès.
Une approche basée sur des observations de la dynamique de l'écoulement est présentée. Des résultats précédents dans la littérature montrent que la recirculation peut être réduite avec succès en agissant sur l'écoulement à la fréquence naturelle de lâchés tourbillonnaires liés à l'instabilité de Kelvin-Helmholtz de la couche cisaillée crée par la marche. Une éthode basée de détection de vortex est introduite pour calculer cette fréquence, qui est ensuite utilisée dans une boucle de contrôle qui assure que l'écoulement est toujours pulsé à la bonne fréquence. Ainsi en utilisant des capteurs optiques la recirculation est réduite de façon simple.
Ensuite nous implémentons un contrôle de type feed-forward dont l'efficacité a préalablement été démontrée en simulation. Cette approche vise à prévenir l'amplification de perturbations amont par la couche cisaillée. Nous montrons comment une telle méthode peut être implémentée avec succès dans un contexte expérimental.
Enfin, nous implémentons également une approche radicalement différente basée sur un algorithme génétique. Des lois de contrôle aléatoires sont testées et évaluées. Les meilleurs sont répliquées, mutées et croisées. Ce processus se poursuit itérativement jusqu'à ce que le coût soit minimisé. Bien que lente à converger cette approche donne des résultats encourageants à travers une loi de commande originale.

0.3 Preface

This thesis deals with flow control using optical sensors. part I presents the basic concepts and methods. Part II contains the results. All but the first chapter of part II feature papers. They are adjusted to comply with the format of this manuscript, however their contents have not been altered. The introduction and core experimental setup, described in part I are common to all studies, thus the reader should not be amiss by skipping to the results sections in subsequent chapters.

1. T. Cambonie, N. Gautier, and J-L Aider. 2013
   Experimental study of counter-rotating vortex pair trajectories induced by a round jet in cross-flow at low velocity ratios,
   Experiments in Fluids, post-print available on the arXiv

2. N. Gautier, and J-L Aider. 2014
   Real-time planar flow velocity measurements using an optical flow algorithm implemented on GPU,
   To be published in Journal of Visualization, post-print available on the arXiv

3. N. Gautier, and J-L Aider. 2013
   Control of the flow behind a backward-facing step by visual feedback,
   Royal Society Proceedings A, post-print available on the arXiv

4. N. Gautier, and J-L Aider. 2014
   Effects of pulsed actuation upstream a backward-facing step,
   CRAS, post-print available on the arXiv

5. N. Gautier, and J-L Aider. 2014
   Experimental frequency lock control of the flow behind the backwards facing step,
   Under consideration for publication in Experiments in fluids, pre-print available on the arXiv,

6. N. Gautier, and J-L Aider. 2014
   Feed-forward control of the backward-facing step flow,
   Under consideration for publication in Journal of Fluid Mechanics, pre-print available on the arXiv

7. N. Gautier, J-L Aider, T. Duriez, B.R. Noack, M. Segond, M. Abel. 2014
   Closed-loop control of a wall-bounded separation experiment using machine learning,
   Under consideration for publication in Journal of Fluid Mechanics, pre-print available on the arXiv

Contents

Part I

Introduction

Chapter 1

Introduction

The research effected during this thesis sits at the interface of several disciplines: fluid mechanics, control theory and computer vision.

1.1 Flow control

In addition to being of significant academic interest fluids play a large role in a plethora of industrial applications. A few examples: automobile, aircraft and ship drag, mixing in combustion chambers, and cooling in nuclear power plants (figure 1.1).

Figure 1.1

While a wealth of information can be learned through observation, some seek to go beyond observation, to control. Active flow control is at the interface of fluid mechanics and control theory. Through flow control we could increase vehicle efficiency, reducing our carbon emissions and improving operating costs, mitigating future rises in oil and gas prices. Unfortunately fluids are not so easily commanded, they can be tricky and capricious. Exerting any kind of influence is a difficult task.

The governing equations (Navier-Stokes equations, described in appendix B) for most common fluids, namely water and air, have been known for the past two-hundred years. Despite this a formal mathematical solutions eludes mathematicians and physicists alike. Thus numerical simulations and experiments are used to investigate fluids. Solving these equations numerically is possible but time consuming. Furthermore it is only possible for small volumes and simple geometries. In fact if there are no groundbreaking advances in computing technology completely solving the Navier-Stokes equations for practical flows will remain unattainable. Experimental work, while cumbersome, unyielding and error prone, remains essential to scientific process.
Flow control is a vast discipline. There are two categories for any type of control: passive and active control. Passive means of flow control, where no energy is supplied to the system are common. Automobiles for example are optimized to reduce aerodynamic drag as illustrated on figure 1.2 illustrates this.

(a) High drag shape

(b) Lower drag shape (twice the aerodynamic efficiency)

Figure 1.2

More sophisticated passive control methods involve adding flow control devices to the vehicles. For example in Godart and Stanislas (2005), Godart et al. (2005a,b) passive vortex generators are used to control a decelerating boundary layer. In Aider et al. (2010) active vortex generators (trapezoidal tabs) are used to reduce the drag of a 3D bluff body. Passive control should be attempted before searching for more complex means of control. Figure 1.3 shows real world examples of passive control. However many passive means of control have been exhausted and thoroughly researched. In some cases we have reached the limit of what can be done with passive control, most notably thanks to potential flow theory. In other cases where improvements can be still be made (i.e. most modern cars) other constraints such as aesthetics, size, comfort, safety, reliability and cost prohibit perfect aerodynamic

form. Despite its advantages, passive control has limitations, most notably, once the system is tuned to specific working conditions everything is fixed. Therefore if operating conditions change too much control might become ineffective, or in some cases make things worse. To enable further improvement active control is considered.

(a) Passive blowing to lower drag induced by the wheels

(b) Active vortex generators on the concept Citroën C-Airlounge

Figure 1.3

Control is called active when energy is supplied to the system. Active flow control can be further sub-categorized into open and closed loop control. Wing flaps and rudders on airplanes and boats are a form of active open loop flow control. Energy is supplied to the flaps allowing them to move, thereby modifying airflow around them. Open loop means the control action is not based on any observations of the flow. Open-loop control is common in flow control. The first open-loop active control demonstration for a full sized airplane was performed by Wygnanski (2004). In Protas and Wesfreid (2002a) a cylinder is rotated, for certain configurations this drives the mean flow towards a lower drag state. In Joseph et al. (2013) micro jets were used to increase pressure recovery on the rear of an Ahmed body. In Shaqarin et al. (2013) open-loop control is used to limit separation of a turbulent boundary layer after a sharp variation in wall geometry (a ramp).

1.2 Closed-loop control

The distinction between active and open loop control is fundamental as open-loop control methods cannot adapt to unexpected changes in operating conditions. Closed loop control requires a sensor component. Information is obtained by one or several sensors, which is used to determine optimal control action. Furthermore since the system is monitored, changes in the environment or the system itself can be accounted for ensuring an element of stability and robustness. The great benefits of closed loop control are balanced by its complexity: poorly implemented control can saturate actuators, possibly damaging the system or causing additional unsteadiness. Control theory deals with every manner of closed-loop approaches. The first formal analysis of the field was conducted by James Clerk Maxwell Maxwell (1868) on governors. Figure 1.4 shows an example of closed loop control in the human body.

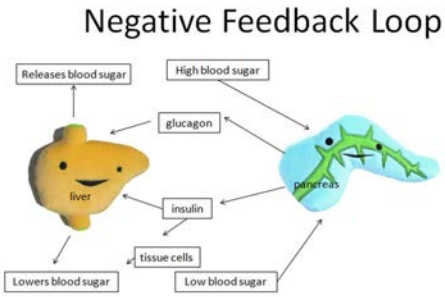

Figure 1.4: Sketch of closed loop control in biology

Since then the field has become a scientific domain of its own. Applying this knowledge to flow control has yielded many different approaches. Here we will briefly detail the main types of approaches, highlighting the advantages and disadvantages of each as well as cases of successful implementation. This, by no means an exhaustive list, is meant to give the reader context and a better understanding of the different flow control approaches featured in this work.

1.2.1 Adaptive control

Adaptive control does not require a model for the system, which is its biggest asset. At each instant system state is ascertained through measurements. The goal of adaptive control is to deliver the best actuation possible in order to bring the system to the desired state regardless of exogenous events such as unwanted perturbations. The proportional integral derivative (PID) controller is simple to apprehend and put to use yet can be very effective. It links the control input to the difference between measured and desired system output. Chapter 5 features an implementation of a PID controller. In Garwon et al. (2003) a PID controller is used to control a separated 2D flow. In Patnaik and Wei (2002) the same type of controller is used to reduce shedding behind a square cylinder. PID control is also used in conjunction

with other non-linear designs to control the span-wise recirculation length downstream a step in Henning and King (2007). This approach has since been expanded upon and used for to alter the lift configuration of a full sized wing (Kerstens et al. (2011)), which could lead to different lift-off and takeoff procedures for airplanes, potentially increasing the throughput of a given airport.
Slope-seeking algorithms are used to bring a measured variable of a system such as drag to an extremum. No modeling is required. Moreover the technique is quite robust. Any system featuring a extrema is susceptible to this type of control. This approach does places several constraints on actuation. In order for this approach to work a low frequency component must be added to actuation. A detailed explanation of this method can be found in Ariyur and Krstic (2004). This is a very general method. In Beaudoin et al. (2006) extremum-seeking is used to pilot a cylinder placed at the separation edge of a bluff body. The same approach is used for an Ahmed body in Beaudoin et al. (2008). Control is able to quickly minimize drag behind the body, resulting in a positive energy balance. In Pastoor et al. (2008) the shear layer behind a bluff body is controlled using a combination of jets together with pressures gauges. A wide array of control methods are featured in this study including extremum and slope-seeking which are used to maximize pressure recovery behind the body, leading to reduced drag. In general it is more difficult to implement than PID controllers.
It should be noted that model-independent controllers while very robust take some time to adapt to changing flow condition making them potentially slower than model based controllers.

1.2.2 Model based control

Another approach consists in modeling the flows as non-linear systems of infinite order (derived from the Navier-Stokes equations). Attempts have been made to design a controller based on the full-order Navier-Stokes equation. In Bewley (2001) optimal control is used on low Reynolds number DNS simulations. Protas and Wesfreid (2002b) use a vorticity equation derived from the Navier-Stokes formula for optimal control. While no reduction is made this kind of approach requires full knowledge of the flow (restricting it to 2D flows for now) and is computationally costly making it impractical for practical applications. However such an approach can be used to determine the full potential of an actuator or given control method.
On the opposite side of the spectrum lie phenomenological models based on observations of the physics of the flow. This approach cannot be made systematic and is not always applicable. However when it is relevant it can yield very simple models for the dominant dynamics of the flow leading to fast and efficient control. For example the wake behind a cylinder at low Reynolds number behaves like a non-linear oscillator (Provansal et al. (1987)) and can be modeled in a very simple fashion (Protas and Wesfreid (2002a), Thiria et al. (2004)). In Pastoor et al. (2008) several control methods are applied to reducing bluff body drag. The study culminates on the development of a very simple physics based model linking the output of a single pressure sensor to edge actuation. The control displays the same drag reduction as extremum-seeking while being 50 times faster at producing the reduction.
In practice however most attempts at model-based flow control feature a reduction step in which a low-order model is created, either directly from the Navier-Stokes equations or

empirical data from simulations and/or experiments. Such a step is crucial in model design. If the flow exhibits linear behavior a number of approaches are possible, J.Kim and Bewley (2007). When it comes to controlling linear systems, control theory literature is very rich. Linear models for flow control have been the subject of intensive study. In Becker et al. (2005) simple linear black-box models are used to describe the behavior of recirculation behind an experimental step, leading to the set point control of recirculation length. Most of the work on linear models for flow control is done in numerical simulations. Linear models can be derived from Galerkin projection of the linearized Navier-Stokes Equation, Rowley et al. (2004). These models are of very high order making computation of the control output too long for real-time control, thus they must first be reduced. Studies show using balanced POD modes yield efficient reduced-order models, Moore (1981), Rowley (2005). In Belson et al. (2013) linear reduced order models are used to determine optimal sensor/actuator placement for the control of a Blasius boundary layer. In Barbagallo et al. (2009) linear quadratic gaussian control is used with reduced order models to stabilize the unstable flow created by an open cavity. In Bagheri et al. (2009) a framework for input-output analysis leading to linear reduced order models is presented.
Linear models enable the use of powerful tools from control theory such as discrete time optimal and model predictive control, therefore it is enviable to seek such models for flow systems. Unfortunately most flows of interest are intrinsically non-linear. Making a linear model approach difficult. Furthermore few have applied these methods to experimental flows. Non-linear modeling is much harder, and thus less common. However examples exist, low-dimensional modeling has been used to effect successful sliding mode control of a bluff body wake, Luchtenburg (2010). Such control is a special case of variable structure control, a form of non-linear discontinuous control. The feedback control law is not a continuous function of time, it switches from one smooth condition to another potentially very quickly. The advantages of this particular method are robustness with regards to model uncertainty and convergence in finite time. However it is likely to quickly wear out actuators (due to fast switching) imposing heavy engineering constraints.

1.2.3 Machine learning

Finally, a radically different approach can be applied handle non-linearities. Genetic programming has been used in other disciplines for some time, when applied to flow control it makes novel approaches possible. It can be used to look for optimal, possibly non-linear control laws. Randomly generated control laws are evaluated with respect to a user defined cost function, from then on the process is completely hands-off. It allows for great freedom in terms of possible controls laws. New counter-intuitive laws can more easily be found bypassing any user bias. This approach is new to flow control. Theoretical and experimental work can be found in Duriez et al. (2014) and chapter 9.

Figure 1.5 summarizes this approach to flow control.

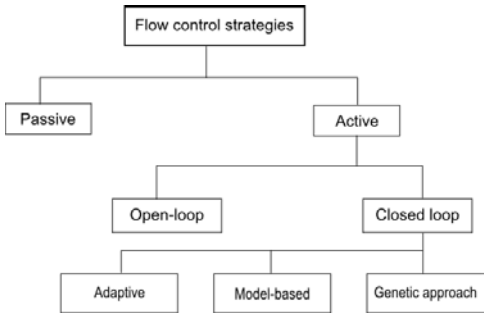

Figure 1.5: An approach to flow control

1.3 The special case of separated flows and the backward facing step geometry

The work presented in this manuscript focuses on the control of separated flows. These are ubiquitous in nature and industrial processes. Figure 1.6 illustrates examples of such flows. In automobile applications, separated flows cause most of the drag experienced by the vehicle. Recirculation on airfoils causes drag and sometimes severe loss of lift. Manipulating separation leads to pressure drag reduction, lift enhancement, stall delay, heat transfer improvement, dynamic load reduction and attenuation of excess noise and vibration. Additionally the performance of fans, turbines, compressors, pumps, and diffusers may be increased by delaying the onset of separation. In the case of separated flows open-loop control has been widely investigated: cavity control, Backward-facing step control, Ramp control, Ahmed Body. Because of it similarity to a moving ground vehicle, the Ahmed body, in all its declinations has been intensively studied, Vino et al. (2005), Fares (2006), Pujals et al. (2010), Joseph et al. (2012, 2013).

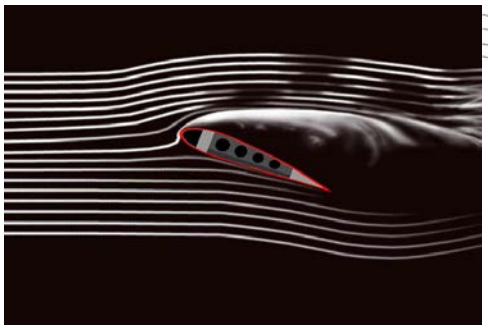

(a) Flow around a wing

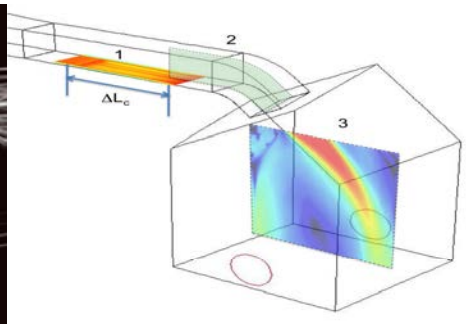

(b) Flow inside a combustion chamber

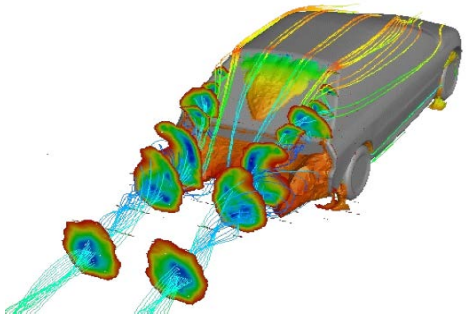

(c) Flow around a car

Figure 1.6

Several geometries can be used to study separated flows, such as the backward facing step, the inclined and rounded ramps. Figure 1.7 illustrates these common geometries. Red and dotted lines indicate typical recirculation locations and shape. Note that for the backwards facing step geometry separation is imposed by the edge, while for configurations feature a mobile separation point.

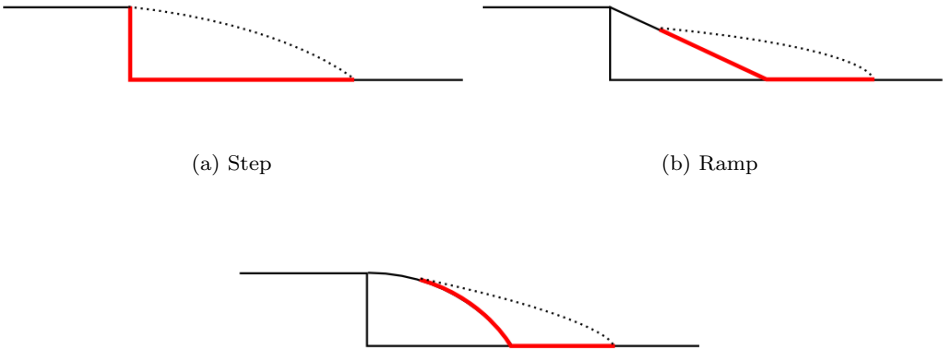

(a) Step

(b) Ramp

(c) Rounded ramp (Duriez et al. (2008))

Figure 1.7

The backward facing step has the advantage of being the simplest possible geometry. Flow separation is imposed at the step edge and therefore perfectly localized in space as shown in figure 1.8. The main feature of the backward facing step flow is the recirculation region, which appears as a result of separation. This flow has been extensively studied both numerically and experimentally (Armaly et al. (1983), Hung et al. (1997), Beaudoin et al. (2004), Aider et al. (2007)). Historically recirculation length has been used to characterize the flow as a whole. In flow control experiments recirculation reduction is almost always the control objective (Chun and Sung (1996), Becker et al. (2005)). However it is interesting to note there is no clear relationship between recirculation size and drag, as shown in chapter 3.

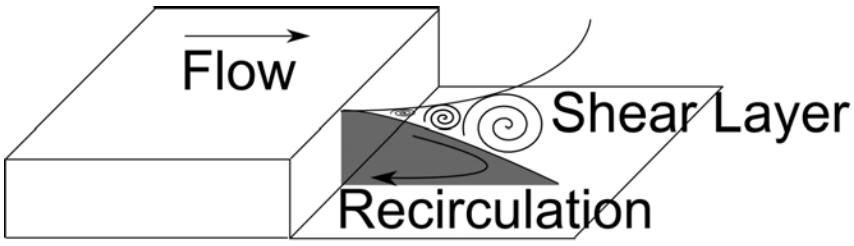

Figure 1.8: Sketch of a backward facing step

1.4 Optical sensors

Optical sensors can be used to effect flow measurements. There are many types of optical sensors, the most common is the human eye. Unfortunately one cannot download data from

them (yet). Therefore we rely on the now ubiquitous video camera. At its most fundamental level a video camera is a photon counting device, doing so many times per second (as opposed to a regular camera) ultimately yielding a series of images. An entire scientific field known as computer vision is dedicated to acquiring, processing, analyzing, and understanding images, usually all this is done in real-time.
Cameras have been used to quantitatively investigate fluid dynamics for over three decades. A common technique consists in seeding the flow with neutrally buoyant particles which act as tracers allowing the experimentalist to compute the flow velocity field. This method is invaluable as it yields rich quantitative information on the state of the flow, in addition velocity fields are essential to the numerical fluids mechanics community as it allows for validation of numerical experiments. However such a process can be burdensome. A typical experiment yields tens of thousands of images which have to be transfered from the camera buffer or the acquisition computer to a computing cluster to a personal workstation for analysis and post-processing. This process can be slow and inconvenient taking up to several days.
Particle Image Velocimetry (PIV) is widely used to compute 2D velocity fields (Westerweel (1993), Melling (1997), Wil (2007), U. Gülan (2012)). In PIV the image is discretized into sub-windows containing an average of five to ten particles. Their motion is estimated using cross correlation between two successive images. High particle concentration is required for optimal resolution. Adrian (2005) gives a thorough review of PIV methods. Other techniques exist to compute flow velocity fields. Particle Tracking Velocimetry (PTV) is based on the tracking of single particles between two successive images (Lüthi et al. (2005)). Particle concentration is typically an order of magnitude lower for PTV. Optical flow has been used in computer vision to compute image intensity displacement in robotic applications. It has successfully been used on images intended for PIV processing (Faure et al. (2010)). Figure 1.9 illustrates the fundamental difference between PIV and PTV.

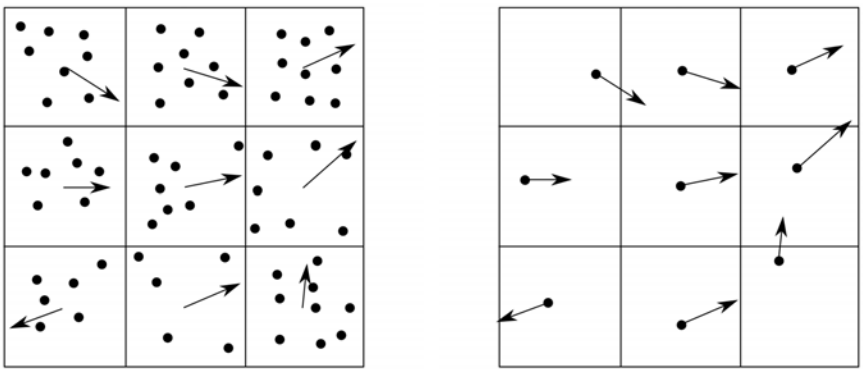

(a) PIV, computes the average displacement of particles

(b) PTV, tracks single particles

Figure 1.9

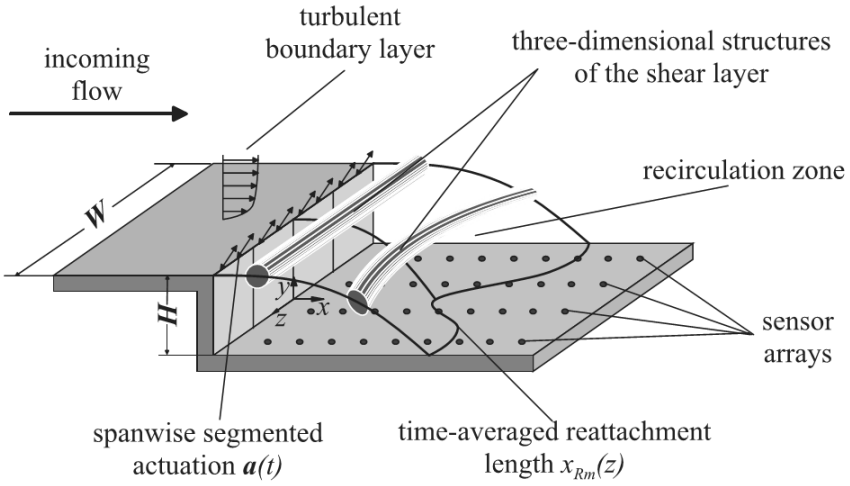

Figure 1.10: Experimental setup featuring wall sensors

Most closed-loop flow control experiments feature wall sensors (pressure, shear rate, see figure 1.10). An essential part of any control loop is the sensor, traditionally wall sensors are used in flow control experiments. Figure 1.10 shows a set-up featuring an array of pressure sensors designed to compute the extent of the recirculation bubble.

Pressure and friction sensors are the most common, they output local data at high frequencies. Their main disadvantage is that they give an incomplete snapshot of the flow. Furthermore the parietal nature of the information can make it difficult to access information far from the wall. Computing the flow state using incomplete information is a subject of ongoing research usually involving sophisticated techniques such as Kalman filters. In some cases a few well placed sensors give sufficient information for successful control (Pastoor et al. (2008)). However determining the most effective placement for these sensors requires time consuming parametric studies.

Recent increases in computing power allow us to consider real-time, i.e. high frequency low latency computation of velocity fields. Essentially binding image acquisition, processing and post-processing into a single streamlined process. This turns every pixel of the camera into a sensor yielding a wealth of information and direct unfettered access to the flow state. Because of rising user demand for graphic intensive applications personal computers now feature both a central processor unit (CPU) and a graphic processor unit (GPU). In terms of raw computing power the GPU far outclasses the CPU as shown in figure 1.11. This is because GPU's feature a massively parallel architecture, using thousands of processing cores whereas modern CPU's typically feature only 4. The difference between CPU and GPU processing is succinctly and colorfully explained in Sav (2010).

Recently GPU programming has become increasingly accessible thanks to efforts made by manufacturers. Programming languages such as OpenCL and CUDA now provide extensions to common languages such as C++ and Fortran. However not all programs benefit from a GPU implementation in the same way. In some cases performance can worsen. In chapter

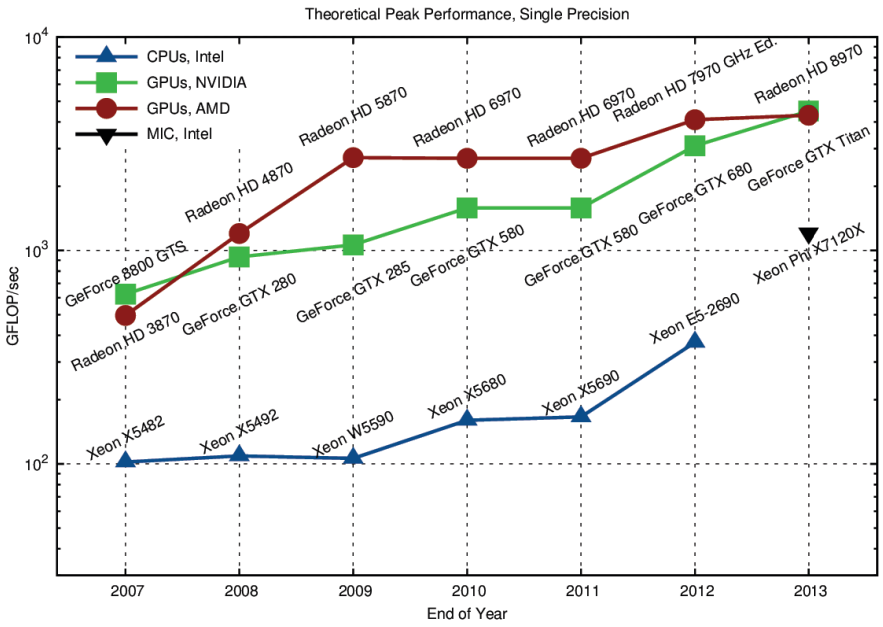

Figure 1.11: CPU vs GPU processing power trend, note the logarithmic scale

4 we will show how computer code developed at ONERA and subsequently improved over the course of this thesis is parallelized to leverage the awesome power of the GPU enabling real-time computation of flow velocity fields.

1.5 Actuation

There are many ways to act on a flow. Cattafesta and Sheplak (2011) gives a thorough review of the different possible actuators. Figure 1.12a shows a possible actuator classification. In dense fluids like water, jet actuation is widely used (Rathnasingham and Breuer (1990), Jacobsen and Reynolds (1998)) however other less conventional means of control have been investigated. Most notably moving the wall itself (Breuer et al. (1989), Endo et al. (2000), Du et al. (2002), Iwamoto et al. (2005), Koberg (2007)). Deployable flaps have shown promise as vortex generators (Choi et al. (1994)). Underwater speakers are another potential option.
When the fluid is lighter such as air, actuators are more plentiful. A lot of research has gone into making viable plasma actuators (T. Duriez (2014), Thomas et al. (2009)). Electrodes are placed in the flow, applying a current strips the fluid molecules of some electrons (ionization) creating a plasma, which can then be manipulated by electromagnetic forces. Plasma actuators can be used to create a body force near the wall. This presents several advantages: this force can be modeled and directly included into the Navier-Stokes equation which makes simulation easier, the force acts very close to the wall making actuation potentially more efficient and effective in addition to being relatively easy to implement. Furthermore the

force is perfectly tangential to the flow allowing for better near wall actuation. The main disadvantage of plasma actuators is that they cannot yet accelerate the fluid past 10 $m.s^{-1}$ which is to slow for practical applications to external aerodynamics of air and ground vehicles.
Speakers placed in the flow are a popular method for acting on light fluids Chun and Sung (1996), Henning and King (2007), they are simple, cheap and easy to control. Mechanical flaps are used for control on airplanes and ships as well as flow control experiments (Lai et al. (2002)). Blowing/suction using jets is also widely used (Yoshioka et al. (2001), Uruba et al. (2007)). Figure 1.12b shows different types of actuators applied to a backward facing step configuration, from Garrido (2014). One should note actuators such as jets or solid vortex generators can be placed upstream the step edge and remain effective as will be shown in chapter 6.

The work presented in this manuscript features wall jets as actuators. The reason for this is twofold: wall jets are relatively easy to implement and remain the simplest way to effect actuation in a dense fluid such as water. Furthermore this work was part of a broader research effort by the instability, control and turbulence team at PMMH. Past researchers have focused on studying the effect of jets on the flow Beaudoin (2004), Duriez (2009), Cambonie (2012). The study of jets in cross-flow is a vast area of fluid mechanics, indeed their behavior is far from simple. Furthermore they occur in a number of natural and industrial processes such as air injection in gas turbines, thrust vector control for high speed vehicles and exhaust plumes for power plants. Making their study relevant to industry. For more information on transverse jets see Karagozian (2010), Margarson (1993).
The beginning of this work was devoted to studying round jets in cross-flow using a novel volumetric velocimetry technique. Three cameras (with set angles) are used to capture a laser illuminated flow volume. Identifying the same particle in all three images allows for the determination of particle position in 3D space. Once this has been done for all image triplets standard tracking techniques are used in pairs of triplets to determine particle velocity, finally interpolation is used to yield a regular 3D velocity grid for the observed volume. This allows for the computation of experimental three-dimensional instantaneous fields. The focus was primarily on jet trajectories. In an effort to further qualify actuation the objective was to determine a scaling law allowing us to predict the position of a jet beforehand. The ultimate goal being better actuators which could better affect the flow, leading to better control. This work culminated in a global scaling law for low velocity ratio round jets, published results are shown in appendix A (Cambonie et al. (2013)). Further exploitation of these and other 3D fields featuring jets with round or different geometries can be found in Cambonie and Aider (2014).

1.6 Control of the recirculation past a backward facing step

Open-loop control of the backward facing step flow has been investigated for a wide range of operating conditions, actuators and sensors. Table 1.1 summarizes the results of several past studies with regards to open-loop performance. The focus was on recirculation length reduction. The most effective actuators are the flapping foil placed inside the shear layer Lai

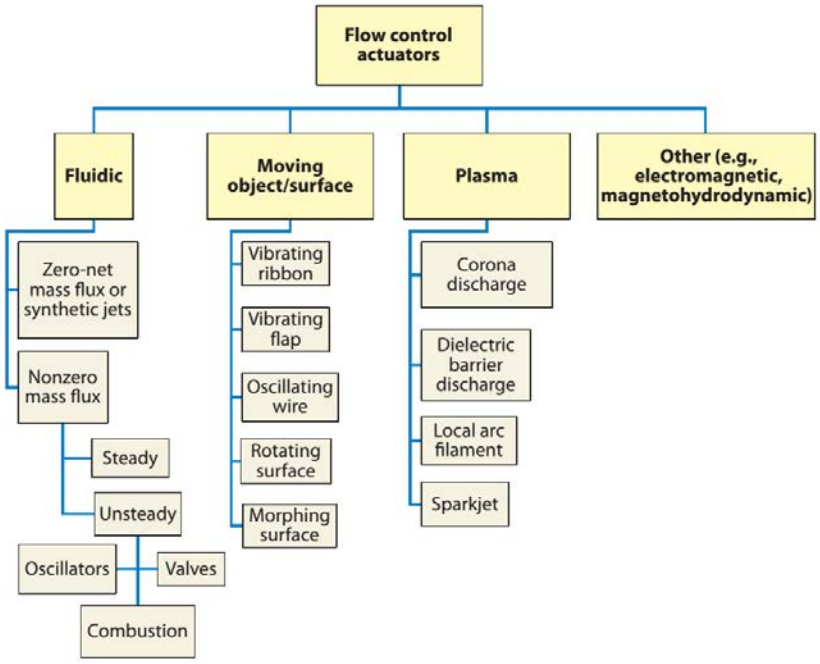

(a) Summary of different actuators applied to the backward facing step flow, from Cattafesta and Sheplak (2011)

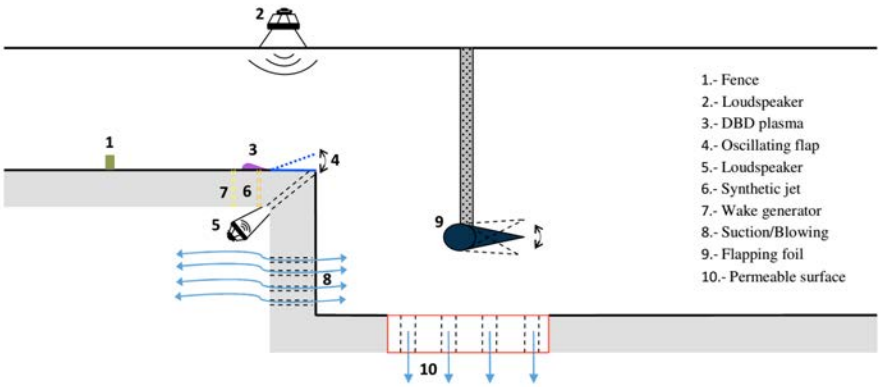

(b) Summary of different actuators and their location applied to the backward facing step flow, from Garrido (2014)

Figure 1.12

	Re_h	St_h	$X_r/X_{r,0}$	Device	Location	Method
Chun and Sung (1996)	$13-33000$	0.27	65 %	Open-loop: Loudspeaker	Step edge	Experimental
Lai et al. (2002)	12700	0.18	30 %	Open-loop: Flapping foil	Immerged shear layer	Experimental
Yoshioka et al. (2001)	$1800-5500$	0.19	69%	Open-loop: Slots	Step edge	Experimental
Chun et al. (2004)	33000	0.2	89%	Open-loop: Wake generator	Step back	Experimental
Uruba et al. (2007)	35000	0	31 %	Open-loop: Blowing/Suction	Step bottom	Experimental
Garrido (2014)	30000	0.25	20 %	Open-loop : Plasma DBD	Upstream step	Experimental
Henning and King (2007)	0-25000	-	65 %	Closed-loop: Loudspeakers	Step edge	Experimental
Wengle et al. (2001)	3000	0.21/0.48	67 %	Open-loop: Loudspeakers	Step edge	Numerical (DNS/LES)
Neumann and Wengle (2003)	3000	0	87 %	Open-loop: Fences	Upstream	Numerical (DNS/LES)

Table 1.1: Results from past studies for recirculation manipulation

et al. (2002), and continuous suction/blowing at the step bottom Uruba et al. (2007).
In the flapping foil case the best placement is where vortex shedding would begin in the uncontrolled shear layer. While considerable reduction is accomplished, introducing a flap inside the flow poses engineering constraints and might be impractical in a more realistic setting. Continuous suction/blowing at the bottom of the step induces significant reduction in Uruba et al. (2007). The only downside might be actuation cost, as constant blowing and/or suction requires more energy than pulsed actuation. It is worthy of mention however that in simulations by Dahan and Morgans (2012) at $Re_h \approx 10000$ pulsed suction/blowing at the step bottom has very little effect (5 % reduction).

1.7 Thesis organization

The first part of this thesis is organized as follow. Chapter 2 presents the experimental setup, chapter 3 general thoughts on the qualification of separated flows, chapter 4 the GPU algorithm used to effect real-time velocity computations, Chapter 6 the effects of upstream

actuation, Chapter 5 our first attempt at flow control by visual feedback, Chapter 7 physically driven separated flow control, Chapter 8 feed-forward control of the backward facing step flow, chapter 9 presents the results obtained using a genetic algorithm.

Bibliography

Particle Image Velocimetry - A Practical Guide. Springer, 2007.

video : Adam and jamie paint the mona lisa in 80 milliseconds, 2010.

R. J Adrian. Twenty years of particle image velocimetry. *Exp. Fluids*, 39(2):159–169, August 2005.

J-L. Aider, A. Danet, and M. Lesieur. Large-eddy simulation applied to study the influence of upstream conditions on the time-dependant and averaged characteristics of a backward-facing step flow. *Journal of Turbulence*, 8, 2007.

Jean-Luc Aider, Jean-François Beaudoin, and José Eduardo Wesfreid. Drag and lift reduction of a 3d bluff-body using active vortex generators. *Exp. Fluids*, 48(5):771–789, 2010.

Kartik B. Ariyur and Miroslav Krstic. Slope seeking: a generalization of extremum seeking. *International journal of adaptive control and signal processing*, 18:1–22, 2004.

B. F. Armaly, F. Durst, J. C. F. Pereira, and B Schonung. Experimental and theoretical investigation of backward-facing step flow. *J. Fluid Mech*, 127:473–496, 1983.

S. Bagheri, D.S. Henningson, J. Hoepffner, and P.J. Schmid. Input-output analysis and control design applied to a linear model of spatially developing flows. *Applied Mechanics Reviews*, 62, 2009.

A. Barbagallo, D. Sipp, and P.J. Schmid. Closed-loop control of an open cavity flow using reduced-order models. *J. Fluid Mech*, 641:1–50, 2009.

J-F. Beaudoin. *Active control and modal structures in transitional shear flows*. PhD thesis, PSA-ESPCI, 2004.

J-F. Beaudoin, O. Cadot, J-L. Aider, and J.E. Wesfreid. Three-dimensional stationary flow over a backwards-facing step. *European Journal of Mechanics*, 38:147–155, 2004.

J.-F. Beaudoin, O. Cadot, J.-L. Aider, and J. E. Wesfreid. Drag reduction of a bluff body using adaptive control methods. *Physics. Fluids*, 18:1, 2006.

J-F. Beaudoin, O. Cadot, J-E. Wesfreid, and J-L. Aider. Feedback control using extremum seeking method for drag reduction of a 3d bluff body. *IUTAM Symposium on Flow Control and MEMS*, 7:365–372, 2008.

R. Becker, M. Garwon, C. Gutknecht, G. Barwolff, and R. King. Robust control of separated shear flows in simulation and experiment. *Journal of Process Control*, 15:691–700, 2005.

B.A. Belson, O. Semeraro, C.W. Rowley, and D.S. Hennginson. Feedback control of instabilities in the two-dimensional blasius boundary layer: The role of sensors and actuators. *Physics of fluids*, 25, 2013.

T.R. Bewley. Flow control: new challenges for a new renaissance. *Prog. Aerospace Sci*, 37: 21–58, 2001.

K.S. Breuer, J.H. Haritonidis, and M.T. Landahl. The control of transient disturbances in a flat plate boundary layer through active wall motion. *Phys. Fluids*, 1(574), 1989.

T. Cambonie. *Study of low velocity ratio jet in cross-flows by volumetric velocimetry.* PhD thesis, ESPCI, 2012.

T. Cambonie and J-L. Aider. Transition scenario of the round jet in crossflow topology at low velocity ratios. *available on the arXiv*, 2014.

T. Cambonie, N. Gautier, and J-L. Aider. Experimental study of counter-rotating vortex pair trajectories induced by a round jet in cross-flow at as a function of re_h velocity ratios. *Exp. Fluids*, 54(3):1–13, 2013.

L. Cattafesta and M. Sheplak. Actuators for active flow control. *Annu. Rev. Fluid Mech*, 43:72–247, 2011.

H. Choi, P. Moin, and J. Kim. Active turbulence control for drag reduction in wall-bounded flows. *J. Fluid Mech*, 262(75), 1994.

K. B. Chun and H. J Sung. Control of turbulent separated flow over a backward-facing step by local forcing. *Exp. Fluids*, 21:417–426, 1996.

S. Chun, Y. Zheng Liu, and H. Sung. Wall pressure fluctuations of a turbulent separated and reattaching flow affected by an unsteady wake. *Exp. Fluids*, 37:531–546, 2004.

J. Dahan and A. Morgans. Feedback control for form-drag reduction on a bluff body with a blunt trailing edge. *J. Fluid Mech*, 704:360–387, 2012.

Y. Du, V. Symeonidis, and G.E. Karniadakis. Drag reduction in wall-bounded turbulence via a transverse travelling wave. *J. Fluid Mech*, 457(1), 2002.

T. Duriez. *Control of separated flows using vortex generators.* PhD thesis, ESPCI, 2009.

T. Duriez, J-L. Aider, and J.E. Wesfreid. Non-linear modulation of a boundary layer induced by vortex generators. *Proceedings of the 4th AIAA conference on flow control, Seattle, USA*, 2008.

T. Duriez, V. Parezanovic, L. Cordier, B. Noack, J. Delville, J.P. Bonnet, M. Segond, and M. Abel. Closed-loop turbulence control using machine learning. *arXiv, submitted to J. Fluid Mech*, 2014.

T. Endo, N. Kasagi, and Y. Suzuki. Feedback control of wall turbulence with wall deformation. *Int. J. heat Fluid Fl*, 21(568), 2000.

E. Fares. Unsteady flow simulation of the ahmed reference body using a lattice boltzmann approach. *Comput. Fluids*, 35:940–950, 2006.

T. Faure, C. Douay, S. Mochki, F. Lusseyrand, and G. Quenot. Stereoscopic piv using optical flow: investigation of a recirculating cavity flow. *8th International ERCOFTAC Symposium on Engineering Turbulence Modeling and Measurements*, 3:905–910, 2010.

Patricia Sujar Garrido. *Active control of the turbulent flow downstream of a backward facing step with dielectric barrier discharge plasma actuators.* PhD thesis, Poitiers University, 2014.

M. Garwon, L.H. Darmadi, F. Urzynicok, G. Bärwolff, and R. King. Adaptative control of separated flows. *Proc. of the 2003 European Control Conference, Cambridge UK*, 2003.

G. Godart and M. Stanislas. Control of a deccelerating boundary layer. part 1: Optimisation of passive vortex generators. *Aero. Sc. Technol*, 10(3):181–191, 2005.

G. Godart, J.M. Foucault, and M. Stanislas. Control of a deccelerating boundary layer. part 2: Optimisation of passive vortex generators. *Aero. Sc. Technol*, 10(5):394–400, 2005a.

G. Godart, J.M. Foucault, and M. Stanislas. Control of a deccelerating boundary layer. part 2: Optimisation of passive vortex generators. *Aero. Sc. Technol*, 10(6):455–464, 2005b.

L. Henning and R. King. Robust multivariable closed-loop control of a turbulent backward-facing step flow. *Journal of Aircraft*, 44, 2007.

L. Hung, M. Parviz, and K. John. Direct numerical simulation of turbulent flow over a backward-facing step. *J. Fluid Mech*, 330:349–374, 1997.

K. Iwamoto, K. Fukagata, N. Kasagi, and Y. Suzuki. Friction drag reduction achievable by near wall turbulence manipulation at high reynolds numbers. *Phys. Fluids*, 17, 2005.

S. Jacobsen and W.C. Reynolds. Active control of streamwise vortices and streaks in boundary layers. *J. Fluid Mech*, 360(179), 1998.

J.Kim and T.R. Bewley. A linear systems approach to flow control. *Annu. Rev. Fluid Mech*, 39:383–417, 2007.

P. Joseph, X. Amandolese, and J. L Aider. Drag reduction on the 25 degrees slant angle ahmed reference body using pulsed jets. *Exp. Fluids*, 52(5):1169–1185, May 2012.

P. Joseph, X. Amandolese, C. Edouard, and J.-L Aider. Flow control using mems pulsed micro-jets on the ahmed body. *Exp. Fluids*, 54(1):1–12, 2013.

Ann Karagozian. Transverse jets and their control. *Progress in Energy and Combustion Science*, 36(5):531–553, OCT 2010.

W. Kerstens, J. Pleiffer, D. Williams, R. King, and T. Colonius. Closed-loop control of lift for longitudinal gust suppression at low reynolds numbers. *AIAA Journal*, 49(8), 2011.

H. Koberg. *Turbulence control for drag reduction with active wall deformation*. PhD thesis, Imperial College, 2007.

S.J.C. Lai, J. Yue, and M.F.Platzer. Control of a backward-facing step flow using a flapping foil. *Exp. Fluids*, 32:44–54, 2002.

B. Lüthi, A. Tsinober, and W. Kinzelbach. Lagrangian measurement of vorticity dynamics in turbulent flow. *J. Fluid Mech*, (528):87–118, 2005.

Dirk Martin Luchtenburg. *Low-dimensional modelling and control of separated shear flows*. PhD thesis, Berlin Institute of Technology, 2010.

R.J. Margarson. Fifty years of jet in cross flow research. *AGARD*, pages 1–141, 1993.

J. Maxwell. On governors. *Proc. Royal Society*, (100), 1868.

A. Melling. Tracer particles and seeding for particle image velocimetry. *Measurement Science and Technology*, (8), 1997.

B. Moore. Principal component analysis in linear systems: Controllability, observability, and model reduction. *IEEE Trans. Autom. Control*, 26(1):17–32, 1981.

J. Neumann and H. Wengle. Dns and les of passively controlled turbulent backward-facing step flow. *Flow, Turbulence and Combustion*, 71:297–310, 2003.

Mark Pastoor, Lars Henning, Bernd R. Noack, Rudibert King, and Gilead Tadmor. Feedback shear layer control for bluff body drag reduction. *J. Fluid Mech*, 608:161–196, 2008.

B.S.V. Patnaik and G.W. Wei. Controlling wake turbulence. *Phys. Rev. Lett*, 88, 2002.

B. Protas and J. Wesfreid. Drag force in the open-loop control of the cylinder wake in the laminar regime. *Phys. Fluids*, 14(808), 2002a.

B. Protas and J. E. Wesfreid. Drag force in the open-loop control of the cylinder wake in the laminar regime. *Physics. Fluids*, 14:810, 2002b.

M. Provansal, C. Mathis, and L. Boyer. Benard-von kármán instability: transient and forced regimes. *J. Fluid Mech*, 182:1–22, 1987.

G. Pujals, S. Depardon, and C. Cossu. Drag reduction of a 3d bluff-body using coherent streamwise streaks. *Exp. Fluids*, 49:1085–1094, 2010.

R. Rathnasingham and K.S. Breuer. Active control of turbulent boundary layers. *J. Fluid Mech*, 495(209), 1990.

C.W. Rowley. Model reduction for fluids, using balanced proper orthogonal decomposition. *Intl J. Bifurcation Chaos*, 15(5):255–289, 2005.

C.W. Rowley, T. Colonius, and R.M. Murray. Model reduction for compressible flows using pod and galerkin project. *Physica D*, 189:115–129, 2004.

T. Shaqarin, C. Braud, S. Coudert, and M. Stanislas. Open and closed-loop experiments to identify the separated flow dynamics of a thick turbulent boundary layer. *Exp. Fluids*, 54: 1432–1114, 2013.

J. Wesfreid G. Artana T. Duriez, J-L. Aider. Control of a backward-facing step flow through vortex pairing and phase locking. *arXiv*, 2014.

B. Thiria, S. Goujon-Durand, and E. Wesfreid. Fluid structure interaction as a factor of drag modification. *J. Fluids Struc*, 2004.

F. Thomas, T. Corke, M. Iqbal, A. Kozlov, and D. Schatzman. Optimization of dielectric barrier discharge plasma actuators for active aerodynamic flow control. *AIAA Journal*, 47 (9), 2009.

M. Holzner A.Liberzon A. Tsinober W. Kinzelbach U. Gülan, B. Lüthi. Experimental study of aortic flow in the ascending aorta via particle tracking velocimetry. *Exp. Fluids*, 53(5): 1469–1485, 2012.

V. Uruba, P. Jonas, and O. Mazur. Control of a channel-flow behind a backward-facing step by suction/blowing. *Heat and Fluid Flow*, 28:665–672, 2007.

G. Vino, S. Watkins, P. Mousley, J. Watmuff, and S. Prasad. Flow structures in the near wake of the ahmed mode. *J. Fluids Struct*, 2005.

H. Wengle, A. Huppertz, G. Bärwolff, and G. Janke. The manipulated transitional backward-facing step flow: an experimental and direct numerical simulation investigation. *European Journal of Mechanics - B/Fluids*, 20:25–46, 2001.

J. Westerweel. *Digital particle image velocimetry: theory and application*. PhD thesis, TU Delft, 1993.

I. Wygnanski. The variables affecting the control of separation by periodic excitation. *AIAA Paper*, pages 2004–2505, 2004.

S. Yoshioka, S. Obi, and S. Masuda. Organized vortex motion in periodically perturbed turbulent separated flow over a backward-facing step. *Int.l Journal of Heat and Fluid Flow*, 22:301–307, 2001.

Chapter 2

Experimental setup

The experimental work presented in this manuscript was effected in a hydrodynamic channel using the following setup.

2.1 Hydrodynamic channel

In this hydrodynamic channel the flow is driven by gravity. A single pump is used for water motion. Water is pumped from a bottom tank to a top tank in a continuous closed loop (see figure 2.1c). The pump is fully submerged and uses ambient water for cooling purposes, this induces a steady rise in temperature. For short experiments this is not a problem as water temperature is monitored and does not vary over the course of the acquisition, longer experiments (up to a week) must be done when water temperature has reached a plateau and viscosity stays constant. The flow in the test section is stabilized by divergent and convergent sections separated by honeycombs (see figure 2.1c). This is done to make the flow laminar and avoid disturbances in the flow downstream. Furthermore any large scale structures created upstream are nullified after passing through the honeycomb mesh. Figure 2.1c shows a sketch of the channel, figure 2.1a shows a rendering of the channel and figure 2.1b

The quality of the main stream can be quantified in terms of flow uniformity and turbulence intensity. The standard deviation σ is computed for the highest free stream velocity of our experimental setup. We obtain $\sigma = 0.059$ cm.s^{-1} which corresponds to turbulence levels of $\frac{\sigma}{U_\infty} = 0.0023$. The channel is fully instrumented: water level, temperature and flow rate are constantly monitored. This is done so that experiments can be more easily reproduced. Furthermore it is convenient to monitor water level so that longer running, unsupervised experiments can be stopped should any problems arise. Free stream velocity U_∞ varies from 0 to 0.22 $m.s^{-1}$. This corresponds to Reynolds number based on step height $Re_h = U_\infty h/\nu$ ranging between 0 and 33000 (for more information on the Reynolds number see appendix B), with U_∞ the free stream velocity and ν the kinematic viscosity.

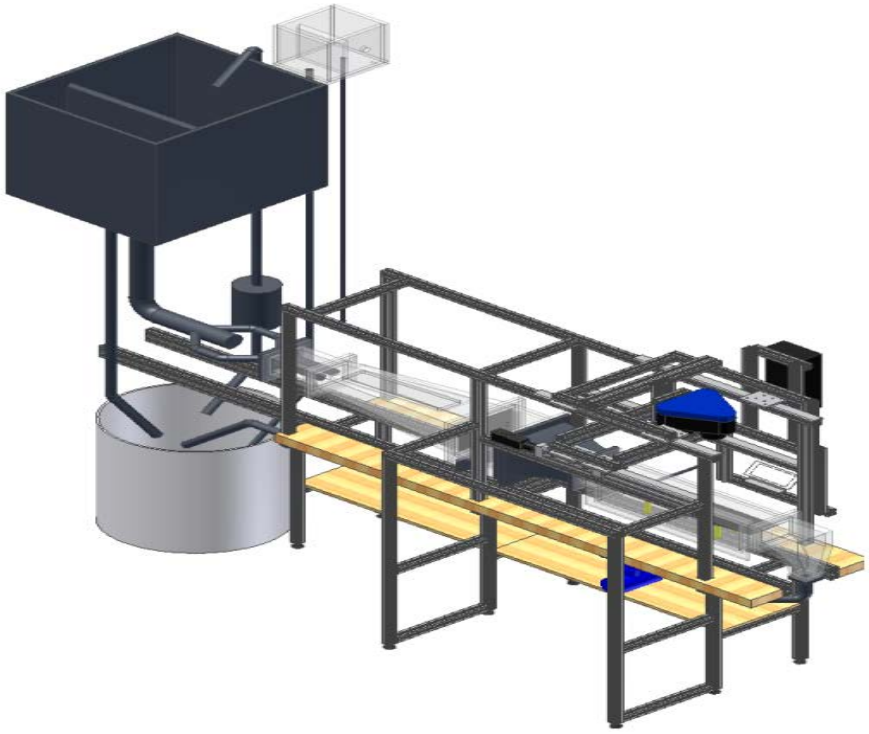

(a) Computer rendering of the channel

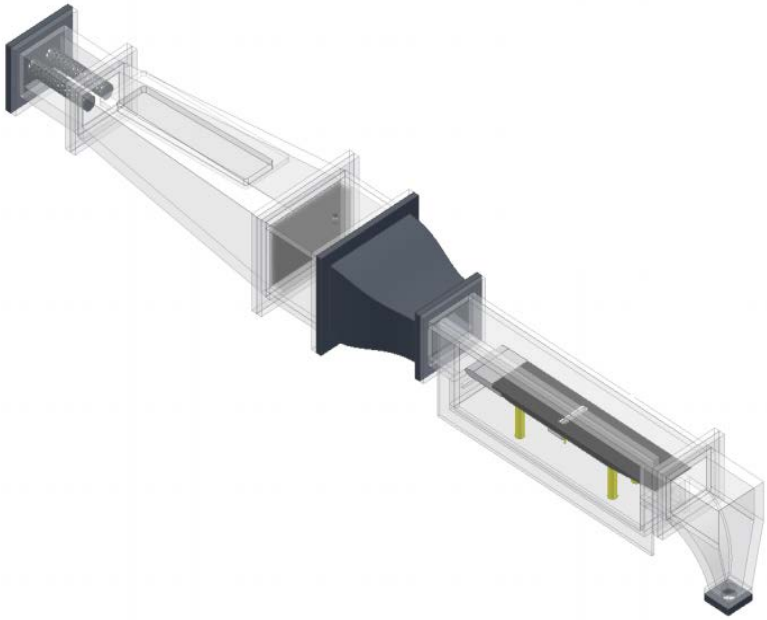

(b) Rendering of the test section with a flat plate, can be switched for the backward facing step configuration.

Figure 2.1

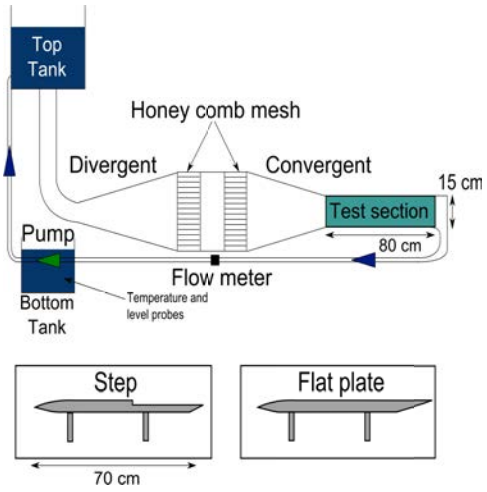

(c) Sketch of the hydrodynamic channel

Figure 2.1

2.2 Leading edge and boundary layer thickness

A custom made plate with a specific leading-edge profile (NACA0019, shown in figure 2.1b and 2.6e) is used to start the boundary layer. Figure 2.2 compares experimental and theoretical velocity profiles at the step edge, illustrating the laminar nature of the boundary layer. Results deviate from the typical Blasius profile near the wall because velocity field computation involves a correlation window, thus near wall results are limited by the size of the window which in turn is limited by displayed particle density. Mean shape factor $H = \delta^*/\theta$ across the range of Reynolds numbers is $\overline{H} = 2.60 \pm 0.05$, while $H_{Blasius} = 2.59$.

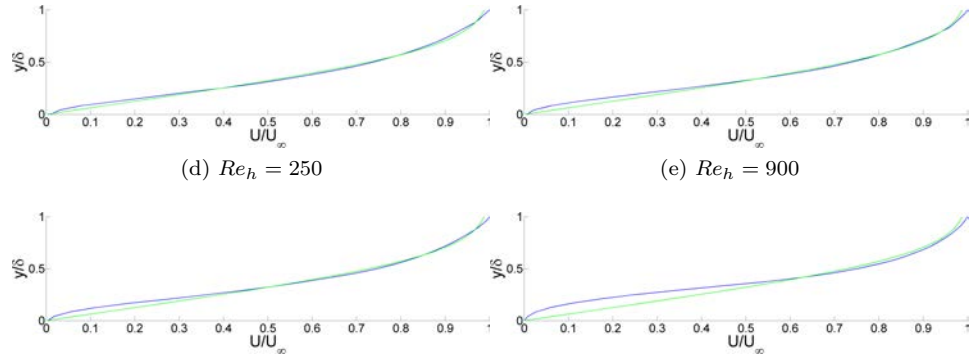

(d) $Re_h = 250$ (e) $Re_h = 900$

(f) $Re_h = 1350$ (g) $Re_h = 3380$

Figure 2.2: Experimental velocity profiles at the step edge (blue) and Blasius velocity profiles (green) for select Reynolds numbers (additional Reynolds numbers can be found in appendix D)

Figure 2.3 shows the evolution of boundary layer thickness at the step edge with Reynolds number, as is expected $\delta \propto \frac{1}{\sqrt{Re_h}}$.

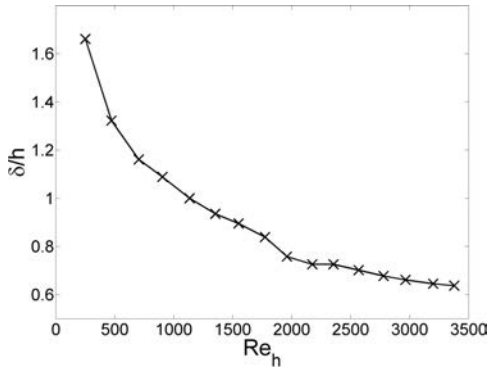

Figure 2.3: Boundary layer thickness scaled by step size as a function of Reynolds number

2.3 The backward facing step

Briefly introduced in the introduction the backward facing step is a benchmark for the study of separated flows. The backward facing step geometry and the main geometric parameters are shown in figure 2.4a. Step height is $h = 1.5$ cm. Channel height is $H = 7$ cm for a channel width $w = 15$ cm. The vertical expansion ratio is $A_y = \frac{H}{h+H} = 0.82$ and the spanwise aspect ratio is $A_z = \frac{w}{h+H} = 1.76$. The injection slot is located $d/h = 2$ upstream of the step edge (figure 2.4a).

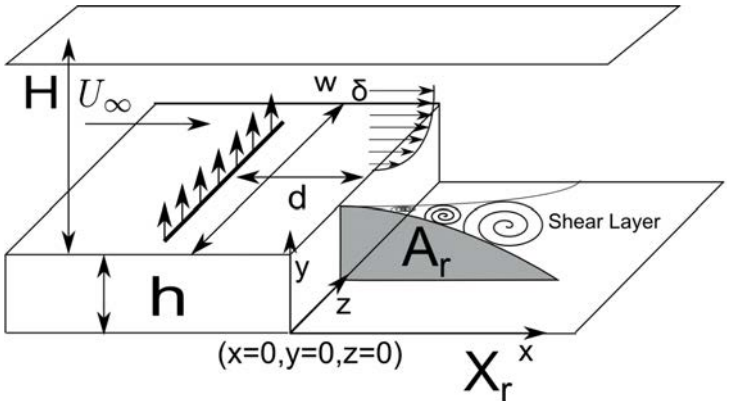

(a) Sketch of the backward facing step geometry and definition of the main parameters

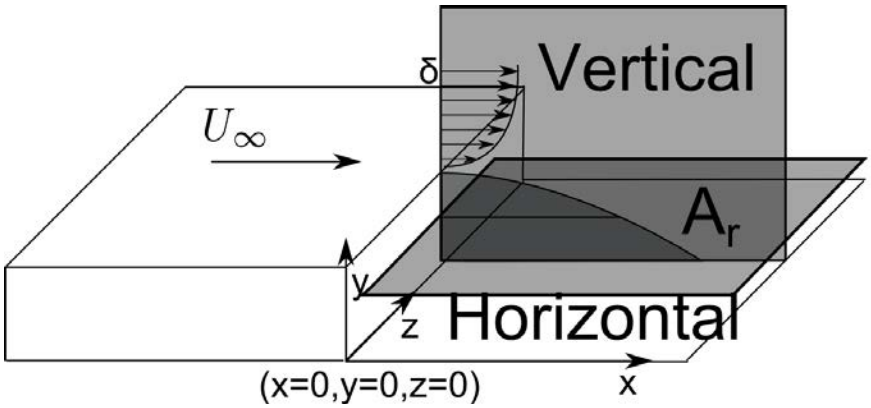

(b) Vertical and horizontal observation planes

Figure 2.4

2.4 Jet injection

Jet injection is initiated in a pressurized tank. A water cooler will suffice for such an application. However they are not very durable and will break (sometimes explosively) after some time (from a couple of days to several weeks depending on usage). A resilient tank was devised and built using Plexiglas, it has not broken (yet). This allows for suction and injection as low pressures will cause the tank to fill up while high pressures while cause the tank to empty. A water level indicator is placed inside the tank, allowing for refilling. This enables experiments to run on their own for days at a time. The apparatus is sketched in figure 2.5.

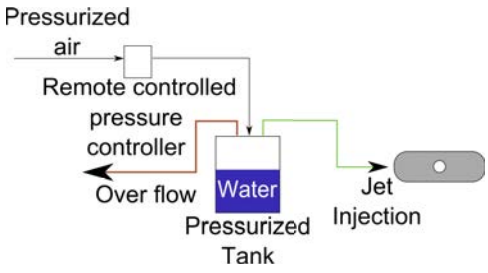

Figure 2.5: Jet supply circuit

Jet exit is handled by the system described in figure 2.6. The water goes through the plenum described in figures 2.6a and 2.6b. It is filled with glass beads sandwiched between two grids. This was designed to homogenize the flow prior to its entry in the injection chamber which is past the top grid. After the injection chamber the flow goes through cover plates of varying geometries. Examples of such cover plates are shown in figures 2.6c for a round jet and 2.6d for a vortex generator configuration. Cover plates are 11 cm across, and 3 cm wide. This system is advantageous as it is highly modular, virtually any exit geometry can be achieved by changing cover plates. Cover plate height can also be modified to change jet exit velocity profile. Figure 2.6e shows the jet injection system combined to a flat plate geometry for boundary layer control.

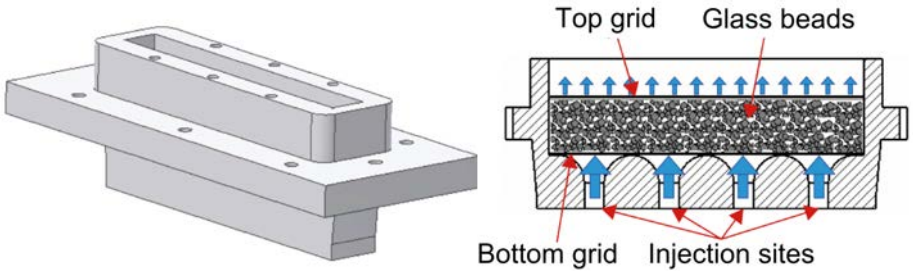

(a) Jet injection system

(b) Jet injection side view

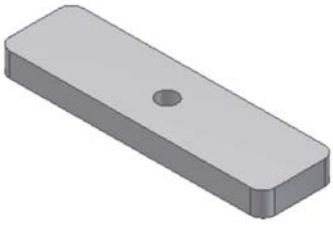

(c) Round jet cover plate

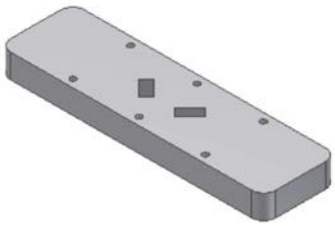

(d) Vortex generator cover plate

Figure 2.6

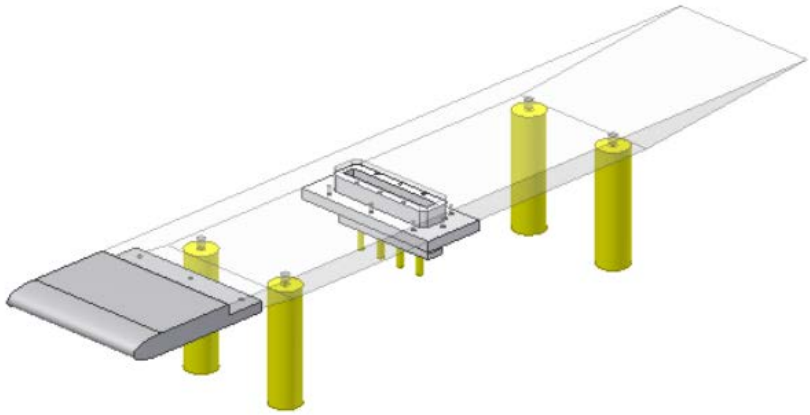

(e) Jet injection system combined to a flat plate

Figure 2.6

Figure 2.7 shows different jet exit configurations. The round jet displayed in figure 2.7f was used (with varying diameters and injection lengths) in the study of jet trajectories described in appendix A. The studies featured in part II make use of the configuration shown in figures 2.7h and 2.7i.

(f) Round configuration

(g) Rectangle configuration

Figure 2.7

(h) Slot configuration

(i) Inclined slot configuration

(j) Vortex generator configuration

Figure 2.7

This automation was developed for the work presented in chapter 9 and has proved particularly effective at facilitating parametric studies. Figure 2.8 shows the relationship between pressure and flowrate for a given tank and tank height above the ground. It should be noted tank design has changed a lot through the course of this thesis. Therefore figure 2.8 should be taken as a qualitative example and is not correct for all studies featured in part II. For each study jet flowrate was determined independently. Flowrate is used instead of jet exit velocity as slots of different sections are used to provide actuation.

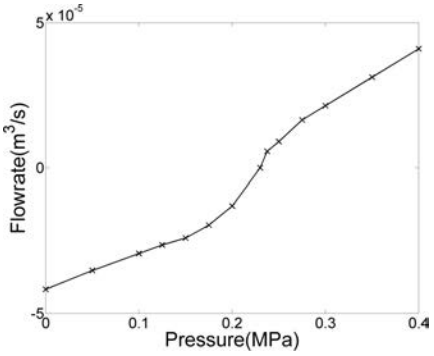

Figure 2.8: Flowrate as a function of pressure in the jet supply tank, for a standard slot configuration flow velocity can vary from $-0.15\ cm.s^{-1}$ to $20\ cm.s^{-1}$

2.5 Real-time velocity computation

The specifics of how real-time velocity field computations were achieved are detailed in chapter 4, they involve the implementation of a GPU algorithm for computing displacements akin to PIV. This method was developed as a means to an end for closed-loop control, however it also holds significant intrinsic worth as a tool for flow investigation. Arguably the method does not yield fields of significantly greater quality than traditional, much slower techniques. However it holds tremendous potential for fast prototyping and tuning in addition to considerably improving user comfort.

It brings ease and speed of use to the user as a single workstation can be used for acquisition, processing and post-processing. This aspect should not be underestimated as transferring data from computer to computer can be quite tedious. Furthermore computations are effected much faster. With the right setup thousands of velocity fields can be computed per second. Results are instantaneous, flow data streams seamlessly to the user allowing for flow state assessment and operating parameters adjustment.

This leads to quicker, more relevant and more pleasant (a benefit which should not be underestimated) experimental campaigns. More widespread implementation of real-time methods in a field still relying heavily on experimental results would greatly accelerate scientific discovery.

With respect to control, this method can be used to quickly evaluate control algorithms and determine which parameters and measurement make a given control approach viable. Real-time velocimetry can then be replaced by more specialized, targeted sensors for practical applications. The method greatly accelerated the studies presented in chapters 6, 8, and 9 in which control could have been accomplished using parietal sensors.

All the velocity data featured in this work save the study described in chapter 4 was obtained using this method.

Part II

Results

Chapter 3

Characterization of the backward facing step flow

Recirculation occurs behind a step at all Reynolds numbers. It is an important feature of many separated flows. It is the most significant feature of the backward-facing step flow and thus is often used to characterize the flow state (Armaly et al. (1983), Chun and Sung (1996)) and as a control objective in flow control experiments (Henning and King (2007)). Its characteristics (such as length) are relatively easy to measure. This chapter will review different ways in which recirculation can be qualified.

3.1 1D: recirculation length

There are many ways of defining recirculation length X_r. The most common is described in equation (3.1) for isotropic incompressible flows, $v = v(x, y, z, t)$ corresponds to longitudinal velocity, y is perpendicular to the bottom wall of the step, η $(m^2.s^{-1})$ is fluid viscosity.

$$X_r = x(\tau_w = 0), \tau_w = \eta \frac{\partial v}{\partial y}\bigg|_{y=0} \tag{3.1}$$

Other definitions result in the same qualitative behavior, as demonstrated by the data featured in figure 3.1a. It shows recirculation length evolution as a function of Re_h based on step height. It also shows the evolution of different length relevant to the confined backward facing step flow. Figure 3.1b shows recirculation length evolution for different data sets and varying expansion ratios (ratio of step height to channel height). These figures illustrate the robust nature of recirculation length evolution, whatever the definition, whatever the confinement recirculation behavior is consistent. As a means of comparison figure 3.1c is taken from chapter 5 and illustrates the evolution of time averaged recirculation length $< X_r >_t$ with Re_h.

Using these definitions for real-time measurements, as is necessary in closed-loop control is difficult as shown in Fernholz et al. (1996), therefore other ways of measuring X_r have been devised. Mabey (1972) shows the root mean square (rms) value of pressure fluctuations

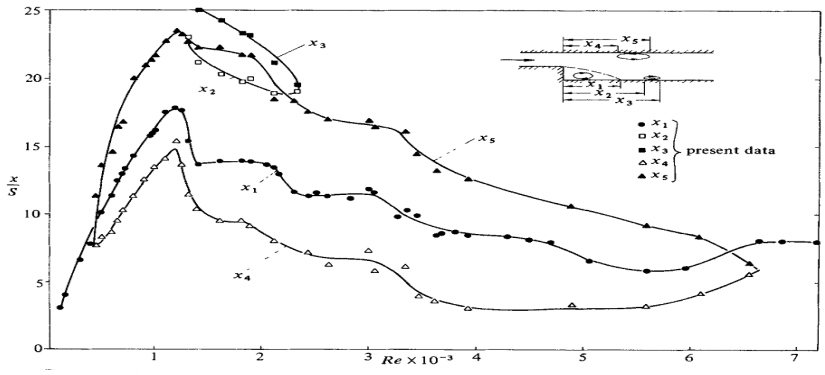

(a) Evolution of recirculation length (x_1), from Armaly et al. (1983)

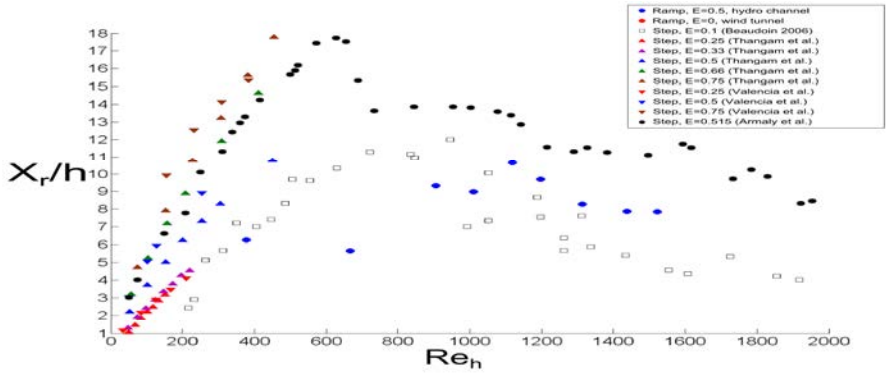

(b) Evolution of recirculation length, different definitions, E is the expansion ratio (ratio of step height to channel height), from Thomas Duriez (2009)

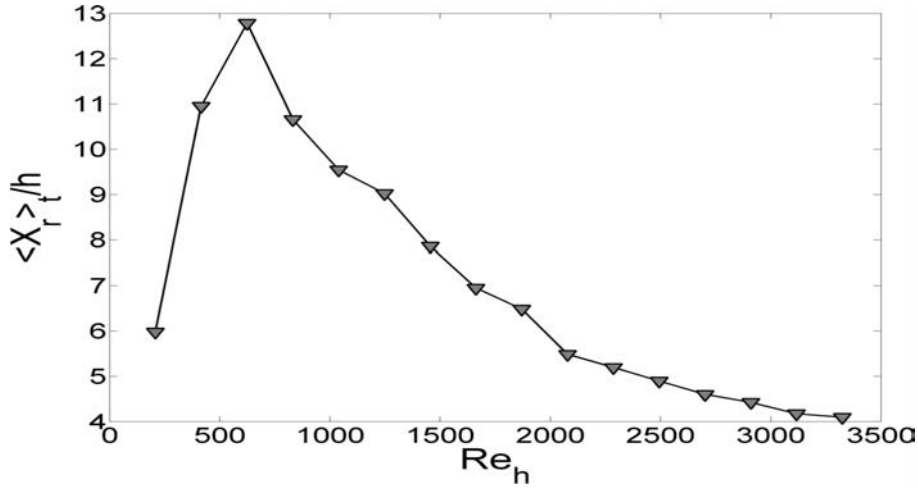

(c) Evolution of recirculation length

Figure 3.1

p'_{rms} downstream the step exhibits a clear maximum slightly upstream of the reattachment point. This has been corroborated by Kiya and Sasaki (1983), Cherry et al. (1984), Lee and Sung (2001), Hudy et al. (2003). Microphone arrays in the bottom downstream wall can be used (in air) to easily detect p'_{rms} making control of the recirculation length possible. This technique was successfully used by Henning and King (2007).

3.2 2D: recirculation area

The definition for X_r described in equation (3.1) is ill suited to 2D velocity fields. In addition to being computationally costly it only uses the most noisy part of the available data, which is velocity vectors near the wall. A straightforward manner of qualifying recirculation in a 2D field is described in equation (3.2).

$$A_r(t) = \int_A H(-v(t))(x, y)\, \mathrm{d}A \tag{3.2}$$

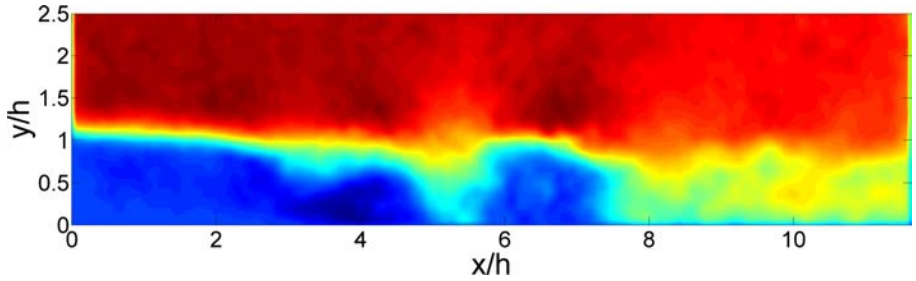

(a) Instantaneous longitudinal velocity field at $Re_h = 2700$

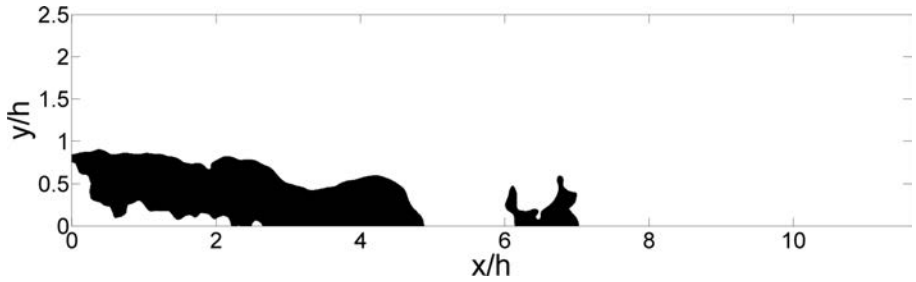

(b) Corresponding $A_r(t)$ $Re_h = 2700$

Figure 3.2

where $v(x, y, t)$ is longitudinal velocity and A is the observed area. A_r is homogeneous to an area, and most of the time will be normalized by h^2. It will henceforth be referred to as recirculation area. This amounts to measuring regions of recirculating flows (where the flow goes in opposition to the free-stream). This definition presents several advantages: it is easy to compute and the computation is intrinsically parallel making its computational cost low. Finally it makes uses of all the data present in a 2D field. This definition is

straightforward and intuitive, however it should be noted it is one amongst many ways of defining recirculation area. Figure 3.4 shows an example of $A_r(t)$ for $Re_h = 1800$, the time series exhibits large fluctuations ($\delta A_r \approx 3.5h^2$).

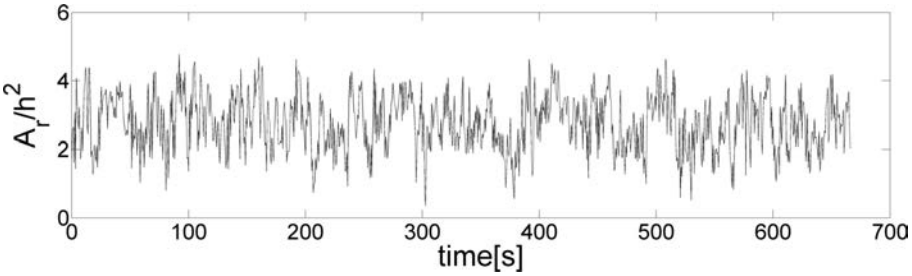

Figure 3.3: $A_r(t)$ for $Re_h = 1800$, red triangle correspond to characteristic states of the backward facing step flow

Figure 3.4 illustrates the evolution of time averaged recirculation area $< A_r >_t$ with Re_h. In red are select Reynolds numbers, that will be used throughout this chapter to illustrate specific states of the flow. Complementary fields for other Reynolds numbers can be found in appendix C. The qualitative agreement across multiple data sets highlights the universal nature of recirculation behavior for the backward facing step.

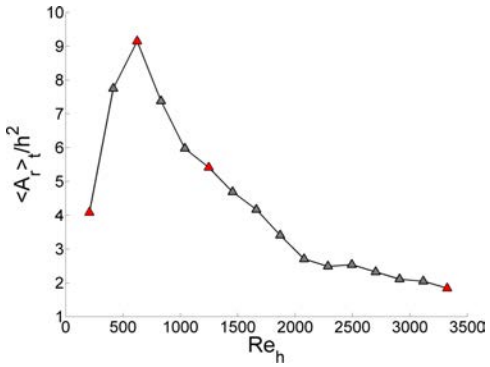

Figure 3.4: Time averaged, normalzied A_r function of Re_h

Unfortunately the time averaging operator does not commute with (3.2), this mean the time averaged recirculation area $< A_r >_t$ does not correspond to the recirculation area of the time averaged velocity field. The ratio of negative to positive longitudinal velocity χ over a given time frame introduced by Simpson (1996) is most relevant for visualization. Figure 3.5 shows an example of χ for $Re_h = 1800$.

As a means of comparison figure 3.6 shows the corresponding recirculation region as defined in equation (3.2) for the time averaged field.

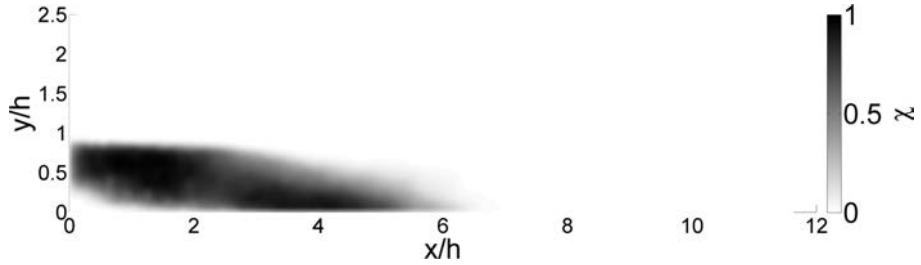

Figure 3.5: χ for $Re_h = 2700$

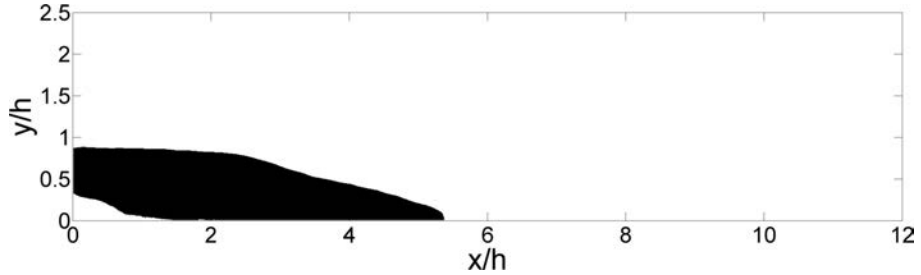

Figure 3.6: Recirculation (in black) computed for the time averaged field, $Re_h = 2700$

Equation (3.3) introduces recirculation intensity, the spatially averaged longitudinal velocity value inside $A_r(t)$. This definition is useful when controlled and uncontrolled recirculation area are of comparable size while recirculation is less intense in one case.

$$R_I(t) = \frac{1}{A_r} \int_{A_r} -v(x, y, t) \, \mathrm{d}A \tag{3.3}$$

Figure 3.8 shows $R_I(t)$ for the same Reynolds number.

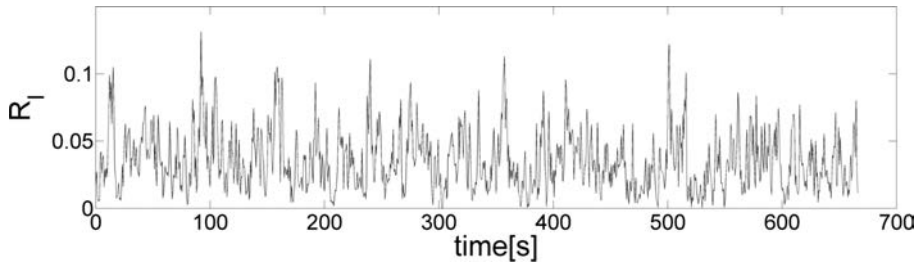

Figure 3.7: R_I for $Re_h = 1800$

Figure 3.8 shows the time averaged, normalized recirculation intensity field described in equation (3.4). While overall recirculation shape is common to figures 3.5,3.6. Figure 3.8 highlights recirculation intensity in the reattachment region.

$$R_{I,field} =< v_{x,y\in A_r(t)} >_t /max_{x,y} < v >_t \tag{3.4}$$

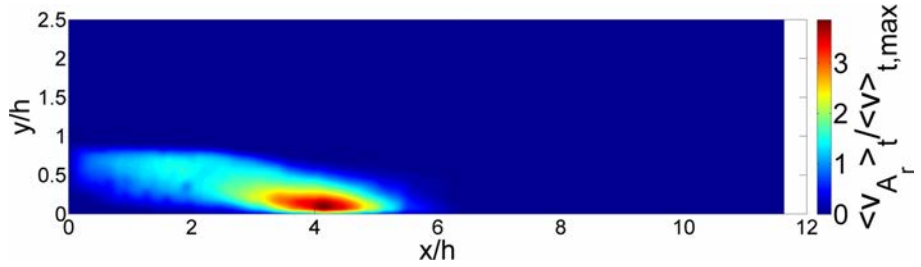

Figure 3.8: Time averaged, normalized recirculation intensity $Re_h = 1800$

Figure 2.4b shows the different observations planes used for the following figures. More details on the similarities and differences between recirculation measurements in the vertical and horizontal plane are available in chapter 5.
Figure 3.9 shows recirculation time fraction for the available range of Reynolds numbers, the red line indicates $\chi = 0.5$. Recirculation increases with Reynolds number up until a certain point where vortex shedding starts ($Re_h = 620$) and gradually intensifies lowering recirculation area until reaching an asymptote, this is coherent with what can be observed in figures 3.1a, 3.1b and 3.1c.

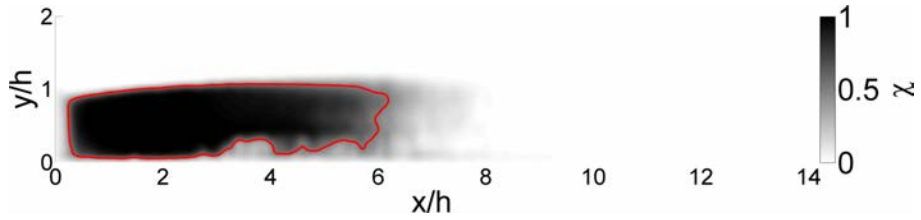

(a) $Re_h = 200$

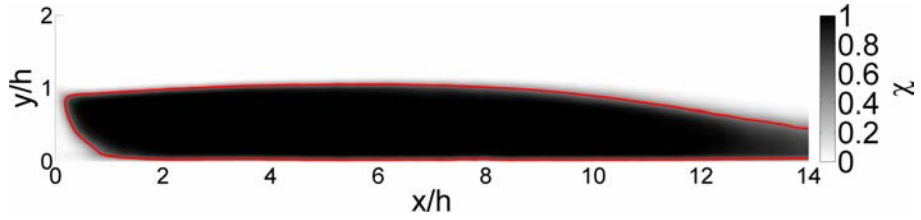

(b) $Re_h = 620$

Figure 3.9: Recirculation time fractions for select Reynolds numbers, middle vertical plane, red line is $\chi = 0.5$

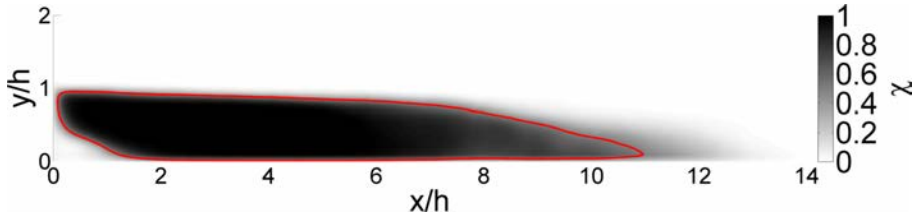

(c) $Re_h = 1250$

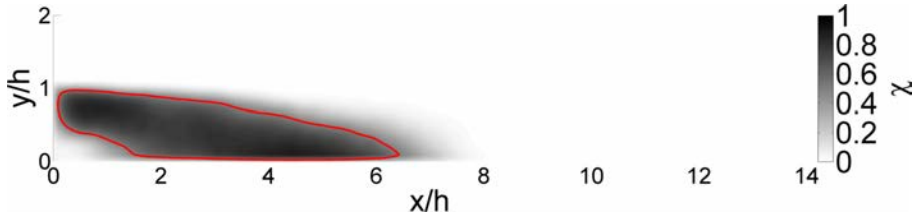

(d) $Re_h = 3250$

Figure 3.9: Recirculation time fractions for select Reynolds numbers, middle vertical plane, red line is $\chi = 0.5$

Figure 3.10 shows corresponding time averaged, normalized recirculation intensity. For high Reynolds numbers recirculation intensity is concentrated around the reattachment area, while lower free-stream velocity flows feature a spread out recirculation.

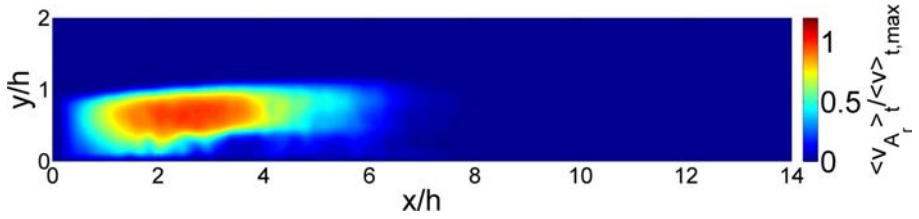

(e) $Re_h = 200$

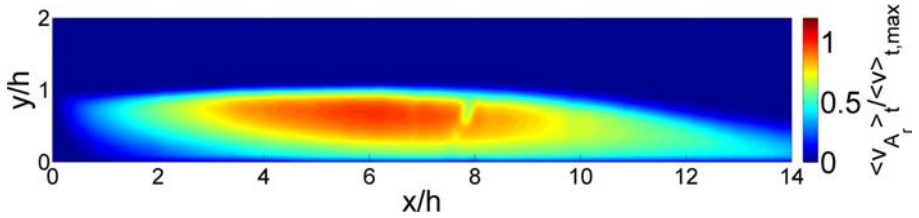

(f) $Re_h = 620$

Figure 3.10: Time averaged, normalized recirculation intensity for select Reynolds numbers, middle vertical plane

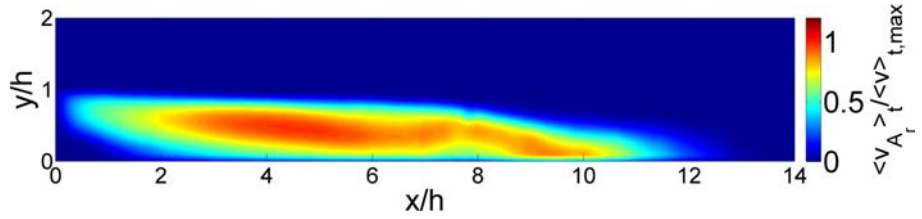

(g) $Re_h = 1250$

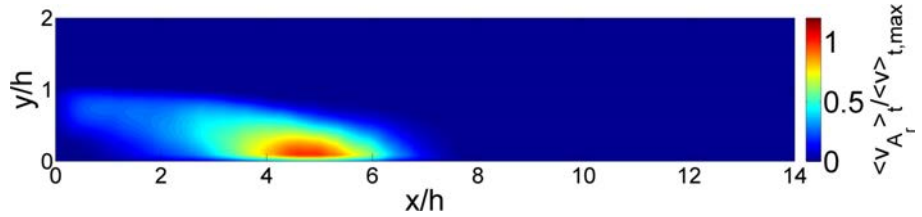

(h) $Re_h = 3250$

Figure 3.10: Time averaged, normalized recirculation intensity for select Reynolds numbers, middle vertical plane

Figure 3.11i shows maximum recirculation intensity as a function of Re_h. Recirculation intensifies linearly with free-stream velocity. This is in stark contrast to the evolution of recirculation size (length, area, volume). The same can be said about maximum fluctuating kinetic energy displayed in figure 3.11j.

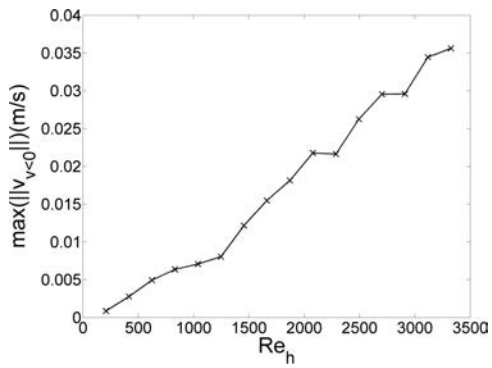

(i) Maximum recirculation intensity as a function of Re_h

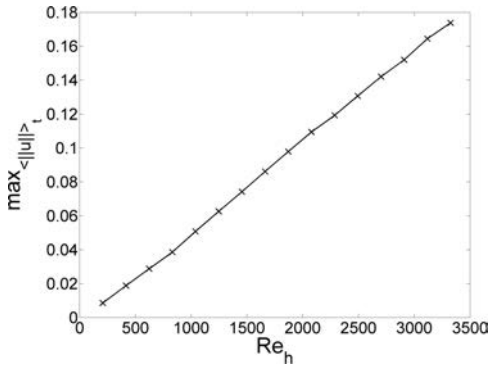

(j) Maximum time averaged fluctuating kinetic energy y as a function of Re_h

Figure 3.11

Figure 3.12 shows corresponding time averaged kinetic energy $< k >_t$ as a function of Re_h, with the instantaneous fluctuating kinetic energy $k = \sqrt{u'^2 + v'^2}$ u' and v' are fluctuating longitudinal and vertical velocity. Prior to $Re_h = 620$ the high fluctuating kinetic energy region is due to flapping of the shear layer, for higher Reynolds numbers vortex shedding is responsible for the majority of fluctuating kinetic energy in the flow.

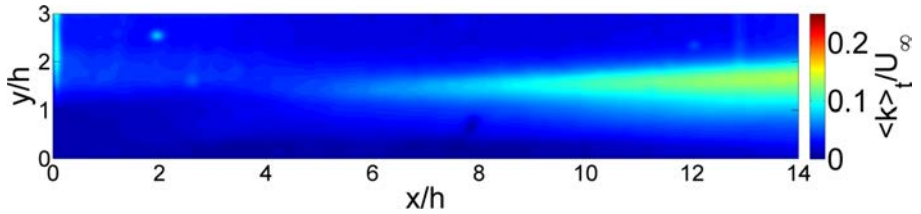

(a) $Re_h = 200$

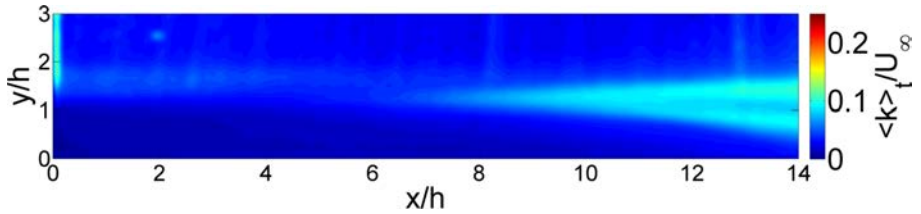

(b) $Re_h = 620$

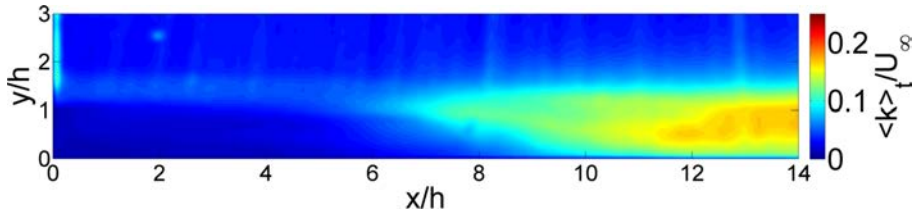

(c) $Re_h = 1250$

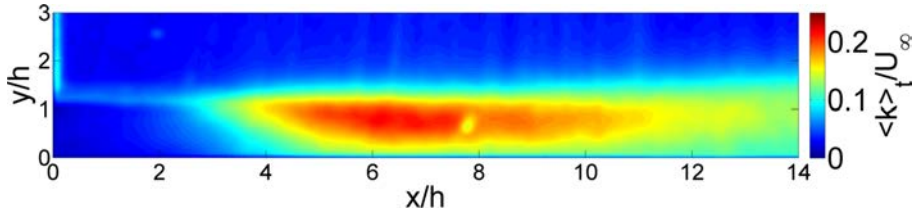

(d) $Re_h = 3250$

Figure 3.12: Time averaged fluctuating kinetic energy field for select Reynolds numbers

Figure 3.13 shows velocity amplitude snapshots as a function of Re_h. These snapshots are meant to give a qualitative representation of the instantaneous flow for select Reynolds numbers. They offer a contrast to the much more common time-averaged representation.

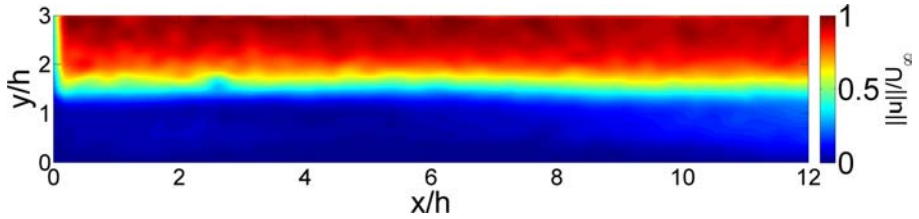

(a) $Re_h = 200$

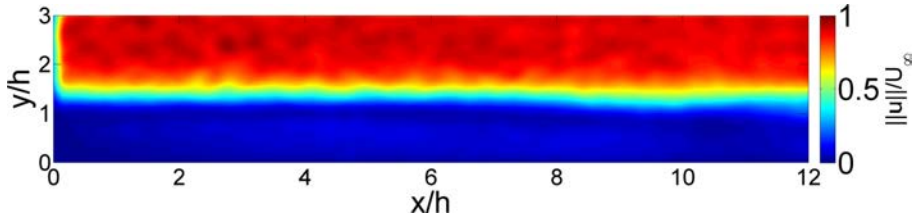

(b) $Re_h = 620$

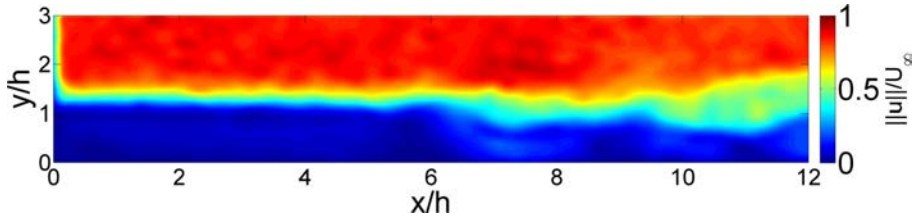

(c) $Re_h = 1250$

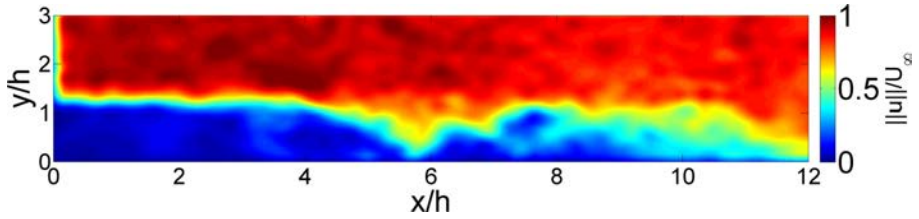

(d) $Re_h = 3250$

Figure 3.13: Instantaneous velocity amplitude snapshots for select Reynolds numbers

Figure 3.14 shows the flow in the middle horizontal plane, the red line indicates $\chi = 0.5$. In this configuration the camera is placed above the step. Recirculation evolution corroborates what has been observed in the vertical plane. This is noteworthy as it guarantees control of the vertical plane recirculation has the same time-averaged effects in the transversal direction. In practice vertical recirculation is a good representative of the transversally averaged recirculation. However if actuation is non transversally homogeneous, measuring recirculation in the horizontal plane is necessary for effective control.

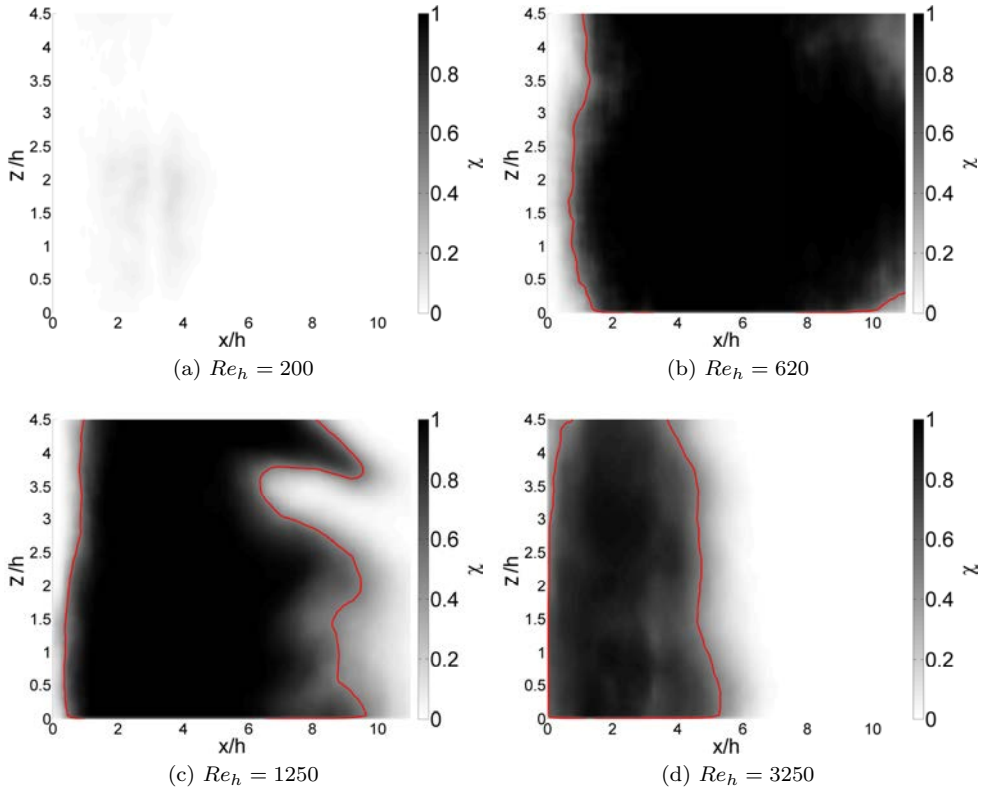

(a) $Re_h = 200$ (b) $Re_h = 620$

(c) $Re_h = 1250$ (d) $Re_h = 3250$

Figure 3.14: Recirculation time fractions for select Reynolds numbers, middle horizontal plane (y=h/2), red line is $\chi = 0.5$

Figure 3.15 shows time averaged, normalized recirculation intensity in the middle horizontal plane. As with the vertical plane, recirculation intensity closely follows recirculation time fractions. For the uncontrolled flow both quantities are equivalent.

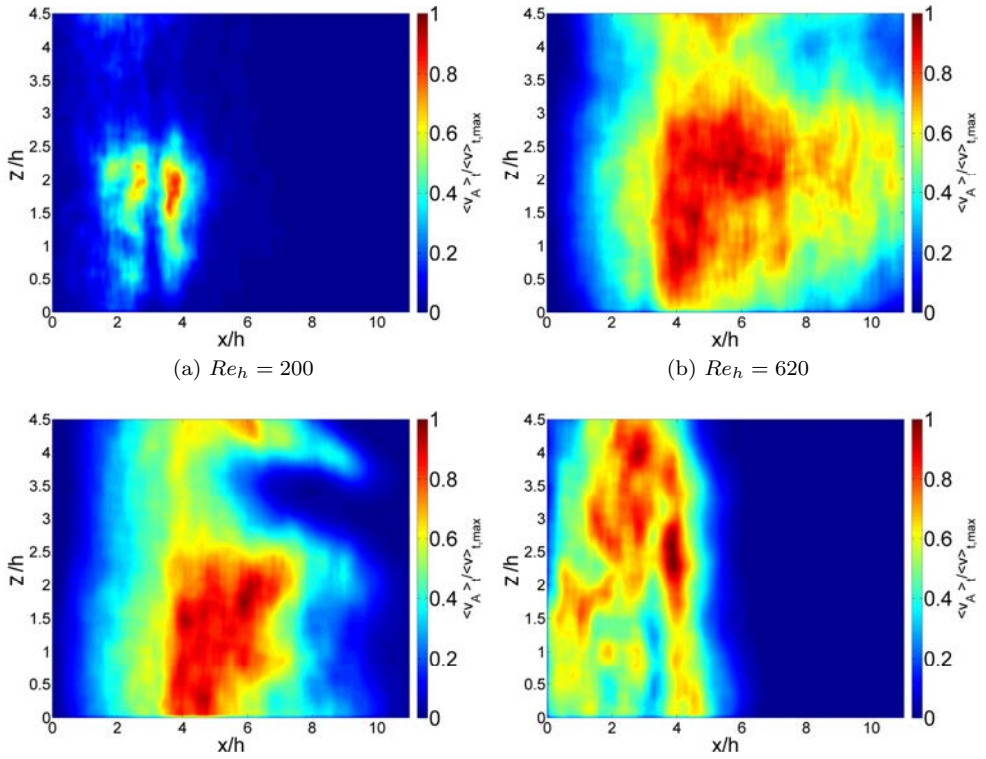

(a) $Re_h = 200$ (b) $Re_h = 620$

(c) $Re_h = 1250$ (d) $Re_h = 3250$

Figure 3.15: Time averaged, normalized recirculation intensity for select Reynolds numbers, middle horizontal plane

3.3 3D: recirculation volume

The definitions of A_r and R_I are easily expanded to 3D. $A_r(t)$ becomes $V_r(t)$ a measure of recirculation volume described in equation (3.5).

$$V_r(t) = \int_V H(-v(t))(x, y, z)\ \mathrm{d}V \tag{3.5}$$

$R_I(t)$ conserves its notations and interpretation becoming, (3.6):

$$R_I(t) = \frac{1}{V_r} \int_{V_r} -v(x, y, z, t)\ \mathrm{d}V \tag{3.6}$$

The definition for χ is also identical. Figure 3.16 shows the iso-surface for $v(x, y, z, t) = 0$ for a 3D experimental velocity field at varying Reynolds numbers. This iso-surface delimits the volume defined in (3.5). The data were obtained using 3D particle tracking velocimetry. Unfortunately it is not yet possible to take these measurements in real-time. These results are presented to illustrate a possible next step for optical based flow control.

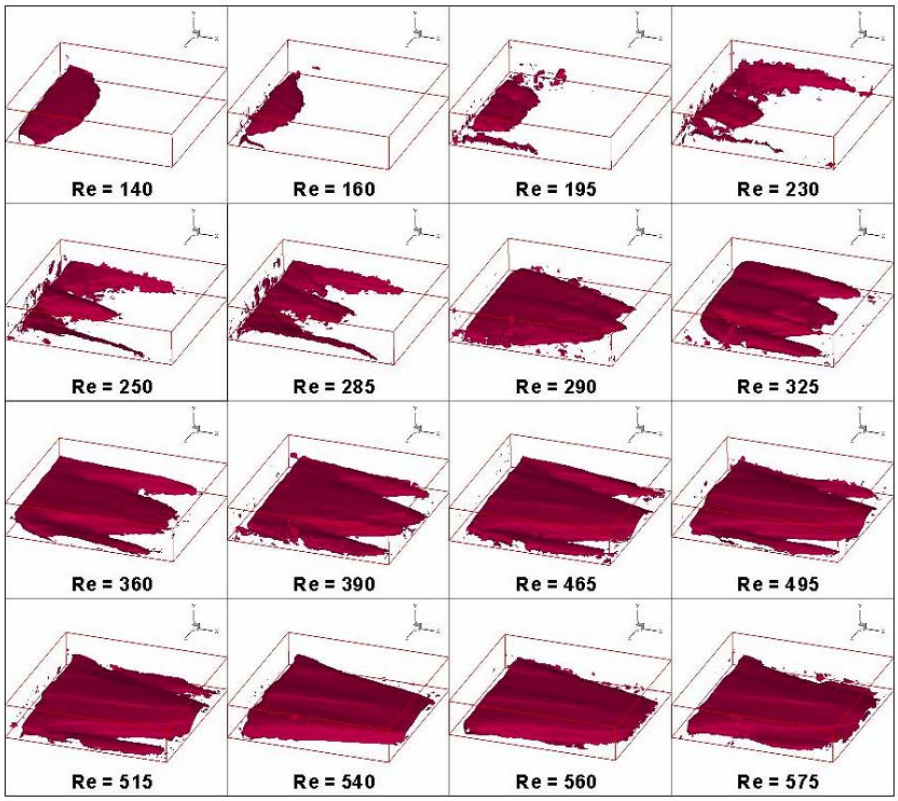

Figure 3.16: Iso-surfaces for null longitudinal velocity as a function of Re_h

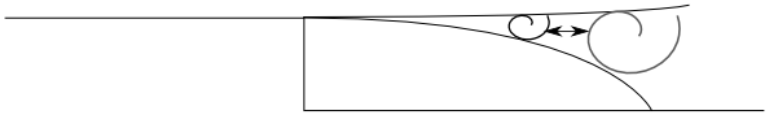

(a) Flapping of the recirculation region

(b) Vortex shedding in the shear layer

Figure 3.17

3.4 Characteristic frequencies

Kelvin-Helmholtz instabilities in the shear layer induce vortex shedding. These are important as they play a major role in the flow dynamics, Brown and Roshko (1974). Shedding and its interactions with the backward facing step flow has been the subject of intense study (Lane and Loehrke (1981), Hillier and Cherry (1981), Kiya and Sasaki (1983)). Figure 3.17a illustrates vortex shedding in the shear layer. The three dimensional nature of these structures has been investigated by Sigurdson and Roshko (1984), Kiya and Sasaki (1985), Sigurdson (1986), Sasaki and Kiya (1991). Many control experiments have focused on periodic forcing of the shear layer, showing significant reduction in recirculation length when actuating close to the shedding frequency,Sigurdson, Chun and Sung (1996), David Greenblatt (2000), Henning and King (2007). The recirculation region itself is subject to flapping, this motion has been observed both numerically and experimentally, Eaton and Johnston (1982), Cherry et al. (1984), Driver et al. (1987), Lee and Sung (2001). This motion is typically slow, one order smaller than the shedding frequency. Figure 3.17b illustrates this flapping motion.

There are several methods for extracting characteristic frequencies from the flow. The most straightforward is inserting a hot-wire probe in the shear layer, thus measuring local velocity amplitude at very high rate. Fourier transform can then be used to identify dominant frequency. Figure 3.18a from Hasan (1992) shows longitudinal velocity spectra for the uncontrolled and controlled backward facing step flow. Figure 3.18b shows a velocity amplitude spectra for roughly the same position in our setup. One can see the peak is not always very clearly defined making it difficult to correctly identify shedding frequency. Other methods involve parietal sensors and detecting passing vortices by the changes in wall pressure or friction they effect. Vortex visualization using dies can be an effective (but tedious) method for identifying shedding frequency. A more sophisticated optical method is discussed

in chapter 7.

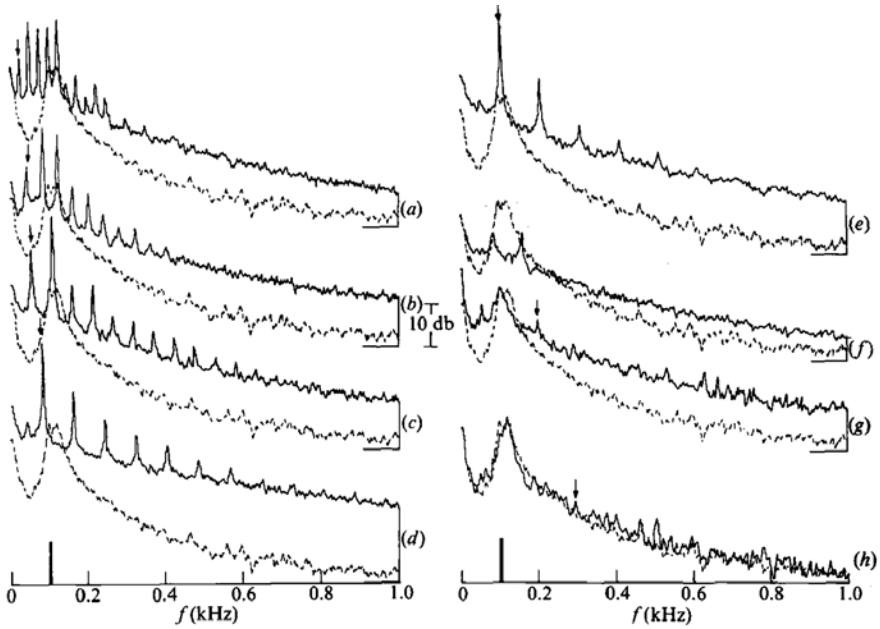

(a) Longitudinal velocity spectra for perturbed and unperturbed flow, measurements are taken at $x = 2h$ and y=0.95h at $Re_h = 11000$ from Hasan (1992)

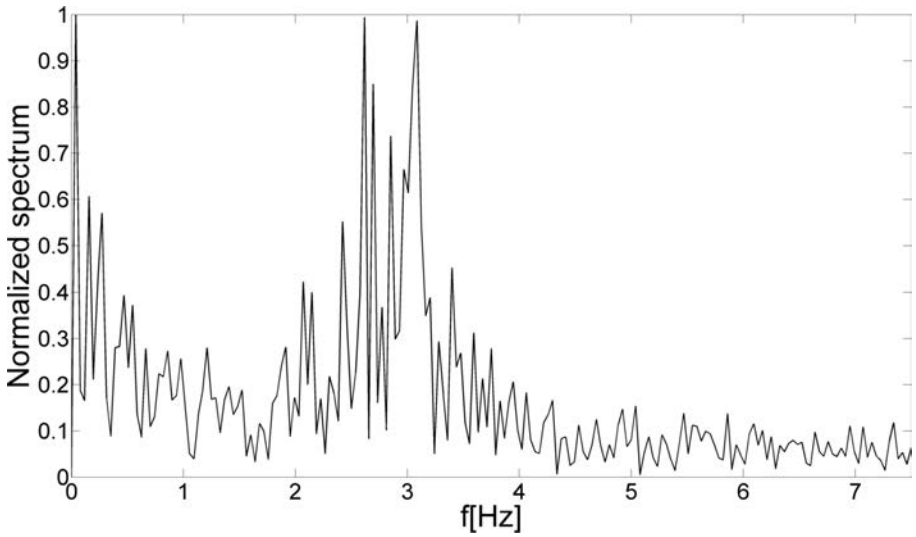

(b) Longitudinal velocity spectrum for the unperturbed flow, measurements are taken at $x = 2.2h$ and y=0.95h, $Re_h = 2800$

Figure 3.18

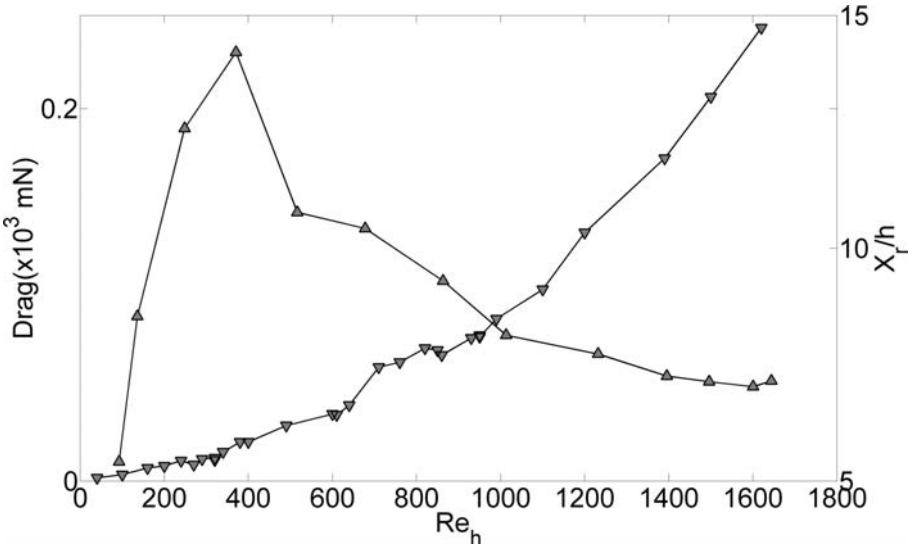

Figure 3.19: Evolution of drag (▼) and recirculation length (▲) as a function of Re_h for the backward facing step flow (Beaudoin (2004))

Effective actuation frequencies vary depending on the experiment (see table 1.1)with the Strouhal number based on height $St_h = fh/U_\infty$ ranging from 0.2 to 0.3. Correctly identifying shedding frequency is useful for control. Actuation at this frequency will enhance kinetic energy production as well as reduce recirculation size (see chapter 7). A novel algorithm based on the control of the slower recirculation flapping motion is introduced in chapter 9.

3.5 Relation between recirculation and drag

Two effects contribute to drag: skin friction and pressure losses. At high Reynolds numbers pressure or form drag is dominant in separated flows, therefore lowering drag is equivalent to improving pressure recovery. The recirculation induced by separation is a low pressure region and is responsible for the pressure loss behind the body. Completely suppressing the recirculation leads to the highest possible drag reduction. In practice however this is not always possible (for example when the edge is too sharp which is the case for the backward facing step flow). Unfortunately the relationship between recirculation shape and size and pressure recovery is complex. For the backward facing step flow the relation is far from trivial. Figure 3.19 shows the evolution of recirculation length measured using wall sensors and drag measured using a balance as a function of Re_h. Data are from Beaudoin (2004) and were conducted with a different experimental setup. While drag is a monotonously increasing function of Reynolds number, such is not the case for recirculation length. Thus there is no guarantee lowering recirculation length leads to lesser drag. In fact it might be the other way around (Browand et al. (2008), Dahan and Morgans (2012)).

We would argue that while qualifying the recirculation is of academic interest, measures

of recirculation are ill-suited as practical flow control objectives. Efforts should be made to explicitly make drag or pressure recovery the control objective. Furthermore the relationship between recirculation characteristics and drag should be clarified.

Bibliography

B. F. Armaly, F. Durst, J. C. F. Pereira, and B Schonung. Experimental and theoretical investigation of backward-facing step flow. *J. Fluid Mech*, 127:473–496, 1983.

J.F. Beaudoin. *Contrôle actif d'écoulement en aérodynamique automobile*. PhD thesis, Ecole des Mines de Paris, 2004.

F. Browand, R. McCallen, and J. Ross. *The Aerodynamics of Heavy Vehicles II: Trucks, Buses, and Trains*. 2008.

G.L. Brown and A. Roshko. On density effects and large structure in turbulent mixing layers. *J. Fluid Mech*, 64:775–816, 1974.

N. J. Cherry, R. Hillier, and M. Latour. Unsteady measurements in a separated and reattaching flow. *J. Fluid Mech*, 144:13–46, 1984.

K. B. Chun and H. J Sung. Control of turbulent separated flow over a backward-facing step by local forcing. *Exp. Fluids*, 21:417–426, 1996.

J. Dahan and A. Morgans. Feedback control for form-drag reduction on a bluff body with a blunt trailing edge. *J. Fluid Mech*, 704:360–387, 2012.

Israel J. Wygnanski David Greenblatt. The control of flow separation by periodic excitation. *Progress in Aerospace Sciences*, 36:487–545, 2000.

D.M. Driver, H.L. Seegmiller, and J.G. Marvin. Time-dependent behavior of a reattaching shear layer. *AIAA Journal*, 25(7):914–919, 1987.

J.K. Eaton and J.P. Johnston. Low frequency unsteadiness of a reattaching turbulent shear layer. *Proceeding of the 3rd International Symposium on Turbulent Shear Flows*, 1982.

H.H. Fernholz, G. janke, M. Schober, and D. Warnack. New developments and applications of skin-friction measuring techniques. *MST*, 7(10):1396–1409, 1996.

M.A.Z. Hasan. The flow over a backward-facing step under controlled perturbation : laminar separation. *J. Fluid Mech*, 238:73–96, 1992.

L. Henning and R. King. Robust multivariable closed-loop control of a turbulent backward-facing step flow. *Journal of Aircraft*, 44, 2007.

R. Hillier and N.J. Cherry. The effects of stream turbulence on separation bubbles. *J. Wind Engng Indust. Aerodyn*, 8:49–58, 1981.

L.M. Hudy, A.M. Naguib, and W.M. Humphreys. Wall-pressure array measurements beneath a separating/reattaching flow region. *Phys. Fluids*, 15(3):706–717, 2003.

M. Kiya and K. Sasaki. Structure of a turbulent separation bubble. *J. Fluid Mech*, 137: 83–113, 1983.

M. Kiya and K. Sasaki. Structure of large-scale vortices and unsteady reverse flow in the reattaching zone of a turbulent separation bubble. *J. Fluid Mech*, 154:463–491, 1985.

J.C. Lane and R.I. Loehrke. Leading edge separation from a blunt plate at low reynolds number. *J. Fluids Engng*, 102:494–496, 1981.

I. Lee and H.J. Sung. Characteristics of wall pressure fluctuations in separated and reattaching flows over a backward-facing step: Part 1. time-mean statistics and cross-spectral analysis. *Exp. Fluids*, 30(3):262–272, 2001.

D.G. Mabey. Analysis and correlation of data on pressure fluctuations in separated flow. *Journal of Aircraft*, 9(9):642–645, 1972.

K. Sasaki and M. Kiya. Three-dimensional vortex structure in a leading-edge separation bubble at moderate reynolds numbers. *J. Fluids Engng*, 113:405–410, 1991.

L.W. Sigurdson. The structure and control of a turbulent reattaching flow.

L.W. Sigurdson. *The structure and control of a turbulent reattaching flow.* PhD thesis, CalTech, 1986.

L.W. Sigurdson and A. Roshko. The large-scale structure of a turbulent reattaching flow. *Bull. Am. Phys. Soc*, 29, 1984.

R.L. Simpson. Aspect of turbulent boundary layer separation. *Progress in Aerospace Sciences*, 32:457–521, 1996.

Jose Eduardo Wesfreid Thomas Duriez, Jean-Luc Aider. Self-sustaining process through streak generation in a flat-plate boundary layer. *Physical Revew Letters*, 103:144502, 2009.

Chapter 4

Real-time planar flow velocity measurements using an optical flow algorithm implemented on GPU

This chapter presents our work on real-time flow velocity computations. It details the algorithm and how it was optimized for performance leading to a two-fold increase in processing speed. Quantitative comparisons between velocity fields computed by the algorithm and traditional PIV techniques are purposefully kept to a minimum. Indeed such comparisons were rigorously carried out by the team responsible for developing the algorithm, as described in Champagnat et al.. The algorithm itself and its original GPU implementation were provided by ONERA. Emphasis was placed on improving its operating speed, a factor seldom considered in flow velocimetry, and integrating it into a novel experimental apparatus capable of effecting, manipulating and displaying flow velocity fields in real-time.

4.1 Abstract

This paper presents a high speed implementation of an optical flow algorithm which computes in real-time planar velocity fields in an experimental flow. Real-time computations of the flow velocity field allows the experimentalist to have instantaneous access to quantitative features of the flow. This can be very useful in many situations: fast evaluation of the performances and characteristics of a new setup, design optimization, easier and faster parametric studies, etc. It can also be used as a visual sensor for an input in closed-loop flow control experiments where fast estimation of the state of the flow is needed. The algorithm is implemented on a Graphics Processor Unit (GPU). The accuracy of the computation is demonstrated. Computation speed and scalability of the processing are highlighted along with guidelines for further improvements. The system architecture is flexible, scalable and can be adapted on the fly in order to process higher resolutions or achieve higher precision. The set-up is applied

on a Backward-Facing Step (BFS) flow in a hydrodynamic channel. For validation purposes, classical Particle Image Velocimetry (PIV) is used to compare with instantaneous optical flow measurements. The important flow characteristics like the dynamics of the recirculation bubble, computed in real-time for the first time, are well recovered. The accuracy of real-time optical flow measurements is comparable to off-line PIV computations.

4.2 Introduction

Optical measurements of 2D-velocity fields in fluid mechanics have been widely used in industrial and academics laboratories for more than a decade. They allow for the thorough investigation of flow physics through non intrusive means and are an invaluable tool for understanding the dynamics of complex flows. The classical measurement technique is the standard 2D2C Particle Image Velocimetry (PIV) which gives access to the 2-Components (2C) of the velocity field in a 2D plane (Adrian (2005)). It consists in illuminating the seeded flow with a plane laser sheet (typically generated by a pulsed YaG laser) and acquiring two images of the illuminated particles field at two successive time steps using 15 Hz double-frame cameras or fast cameras for time-resolved (1 kHz) measurements. Usually, a few hundreds pairs of images are acquired. In these standard PIV setups, data are transferred or stored on the computer and post-processed off-line because the computations to obtain a well defined velocity field with a good spatial resolution (typically a 16×16 cross-correlation window) are time-consuming.

The development of reliable, flexible, accurate and low-cost systems capable of computing flow velocity fields in real-time would be a great step forward for the fluid mechanics community. In addition to saving a lot of time and resources, it would allow academics and industrial researchers to visualize the flow velocity field directly and make adjustments to their experiments on the fly. Accurately targeted measurement campaigns would become feasible even for flows exhibiting high frequency behaviors, like flows downstream a bluff body (Pastoor et al. (2008), Joseph et al. (2012)), a cylinder (Roshko (1961), or a wing Osbron et al. (2004)).

Furthermore such systems would open new perspectives for closed-loop flow control experiments based on visual informations instead of wall-pressure or skin friction measurements. For instance, Henning and King used 4×15 microphones in parallel rows to measure pressure fluctuations downstream of a step. Using quantitative visual informations would be equivalent to mapping the flow with as many captors as the image size divided by the spatial resolution of the 2D velocity field. Visual servoing in flow control has already been suggested and successfully implemented in numerical simulations (Fomena and Collewet (2011)). One can find experimental demonstrations on improvement of the aerodynamic properties of micro air vehicles (C. Willert (2010)), or control of the flow behind a flap (Roberts (2012)). Achieving increased performances would allow for additional means of control, such as vortex tracking or slope-seeking (Henning and King (2005)). Several approaches have been suggested to achieve real-time PIV. For instance, a bare bones PIV algorithm has been implemented by (C. Willert (2010)) on a single processor, obtaining engaging performances, while Roberts (2012) has implemented a basic PIV algorithm on a GPU. However these approaches led to velocity fields from small images at relatively low frame rates (less than

20 fps). Direct cross-correlation PIV, and particle tracking velocimetry (PTV) algorithms have been programmed into Field Programmable Gate Arrays (FPGA) (Lelong et al. (2003), H. Yu and Siegel (2005), Kreizer et al. (2010)). However a specific Hardware Description Language (HDL) is required to successfully operate them, which is a strong limitation. The spectacular increase in computing power of GPUs (the peak GFLOPS performance roughly doubles every year) allows for an alternative means of achieving real-time processing. Indeed, the processing power of graphics cards has risen at a rate superior to that of Central Processing Units (CPU, doubles every two years). Until recently, it was difficult for the layman to access that power for something other than specific applications. With the introduction of GPU extensions for mainstream computing languages (C/C++, Fortran, Python, Matlab) implementing GPU code in a flexible manner has become accessible to a broader population.

A comprehensive overview of the algorithms used to compute flow velocity fields can be found in Heitz et al. (2010). In the present experimental study, a dense optical flow algorithm developed by Besnerais and Champagnat (2005) was used. Its characteristics and performances in comparison to PIV algorithms are comprehensively detailed in Champagnat et al. and Champagnat et al. (2009). This algorithm is notable for its performance. Performance of the algorithm increases hand in hand with GPU computing power. While optical flow algorithms have been used before to compute flow velocity fields they have never, to our knowledge, been used in a real time setup.

Furthermore a traditional PIV setup can be cheaply upgraded to a real time PIV setup. To demonstrate the efficiency and quality of real-time velocity computations, it has been tested on a backward-facing step flow. Boundary layer separation and reattachment occur in many natural and industrial systems, such as diffusors, combustors or external aerodynamics of ground or air vehicles. The backward-facing step is the simplest geometry to study a separated flow. Though the geometry is simple, the complexity of separated flows is recovered as shown in figure 4.1. In this case, the separation is imposed by a sharp edge, allowing for the separation-reattachment process to be examined by itself. A dominant, global feature of the flow is the creation of a large recirculation bubble downstream the step edge, as shown in figure 4.1. This flow has been extensively studied through experimental and numerical investigations, see Armaly et al. (1983), Chun and Sung (1996), Hung et al. (1997), Beaudoin et al. (2004), Aider et al. (2007). As the objective of the present paper is exclusively the experimental demonstration of high-speed, efficient and reliable real-time velocity measurements, the BFS flow characteristics will not be discussed thoroughly but solely used as a valuable benchmark for this experimental technique.

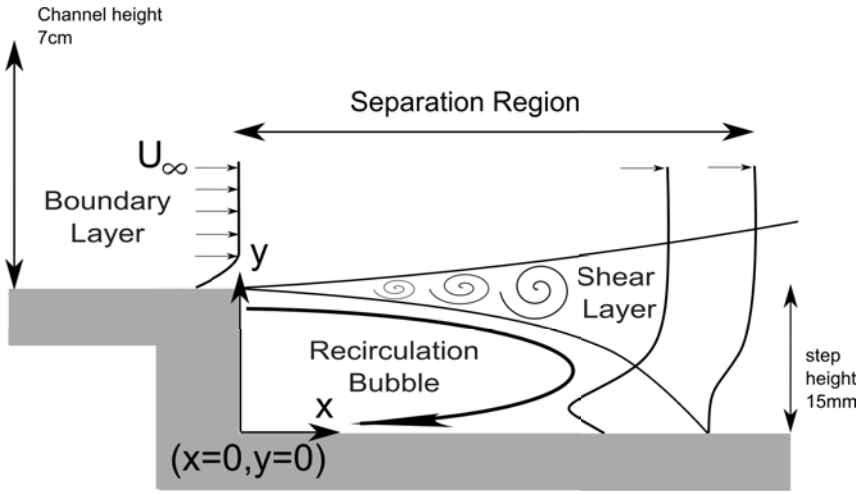

Figure 4.1: Sketch of the backward facing step flow and the main phenomena (shear layer and recirculation bubble).

4.3 Experimental Setup

4.3.1 Water tunnel

Experiments were carried out in a hydrodynamic channel in which the flow is driven by gravity. The walls are made of Altuglas for easy optical access from any direction. The flow is stabilized by divergent and convergent sections separated by honeycombs. The test section is 80 cm long with a rectangular cross section 15 cm wide and 10 cm high.
The mean free stream velocity U_∞ ranges between 1.38 to 22 $cm.s^{-1}$. The quality of the main stream can be quantified in terms of flow uniformity and turbulence intensity. The standard deviation σ is computed for the highest free stream velocity featured in our experimental set-up. We obtain $\sigma = 0.059\ cm.s^{-1}$ which corresponds to turbulence levels $\frac{\sigma}{U_\infty} = 0.0023$.

4.3.2 Optical flow measurement set-up

The flow is seeded with 20 μm polyamid seeding particles. The vertical middle plane of the test section is illuminated from above (figure 4.2) by a laser sheet created by a 2W continuous CW laser operating at a wavelength $\lambda = 532$ nm.

The pictures of the illuminated particles are recorded using a relatively low cost (compared to double-fame or high-speed cameras traditionally used for PIV), Basler acA 2000-340km 8bit CMOS camera,with a maximum bandwith of 680 Mb/s. Its resolution is 2048 $\times$ 1088 pixels. The maximum frame rate for full-frame acquisition is $F_{acq} = 340\ Hz$. The camera is controlled by a camera-link NI PCIe 1433 frame grabber allowing for real-time acquisition and processing. It should be noted that CPU performance is irrelevant with regards to the performance of the optical flow algorithm which runs entirely on the GPU. In our set-up, a NVIDIA Gforce 580 GTX GPU card, with 520 processing cores clocked at

800 Mhz, has been used. A complete description of this GPU's architecture can be found in nVidia (2010). The data flow for the acquisition apparatus is detailed in figure 4.2. The images can either be written to a solid state drive or computed in real-time on the GPU. Usually no data is written during visualization of velocity fields to improve performance and frequency rate of the computation. The optical flow algorithm and camera acquisition software are integrated into a single interface using LabView. It is important to emphasize the only requirement to upgrade a classic PIV setup featuring a camera streaming images to an acquisition computer, to a setup capable of real-time flow velocity computations is adding a graphics card to the acquisition computer. Therefore this can be done cheaply and with minimal effort.

4.3.3 Backward-facing step geometry

The backward-facing step geometry is shown in figure 4.2. A specific leading-edge profile is used to smoothly start the boundary layer which then grows downstream along the flat plate, before reaching the edge of the BFS. The boundary layer has a shape factor $H \approx 2$. Step height h is 15mm allowing for a range of Reynolds numbers $0 < Re_h = \frac{U_\infty h}{\nu} < 3000$, ν being the kinematic viscosity.

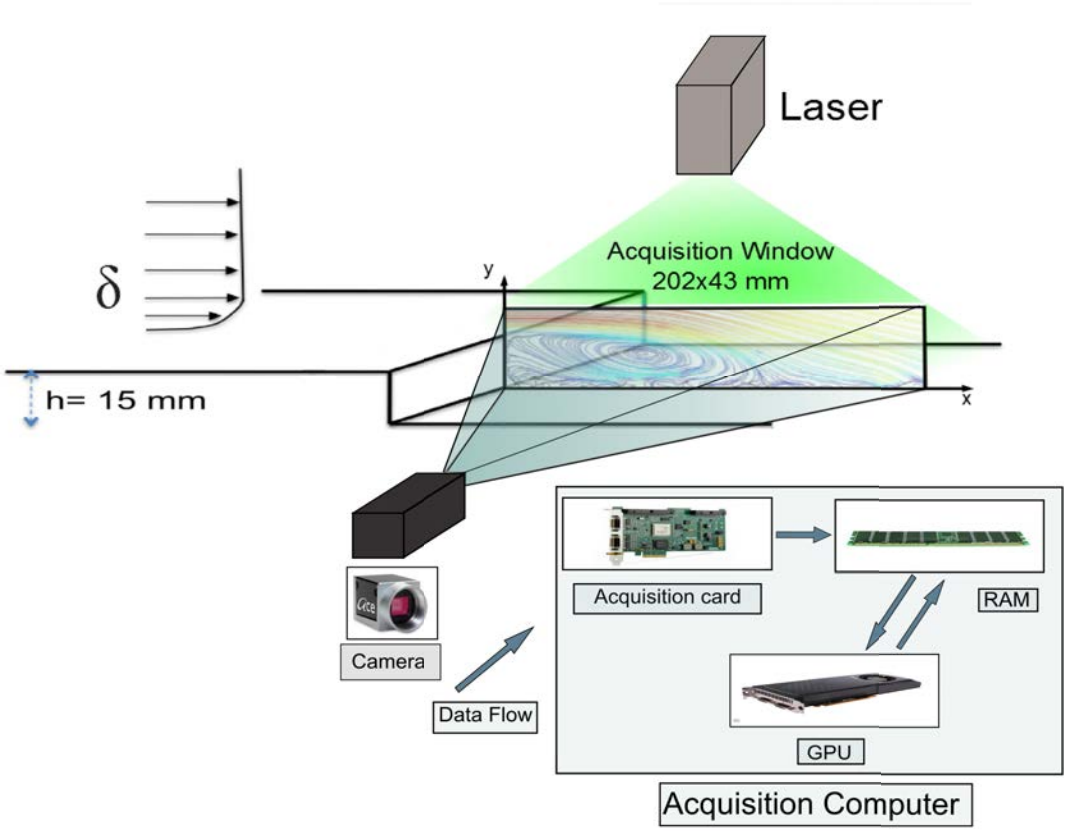

Figure 4.2: Sketch of the backward-facing step and data flow for the acquisition apparatus

4.3.4 Optical flow algorithm

Optical flow is related to the domain of image motion or optical flow estimation in computer vision. This particular algorithm called FOLKI was written in C++/CUDA. It was developed, implemented and rigorously validated by Champagnat et al. at ONERA. To achieve optimal performances further improvements were made by improving memory transfers and enhancing kernel concurrency. A guide on CUDA programming is available in nVidia (2007). This algorithm was used by Davoust et al. (2012), Sartor et al. (2012), and Rabinovitch et al. (2012). It is a local iterative gradient-based cross-correlation optimization algorithm which yields dense velocity fields, i.e. one vector per pixel. It belongs to the Lucas-Kanade family of optical flow algorithms (Lucas (1984)). It should be noted that the dense nature of the output is intrinsically tied to the nature of the algorithm. The spatial resolution however is tied to the window size, like any other window based PIV technique. However the dense output is advantageous since it allows the sampling of the vector field very close to obstacles, yielding good results near walls, as shown in Champagnat et al.. Computing dense fields allows for a highly parallel algorithm which can take full advantage of the GPU architecture.

The interrogation window radius $r = 10$ pixels was chosen, following the guidelines given by Champagnat et al.. It should be noted that similar performances would be achieved using other programming languages, such as OpenCL in conjunction with any GPU, though the algorithm would need to be tweaked for the specific GPU architecture.

The principle of the featured optical flow algorithm is as follows. The original images are reduced in size by a factor of 4 iteratively until intensity displacement in the reduced image is close to 0. This gives a pyramid of images as illustrated in figure 4.3. The displacements are computed in the top image with an initial guess of zero displacement using an iterative Gauss-Newton scheme to minimize a sum of squared difference criterion. This displacement is then used as an initial estimate for the same scheme in the next pair of images in the pyramid. The process is repeated until the base of the pyramid which corresponds to the initial image, thus giving the final displacements field.

The optical setup is tuned for the displacement of the particles to be small enough for the optical flow algorithm to converge. Thus there are two inputs to the algorithm, besides image size, that have a major impact on performance: the number of levels in the pyramid n_{lev}, and the number of iterations per level n_{iter} required to achieve convergence of the velocity field. Computing speed is a function of these two integers. If $(\delta x)_{max}$ is the maximum displacement, as a general rule n_{lev} must verify equation 4.1 from Champagnat et al.:

$$(\delta x)_{max}/2^{n_{lev}-1} < 3\ pixels \tag{4.1}$$

One can see that choosing the time step between images defines the value of n_{lev}. One must then choose n_{iter}. A low value will give higher performances with slightly lower result quality. When working in real-time a low value (1 or 2) of n_{iter} is recommended. However for off-line computations the value should be raised to ensure full convergence. Performances should still be greater than with commercial PIV software.

While a number of pre and post-processing options are usually used to enhance the computed velocity fields, these operations have a computational cost. Therefore a balance must be found between obtaining usable data and processing speed.

Raw images are pre-processed using a standard local equalization algorithm. This step is implemented on the GPU for increased performance. We have found this step to be mandatory for experimental images processing. Without, the computation does not yield usable data.

Original image intensity is normalized following equation 4.2:

$$\forall (x,y) \in I, \tilde{I}(x,y) = \frac{I(x,y) - \bar{I}(x,y)}{\sqrt{\bar{I}^2(x,y) - \overline{I^2}(x,y)}} \tag{4.2}$$

where $\bar{I}$ is a *local* mean for a given radius. We choose a radius of 5 pixels. This zero normalized sum of square differences (ZNSSD) is common for PIV pre-filtering. The aim is to eliminate the influence of illumination inhomogeneities. For each pixel the mean intensity value is subtracted (zero mean) and divided by the local intensity standard deviation (normalized).

The nature of the algorithm is such that computed velocity fields are naturally smooth. Thus there is no post processing required to cull spurious vectors.

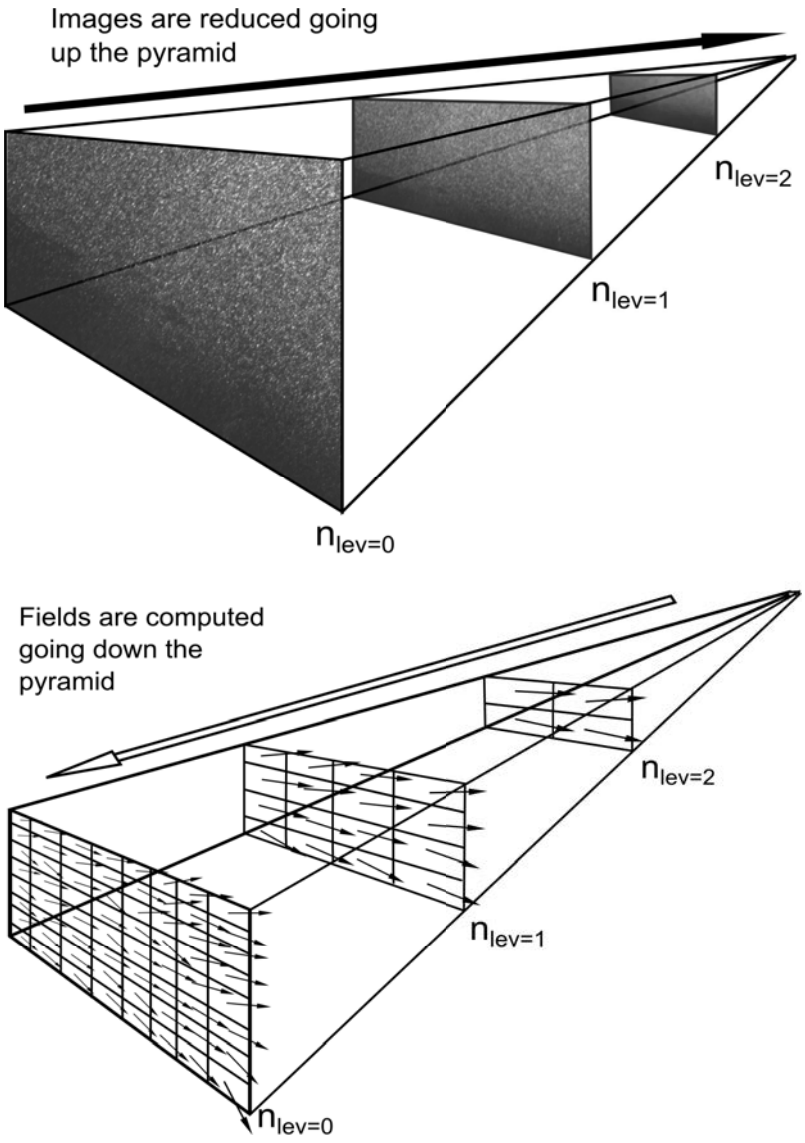

Figure 4.3: Sketch of the computation pyramid. The resolution of the original picture is divided by two in both directions n times leading to coarser and coarser images with smaller and smaller displacements. The displacements are first evaluated on the coarser level which can then be used as first guess for the next level. We illustrate the case of a pyramid with $n = 2$ level.

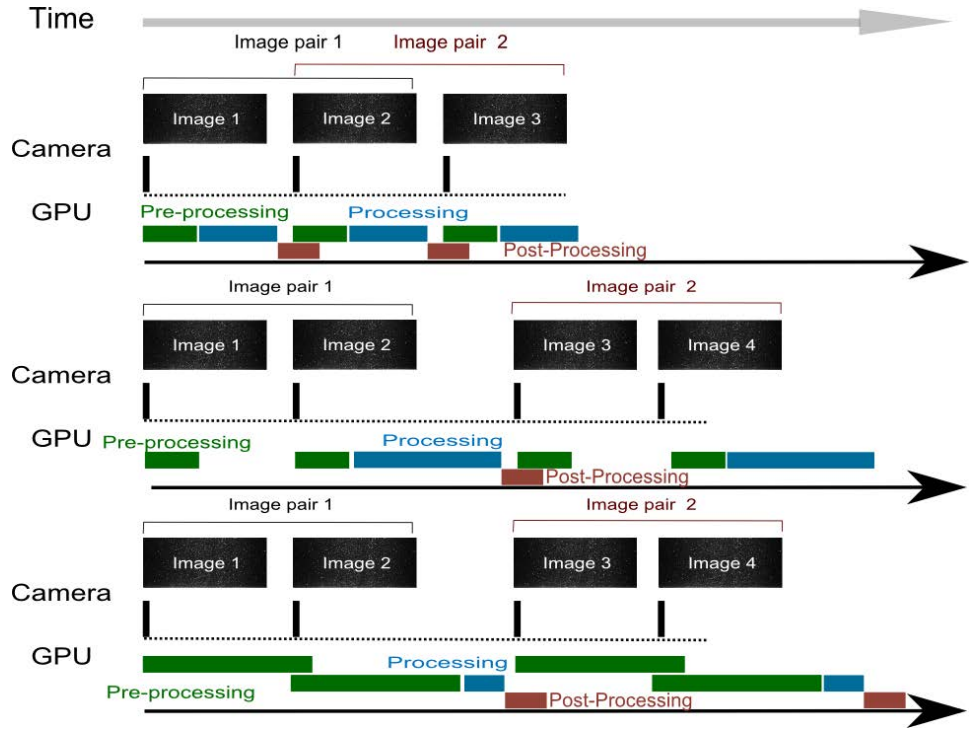

Figure 4.4: Different computing schemes

For our setup, only a fraction of the camera resolution is used (the region of interest (ROI) = 1792 × 384). It is enough to capture the whole recirculation bubble downstream the BFS, while ensuring good computing performances. Reducing the time step δt between two pictures acquisitions allows lower values of n_{lev} and higher performances. n_{lev} can be lowered to 0 with a small enough displacement. Decreasing n_{lev} shifts the burden of performance to the camera. n_{iter} should be raised until the computed velocity field does not vary, with $n_{iter} \geq 1$. $n_{iter} \geq 10$ is seldom needed. With current hardware it is difficult to achieve satisfactory performances with a high number of iterations ($n_{iter} > 4$). n_{iter} can be brought down as low as 1 and still yield usable quantitative information on the flow, with a significant improvement in computing times.

Concerning latency, depending on GPU performances and camera acquisition frequency, different computing schemes are implemented for optimal performances as shown in figure 4.4.

The first scheme is used when computation is fast enough to keep up with the camera. This is the fastest scheme by far since each field computation requires only one image to be processed. The second is used when the first cannot and pre-processing time is lower than camera exposure. Finally when preprocessing takes too long, preprocessing on the second image starts while preprocessing on the first image is finishing. Latency varies depending on the scheme but is upper bounded by exposure time plus the time required to preprocess one

image and compute the corresponding field. Post-processing can also be *hidden* during copy from the camera to the GPU, a period during which the GPU is iddle. Post-processing here refers to the computation of integral quantities from the data.

4.3.5 PIV computations

To validate the optical flow measurements standard PIV algorithms were used off-line. The Davis software from LaVision was used, using a PIV multi-pass cross-correlation algorithm with a final 16×16 pixel interrogation window with 50 % overlap, thus leading to PIV fields with a 8 × 8 pixel grid resolution.

4.4 Results

4.4.1 Real-time computation of instantaneous 2D velocity fields

Figure 4.5a shows the instantaneous velocity amplitude for $Re_h = 2500$ obtained using PIV. Figure 4.5b shows the velocity amplitude computed from the same pair of images using the optical flow algorithm. One can see that the instantaneous shear layer and recirculation bubble are well captured and very similar in both cases. To evaluate more quantitatively the difference between the two instantaneous velocity fields, the non-dimensional difference between the two fields is computed and shown on figure 4.5c. The differences are small over the whole velocity field, apart from small spots where difference are higher. This can be explained by small local shift of spots where velocity gradients are high. The differences between the two velocity fields are also mainly due to poorer results for the PIV algorithm near the edges of the acquisition window. One can also notice a poorly resolved region in the PIV field right after the step. This illustrates how the optical flow output can sometimes be superior to PIV even in the free stream region.

4.4.2 Comparison of the real-time optical flow measurements with off-line PIV computations

The accuracy of the algorithm has been demonstrated *off-line* for numerical and experimental data by Champagnat et al.. In this section we will focus on the computation of an integral scalar value derived in real-time from the instantaneous velocity fields. The objective is twofold: illustrate the real-time computation of a global quantity extracted from instantaneous velocity fields in real-time and evaluate the accuracy of the optical flow computations compared to standard PIV computations.

There are a number of pertinent integral values which can be used to characterize the separated flow. In this experiment we choose to compute a measure of the recirculation area in the instantaneous 2D velocity field. It is straightforward and quick to compute while remaining a good way of evaluating the state of the flow. Equation 9.1 describes how recirculation area is defined:

$$A_r = \int H(-v)(x,y)dxdy \tag{4.3}$$

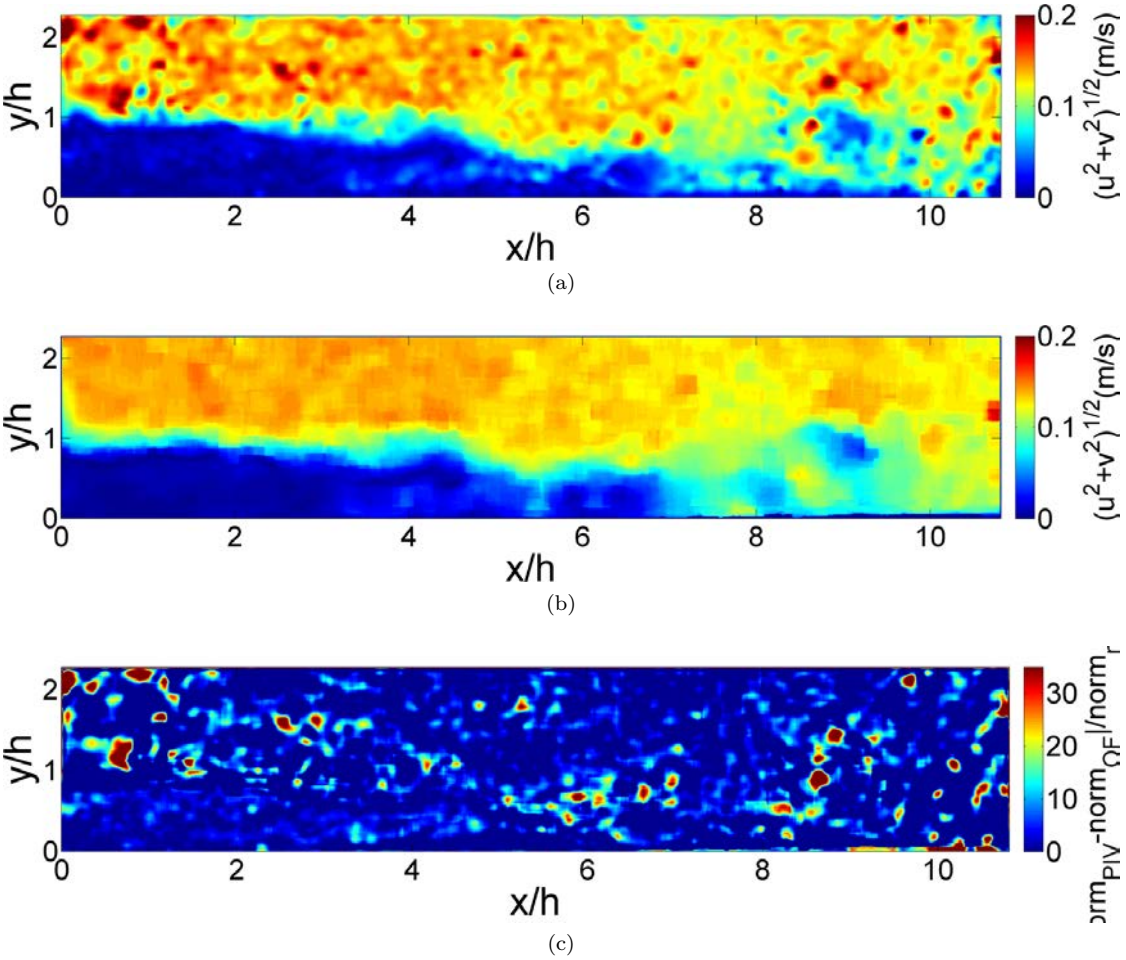

Figure 4.5: Contour of instantaneous velocity magnitude field downstream the BFS for $Re_h = 2500$ computed by PIV (a) and by optical flow (b). Figure (c) shows the absolute value of the norm difference scaled by the maximum norm.

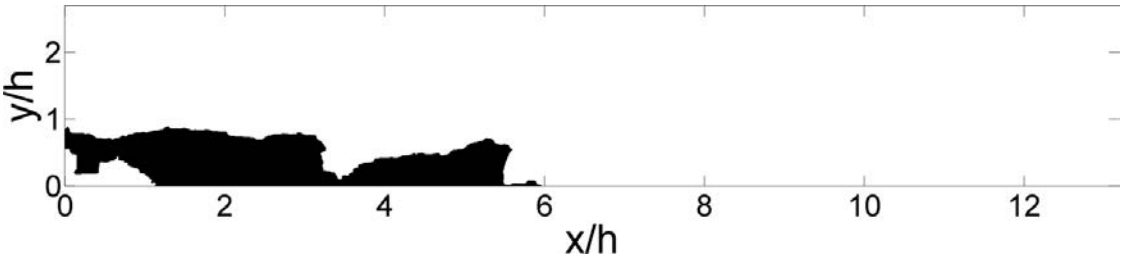

Figure 4.6: Visualization of the recirculation area (black region). A_r is computed in real-time.

where H is the Heaviside function and v is longitudinal velocity. In the following A_r will be normalized by h^2. It should be noted this is one way of defining recirculation area. Another definition is th region bounded by the wall and the streamline connecting the separation point at the step edge and the reattachment point, the upper half of this area has positive longitudinal velocity. Thus the former definition for recirculation area would be about half of the latter.

Figure 4.6 shows the recirculation area (in black) for an instantaneous velocity field. Such computations are carried out for both optical flow and PIV velocity fields. The recirculation bubble area can be correlated to the reattachment length L_R usually used to characterize the BFS flow (Armaly et al. (1983), Aider et al. (2007)). Such an integral value could, for example, be used as an input in a feedback loop.

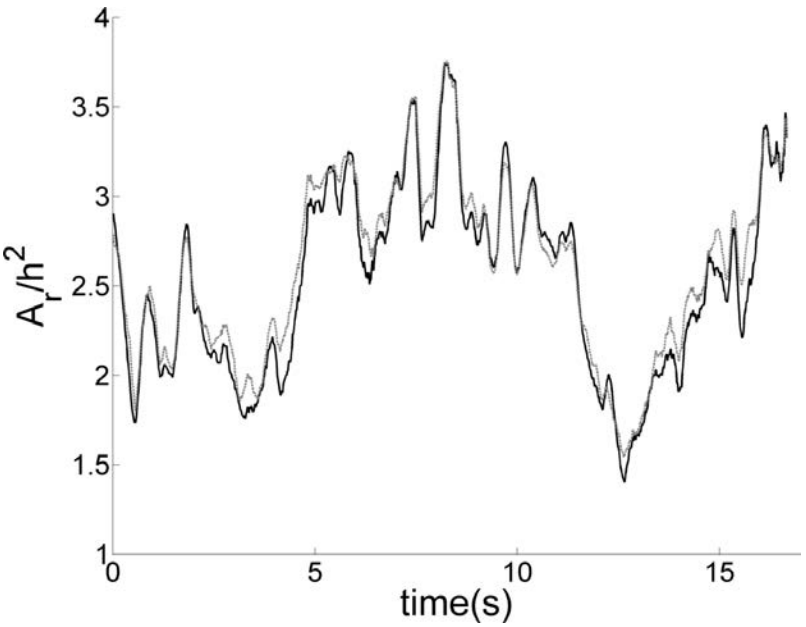

Figure 4.7: Comparison of time series of recirculation bubble surface A_r computed using Optical flow (black full line) and PIV (grey dotted line) for a time-resolved velocity measurement.

Figure 4.7 shows time series of instantaneous A_r computed with optical flow and with PIV for a time-resolved series computed off-line. Data featured in figure 4.7 are for $Re_h = 2500$ and with an acquisition rate of 60 image pairs per second. One can see that there is a good agreement between the two time-series. Differences can be explained by the fact some images do not contain enough particles in the recirculation region, thus both algorithm converge to slightly different values in this region, furthermore window interrogation sizes are different (10 for optical flow, 16 for PIV) and overlap is also different (90 % for optical flow, 50 % for PIV). Because of the dense nature of the optical flow output, more information is available near the walls (Champagnat et al.). The computed recirculation bubble is more clearly defined and is subject to greater variations as shown in figure 4.7.

Figure 4.8a shows a comparison of the surface of the mean recirculation bubble as a function of Reynolds number computed by PIV or optical flow. Figure 4.8b shows the relative difference between results obtained with both algorithms. Agreement is good with a relative difference always lower than 3%. It shows that the optical flow computations is robust over a wide range of Reynolds numbers corresponding to complex instantaneous flows.

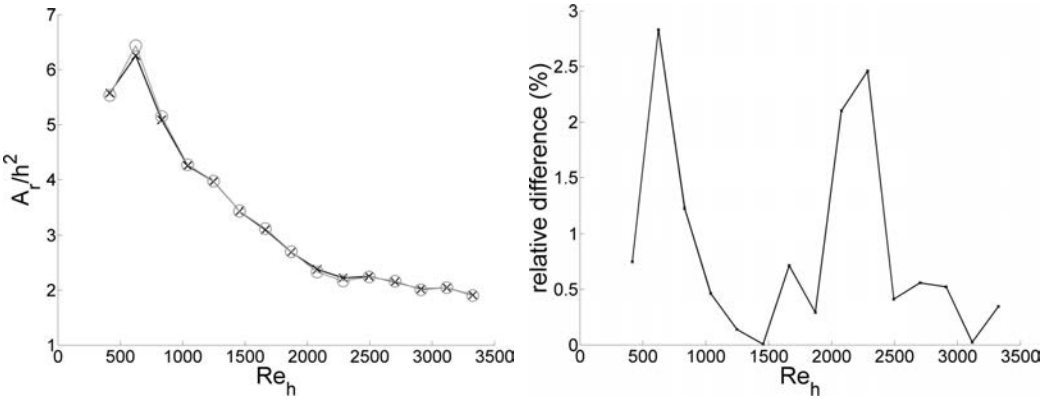

(a) (b)

Figure 4.8: (a) Comparison of mean A_r computed with PIV ($\times$ and full line) and optical flow ($\circ$ and dotted line) algorithms.(b) Relative difference on recirculation bubble surface between PIV and optical flow

4.4.3 Optimizing the computation frequency

		n_{iter}						
		1	2	3	4	5	6	7
n_{lev}	3	4.81% 224.0 fps	2.10% 148.0 fps	1.47% 112.0 fps	1.12% 89.3 fps	0.98% 73.5 fps	0.97 % 63.0 fps	0.3 % 55.7 fps
	4	3.66% 220.0 fps	2.13% 147.0 fps	1.46% 110.1 fps	1.13% 87.2 fps	0.99% 72.4 fps	0.94% 62.0 fps	0% 55.6 fps

Table 4.1: Error and fields per second (fps) as a function of computing parameters.

This setup allows for accurate computations of the 2D velocity fields in real-time. If the aim of the user is real time visualizations and/or quick computations of flow properties for a feedback loop, constraints on the algorithm can be relaxed. Indeed, some compromise can be found if increased computations speed is called for. If the aim is the computation of accurate velocity fields, constraints should be increased to achieve maximum accuracy, while still retaining fast computing times in real time.

Table 4.1 shows how one can drastically improve computation speed, by lowering the number of levels and iterations while still retaining a meaningful integral information from the flow. n_{iter} is the most important parameter when it comes to performance, with n_{lev} a distant second, This is understandable as higher tiered levels of the pyramid have much smaller images sizes causing little increase in processing costs.

A video is linked to this article showing flow images and real-time computed fields as well as A_r history. Higher frame rate can be achieved by shortening the time step between two images in order to lower the maximum displacement and thus allowing $n_{lev} \to 0$. It can lead to a maximum of 350 fps at this resolution. Higher sampling frequency can be achieved by reducing the field of view, for example by focusing on an area of interest or using masks to avoid computations over obstacles or side walls.

The aforementioned performances are achieved with a given hardware. The scalability of the algorithm ensures greater performance with better GPUs. Moreover since the computation of a velocity field is independent of all other computations, adding additional graphic cards to the setup would allow for a proportional increase in computation speed. The only limit to the achievable frame rate are the acquisition rate of the camera image quality. For very high acquisition frequencies, a more powerful CW laser, a pulsed YaG laser and/or a more sensitive and faster camera are required.

4.5 Conclusion and perspectives

We have shown how a simple and relatively low cost setup can be configured to achieve high speed real-time computations of a flow velocity field. The key feature of the setup is the use of an optical flow algorithm which takes advantage of the massively parallel processing capabilities of GPUs. It is now possible to compute in real-time any local or global relevant quantity from this velocity field. It is now easy to evaluate the state of a complex flow in real time, which a major step-forward for experimental fluid mechanics community. The relevant flow characteristics can be computed and stored without keeping the raw data (images time series). This can lead to major savings in both time and data storage facilities. This work is useful to experimentalists who wish to quickly analyze flow properties, it can also be useful to those who wish to use high frequency flow data to implement closed loop control in flow control experiments. We have demonstrated the accuracy of the method by comparing our results with results obtained by the more widely used PIV approach, computed off-line. Finally, ways of improving computing speed and reaching higher frame rates have also been discussed.

4.6 Acknowledgments

The authors gratefully acknowledge the financial support of the DGA, as well as Aurelien Plyer (ONERA) for all his helpful advices.

Bibliography

R. J. Adrian. Twenty years of particle image velocimetry. *Exp Fluids*, 39(2):159–169, August 2005.

J-L. Aider, A. Danet, and M. Lesieur. Large-eddy simulation applied to study the influence of upstream conditions on the time-dependant and averaged characteristics of a backward-facing step flow. *Journal of Turbulence*, 8:N51, 2007.

B. F. Armaly, F. Durst, J. C. F. Pereira, and B. Schonung. Experimental and theoretical investigation of backward-facing step flow. *J Fluid Mech*, 127:473–496, 1983.

J-F. Beaudoin, O. Cadot, J-L. Aider, and J.E. Wesfreid. Three-dimensional stationary flow over a backwards-facing step. *European Journal of Mechanics*, 38:147–155, 2004.

G. Le Besnerais and F. Champagnat. Dense optical flow by iterative local window registration. *ICIP*, 1:137–140, 2005.

M. Gharib C. Willert, M. Munson. Real-time particle image velocimetry for closed-loop flow control applications. volume 1, pages 1–1. 5th Intal Symposium on Applications of laser techniques to fluid mechanics, 05-08 Jul. 2010. Lisbon Portugal, 2010.

F. Champagnat, A. Plyer, G. Le Besnerais, B. Leclaire, S. Davoust, and Y. Le Sant. Fast and accurate piv computation using highly parallel iterative correlation maximization. *Exp Fluids*, 50:1169–1182. ISSN 0723-4864.

F. Champagnat, A. Plyer, G. Le Besnerais, B. Leclaire, and Y. Le Sant. How to calculate dense piv vector fields at video rate., 2009.

K. B. Chun and H. J. Sung. Control of turbulent separated flow over a backward-facing step by local forcing. *Exp Fluids*, 21:417–426, 1996.

S. Davoust, L. Jacquin, and B. Leclaire. Dynamics of m = 0 and m = 1 modes and of streamwise vortices in a turbulent axisymmetric mixing layer. *J Fluid Mech*, 709:408–444, 2012.

R.T. Fomena and C. Collewet. Fluid flow control : A vision-based approach. *Intal Journal of Flow Control*, 3:133–169, 2011.

G. Tadmor H. Yu, M. Leeser and S. Siegel. Real-time particle image velocimetry for feedback loops using fpga implementation. *43rd AIAA Aerospace Sciences Meeting and Exhibit*, 2005.

D. Heitz, E. Mémin, and C. Schnörr. Variational fluid flow measurements from image sequences : Synopsis and perspectives. *Exp Fluids*, 48:369–393, 2010.

L. Henning and R. King. Drag reduction by closed-loop contriol of a separated flow over a bluff body with a blunt trailing edge. *44th Institute of Electrical and Electronics Engineers (IEEE) Conference on Decision and control and European Conference (ECC), IEEE, Psicataway, NJ,2005*, 1:494–499, 2005.

Lars Henning and Rudibert King.

L. Hung, M. Parviz, and K. John. Direct numerical simulation of turbulent flow over a backward-facing step. *J Fluid Mech*, 330:349–374, 1997.

P. Joseph, X. Amandolese, and J. L. Aider. Drag reduction on the 25 degrees slant angle ahmed reference body using pulsed jets. *Exp Fluids*, 52:1169–1185, May 2012.

M. Kreizer, D. Ratner, and A. Liberzon. Real-time image processing for particle tracking velocimetry. *Exp Fluids*, 48:105–110, 2010.

L. Lelong, G. Motyl, J. Dubois, A. Aubert, and G. Jacquet. Image processing in fluid mechanics by cmos image sensor. In *Proceedings of PSFVIP-4*, 2003.

Bruce D. Lucas. *Generalized image matching by the method of differences*. Phd, Carnegie Mellon University, 1984.

nVidia. Cuda c programming guide, 2007.

nVidia. White paper, fermi architecture, 2010.

R. Osbron, S. Kota, J. Hetrick, D. Geister, C. Tilmann, and J. Joo. Active flow control using high-frequency compliant structures. *Journal of Aircraft*, 41:603–609, 2004.

Mark Pastoor, Lars Henning, Bernd R. Noack, Rudibert King, and Gilead Tadmor. Feedback shear layer control for bluff body drag reduction. *J Fluid Mech*, 608:161–196, 2008.

J. Rabinovitch, V. Brion, and G. Blanquart. Effect of a splitter plate on the dynamics of a vortex pair. *Phys Fluids*, 24:74–110, 2012.

J. Roberts. *Control of underactuated fluid-body systems with real-time image velocimetry*. Phd, MIT, 2012.

A. Roshko. Experiments on the flow past a circular cylinder at very high reynolds number. *J Fluid Mech*, 10:345–356, 1961.

F. Sartor, G. Losfeld, and R. Bur. Piv study on a shock-induced transition in subsonic flow. *Exp Fluids*, 53:815–827, 2012.

Chapter 5

Control of the separated flow downstream a backward-facing step using visual feedback

This paper demonstrates the feasibility and viability of flow control by visual feedback. The objective was to implement the most basic form of closed-loop control which included an optical sensor, substituting traditional parietal or hot-wire sensors with optical sensors. A basic PID algorithm is shown to effect set point control of the recirculation area and swirling strength for the backward-facing step flow. In addition a simple gradient descent scheme is shown to successfully minimize recirculation. Recirculation was measured in both vertical and horizontal middle planes. The flow is controlled by varying the amplitude of continuous upstream jets. This work was crucial in validating flow control through visual feedback. To the author's knowledge this was the first time a study involving closed loop flow control with optical sensors was published in a peer reviewed experimental study.

5.1 Abstract

The separated flow downstream a backward-facing step is controlled using visual information for feedback. This is done when looking at the flow from two vantage points. Flow velocity fields are computed in real-time and used to yield inputs to a control loop. This approach to flow control is shown to be able to control the detached flow in the same way as has been done before by using the area of the recirculation region downstream the step as input for a gradient descent optimization scheme (Henning and King (2007)). Visual feedback using real-time computations of 2D velocity fields also allows for novel inputs in the feedback scheme. As a proof of concept, the spatially averaged value of the swirling strength λ_{ci} is successfully used as input for an automatically tuned PID controller.

5.2 Introduction

Flow separation is a subject of scientific and industrial importance. Separated flows can strongly influence the performances for many industrial devices, such as diffusers, airfoils, air conditioning plants, moving vehicles, and many other industrial systems (Simpson (1996), Hucho (2005), Paschereit et al. (2000)). Usually the focus is on minimizing the size of the recirculation region, also called recirculation bubble, to improve drag, reduce lift, reduce vibrations or lower aeroacoustic noise.

To manipulate a detached flow many kinds of actuations have been considered. A list of actuations can be found in Fiedler and Fernholz (1990). In the case of open-loop flow control, passive actuation often improves characteristics of the flow only for given operating conditions. Active actuators have also been used in open-loop experiments, (see Chun and Sung (1996), Uruba et al. (2007)), but they are unable to adapt to exogenous parameter changes. Feedback control strategies, or closed-loop flow control, offer the possibility of adapting the actuation to external perturbations or changes in the experimental conditions, thus improving the robustness of the control. One can cite a few recent examples of closed loop control strategies implemented either numerically or experimentally: Beaudoin et al. (2006), Henning and King (2007), Pastoor et al. (2008).

The backward-facing step (BFS) is considered as a benchmark geometry for studying detached flow. Separation is imposed by a sharp edge, thus allowing the separation process to be examined by itself. The main features of the BFS flow are the creation of a recirculation downstream of the step together with a strong shear layer in which Kelvin-Helmholtz instability can trigger the creation of spanwise vortices. The flow downstream a backward-facing step has been extensively studied both numerically and experimentally, see Armaly et al. (1983), Hung et al. (1997), Beaudoin et al. (2004), Aider et al. (2007).

An essential part of many control strategies is determining one or several control variables. The variable is either directly computable from sensor data, such as local pressure or drag measurement, or obtained by combining sensor data and a model. This model can be simple (Henning and King (2007) recover recirculation length via its correlation to pressure fluctuations) or complicated (Sipp et al. (2010) recovers an approximation of the flow state through Kalman filtering). In the case of the backward-facing step, sensors are almost always pressure sensors, and the control variable is usually the recirculation length. While wall based sensors present the advantage of high frequency acquisition they also present a limited view of the flow: many phenomena are difficult to access because buried in noise or simply unobservable. Furthermore they are intrusive.

Using the flow velocity field computed from visual data to control a flow has been suggested and successfully implemented in numerical simulations (Fomena and Collewet (2011)). Control using visual feedback was implemented as a proof of concept by C. Willert (2010). Roberts (2012) was successful in improving the control of the flow behind a flap using real-time instantaneous velocity data. The exponential rise in computing power allows for the computation of large, dense, accurate velocity fields at high frequencies as shown in Gautier and Aider (2013).

In this paper we investigate the feasibility of controlling the separated flow behind a backward-facing step using flow velocity fields computed in real-time from visual data. The flow is observed both from the side and from above. Two control variables are used, the recirculation area and the spatially averaged swirling intensity. A jet is used to act on the flow. The

evolution of the control variables with Reynolds number (based on step height h) or the jet velocity is determined. Two basic schemes are implemented to control the flow. To show how visual feedback can be used in the same control schemes as have been previously proposed the recirculation area is used as input variable to a gradient descent optimization scheme. To show visual servoing can be used to control the flow in novel ways, the control variable based on swirling strength is used as input to a PID controller. The aim of this paper is to show the relevance of visual feedback for detached flows. Thus the injection geometry, control variables and control schemes are reduced to their simplest expression.

5.3 Experimental setup

5.3.1 Water tunnel

Experiments were carried out in a hydrodynamic channel in which the flow is driven by gravity. The walls are made of Altuglas for easy optical access from any direction. The flow is stabilized by divergent and convergent sections separated by honeycombs. The test section is 80 cm long with a rectangular cross section 15 cm wide and 10 cm high.

The mean free stream velocity U_∞ ranges between 1.38 to 22 cm.s^{-1}. A specific leading-edge profile is used to smoothly start the boundary layer which then grows downstream along the flat plate, before reaching the edge of the step 33.5 cm downstream. The boundary layer is laminar and follows a Blasius profile. The quality of the main stream can be quantified in terms of flow uniformity and turbulence intensity. The standard deviation σ is computed for the highest free stream velocity featured in our experimental set-up. We obtain $\sigma = 0.059$ cm.s^{-1} which corresponds to turbulence levels of $\frac{\sigma}{U_\infty} = 0.0023$.

5.3.2 Backward-facing step geometry

The backward-facing step geometry and the main geometric parameters are shown in figure 9.1. The height of the BFS is $h = 1.5$ cm, leading to Reynolds numbers $Re_h = \frac{U_\infty h}{\nu}$ ranging between 0 and 3300 (ν being the kinematic viscosity). Channel height is $H = 7$ cm for a channel width $w = 15$ cm. One can define the vertical expansion ratio $A_y = \frac{H}{h+H} = 0.82$ and the spanwise aspect ratio $A_z = \frac{w}{h+H} = 1.76$. The distance between the injection slot and step edge is $d = 3.5$ cm.

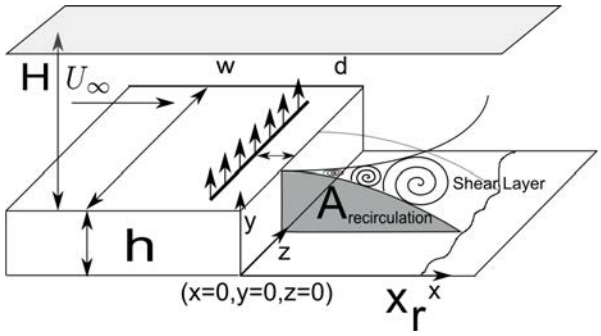

Figure 5.1: Sketch of the BFS geometry and definition of the main parameters.

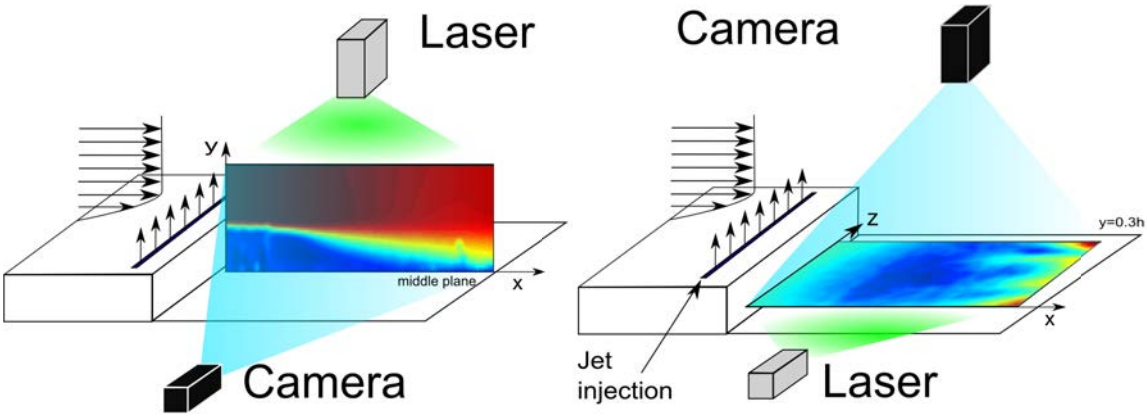

Figure 5.2: Definition of the two measurement configurations used to characterize the separated flow downstream the backward-facing step: measurements in the symmetry plane (SP) and in a $y = 0.5$ cm horizontal plane (HP).

5.3.3 Real-time 2D2C velocimetry

The flow is seeded with 20 μm neutrally buoyant polyamid seeding particles. The test section is illuminated by a laser sheet created by a 2W continuous CW laser beam operating at wavelength $\lambda = 532$ nm passing through a cylindrical lens. The pictures of the illuminated particles are recorded using a Basler acA 2000-340km 8bit CMOS camera. The camera is controlled by a camera-link NI PCIe 1433 frame grabber allowing for real-time acquisition and processing. Velocity field computations are run on the Graphics Processor Unit (GPU) of a Gforce GTX 580 graphics card.

The 2D2C (measurements of two components in a 2D plane) velocimetry measurements are obtained using an optical flow algorithm called FOLKI, developped by Champagnat et al. (2011). It is a local iterative gradient-based cross-correlation optimization algorithm which yields dense velocity fields, i.e. one vector per pixel. It belongs to the Lucas-Kanade family of optical flow algorithms (Lucas (1984)). The spatial resolution however is tied to

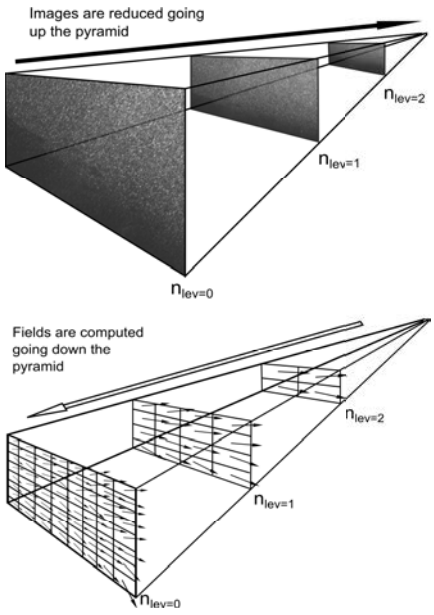

Figure 5.3: Sketch of the computation pyramid.

the window size, like any other window based PIV technique. However the dense output is advantageous as it allows the sampling of the vector field very close to obstacles, yielding good results near walls, as shown in Champagnat et al. (2011). The algorithm was used by Davoust et al. (2012), Sartor et al. (2012), and Rabinovitch et al. (2012).
Description of the algorithm and how it is implemented on a GPU is available in Champagnat et al. (2011). Moreover its offline accuracy was extensively studied by Champagnat et al. (2011). GPU implementation allows it to run at high frequencies. Its online efficacy at high frequencies was demonstrated in Gautier and Aider (2013). No changes were made to the algorithm, however pre-processing routines were written to ensure smooth operation, as described in Champagnat et al. (2011). Code optimizations and tweaks were also made in order to increase operating frequencies, most of which are detailed in Gautier and Aider (2013). All post-processing routines run independantly of the core code, and therefore do not affect the quality of the output fields.

The principle of the featured optical flow algorithm is as follows. The original images are reduced in size by a factor of 4 iteratively until intensity displacement in the reduced image is close to 0. This gives a pyramid of images, described in figure 5.3. Displacement is computed in the top image with an initial guess of zero displacement using an iterative Gauss-Newton scheme to minimize a sum of squared difference criterion. This displacement is then used as an initial estimate for the same scheme in the next pair of images in the pyramid. And so on until the base of the pyramid, corresponding to the initial images is reached, thus giving the final displacement.

It should be noted this pyramidal process allows the algorithm to converge for small and high displacements indiscriminately making it ideally suited to compute velocities in

separated flows where regions of low and high velocity fluid often coexist.

Because of its intrinsically parallel nature the algorithm is able to fully utilize the processing power of modern GPUs. It is not uncommon to reach 99% GPU loads. Allowing it to accurately compute flow velocity fields for large images (typically 2 Megapixels) at relatively large frame rates (24 frames per second or greater frequencies with the given hardware). Furthermore it scales exceptionally well with increasing computing power. Although there are differences with classic PIV algorithms, output velocity field resolution is still tied to the size of the interrogation window. Nevertheless, the output field is dense (one vector per pixel) giving better results in the vicinity of edges and obstacles. Furthermore this gives exceptionally smooth fields.

Two configurations are used in the following: the first is the classic vertical symmetry plane (SP) and the second is a horizontal plane (HP), as illustrated in figure 5.2. The position of the horizontal plane, for the HP configuration, was $y = 0.5$ cm. The position was the result of a compromise. The plane was placed as close to the lower wall as possible while still getting good image quality. When the plane is too close to the wall, the light reflected by the particles on the bottom wall makes the measurement difficult. Figure 5.2 shows how the flow was observed both from the side and from above. Characteristics of the measurement for both configurations are detailed in table 5.1.

	Symmetry plane (SP)	Horizontal plane (HP)
Position	Medium plane	5mm from bottom
Image resolution	1792x384	1920x1024
mm/pixel	0.107	0.07
Interrogation window size	10x10	32x32

Table 5.1: Characteristics of measurement windows for SP & HP configurations

5.3.4 Actuation & Feedback loop

The flow is controlled using a spanwise, normal to the wall, slot jet, 0.1 cm long and 9 cm wide. The slot is located 3.5 cm upstream the step edge (figure 9.1). Water coming from a pressurized tank enters a plenum and goes through a volume of glass beads designed to homogenize the incoming flow. Jet output is controlled by changing the tank pressure. The injection geometry was chosen to avoid 3D effects and keep the perturbation as bi-dimensional as possible. The control parameter, or manipulated variable, is the mean jet velocity V_j. Mean jet velocity varies from - 5 to 35 cm.s^{-1}. Since the jet supply tank is below the channel tank there is some suction when no pressure is supplied to the jet tank, allowing easy refilling of the tank. The dimensionless actuation amplitude is defined as the ratio of the mean jet velocity to the flow velocity $a_0 = \bar{V_j}/U_\infty$.
The feedback loop is summarized in figure 5.4.

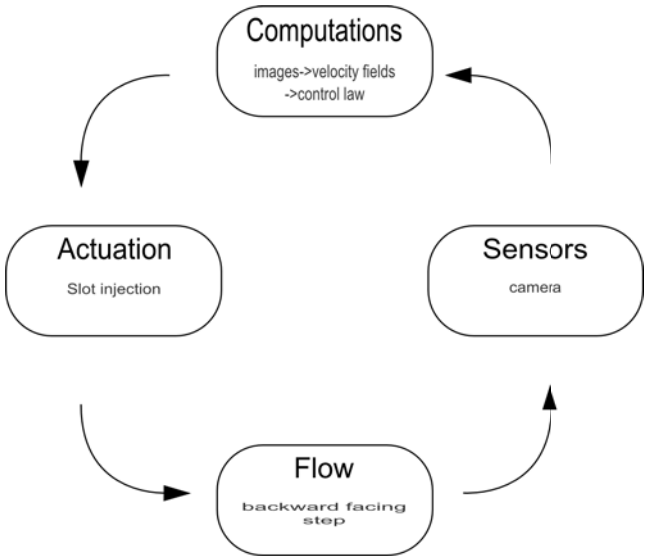

Figure 5.4: Feedback scheme

In the following, open-loop experiments are carried out for all Reynolds numbers while closed-loop control experiments are carried out for one single Reynolds number, $Re_h = 2900$. For all Reynolds , vortex shedding frequency does not exceed 3.62 Hz, figure 7.10b shows a frequency spectrum for vortex shedding, it was obtained for the highest Reynolds. It was obtained by spatially averaging λ_{Ci} in the vertical direction at $x = 2.5h$. As a rule of thumb discrete time control should be effected ten times as fast as the phenomena one whishes to control, thus a frequency of 40 Hz should be sufficient to control the flow . The real-time velocimetry allows for feedback acquisition frequency up to 73 Hz for the SP case and 22.5 Hz for the HP case. The frequency is lower for the HP case because the images are bigger. It should be noted higher frequencies can be achieved for both cases but it was not needed for the current experiments. Since to high a frequency can cause instabilities sample rate was fixed at 40 Hz.

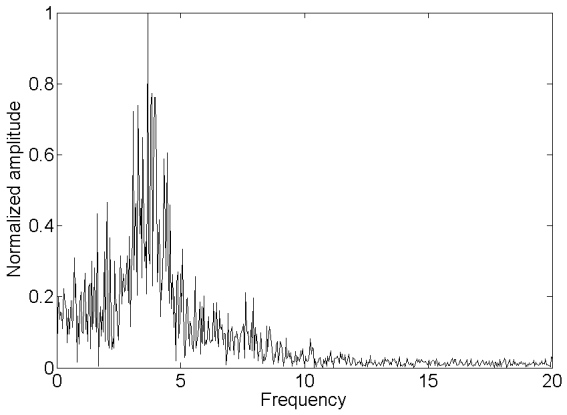

Figure 5.5: Frequency spectrum for $Re_h = 3300$, peak frequency is 3.62 Hz.

5.4 Characterization of the uncontrolled flow

5.4.1 Evolution of the recirculation with Re_h

The first step is to choose and properly define the quantity to be controlled. In the case of separated flows, specifically backward-facing step flows, the recirculation length X_r is commonly used as input variable (Henning and King (2007), Chun and Sung (1996)). Because 2D velocity data are now available for the flow, the recirculation can be characterized by its area instead of its length. The recirculation area can be considered to be the area occupied by the region(s) of flow where longitudinal velocity is negative. Recirculation area $A_{recirculation}$ is then defined in equation 6.1:

$$A_{recirculation}(t) = \int_A H(-v_x)da \tag{5.1}$$

where $v_x(x, y)$ (respectively $v_x(x, z)$ for the HP case) is the streamwise velocity measured in the vertical (x, y) (respectively (x, z)) plane. This definition presents several advantages. It is applicable regardless of camera position. It is simple, straightforward and can be implemented at low computational cost, thus computation does not slow down the feedback loop. Moreover no past data need be computed. Figure 5.6 shows instantaneous bubbles areas for both configurations. Black regions correspond to the separated flow. One can see that the regions are well-defined. The contours are irregular, with holes especially in the HP configuration. This is consistent with previous observation of instantaneous recirculation (Aider et al. (2007)): the reattachment line is fully three-dimensional because of the destabilization of the transverse Kelvin-Helmholtz vortices shed in the shear layer. The scalar quantity used as an input for the closed-loop experiments can be $A_{recirculation}(t)$, the spatial average of the regions in the instantaneous 2D velocity field where a backward flow is measured at time t.

It is also interesting to compute the time-averaged recirculation length $< X_r >_t$ or area $< A_{recirculation} >_t$ as a function of the Reynolds number to compare with previous experimental

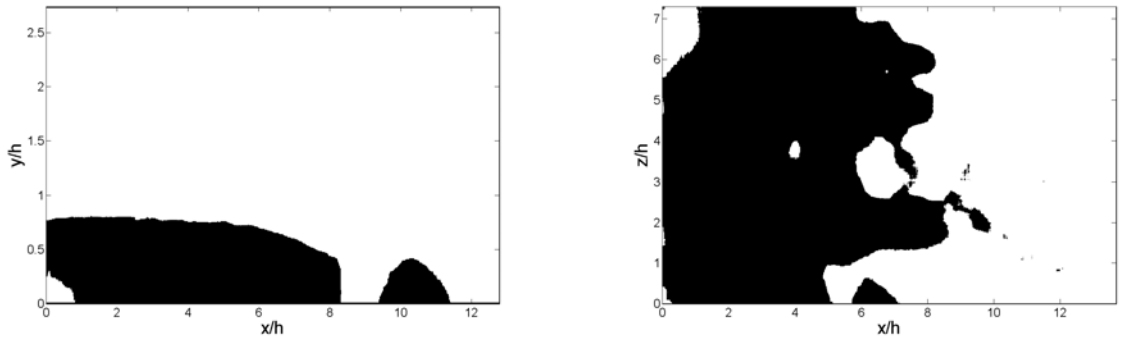

a) b)

Figure 5.6: a) Visualization of the instantaneous recirculation area (black region) for configuration SP (a) and HP (b).

or numerical studies. In the following, 1000 image pairs were taken at a sampling frequency $F_s = 3.06$ Hz for 16 Reynolds numbers and for both configurations.

Figure 5.7a shows the evolution of the mean recirculation area (normalized by h^2) for the SP configuration and mean recirculation length $< X_r >_t$ (normalized by h) extracted from the mean longitudinal velocity field, choosing the second point at the wall where longitudinal velocity changes from negative to positive. Figure 5.7b shows the evolution of mean recirculation area (normalized by h^2) for the HP configuration. The normalized values are higher since the area is effectively larger when observed from above, however the trend is similar. Thus observing the flow from above allows for the determination of the recirculation state. Moreover observing from above gives access to the span wise fluctuations of the recirculation. It can be useful if one wishes to control the span wise reattachment, as was done by Henning and King (2007) using a grid of 60 pressure sensors.

Recirculation length evolves in a way consistent with previous observations (Armaly et al. (1983)). Furthermore, normalized recirculation area closely follows the evolution of normalized recirculation length, therefore making it a relevant parameter to characterize the flow state. These results also show how the evolution of the recirculation can be followed whichever plane the flow is observed from. This enables visual servoing to be used with any control scheme using the recirculation area as control variable.

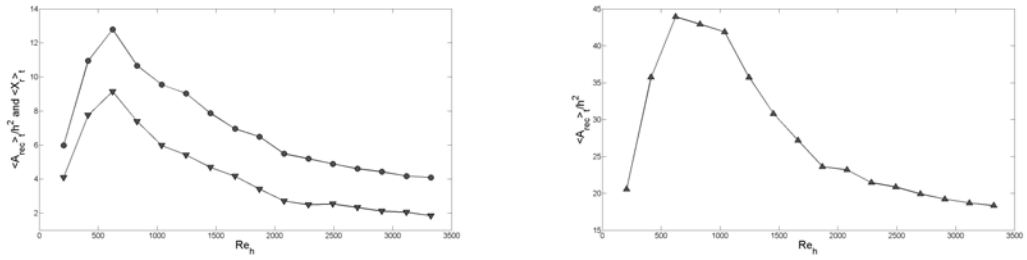

a) b)

Figure 5.7: a) Mean recirculation length (●) and mean recirculation area (▼) as a function of Re_h for the side configuration. b) Mean recirculation length (▲) as a function of Re_h for the HP configuration.

5.4.2 Evolution of the swirling intensity with Re_h

A great advantage of visual servoing is that it also allows the experimentalist to compute previously inaccessible control variables, such as those proposed by Choi et al. (1999), i.e. variables involving quantities derived from the flow field such as velocity fluctuations, pressure fluctuations, and vorticity.

We chose to compute the swirling strength criterion $\lambda_{ci}(s^{-1})$ which was first introduced by Chong et al. (1990) who analyzed the velocity gradient tensor and proposed that the vortex core be defined as a region where $\nabla\mathbf{u}$ has complex conjugate eigenvalues. For 2D data we have $\lambda_{Ci} = \frac{1}{2}\sqrt{4\det(\nabla\mathbf{u}) - \mathrm{tr}(\nabla\mathbf{u})^{\mathbf{2}}}$ when such a quantity is defined, else $\lambda_{Ci} = 0$. It was later improved and used for the identification of vortices in three-dimensional flows by Zhou et al. (1999). This criterion allows for an effective detection of vortices even in the presence of shear (Cambonie et al. (2013)). The value $\frac{2\pi}{\lambda_{ci}}$ at a given position is the time an element of fluid at this position would take to rotate around the nearest vortex core.

Figure 5.8 shows an instantaneous map of λ_{ci} for $Re_h = 2900$. Regions of high swirling intensity are vortices created in the shear layer. It is then possible to spatially average λ_{ci} to compute a scalar, hereafter noted $I_v(t) = \frac{1}{A}\int_A \lambda_{ci}(t)da$, which effectively measures the combined intensity of the vortices present in the flow at a given time. Computation of $I_v(t)$ is implemented on GPU to maintain high frequency sampling. Figure 5.8b shows the evolution of spatially and time averaged swirling strength $< I_v >_t$ for the SP configuration. Only the SP configuration is used since it is best suited to detecting vortices in the shear layer. The figure shows how the mean swirling strength increases with linearly with Re_h.

5.5 Open-loop experiments

Before turning to closed-loop experiments, it is important to characterize the open loop response of the system for both configurations, with $Re_h = 2900$. It is a necessary step in order to choose a proper closed-loop algorithm. Twelve actuation amplitudes were sampled

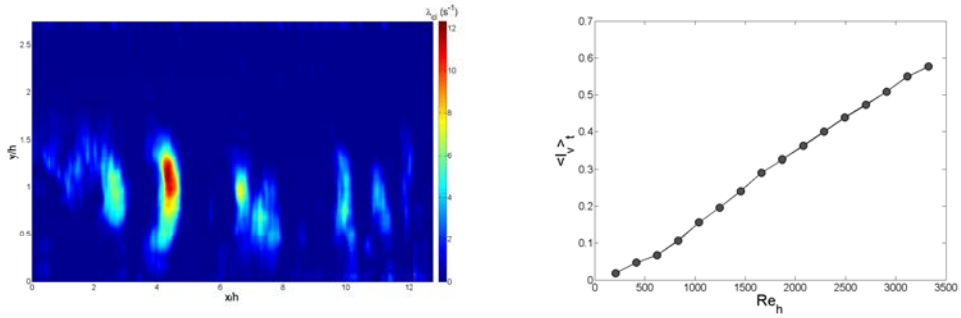

a) b)

Figure 5.8: a) Contour of instantaneous values of λ_{ci} for $Re_h = 2900$. b) Time averaged values of $I_v(t)$ as a function of Reynolds number for the SP configuration.

for each configurations. Figure 5.9 shows the evolution of the mean recirculation length for both configurations as a function of actuation amplitude.

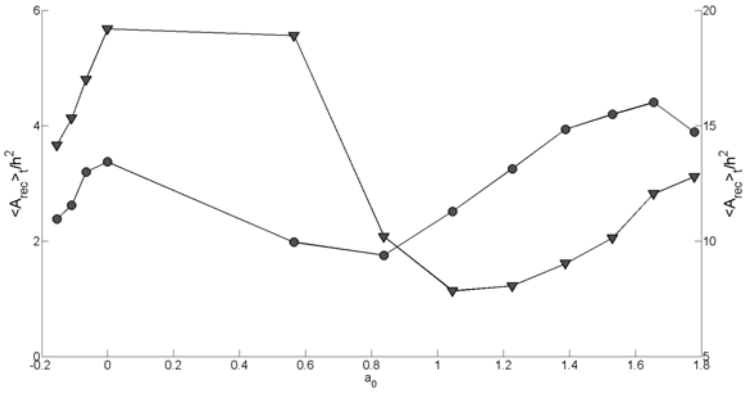

Figure 5.9: Mean recirculation length as a function of actuation amplitude for the SP configuration (●) and for the HP configuration (▼).

Both plots present the same qualitative characteristics: an increasing recirculation area until jet output is null followed by a decrease to a minimum and a subsequent increase. When actuation amplitude is negative (suction) the recirculation shrinks, it grows in size as suction amplitude diminishes. Once amplitude becomes positive the flow remains unperturbed until the jet is strong enough the affect the recirculation. Once this happens recirculation area quickly diminishes. In both cases, recirculation is minimum when $a_0 \approx 1$, i.e. when the jet velocity is close to the freestream velocity. At the optimal actuation point the shear layer is thickened by the jet, instabilities appear sooner in the flow, thereby lowering the overall recirculation. When the actuation amplitude becomes strong enough, the jet creates a fluid wall, essentially protecting the recirculation region from the incoming flow, causing recircu-

lation area to increase once again. Since the relation between $A_{recirculation}$ and actuation amplitude presents a global minimum (-60% in both cases), a gradient descent type control algorithm is advisable.

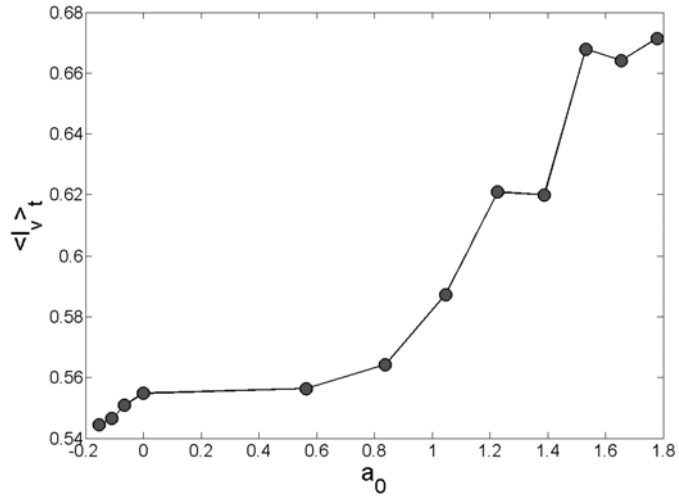

Figure 5.10: Evolution of $< I_v >_t$ with actuation amplitude for $Re_h = 2900$.

Figure 5.10 shows the spatially and time averaged values of swirling strength $< I_v >_t$ as a function of jet intensity. It increases with actuation amplitude. At first, actuation reinforces the vortices present in the shear layer. Once the jet is strong enough to create vortices outside of the shear layer the strength of these vortices is added to the vortices created in the shear layer resulting in an overall higher swirling intensity I_v.

5.6 Closed-loop experiments

5.6.1 Gradient-descent algorithm

As mentioned previously, the evolution of the manipulated variable $A_{recirculation}$ as a function of actuation amplitude exhibits a clear minimum. It is thus well-suited to a gradient-descent control such as slope-seeking (Krstic (2000), Beaudoin et al. (2006)). However, it is not possible with the present experimental setup to add a periodic excitation. A simpler, albeit less robust, implementation of gradient-descent will be used in order to demonstrate the feasibility and advantages of visual servoing when controlling a separated flow. The algorithm used is a basic gradient descent algorithm. Actuation is changed iteratively in opposition to the controlled variable's slope.

Figure 5.11a shows the evolution of $A_{recirculation}$ as a function of time during minimum seeking. Figure 5.11b shows the corresponding evolution of actuation amplitude. One can see that when actuation starts, $A_{recirculation}$ decreases regularly until reaching a minimum (giving -60% reduction) after 20 seconds. The system remains in this state as long as

actuation is applied. Actuation amplitude increases regularly until reaching a plateau at $a_0 = 0.95$ which corresponds to the optimal amplitude leading to the minimal recirculation obtained in the open-loop experiment.

This clearly demonstrates how a visual feedback system can be used to implement the same control methods as those using recirculation length as control variable. Convergence speed is 20 seconds, this could be improved by improving the control algorithm.

5.6.2 PID control

Because $< I_v >_t$ is a monotonous function of the actuation amplitude, it is well suited to control via a PID algorithm. The PID (Proportional-Integral-Derivative) controller is fundamental in control theory and is very useful when no model of the system is available. For informations on PID control, see Astrom and Hagglund (2001). Essentially, an arbitrary setpoint command is given to the controller which then computes the appropriate actuation required to bring the system to a state giving the desired setpoint value. Following the methodology described in Zhuang and Atherton (1993), a automatically tuned PID controller was implemented. The controller is made to bring the output variable into a state of controlled oscilations. It does this in the following way: a constant actuation is given, as soon as output goes above a predetermined value, actuation is turned off, this is done many times. Over time the auto tune algorithms computes PID variables best suited to the response of the system. The PID algorithm is detailed in figure 5.12. The control action a_0 on the flow is a function of the difference e between output and setpoint. Control action is a sum of three terms. A term proportional to e, a term proportional to e integrated over time, and finally a term proportional to the derivative of e.

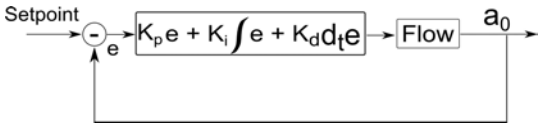

Figure 5.12: PID algorithm in block form.

Figure 5.13a shows the evolution of the control variable during PID control and figure 5.13b the corresponding changes in actuation amplitude. These figures show how mean swirling strength can be drastically changed.

5.7 Conclusion

An experimental study of control by visual feedback on the detached flow downstream a backward facing-step has been carried out in an hydrodynamic channel. High frequency, low latency computations of the velocity field behind the step were used to define and compute two novel control variables: recirculation area and mean swirling strength. The evolution of these variables as a function of the Reynolds number and as a function of actuation amplitude for a given Reynolds number have been studied.
$A_{recirculation}$ is shown to behave in much the same way as its length. Hence visual informations can be used to control the BFS flow using standard feedback schemes. Since the open

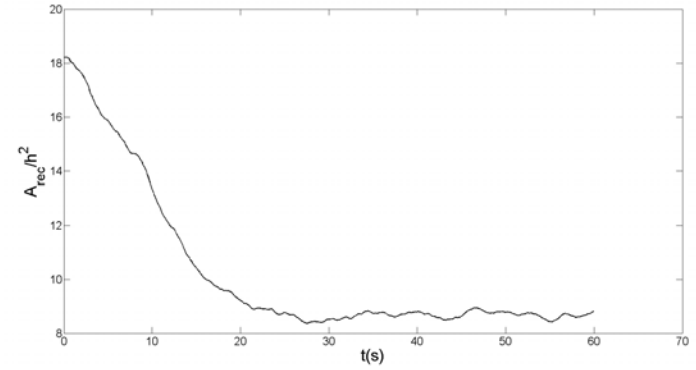

a)

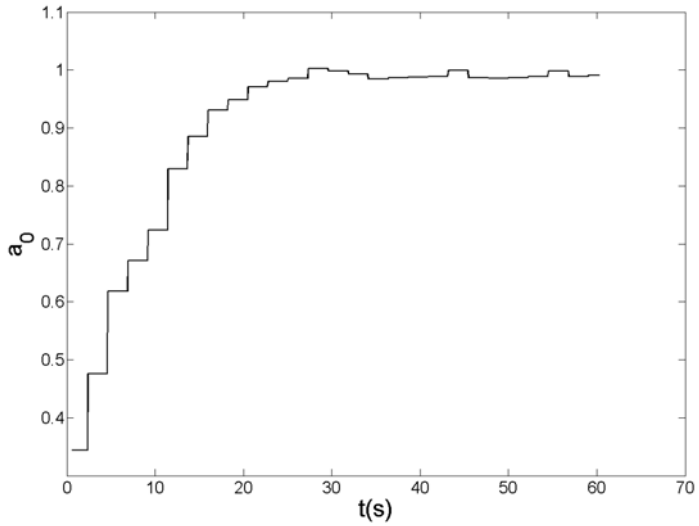

b)

Figure 5.11: a) Closed loop recirculation area during gradient descent for the HP configuration at $Re_h = 2900$. b) Corresponding evolution in actuation amplitude.

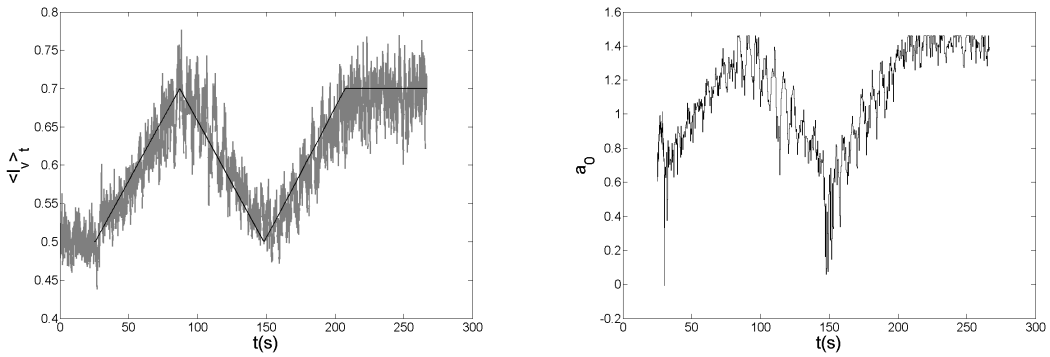

a) b)

Figure 5.13: a) Closed loop values of $I_v(t)$ during PID control for configuration SP and $Re_h = 2900$. Control variable in grey, setpoint(target) in black. b) Corresponding evolution in actuation amplitude.

loop evolution of the recirculation area presents a minimum when the actuation amplitude is varied, a gradient descent algorithm has been chosen and successfully implemented in the feedback loop.
Thanks to the real-time velocity measurements, new control variables can be defined. The spatially averaged swirling strength allows for the estimation of the intensity of the vortices created in the separated flow. This is the first time such a variable is computed in real-time from online flow velocity data, demonstrating the new avenues opened for control by visual servoing. The open loop response shows a relatively smooth evolution of the mean swirling strength as a function of the actuation amplitude, well fitted for a PID controller. A closed loop implementation demonstrates how swirling strength in a detached flow can be dynamically controlled through visual feedback.

5.8 Acknowledgments

The authors gratefully acknowledge the support of the DGA.

Bibliography

J-L. Aider, A. Danet, and M. Lesieur. Large-eddy simulation applied to study the influence of upstream conditions on the time-dependant and averaged characteristics of a backward-facing step flow. *Journal of Turbulence*, 8, 2007.

B. F. Armaly, F. Durst, J. C. F. Pereira, and B. Schonung. Experimental and theoretical investigation of backward-facing step flow. *Journal of Fluid Mechanics*, 127:473–496, 1983.

KJ. Astrom and T. Hagglund. The future of pid control. *Control Engineering Practice*, 9: 1163–1175, 2001.

J-F. Beaudoin, O. Cadot, J-L. Aider, and J.E. Wesfreid. Three-dimensional stationary flow over a backwards-facing step. *European Journal of Mechanics*, 38:147–155, 2004.

J.-F. Beaudoin, O. Cadot, J.-L. Aider, and J. E. Wesfreid. Drag reduction of a bluff body using adaptive control methods. *Physics. Fluids*, 18:1, 2006.

M. Gharib C. Willert, M. Munson. Real-time particle image velocimetry for closed-loop flow control applications. 15th international Symposium on Applications of laser techniques to fluid mechanics, 05-08 Jul. 2010. Lisbon Portugal, 2010.

T Cambonie, N Gautier, and J-L Aider. Experimental study of counter-rotating vortex pair trajectories induced by a round jet in cross-flow at low velocity ratios. *Experiments in Fluids*, 54(3):1–13, 2013.

F. Champagnat, A. Plyer, G. Le Besnerais, B. Leclaire, S. Davoust, and Y. Le Sant. Fast and accurate piv computation using highly parallel iterative correlation maximization. *Experiments in Fluids*, 50:1169–1182, 2011. ISSN 0723-4864.

H. Choi, M. Hinze, and K. Kunisch. Instantaneous control of backward-facing step flows. *Applied Numerical Mathematics*, 31:133–158, 1999.

M.S. Chong, A.E. Perry, and B.J. Cantwell. A general classification of 3-dimensional flow fields. *Physics of Fluids*, 2:765–777, 1990.

K. B. Chun and H. J. Sung. Control of turbulent separated flow over a backward-facing step by local forcing. *Experiments in Fluids*, 21:417–426, 1996.

S. Davoust, L. Jacquin, and B. Leclaire. Dynamics of m = 0 and m = 1 modes and of streamwise vortices in a turbulent axisymmetric mixing layer. *Journal of Fluid Mechanics*, 709:408–444, 2012.

H. Fiedler and H.H. Fernholz. On the management and control of turbulent shear flows. *Prog. Aerospace Sci.*, 72:305–387, 1990.

R.T. Fomena and C. Collewet. Fluid flow control : A vision-based approach. *International Journal of Flow Control*, pages 133–169, 2011.

N. Gautier and J-L. Aider. Real time, high frequency planar flow velocity measurements. *Submitted Open Journal of Fluid Dynamics, avalaible at arXiv under Real-time planar flow velocity measurements using an optical flow algorithm implemented on GPU*, 2013.

L. Henning and R. King. Robust multivariable closed-loop control of a turbulent backward-facing step flow. *Journal of Aircraft*, 44, 2007.

W.D. Hucho. *Aerodynamic of Road Vehicles*. Vieweg, 2005.

L. Hung, M. Parviz, and K. John. Direct numerical simulation of turbulent flow over a backward-facing step. *Journal of Fluid Mechanics*, 330:349–374, 1997.

Miroslav Krstic. Performance improvement and limitations in extremum seeking control. *Systems & Control Letters*, 39:313–326, 2000.

Bruce D. Lucas. *Generalized image matching by the method of differences*. Phd, Carnegie Mellon University, 1984.

C. O Paschereit, E. Gutmark, and W. Weisenstein. Excitation of thermoacoustic instabilities by the interaction of acoustics and unstable swirling flow. *AIAA Journal*, 38:1025–1034, 2000.

Mark Pastoor, Lars Henning, Bernd R. Noack, Rudibert King, and Gilead Tadmor. Feedback shear layer control for bluff body drag reduction. *Journal of Fluid Mechanics*, 608:161–196, 2008.

J. Rabinovitch, V. Brion, and G. Blanquart. Effect of a splitter plate on the dynamics of a vortex pair. *Physics of Fluids*, 24, 2012.

J. Roberts. *Control of underactuated fluid-body systems with real-time image velocimetry*. Phd, MIT, 2012.

F. Sartor, G. Losfeld, and R. Bur. Piv study on a shock-induced transition in subsonic flow. *Experiments in Fluids*, 53:815–827, 2012.

R.L. Simpson. Aspect of turbulent boundary layer separation. *Progress in Aerospace Sciences*, 32:457–521, 1996.

D. Sipp, A. Barbagallo, and P. Schmid. Closed-loop control of an unstable open cavity. *Journal of Fluid Mechanics*, 641:1–50, 2010.

V. Uruba, P. Jonas, and O. Mazur. Control of a channel-flow behind a backward-facing step by suction/blowing. *Heat and Fluid Flow*, 28:665–672, 2007.

J. Zhou, R.J. Adrian, S. Balachandar, and T.M. Kendall. Mechanisms for generating coherent packets of hairpin vortices. *J Fluid Mech*, 387:535–396, 1999.

M. Zhuang and D.P. Atherton. Automatic tuning of optimum pid controllers. *IEEE Proc Control Theory and Appl*, 140, 1993.

Chapter 6

Upstream open loop control of the recirculation area downstream of a backward-facing step

This article features a parametric study aimed at determining the effectiveness of upstream actuation for the backward-facing step flow. Control for this type of flow is usually effected at the step edge because this is where the shear layer is most sensitive and thus most effectively actuated, (Dahan and Morgans (2012), Henning and King (2007), Chun and Sung (1996)). Engineering constraints can make step edge actuation prohibitively difficult and our setup does not permit edge actuation. This work led to increased automation which enabled the machine learning approach described in chapter 9. Furthermore this study helped us gain insight into how the jets behaved and their effect on the flow. This was also the first time pulsed actuation was used. Upstream pulsed actuation was found to be viable, yielding satisfying results when attempting to reduce downstream recirculation. In addition investigations into the signal used for actuation showed how momentum injection could be lowered thus impacting energy expenditure without loss of effect. This study paved the way for a simple yet effective control algorithm described in the next chapter.

6.1 Abstract

The flow downstream a backward-facing step is controlled using a pulsed jet placed upstream of the step edge. Experimental velocity fields are computed and used to the recirculation area quantify. The effects of jet amplitude, frequency and duty cycle on this recirculation area are investigated for two Reynolds numbers ($Re_h = 2070$ and $Re_h = 2900$). The results of this experimental study demonstrate that upstream actuation can be as efficient as actuation at the step edge when exciting the shear layer at its natural frequency. Moreover it is shown that it is possible to minimize both jet amplitude and duty cycle and still achieve optimal

efficiency. With minimal amplitude and a duty-cycle as low as 10% the recirculation area is nearly canceled.

6.2 Introduction

Separated flows are ubiquitous in nature and industrial processes. They occur in many devices such as combustion chambers, air conditioning plants, moving ground and air vehicles (see Simpson (1996), Hucho (2005), Paschereit et al. (2000)). The main feature of separated flows is the recirculation bubble i.e. the region where the direction of the flow is reversed (Armaly et al. (1983)). In most industrial applications it is important to reduce recirculation in order to improve drag, increase lift, suppress vibrations or lower aeroacoustic noise. Sometimes an increase in recirculation is welcome, for instance to increase mixing in a combustion chamber.

The Backward-Facing Step (BFS) flow is a benchmark problem, and is commonly used to study massively separated flows both numerically and experimentally (see Armaly et al. (1983), Hung et al. (1997), Beaudoin et al. (2004), Aider et al. (2007)). The main features of the BFS flow are the creation of a recirculation downstream of the step together with a strong shear layer in which Kelvin-Helmholtz instability can trigger the creation of spanwise vortices (Figure 9.1). Because separation of the boundary layer is imposed by the step edge, flow control strategies are also limited: it is not possible to delay or trigger the flow separation but only to force the shear layer in a different state to modify the overall recirculation and location of reattachment point (Darabi and Wygnanski).

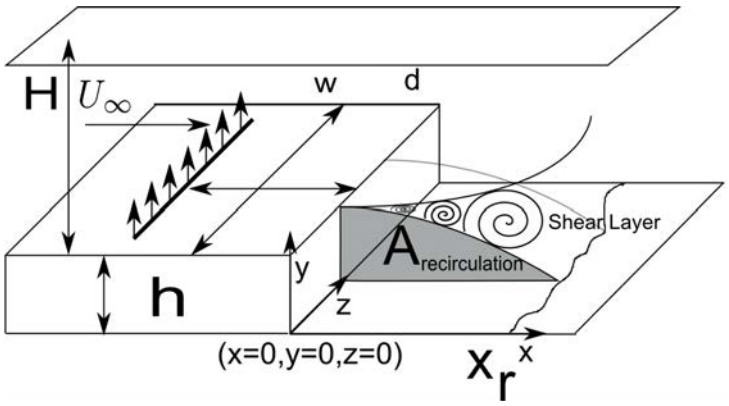

Figure 6.1: Sketch of the BFS geometry and definition of the main parameters

There are many ways of controlling separated flows as detailed by Fiedler and Fernholz (1990). Both passive and active actuation methods have been the subject of much research (Chun and Sung (1996), Uruba et al. (2007)). Active actuations using either pulsed or synthetic jets are always located at the step edge in order to ensure maximum effect on the shear layer. Furthermore this is only possible for geometries where the separation line is well-defined, which is not the case for rounded walls or ramps. While this is effective it does

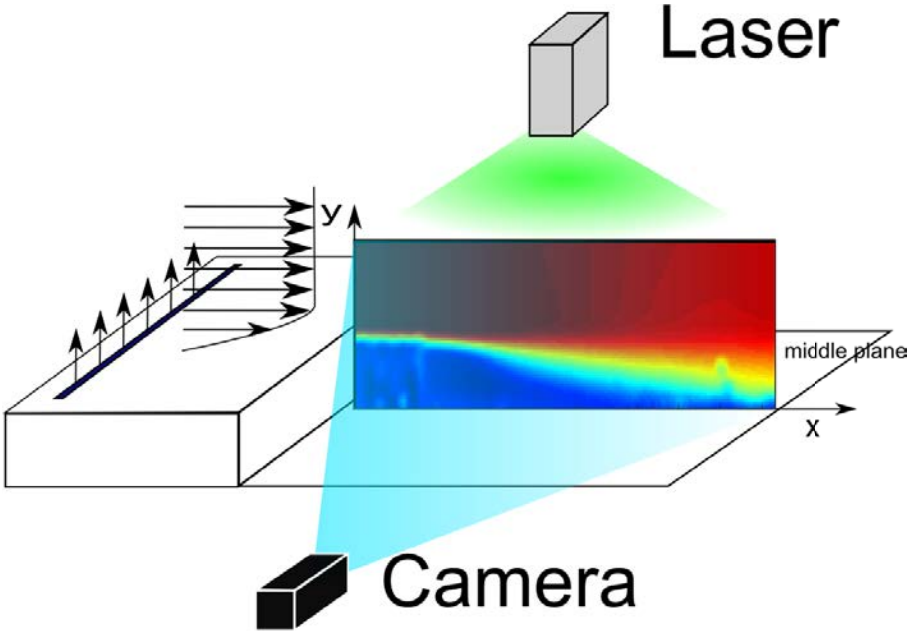

Figure 6.2: Sketch of the acquisition apparatus

burden any setup with additional engineering constraints. For academic purposes this is of lesser concern, while for industrial purposes the cost of spatially imposed actuation can be prohibitive. Furthermore it has been shown that for geometries where separation point can move because of changing external conditions the effectiveness of flow control can be lowered because actuation is no longer where the flow is most receptive (Narayan et al. (2002)). Therefore knowing where actuation can be placed upstream while retaining effectiveness is of particular interest. Because of its ability to excite instabilities in the shear layer, pulsed actuation is most efficient when controlling separated flows, as has been shown by Chun and Sung (1996), M'Closkey et al. (2002), Eroglu and Breidenthal (2001) and used by Pastoor et al. (2008), Henning and King (2007), Chun and Sung (1996). Pulsed jets actuations are defined by several parameters. However while the influence of jet amplitude and frequency are always modified, signal shape and duty cycle are seldom investigated.

An important step in most of closed-loop control strategies is choosing one or several control parameters. The parameter should be either directly computable from sensor data, such as local pressure or drag measurement, or obtained by combining sensor data and a model. The model for closed-loop actuation can be simple (Henning and King (2007) recover recirculation length via its correlation to pressure fluctuations) or complicated (Sipp et al. (2010) recovers an approximation of the flow state through Kalman filtering). In the case of the BFS flow, sensors are most often pressure or skin friction sensors, and the control variable is usually the recirculation length X_r (see figure 9.1). Wall based sensors present the advantage of high frequency acquisition however they give a limited view of the flow: many phenomena

are difficult to access because buried in noise or simply unobservable because vortices in the flow are not visible by the wall sensors.
Velocity fields can be analyzed to yield a recirculation *area* instead of a length, as show by Gautier and Aider (2013). It is a measure of how much recirculation is present in a 2D slice of the flow. While the behavior of the recirculation area is often similar to the recirculation length it is not always the case. Because more information about the flow is used to compute the recirculation area it makes sense to use such a variable when possible.
In this paper we investigate the effect of an upstream pulsed jet on the recirculation area downstream of a BFS. The flow state is characterized in the middle plane using real-time optical flow measurements. The parametric space formed by jet amplitude, frequency, and duty cycle is explored for two Reynolds numbers.

6.3 Experimental Setup

6.3.1 Water tunnel

Experiments were carried out in a hydrodynamic channel in which the flow is driven by gravity. The flow is stabilized by divergent and convergent sections separated by honeycombs. The test section is 80 cm long with a rectangular cross section 15 cm wide and 10 cm high. The quality of the main stream can be quantified in terms of flow uniformity and turbulence intensity. The standard deviation σ is computed for the highest free stream velocity featured in our experimental set-up. We obtain $\sigma = 0.059$ cm.s^{-1} which corresponds to turbulence levels of $\frac{\sigma}{U_\infty} = 0.0023$.
The mean free stream velocity U_∞ can go up to 22 cm.s^{-1}. The Reynolds number is based on the step height h, $Re_h = \frac{U_\infty h}{\nu}$, ν being the kinematic viscosity. A specific leading-edge profile is used to smoothly start the boundary layer which then grows downstream along the flat plate, before reaching the edge of the step 33.5 cm downstream. The boundary layer is laminar and follows a Blasius profile. The boundary layer thickness is $\delta = 0.75$ cm for $Re_h = 2070$ and $\delta = 0.89$ cm for $Re_h = 2900$.

6.3.2 Backward-facing step geometry

The backward-facing step geometry and the main geometric parameters are shown in figure 9.1. The height of the BFS is $h = 1.5$ cm. Channel height is $H = 7$ cm for a channel width $w = 15$ cm. One can define the vertical expansion ratio $A_y = \frac{H}{h+H} = 0.82$ and the spanwise aspect ratio $A_z = \frac{w}{h+H} = 1.76$.

6.3.3 Velocity fields computation

The flow is seeded with 20 μm neutrally buoyant polyamid seeding particles. The vertical symmetry plane of the test section is illuminated by a laser sheet created by a 2W continuous CW laser beam operating at wavelength $\lambda = 532$ nm passing through a cylindrical lens (Figure 6.2). The pictures of the illuminated particles are recorded using a Basler acA 2000-340km 8bit CMOS camera. The camera is controlled by a camera-link NI PCIe 1433 frame grabber. Velocity field computations are run in real-time on athe GPU of a Gforce

GTX 580 graphics card.

The two components of the planar velocity fields (U, V being respectively the streamwise and vertical components) are computed in real-time using an optical flow algorithm (Lucas (1984)). Its offline accuracy has been demonstrated by Champagnat et al. (2011). Although there are differences with classic PIV algorithms output velocity field resolution is still tied to the size of the interrogation window. However the output field is dense (one vector per pixel) giving better results in the vicinity of edges and obstacles, which is crucial in BFS flows. Furthermore this gives exceptionally smooth fields. The algorithm was used by Davoust et al. (2012), Sartor et al. (2012), Gautier and Aider (2013).

6.3.4 Relationship between recirculation length and area.

In the case of separated flows, specifically backward-facing step flows, the length of the recirculation X_r is commonly used as input variable (Henning and King (2007), Chun and Sung (1996)). There are many ways of computing the recirculation length, however they all give qualitatively similar results (Armaly et al. (1983)). Because 2D two-components velocity fields are measured, the recirculation area can be characterized by its area instead of its length (Gautier and Aider (2013)). Building upon 1D definitions the recirculation area can be considered to be the area occupied by the region(s) of flow where longitudinal velocity is negative. The instantaneous recirculation area A_{rec} is then defined in equation 6.1:

$$A_{rec}(t) = \int_A H(-v_x)da \tag{6.1}$$

where H is the Heavyside function. Figures 6.3a and 6.3b show an example of an instantaneous recirculation area. In the following we will consider the mean recirculation area i.e. A_{rec} is computed for every time step for each instantaneous velocity fields before being averaged. It should be noted that it is different from the recirculation area of the mean velocity field.

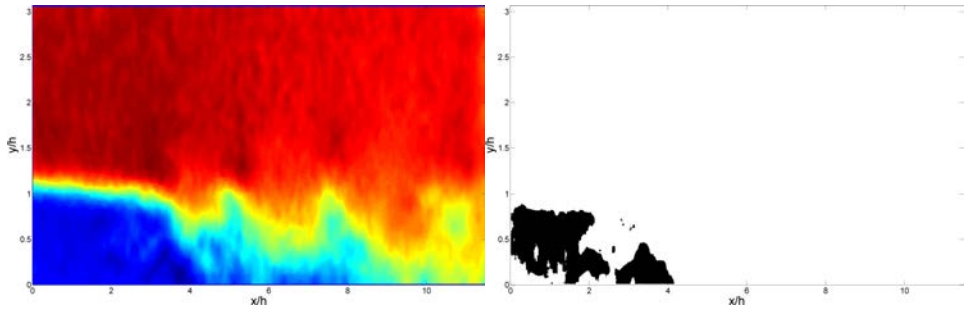

(a) Longitudinal velocity field, $Re_h = 2900$, no actuation

(b) Corresponding instantaneous recirculation area in black using equation 6.1

Figure 6.3

Because recirculation area is computed from 2D data it has the potential to give a more accurate measure of recirculation in the flow than recirculation length.

It has been shown by Gautier and Aider (2013) that the recirculation area behaves similarly to the recirculation length for varying Reynolds numbers. Moreover previous studies (Armaly et al. (1983)) have shown the evolution of the recirculation length as a function of the Reynolds number reaches a maximum between $600 < Re_h < 1000$ before reaching its asymptotic value for $Re_h > 2000$. The Reynolds numbers featured in this study are high enough to ensure recirculation area has reached its asymptotic regime where recirculation length no longer depends on Reynolds number. For each flow configuration the recirculation area was computed and recorded over 5 minutes with a sampling frequency $f_a = 70$ Hz to ensure convergence. The time series is then averaged over time. It should be noted the recirculation area is computed in real-time, concurrently with image acquisition, therefore only the recirculation area is saved. It avoids saving images and velocity fields, making experimental data very light and greatly hastening the data processing and analysis.

6.3.5 Actuation

Actuation is provided by a flush slot jet, 0.1 cm long and 9 cm wide. Injection is normal to the wall. The slot is located at a distance $d = 3.5$ cm $= 2.11h$ upstream the step edge (figure 9.1). Water coming from a pressurized tank enters a plenum and goes through a volume of glass beads designed to homogenize the incoming flow. Jet amplitude is controlled by changing tank pressure. The injection geometry was chosen to keep the perturbation as bi-dimensional as possible.

The flow is modulated by a one-way voltage driven solenoid-valve. It is controlled by a square-wave signal described in figure 6.4 with an actuation frequency f_a. The square wave signal was chosen for its simplicity, other signal forms could be considered.

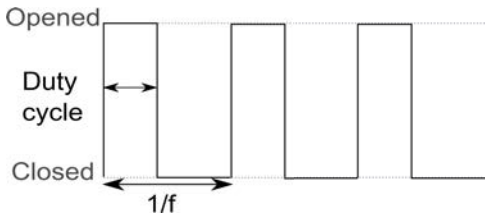

Figure 6.4: Square wave signal and definition of duty-cycle

The duty-cycle dc (in %) is the ratio between the time for which the valve is opened over time of a cycle. Jet amplitude is defined as the ratio between mean jet exit velocity when the jet is active and cross flow velocity $a_0 = \frac{U_{jet}}{U_0}$. The duty cycle therefore has no impact on jet amplitude.

6.3.6 Natural shedding frequency

Kelvin-Helmholtz instabilities in the shear layer create spanwise vortices which in turn influence the recirculation area. An effective way of detecting such vortices is to compute on

the two-components 2D velocity fields the swirling strength criterion $\lambda_{ci}(s^{-1})$. It was first introduced by Chong et al. (1990) who analyzed the velocity gradient tensor and proposed that the vortex core be defined as a region where $\nabla \mathbf{u}$ has complex conjugate eigenvalues. For 2D data we have $\lambda_{Ci} = \frac{1}{2}\sqrt{4\det(\nabla \mathbf{u}) - \mathrm{tr}(\nabla \mathbf{u})^{\mathbf{2}}}$ when such a quantity is real, else $\lambda_{Ci} = 0$. It was later improved and used for the identification of vortices in three-dimensional flows by Zhou et al. (1999).

The shedding frequency is obtained by spatially averaging λ_{Ci} in the vertical direction at $x = 3h$ with a sampling frequency $f_s = 40$Hz. Essentially vortices are counted as they pass through an imaginary line. Figure 6.5 shows frequency spectra obtained by Fourier transform for both Reynolds numbers, where $St_h = \frac{fh}{U_0}$ is the Strouhal number based on the step height.

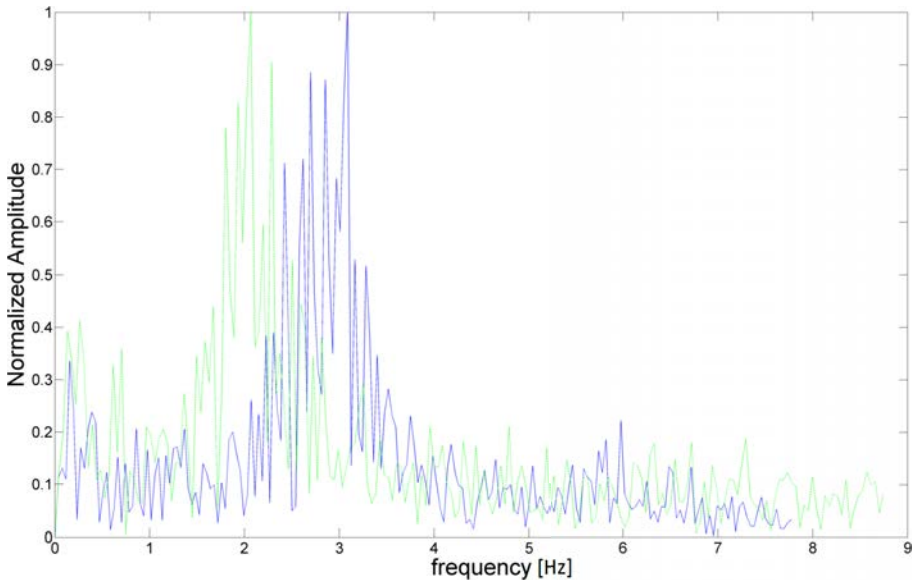

Figure 6.5: Frequency spectrum for $Re_h = 2070$ (peak at $St_h = 0.258$) in dashed green and for $Re_h = 2900$ (peak at $St_h = 0.272$) in solid blue

6.4 Results

6.4.1 Influence of frequency

Figure 7.4 shows the evolution of recirculation area (non-dimensionalized by the uncontrolled recirculation area A_0) when frequency varies for both Reynolds numbers. Jet amplitude and duty cycle are kept constant. Jet amplitudes were chosen empirically. Previous open-loop control experiments have shown reduction in circulation length of up to 40 % (Chun and Sung (1996)). Here recirculation area is decreased by as much as 80 %. The reduction is maximum when the pulsing frequency is close to vortex shedding frequency, $f \simeq f_0$, i.e. $F^+ = \frac{f_a}{f_0} \approx 1$. This result is similar to the effect of flow control at the step edge.

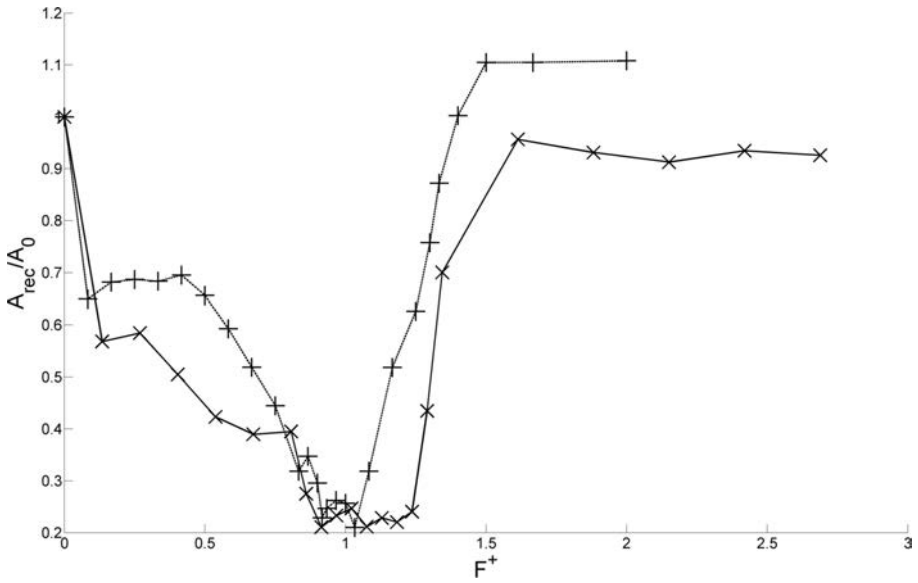

Figure 6.6: Evolution of time averaged recirculation area $\frac{A_{rec}}{A_0}$ as a function of the frequency for $Re_h = 2070$ ($\times$) and $Re_h = 2900(+)$ with $dc = 50\%$ and $a_0 = 0.040$.

These results show how upstream actuation can effectively control a backward-facing step flow. The influence of the upstream location of the actuator was beyond the scope of the present study.

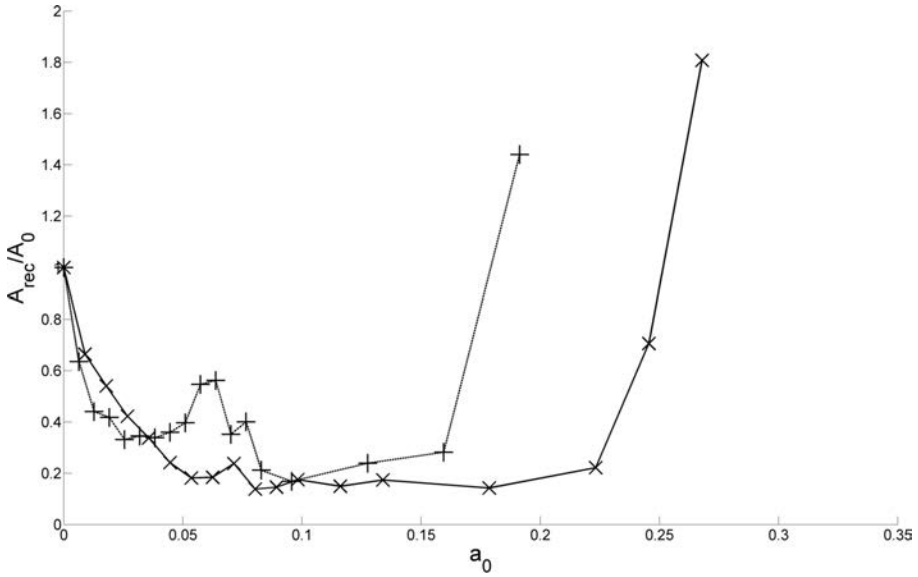

Figure 6.7: Evolution of time averaged recirculation area $\frac{A_{rec}}{A_0}$ as a function of a_0 for $Re_h = 2070$ ($\times$) and $Re_h = 2900$(+) with $F^+ \approx 1$ and $dc = 50\%$

Figure 6.8: Evolution of

6.4.2 Influence of jet exit velocity

Figure 6.8 shows the evolution of recirculation area when jet amplitude varies, for both Reynolds numbers. The actuation frequency giving maximum reduction was chosen for both Reynolds numbers ($F^+ \approx 1$) and duty cycle was kept constant at $dc = 50\%$. One can clearly see that there is an optimal amplitude for the jet: if too small or too large, the control looses its efficiency, the optimum ratio being around $a_0 \approx 0.1$. In this case, the reduction of the recirculation area is even larger, close to 85%.

These results highlight the main difference between edge and upstream jet actuation. Similarly to edge injection, a minimal jet amplitude is required to affect the flow. However for upstream actuation, recirculation area increases with increasing jet amplitude instead of decreasing. Indeed, for high amplitudes the jet fully penetrates the cross-flow effectively becoming an obstacle to the incoming flow, leading to a massive increase of the recirculation area. One also notes that flow behavior is similar for both Reynolds numbers. Once again while the recirculation area of the controlled mean field is near 0 % mean recirculation area is closer to 10 % of the uncontrolled values.

6.4.3 Influence of duty cycle

Figure 6.9 shows the evolution of the recirculation area as a function of the duty-cycle for both Reynolds numbers and for the optimal actuation frequency and amplitude previously found.

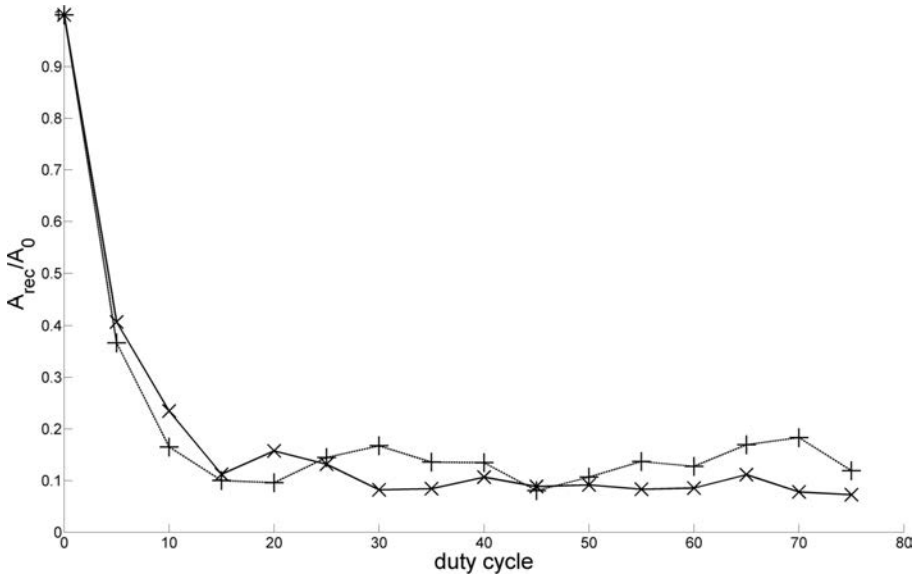

Figure 6.9: Time averaged recirculation area as a function of the duty cycle for $Re_h = 2070$ ($\times$) and $Re_h = 2900$ ($+$) with $F^+ \approx 1$ and $a_0 = 0.083$

Recirculation reduction area is increased, reaching nearly 90%. A minimal duty cycle of 10 % is required to fully affect the flow, much lower than the usual 50 % used in most of the previous studies. This is an important result: the duty cycle can be brought down significantly while still maintaining an effective control and then allowing a strong improvement of the overall energy balance between power used by the actuation and power gain (if related to a drag decrease, for instance).

6.4.4 Recirculation suppression

It appears one major difference between recirculation area and recirculation length is its sensitivity to actuation. While the recirculation length can be reduced by 40 %, the recirculation area can be reduced by nearly 90 %. To explain this, velocity fields were computed at optimal parameters for both Reynolds numbers. Figures 6.10 and 6.11 show the recirculation area of the mean field in the uncontrolled and optimally controlled cases. On average there is very little recirculation in the controlled cases. Indeed, recirculation area can be almost null while recirculation length remains significant.

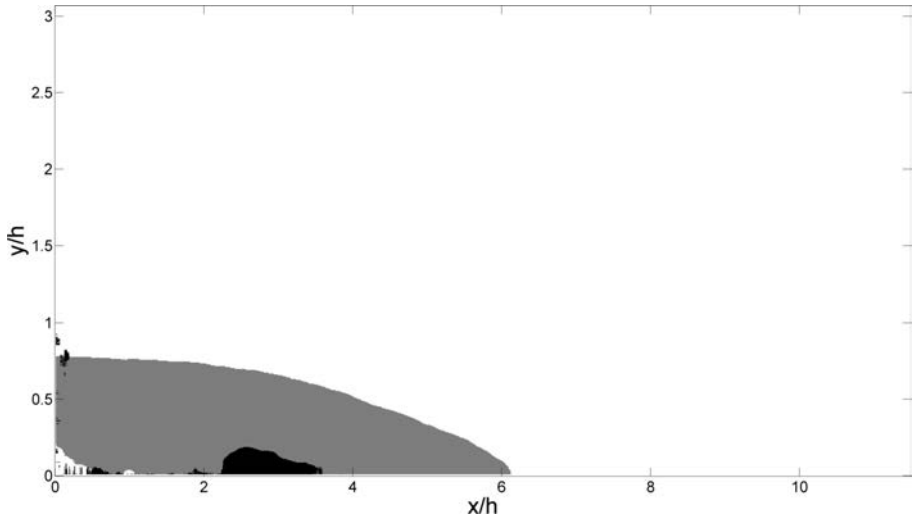

Figure 6.10: Comparison of time averaged recirculation area obtained for $Re_h = 2070$ for the uncontrolled (grey) and controlled (black) configuration ($F^+ \approx 1$, $dc = 20$, $a_0 = 0.083$

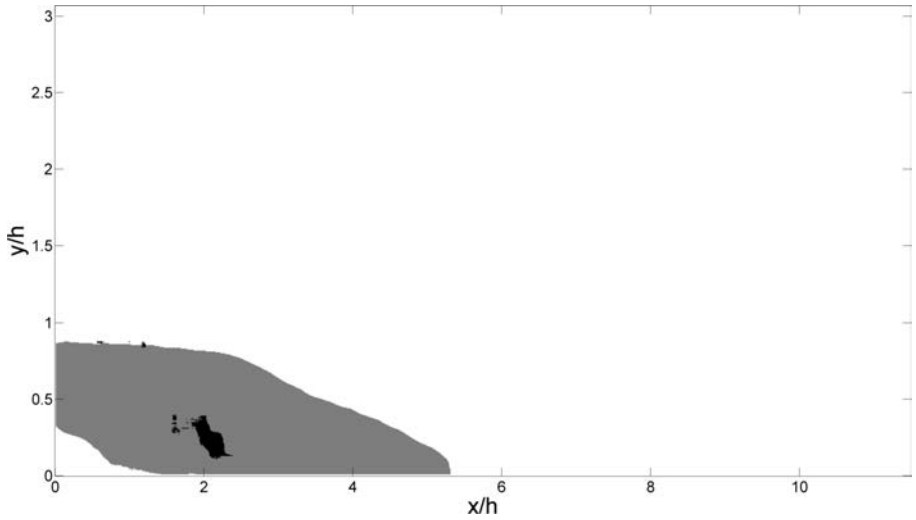

Figure 6.11: Comparison of time averaged recirculation area obtained for $Re_h = 2900$ for the uncontrolled (grey) and controlled (black) configuration ($F^+ \approx 1$, $dc = 20$, $a_0 = 0.088$)

These figures illustrate how, in the mean sense, recirculation can be cancelled through targeted control. Presumably the same results could be obtained using a pulsed actuation at the step edge, but it has to be confirmed.

6.5 Conclusion

The flow downstream of a backward-facing step controlled by an upstream pulsed jet was experimentally studied in a hydrodynamic channel. A measure of the recirculation area downstream of the BFS was introduced and used to quantify the effect of actuation for several flow configurations. The parametric space formed by jet amplitude, actuation frequency and duty cycle was explored for Reynolds numbers $Re_h = 2070$ and $Re_h = 2900$.
Results show recirculation can be greatly reduced, and in some cases nearly suppressed, for a fairly wide ranges of actuation parameter. Furthermore while this phenomenon is clearly observed when considering recirculation area, it can be missed when considering only recirculation length. It emphasizes the importance of properly choosing the criterion used to evaluate the state of the separated flow. Recirculation area gives a more global evaluation of the state of the flow than recirculation length.
The investigation of jet amplitude shows that, in the same way as injection at the step edge, a minimal jet amplitude is required to better control the flow. However step injection and upstream injection differ at high jet amplitudes. In contrast to step injection where it has been shown that raising jet amplitude merely increases actuation effectiveness, albeit with diminishing returns, upstream injection jet amplitude reaches a threshold above which recirculation is greatly increased instead of decreased. In the case of upstream actuation, an optimal jet amplitude can be found.
Finally actuation is shown to be effective over a wide range of duty cycles, reaching a reduction of the recirculation area close to 90 %. Moreover, it is shown that the duty cycle can be lowered to 10 % while keeping recirculation at a minimum. Furthermore it is likely this limit is a consequence of the imperfect nature of the actuator. A better actuator could achieve lower duty cycles. Thus performances can be maintained while considerably lowering flow rate injection, and therefore energy expenditure. This result is of great interest for flow control applications where energy balance is a crucial point.

Acknowledgement

The DGA (Direction Générale de l'Armement) is gratefully acknowledge for its financial support.

Bibliography

J-L. Aider, A. Danet, and M. Lesieur. Large-eddy simulation applied to study the influence of upstream conditions on the time-dependant and averaged characteristics of a backward-facing step flow. *Journal of Turbulence*, 8, 2007.

B. F. Armaly, F. Durst, J. C. F. Pereira, and B. Schonung. Experimental and theoretical investigation of backward-facing step flow. *Journal of Fluid Mechanics*, 127:473–496, 1983.

J-F. Beaudoin, O. Cadot, J-L. Aider, and J.E. Wesfreid. Three-dimensional stationary flow over a backwards-facing step. *European Journal of Mechanics*, 38:147–155, 2004.

F. Champagnat, A. Plyer, G. Le Besnerais, B. Leclaire, S. Davoust, and Y. Le Sant. Fast and accurate piv computation using highly parallel iterative correlation maximization. *Experiments in Fluids*, 50:1169–1182, 2011. ISSN 0723-4864.

M.S. Chong, A.E. Perry, and B.J. Cantwell. A general classification of 3-dimensional flow fields. *Physics of Fluids*, 2:765–777, 1990.

K. B. Chun and H. J. Sung. Control of turbulent separated flow over a backward-facing step by local forcing. *Experiments in Fluids*, 21:417–426, 1996.

J. Dahan and A. Morgans. Feedback control for form-drag reduction on a bluff body with a blunt trailing edge. *J. Fluid Mech.*, 704:360–387, 2012.

A. Darabi and I. Wygnanski.

S. Davoust, L. Jacquin, and B. Leclaire. Dynamics of m = 0 and m = 1 modes and of streamwise vortices in a turbulent axisymmetric mixing layer. *Journal of Fluid Mechanics*, 709:408–444, 2012.

A. Eroglu and R.E. Breidenthal. Structure, penetration, and mixing of pulsed jets in cross-flow. *AIAA Journal*, 39:417–423, 2001.

H. Fiedler and H.H. Fernholz. On the management and control of turbulent shear flows. *Prog. Aerospace Sci.*, 72:305–387, 1990.

N. Gautier and J-L. Aider. Control of the flow behind a backwards facing step with visual feedback. *submitted to Royal Society Proceedings, available at arXiv*, 2013.

L. Henning and R. King. Robust multivariable closed-loop control of a turbulent backward-facing step flow. *Journal of Aircraft*, 44, 2007.

W.D. Hucho. *Aerodynamic of Road Vehicles*. Vieweg, 2005.

L. Hung, M. Parviz, and K. John. Direct numerical simulation of turbulent flow over a backward-facing step. *Journal of Fluid Mechanics*, 330:349–374, 1997.

Bruce D. Lucas. *Generalized image matching by the method of differences*. Phd, Carnegie Mellon University, 1984.

R.T M'Closkey, J.M. King, L. Cortelezzi, and A.R Karagozian. The actively controlled jet in crossflow. *Journal of Fluid Mechanics*, 452:325–335, 2002.

S. Narayan, B.R. Noack, A. Banaszuk, and A.I. Khibnik. Active separation control concept: Dynamic forcing of induced separation using harmonically related frequency, 03 2002.

C. O Paschereit, E. Gutmark, and W. Weisenstein. Excitation of thermoacoustic instabilities by the interaction of acoustics and unstable swirling flow. *AIAA Journal*, 38:1025–1034, 2000.

Mark Pastoor, Lars Henning, Bernd R. Noack, Rudibert King, and Gilead Tadmor. Feedback shear layer control for bluff body drag reduction. *Journal of Fluid Mechanics*, 608:161–196, 2008.

F. Sartor, G. Losfeld, and R. Bur. Piv study on a shock-induced transition in subsonic flow. *Experiments in Fluids*, 53:815–827, 2012.

R.L. Simpson. Aspect of turbulent boundary layer separation. *Progress in Aerospace Sciences*, 32:457–521, 1996.

D. Sipp, A. Barbagallo, and P. Schmid. Closed-loop control of an unstable open cavity. *Journal of Fluid Mechanics*, 641:1–50, 2010.

V. Uruba, P. Jonas, and O. Mazur. Control of a channel-flow behind a backward-facing step by suction/blowing. *Heat and Fluid Flow*, 28:665–672, 2007.

J. Zhou, R.J. Adrian, S. Balachandar, and T.M. Kendall. Mechanisms for generating coherent packets of hairpin vortices. *J Fluid Mech*, 387:535–396, 1999.

Chapter 7

Frequency lock reactive control of a separated flow enabled by visual sensors

This paper features a simple and physical based approach to recirculation reduction based on the well-validated paradigm of periodic forcing. While past setups feature parietal sensors, which are not well suited to detecting shedding frequency, access to flow velocity opens up new ways of computing natural shedding frequency. By detecting vortices as they are created in the shear layer the shedding rate can be accurately computed. This allows a feedback control loop that successfully maintains minimum recirculation despite large random variations in flow conditions. This algorithm is presented in its essential form, it could easily be made more robust by monitoring other factors susceptible of changing natural shedding frequency. For example temperature monitoring could be added as significant changes temperature would cause a viscosity change thereby modifying shear layer properties.

7.1 Abstract

In this study, a physical based algorithm is used to control the separated flow downstream of a backward-facing step. It is well known that the spatial extent of the recirculation bubble can be minimized when acting on the shear layer at the shedding frequency. Using this information in a closed-loop algorithm is not straight-forward because of the difficulty of measuring in real-time the shedding frequency accurately without disturbing the flow. A novel real-time analysis of 2D velocity fields uses vortex detection to dynamically measure the shedding frequency. Actuation (pulsed jet) is then locked on this frequency. If flow characteristics stray too far from a set point, shedding frequency is updated. The present work demonstrates the efficacy and robustness of this approach in reducing recirculation while Reynolds number is randomly varied between 1400 and 2400.

7.2 Introduction

A recirculation bubble is created when the separation of a boundary layer is followed by its reattachment (Bradshaw and Wong (1972)). Depending on the application, this can be either a detriment (higher drag, lower lift for external aerodynamics) or an advantage (enhanced mixing). Because it forces the separation of the boundary layer at the step edge and because of its very simple geometry, the Backward-Facing Step (BFS) has become a benchmark geometry to study separated flows.

Control of the flow downstream of a BFS has been the subject of much numerical and experimental research. There are three distinct approaches to flow control that have been applied to the BFS flow. Passive control involves permanent modifications of the geometry to yield the desired effect (Neumann and Wengle (2003)), open-loop control where power is supplied to the system to modify its operating conditions (Chun and Sung (1996), Bhattacharjee et al. (1986), Roos and Kegelman (1986)). Finally closed-loop control (Becker et al. (2005), Henning and King (2007), Dahan et al. (2012), Huang and Kim (2008)) improves open-loop control by using a feedback element to evaluate the flow state in order to compute appropriate commands and reject disturbances.

Closed loop control has the potential to be the most effective if correctly implemented. It can be further declined: extremum-seeking controllers, where a cost variable is defined and minimized (Becker et al. (2005), Beaudoin et al. (2006), Belson et al. (2013)); black box control where the flow is excited in order to compute an input-output map for the flow system without the use of *a priori* physical knowledge (Hervé et al. (2012)); model based control, where a model of the flow system is devised using physical knowledge and empirical data, which is then used to compute appropriate actuation (Pastoor et al. (2003)). A good overview of various control methods is given in Henning and King (2007).

For the BFS flow, periodic forcing can enhance Kelvin-Helmholtz (KH) instabilities in the shear layer which prompts the creation of vortices. Forcing the shear layer close to its shedding frequency has been shown to be most effective at reducing the recirculation bubble in separated flows (Chun and Sung (1996)). Thus, dynamically identifying the uncontrolled shedding frequency in a robust manner can lead to a simple yet efficient control method. Unfortunately, from an experimental point of view, measuring this frequency can be challenging, especially with traditional wall sensors. Control of the BFS flow using visual sensors has been conducted in Gautier and Aider (2013b). The control algorithms featured in the study are basic PID and gradient descent schemes that do not fully leverage the potential of the sensors.
The aim of this paper is to demonstrate the effectiveness of a simple physical model based control scheme. The principle is simple and consists in forcing the shear layer at its natural shedding frequency. This approach is made practical by using novel real-time computations of velocity fields measured by real-time particle image velocimetry which are used to compute the shedding frequency.

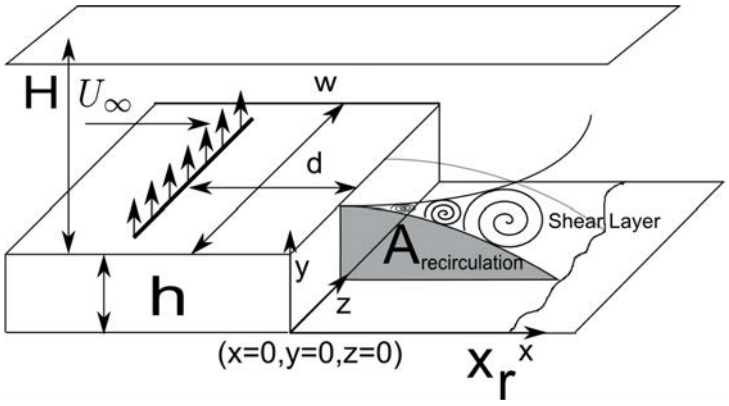

Figure 7.1: Sketch of the BFS geometry and definition of the main parameters, inspired by Gautier and Aider (2013b)

7.3 Experimental Setup

7.3.1 Water tunnel

It should be noted that the experimental setup is very similar to the one used in Gautier and Aider (2013b). This study however features pulsed actuation enabling the control approach. Experiments were carried out in a hydrodynamic channel in which the flow is driven by gravity. The flow is stabilized by divergent and convergent sections separated by honeycombs. The test section is 80 cm long with a rectangular cross section 15 cm wide and 10 cm high. The quality of the main stream can be quantified in terms of flow uniformity and turbulence intensity. The standard deviation σ is computed for the highest free stream velocity featured in our experimental set-up. We obtain $\sigma = 0.059$ cm.s^{-1} which corresponds to turbulence levels of $\frac{\sigma}{U_\infty} = 0.0023$.
The maximum mean free stream velocity U_∞ is 22 cm.s^{-1} leading to a maximum Reynolds number $Re_h = \frac{U_\infty h}{\nu} = 3300$. However in the following experiments the maximum Reynolds number is $Re_h = 2800$. A specific leading-edge profile (NACA 0019) is used to smoothly start the boundary layer which then grows downstream along the flat plate, before reaching the edge of the step 33.5 cm downstream. The boundary layer is laminar and follows a Blasius profile. More details can be found in Cambonie et al. (2013).

7.3.2 Backward-facing step geometry

The BFS geometry and the main geometric parameters are shown in figure 9.1. BFS height is $h = 1.5$ cm. Channel height is $H = 7$ cm for a channel width $w = 15$ cm. The vertical expansion ratio is $A_y = \frac{H}{h+H} = 0.82$ and the span-wise aspect ratio is $A_z = \frac{w}{h+H} = 1.76$.

7.3.3 Velocity fields computation

The flow is seeded with 20 μm neutrally buoyant polyamid seeding particles. They are illuminated by a laser sheet created by a 2W continuous laser beam operating at $\lambda = 532$ nm. Images of the symmetry plane are recorded using a Basler acA 2000-340km 8bit CMOS camera. Velocity field computations are run on a Gforce GTX 580 graphics card.

Real-time PIV processing has been implemented before. For instance Willert et al. (2010) used a basic PIV algorithm implemented on CPU to demonstrate the concept of vision based control. Roberts (2012) used an (unspecified) algorithm to compute flow velocity fields in order to improve commands in a benchmark fluid-structure control problem. Kreizer et al. (2009) used smart cameras to enable real-time PTV of the flow inside a cavity.

The algorithm used to compute the velocity fields in the following experiments is a Lukas-Kanade optical flow algorithm (Besnerais and Champagnat (2005)) called FOLKI, developed at ONERA. At each pixel small displacements are computed by least square Gauss-Newton minimization over a correlation window (20×20 pixels). A pyramid scheme is used to handle large displacements. Its offline and online accuracy has been rigorously demonstrated and detailed by Champagnat et al. (2011), Gautier and Aider (2013a). The algorithm was used off-line by Davoust et al. (2012), Sartor et al. (2012). The GPU version (FOLKI-GPU) was improved by Gautier and Aider (2013a) to allow for *real time* computation of instantaneous velocity fields. The algorithm works even when velocity changes by as much as a factor of 2 without adjusting acquisition or computation parameters. This is particularly interesting for the following experiments where the Reynolds number is varied. The size of the velocity field is $11.45h \times 3.0h$ which is enough to capture the whole recirculation bubble for all Reynolds numbers, the largest mean recirculation length being $X_r = 6.75h$.

7.3.4 Actuation

The actuator is a span-wise flush continuous slotted jet (9 cm wide). The rectangular jet nozzle is very small in the stream-wise direction (0.1 cm). Injection is normal to the wall. The slotted jet is located at a distance $d = 3.5$ cm $= 2.3h$ upstream of the step edge (figure 9.1). The jet is controlled by a pressurized water tank. Water is pushed from the pressurized tank through a plenum and through a volume of glass beads designed to homogenize the incoming flow. This action results in the creation of a planar jet, normal to the wall and homogeneous along the span-wise direction. The jet amplitude is controlled by changing tank pressure. The amplitude of the actuation $a_0 = \frac{U_{jet}}{U_\infty}$ is defined as the ratio between the mean jet exit velocity U_{jet} when the jet is active and the free-stream velocity U_∞.
The flow is modulated by a one-way voltage driven solenoid-valve. A constant amplitude square signal is sent to the valve. The duty cycle dc, defined as the ratio between the time during which the valve is opened T_{on} and total cycle time T_{ac}, is kept constant at $dc = \frac{T_{on}}{T_{ac}} = 20$ % which has been shown to be an optimal value for this setup (Gautier and Aider (2014)). The only control parameter is the frequency of the actuation F_{ac}. It has been shown in Gautier and Aider (2014) that the optimal actuation amplitude depends on

the free-stream velocity. It was also shown that only a small amplitude can be efficient to control the flow for each Reynolds numbers. Furthermore using higher amplitude has no effect. For the first control scheme, actuation amplitude is kept constant so that it is either optimal or above optimal for all Reynolds numbers, ensuring maximum impact. In practice it means that the actuation amplitude is larger than the optimal value for lower Reynolds number. However this does not affect control effectiveness. It is merely sub-optimal when considering the optimization of the energy balance. The second control scheme varies the actuation amplitude as a function of free-stream velocity to increase efficiency.

7.3.5 Flow state qualification

The most commonly used variable to qualify the flow state downstream the BFS is the length of the recirculation bubble X_R (Chun and Sung (1996), Becker et al. (2005), Henning and King (2007)). In most cases, it is a mean quantity defined through time-averaged wall measurements (wall shear stress, wall pressure) in the symmetry plane. Unfortunately, it is difficult to measure $X_R(t)$ in instantaneous velocity fields. The nature of PIV algorithms makes measurements close to the the wall unreliable. To face this issue, we introduce a measure of the area of the instantaneous recirculation $A_{rec}(t)$, as defined in equation (9.1):

$$A_{rec}(t) = \int H(-v_x(t))(x, y)\ \mathrm{d}x\mathrm{d}y \tag{7.1}$$

where A is the 2D velocity field area, H is the Heaviside function and v_x the longitudinal velocity. Essentially, the regions where the stream-wise velocity is negative are considered as belonging to the recirculation bubble. This expression is chosen because it is straightforward, easy and quick to compute, especially on GPU's (Gautier and Aider (2013b,a, 2014)). Furthermore it is coherent with the definition of recirculation length and can easily be extended to 3D velocity fields. Because $A_{rec}(t)$ is computed using the whole instantaneous 2D velocity field, it is well-suited to measure the influence of the actuation on flow structures near the step edge and its influence on the whole recirculation bubble.
Moreover, the recirculation length and the recirculation area are strongly correlated as shown by Gautier and Aider (2013b). A typical time series of $A_{rec}(t)$ as a function of time is shown in figure 7.2b for the uncontrolled flow at $Re_h = 2070$. An example of instantaneous recirculation area is shown in figure 7.2a.

7.4 Results

7.4.1 Shedding frequency

Computation

The Kelvin-Helmholtz span-wise vortices created in the shear layer downstream of the BFS (figure 9.1) strongly influence the recirculation area. Identifying the shedding frequency can be difficult. Spazzini et al. (2001) show skin friction spectra at different downstream positions. Reliably extracting a frequency from such data would be a challenge. Chun and Sung (1996) place hotwire probes in the shear layer near the reattachment point to yield shedding frequency, which is effective. However the reattachment point changes with

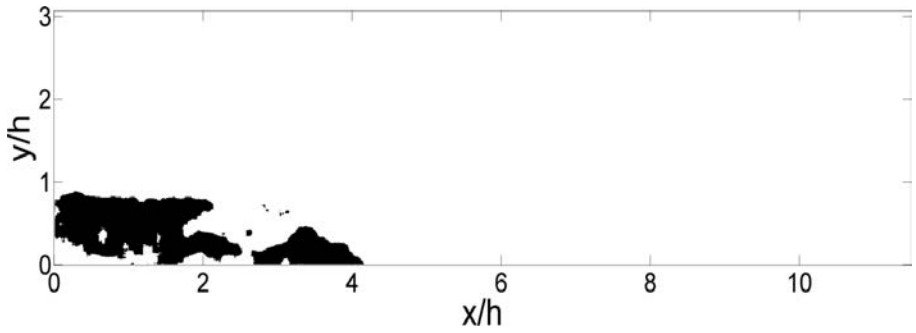

(a) Snapshot showing the instantaneous recirculation area for $Re_h = 2070$.

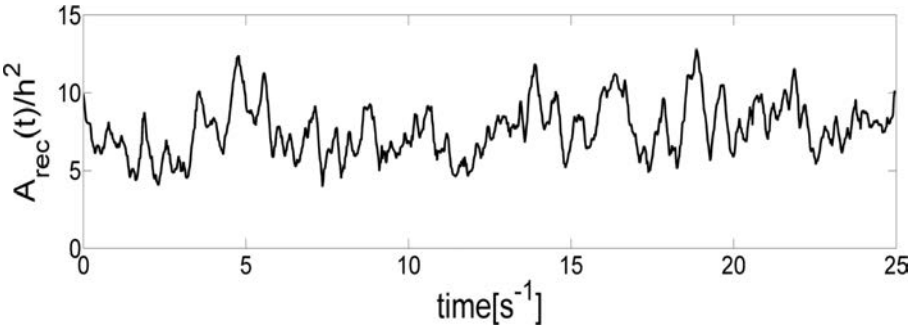

(b) Evolution of $A_{rec}(t)$ for $Re_h = 2070$ and a sampling frequency of 40 Hz.

Figure 7.2

Reynolds number, which makes frequency identification cumbersome with changing free-stream velocity as the probe has to be moved to an *a priori* unknown position. In addition the probe is intrusive and perturbs the flow.
Because the instantaneous 2D velocity fields are computed in real-time, it is possible to identify vortices at each time steps as they are shed in the shear layer. An effective way of detecting vortices is to compute the swirling strength criterion $\lambda_{Ci}(s^{-1})$ in the instantaneous two-components velocity fields. This criterion was first introduced by Chong et al. (1990) who analyzed the velocity gradient tensor $\mathcal{D} = \overrightarrow{\nabla}\overrightarrow{u}$ and proposed that the vortex core be defined as a region where $\nabla\mathbf{u}$ has complex conjugate eigenvalues. It was subsequently improved by Zhou et al. (1999) and by Chakraborty et al. (2005, 2007). It was recently successfully applied to visualize the 3D vortices created by a Jet in Cross-Flow measured by volumetric velocimetry (Cambonie and Aider (2014)). Some more details about the λ_{Ci} criterion can also be found in this reference. For 2D data, λ_{Ci} can be computed quickly and efficiently using equation (9.4) when such a quantity is real, else $\lambda_{Ci} = 0$:

$$\lambda_{Ci} = \frac{1}{2}\sqrt{4\det(\nabla\mathbf{u}) - \mathrm{tr}(\nabla\mathbf{u})^{\mathbf{2}}} \tag{7.2}$$

This is illustrated on Figure 7.3a where an instantaneous snapshot of $\lambda_{Ci}(x, y)$ is shown for $Re_h = 2800$. One can clearly see the K-H vortices shed downstream of the edge of the BFS. This method works best on span-wise vortices. Tilted vortices are more difficult to identify.

From these time-series of $\lambda_{Ci}(x, y, t)$, measured with a sampling frequency $f_s = 40$Hz, it is possible to compute shedding frequency. The first step consists in spatially averaging λ_{Ci} in the vertical direction at a given $x = 5h$ position: $\Lambda_{Ci}(t) =< \lambda_{Ci}(5h, t) >_y$. One can see that Λ_{Ci} will be maximum when a vortex goes through the chosen vertical line (Figure 7.3a). The red rectangle indicates the region over which free-stream velocity u_{check} is computed. Computing this quantity is essential to the control loop. Figure 7.3b shows a typical time series of fluctuations of $\Lambda_{Ci}(t)$ for $Re_h = 2800$. Each peak corresponds to a vortex moving across the $x = 5h$ line. Figure 7.3c shows the corresponding frequency spectrum obtained by Fast Fourier Transform (FFT). The peak corresponding to the uncontrolled shedding frequency $f_{KH} = 3$ Hz is sharp and well defined. It leads to a Strouhal number based on step height $St_{KH} = f_{KH}h/U_\infty = 0.247$ for the shedding frequency. Because this method filters out everything but vortices, it allows us to get a well-defined shedding frequency peak. One could also find other characteristic frequencies of the flow, associated to various mechanisms such as vortex pairing or the flapping of the shear layer (Aider et al. (2007)) however the shedding frequency is the most energetic frequency in the spectrum. Furthermore the highest peaks in the time-series shown in figure 7.3c are close to the main peak. In the rare case where a neighboring peak overtakes the main peak, the identified shedding frequency remains close to the actual shedding frequency, leading to effective and robust control.

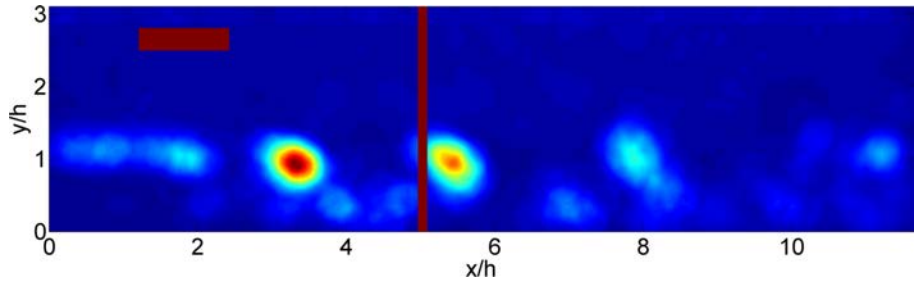

(a) Contours of $\lambda_{Ci}(x, y)$ at a given time step for $Re_h = 2800$. The vertical line shows the position where $\lambda_{Ci}(x = 5h, y)$ is integrated to identify shedding frequency. The red rectangle shows the position where flow velocity is computed.

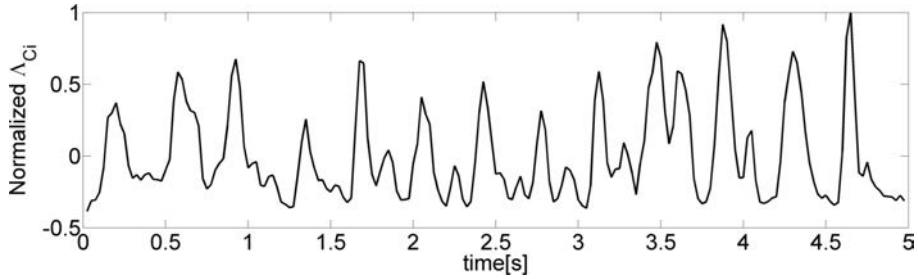

(b) Λ_{Ci} time series at $x = 5.0h$ for $Re_h = 2800$. Each peak corresponds to the passage of one vortex.

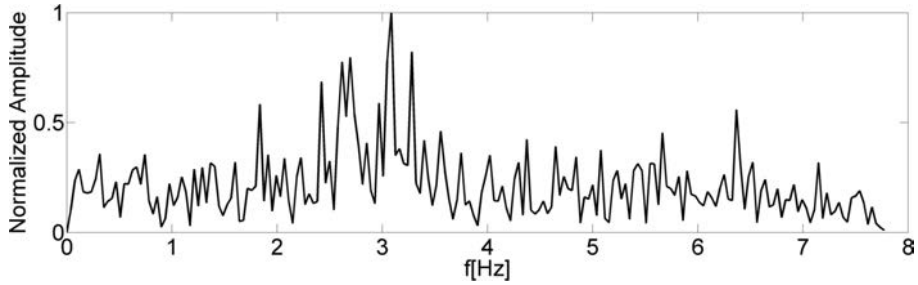

(c) Frequency spectrum for this time series showing a stronger peak at $f_{KH} = 3.08$ Hz

Figure 7.3

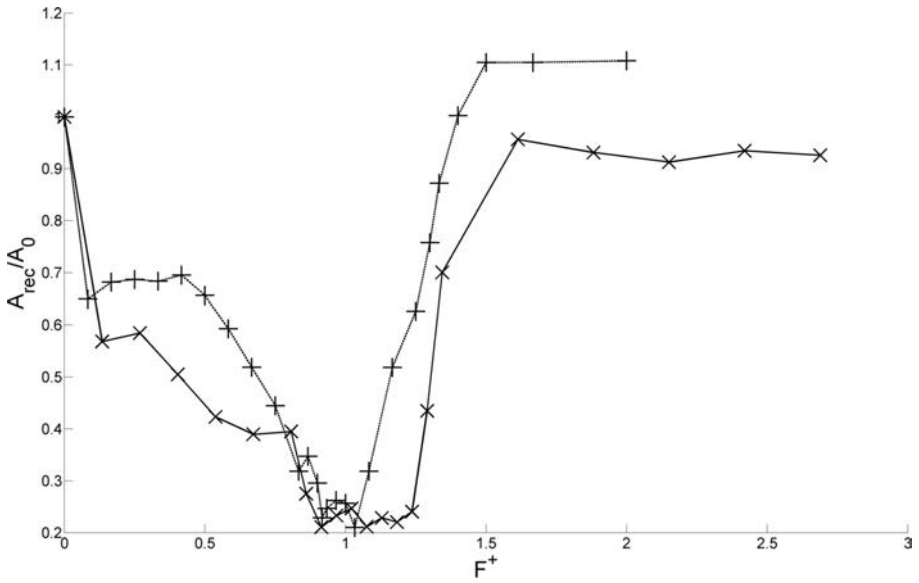

Figure 7.4: Evolution of time averaged recirculation area A_{rec}/A_0 as a function of F^+ for $Re_h = 2070$ ($\times$) and $Re_h = 2800$(+) with a 50% duty cycle and $a_0 = 0.040$, from Gautier and Aider (2014)

Figure 7.4 shows the evolution of the recirculation area (non-dimensionalized by the uncontrolled recirculation area A_0) as a function of $F^+ = f_{ac}/f_{KH}$, the actuation frequency normalized by uncontrolled shedding frequency, for two Reynolds numbers. The result found in previous studies is recovered: the recirculation area is minimized when actuating close to the uncontrolled shedding frequency. Despite the difference in the actuation compared to previous studies (forcing at the step edge most of the time), we find that forcing the shear layer at a frequency centered around shedding frequency results in optimal reduction. Furthermore exciting the shear layer close to this frequency can also be as effective allowing some leeway when it comes to shedding frequency identification.

Because the recirculation bubble changes with Re_h and control actuation, it is important to choose a position where shedding frequency can be reliably computed. This is done by placing the detection line at a stream-wise position downstream of the initial vortex shedding position whatever the operating conditions. In practice, one has to find a region where the shedding frequency is well defined and does not change in space for the different Reynolds numbers. Figure 7.5 shows the computed peak frequency as a function of the stream-wise position x/h for two Reynolds numbers ($Re_h = 2070$ and $Re_h = 2800$). In the region $2 < x/h < 6$ the computed frequency is independent of x/h for both Reynolds numbers. In the following the detection area is located at $x/h = 5$ for all Reynolds numbers.

Frequency identification convergence

Different approaches to frequency identification were attempted. We found that while specific methods might work better for certain cases, the simple FFT was the most robust overall.

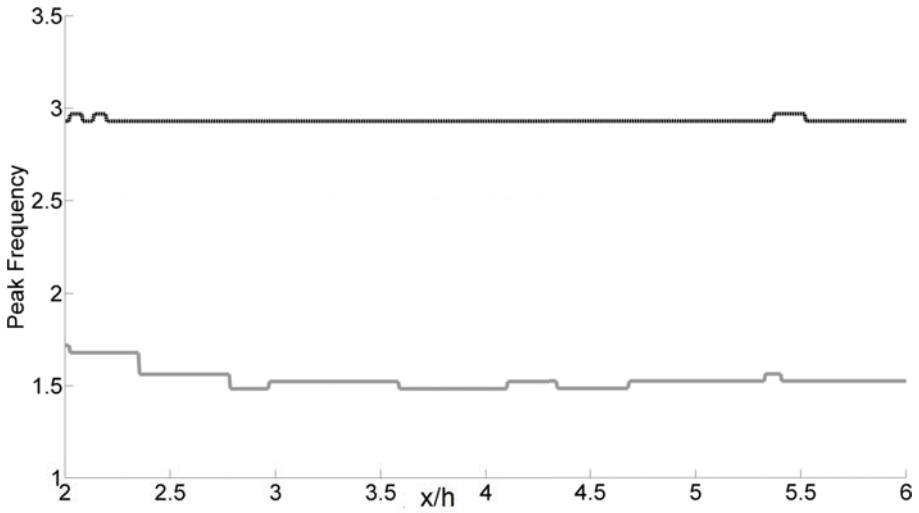

Figure 7.5: Natural shedding frequency identification as a function of x/h for Reynolds numbers 2070 (grey) and 2800 (dotted black)

The problem remains of choosing the time window used to compute the FFT. Short times will make control more responsive while longer times will increase robustness.
Ideally the window size used to compute the dominant frequency would vary with Re_h. Low Reynolds number flows feature lower shedding frequencies, thus longer evaluation is required to yield a frequency. However changing the size of the evaluation window as a function of the Reynolds number is not practical, thus we searched for a window size which allows for reliable frequency identification in the whole range of Reynolds numbers while being as short as possible in order to improve control responsiveness.

To evaluate the minimal duration over which the FFT should be computed, it is useful to plot $Err(f) = \Delta f / f_{ref}$ the error made in the evaluation of the shedding frequency when changing the length of the signal used to compute the FFT. The reference shedding frequency f_{ref} is computed over a very long time series, in this case 30 minutes, and $\Delta f = f - f_{ref}$. Figure 7.6 shows $Err(f)$ as a function of the time window size. The sample signal is obtained by applying the λ_{Ci} sensor to the uncontrolled flow at $Re_h = 2000$. For each time-step, the FFT is computed over a centered window, yielding multiple dominant frequency as a function of time for every window size. One can see that the error is small larger windows than 20 s. In the following we will compute the shedding frequency in real-time over a 20 s window, in practice very few computations yield incorrect frequencies.

Comparison to other means of frequency identification

To illustrate the robustness and relevance of this method we compare it to a more traditional approach where local probes, like hot-wire Laser Doppler velocimetry, would be used to evaluate shedding frequency. For this purpose, we emulate hot-wire data by monitoring local velocity amplitude fluctuations at different points in the flow field. Figure 7.7 shows

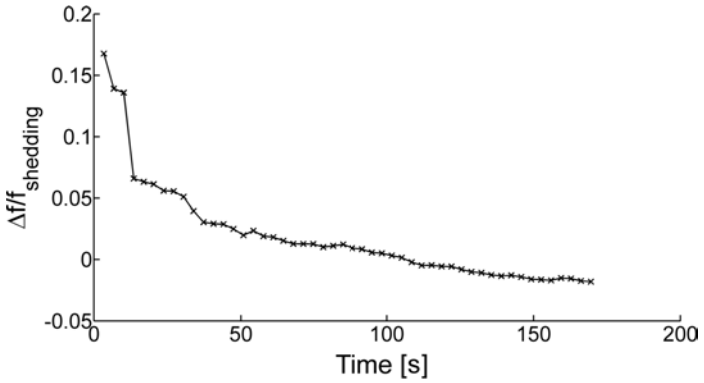

Figure 7.6: Relative difference between mean frequency computed for every window size and frequency computed over the whole signal

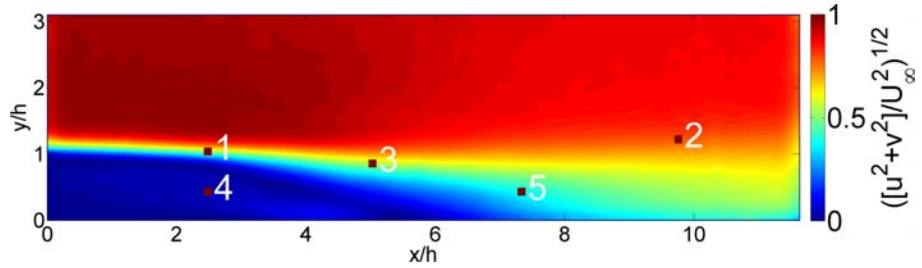

Figure 7.7: Positions of the five local probes downstream of the BFS used to simulate hot-wire measurements in the time averaged velocity amplitude field

sensors positions downstream of the BFS in the time averaged velocity amplitude field. The sensors size is 20×20 pixels, the same size as the correlation window used for velocity field computation. Velocity amplitude is averaged over the sensor area for each time step.

Figure 7.8 shows velocity amplitude fluctuations spectra obtained with the five local probes to be compared with the λ_{Ci} sensor spectrum. Frequency identification is very sensitive to sensor position. Only sensor 1 identifies the frequency. Unsurprisingly it is located in the shear layer close to the shedding position. However since shear layer position changes with Re_h using such sensors would be unreliable making control less robust.

7.4.2 Control algorithm

The reactive control algorithm is described in figure 7.9. A quantity called $u_{check}(t)$ is introduced. It corresponds to the spatially averaged upper corner of the longitudinal velocity field, far from the boundaries (Figure 7.3a). When the incoming flow is steady, i.e. when $u_{check}(t)$ does not change for $\Delta T_{steady} = 5s$, then the shedding frequency f_{KH} is computed over $\Delta T_{computation} = 20s$. Once f_{KH} has been estimated, actuation begins: the jet starts pulsing at the corresponding natural shedding frequency, i.e. $f_{ac} = f_{KH}$. At this point the shedding frequency is locked to the actuation frequency leading, in principle, to a minimiza-

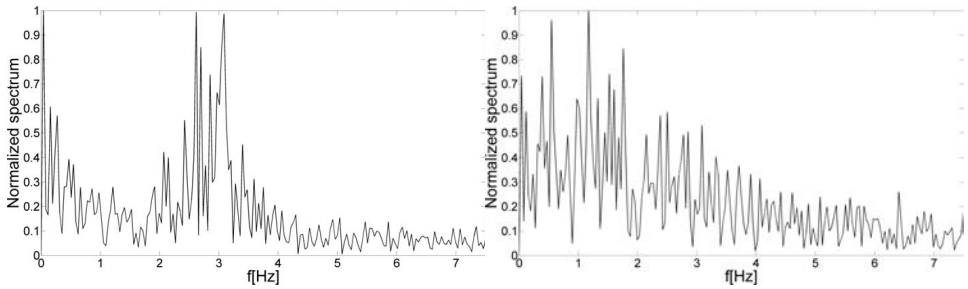

(a) Spectrum for sensor 1

(b) Spectrum for sensor 2

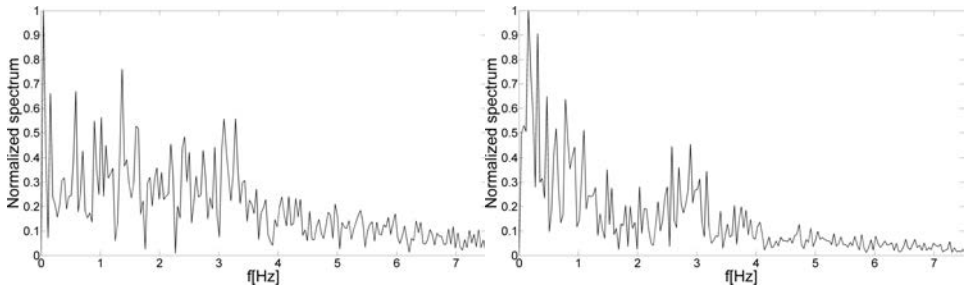

(c) Spectrum for sensor 3

(d) Spectrum for sensor 4

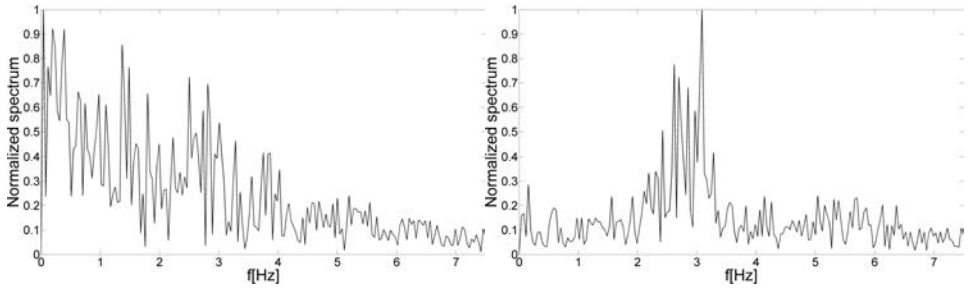

(e) Spectrum for sensor 5

(f) Spectrum for λ_{Ci}

Figure 7.8: Velocity amplitude spectra for different sensor locations, as well as spectrum for the λ_{Ci} sensor. $Re_h = 2800$.

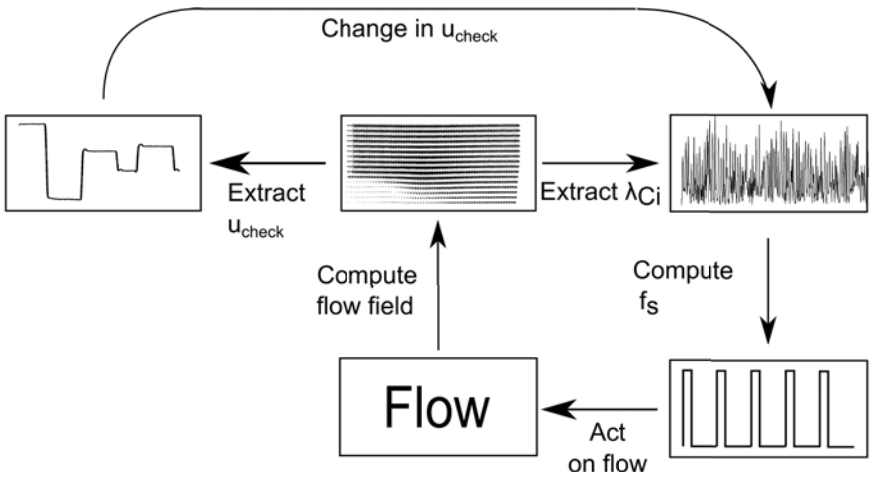

Figure 7.9: Block diagram of the frequency lock algorithm.

tion of the recirculation area (Figure 7.4). It is important to emphasize that while f_{KH} is being computed actuation is turned off.
The actuation is kept constant as long as Δu_{check} does not change. This is done by continuously polling the value described in equation (7.3):

$$\Delta u_{check}(t) = \frac{u_{check}(t) - u_{check}(t - \Delta t)}{u_{check}(t - \Delta t)} \tag{7.3}$$

It is a measure of how much the flow has changed since the last frequency computation. If the value goes above a given threshold, frequency is re-computed, thus completing the loop. The threshold depends on the noise of the monitoring variable and should be chosen such that only significant changes prompt re-computation. Since the flow is isothermal, the shedding frequency remains constant as long as the free-stream velocity remains unchanged.

This approach has some limitations. For instance, because a fixed time is required to compute shedding frequency this method cannot handle frequent changes in operating conditions. Ideally, the time between re-computations should be as long as possible. In addition, this approach is viable only if a dominant frequency exists and can be easily identified. For higher Reynolds numbers it might become more difficult to reliably and correctly identify this frequency. Because the λ_{Ci} criterion is used to find the KH vortex and evaluate the KH frequency, this approach should still work for higher Reynolds numbers but the computation location should probably be placed closer to the step edge.

Small variations in f_{KH} for the same input flow can be allowed since the flow is sensitive to actuation close to f_{KH}. Longer checking and computation times ensure a more reliable but less responsive system.

Other control algorithms could be considered, the most obvious one being slope seeking when considering the evolution of recirculation area as a function of forcing frequency (Figure 7.4). Unfortunately effective implementation of slope seeking on this setup is impossible

due to the nature of the actuators. Indeed, an additional frequency component must be added to the control signal for slope seeking which is not feasible with this experimental setup.

Other sensors could be used to compute shedding frequency, such as hot wire probes placed in the flow or wall sensors on the bottom wall. However the present method has the advantage of not perturbing the flow. Furthermore, since vortices are detected at their inception, shedding frequency can be reliably computed. Wall sensors or local probes would lead to wider and richer frequency spectra, making frequency identification difficult and less reliable as shown in section 3.2.

7.4.3 Frequency-lock approach for varying Reynolds numbers

To demonstrate the efficiency of the frequency-lock approach, free-stream velocity is randomly varied. The variations in $Re_h(t)$ (based on $u_{check}(t)$) are shown in figure 7.10a. To ensure strong variations in the shedding frequency, a wide range of Reynolds numbers is explored (from $Re_h = 1400$ to 2400). Each time the Reynolds number is changed, shedding frequency is evaluated, as shown in figure 7.10b. Actuation amplitude is constant, figure 7.10c shows the evolution of jet to cross-flow velocity ratio. Finally, figure 7.10d shows the evolution of $A_{rec}(t)$ normalized by the uncontrolled value A_{0,Re_h} for this Reynolds number. The mean value is also computed over each controlled phase (red lines on figure 7.10d). Re-computation only occurs for major changes in u_{check}. What constitutes a major change is up to the user. Because shedding frequency is locked to actuation frequency, control is successful even when natural shedding frequency varies slightly. Each peak in $A_{rec}(t)$ corresponds to a re-computation of f_{KH}. When the flow is controlled, the reduction in A_{rec} varies between 70 % to 85 % compared to the uncontrolled value. These values are consistent with those found by Gautier and Aider (2014) in open-loop experiments. This illustrates the robustness of this control strategy based on frequency lock on shedding frequency estimated by real-time instantaneous optical measurements.

Figure 7.11a shows the time-averaged recirculation area for the mean controlled and uncontrolled flows at $Re_h = 1600$. Figure 7.11b compares two instantaneous recirculation area snapshots for the same flow. Recirculation area reduction is larger than recirculation length reduction. This is easily understood when looking at Figure 7.11a: the controlled flow recirculation length does not account for the large reduction in recirculation near the step.

A bare bones version of this method would involve mapping the relationship between u_{check} and f_{KH}, thus the identification part of the algorithm could be removed leading to increased adaptation speed. However time-consuming mapping would be necessary. Another avenue for improvement would be implementing a frequency check at regular intervals to ensure actuation is optimal.

7.4.4 Improved algorithm featuring varying amplitude

In the previous experiments jet velocity amplitude was kept constant. In order to improve control efficiency, the control scheme has been modified to adjust amplitude. For lower

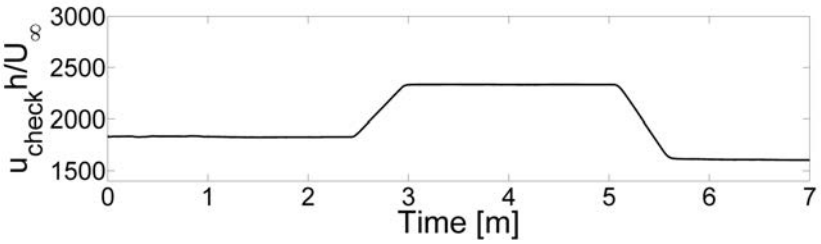

(a) Random variations of the Reynolds number Re_h as a function of time.

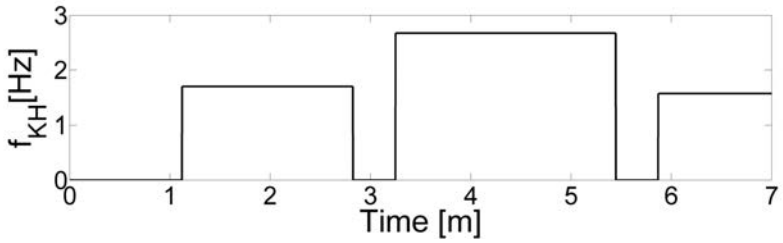

(b) Corresponding evolution of f_{KH} as a function of time, following the variations of $Re_h(t)$.

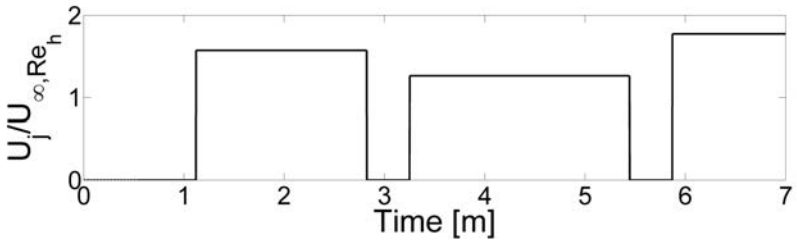

(c) Evolution of jet to cross-flow ratio as a function of time.

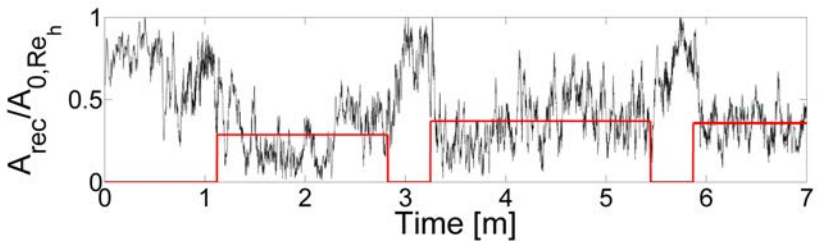

(d) Evolution of $A_{rec}/A_{0,Re_h}$ as a function of time. Time series are normalized by the uncontrolled recirculation area for the corresponding Reynolds number. Mean values of the controlled signal are shown in red. They are computed for each period when Re is changed.

Figure 7.10

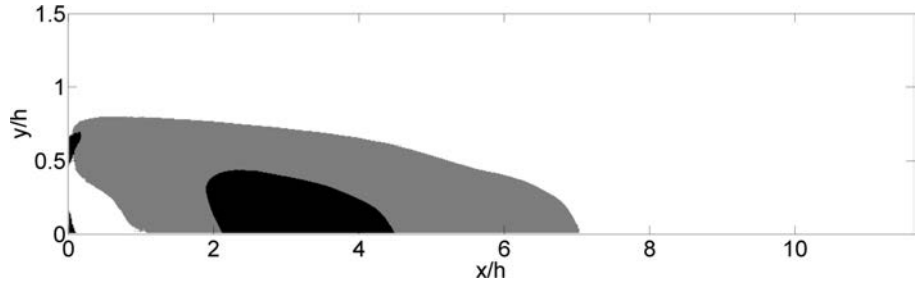

(a) Uncontrolled (gray) and Controlled (black) mean recirculation for $Re_h = 1600$.

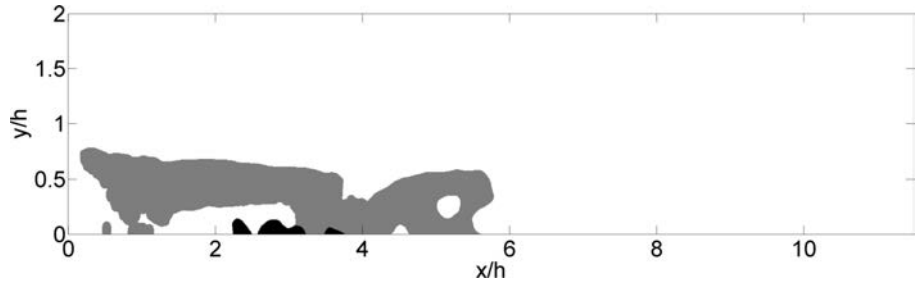

(b) Uncontrolled (gray) and Controlled (black) instantaneous recirculation for $Re_h = 1600$, see supplementary material for a video featuring a dynamic comparison.

Figure 7.11

Reynolds numbers effective control can be achieved with lower jet amplitude. Optimal amplitude is determined for the lowest and highest Reynolds numbers, and a linear interpolation is effected to determine jet amplitude as a function of u_{check}. Figure 7.12d shows the reduction in recirculation area. Figure 7.12c displays the corresponding jet to cross-flow velocity ratio throughout the experiment. It is interesting to notice that the optimal velocity ratio is nearly constant and close to 1.2 for all Reynolds numbers. The control scheme is successfully modified for optimal efficiency by using u_{check} to better tune actuation.

7.5 Conclusion

The experimental study of a frequency lock flow control algorithm was conducted on the separated flow downstream of a backward facing step. The objective of the reactive flow control experiment was to reduce the recirculation bubble downstream of the step. The key point of these experiments is the use of 2D velocity fields to identify vortex shedding frequency. Reliable and robust vortex identification leading to estimation of the shedding frequency is made possible by real-time computations of the 2D velocity field and corresponding instantaneous λ_{ci}. The flow is periodically excited at the computed shedding frequency through upstream actuation. A polling loop continuously checks for changes in flow variables allowing the control to react to random changes in experimental conditions. Few parameters are required for successful operation. Furthermore responsiveness and reliability can be easily

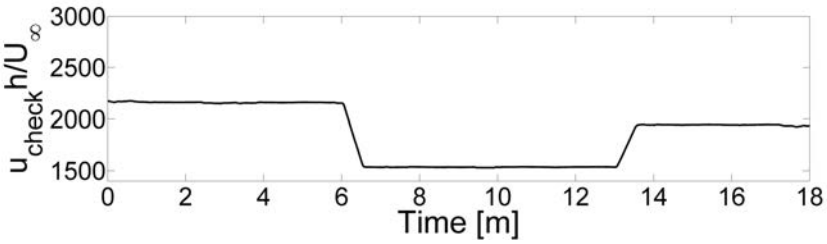

(a) Random variations of the Reynolds number Re_h as a function of time.

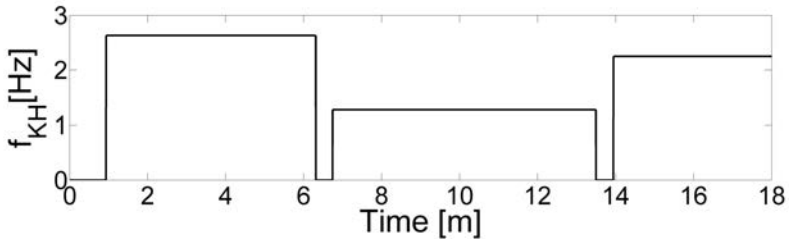

(b) Corresponding evolution of f_{KH} as a function of time, following the variations of $Re_h(t)$.

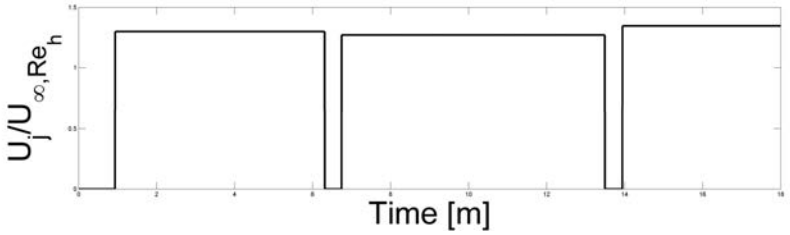

(c) Evolution of jet to cross-flow ratio as a function of time.

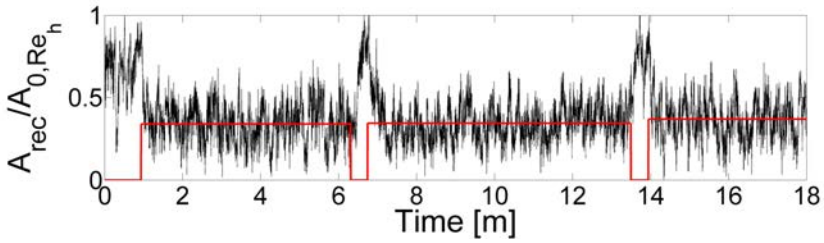

(d) Evolution of $A_{rec}/A_{0,Reh}$ as a function of time. Time series are normalized by the uncontrolled recirculation area for the corresponding Reynolds number. Mean values of the controlled signal are shown in red. They are computed for each period when Re is changed.

Figure 7.12

and intuitively tweaked based on knowledge of the time scales involved in the relevant flow processes. Control efficiency is improved by allowing for changing actuation amplitude. This simple approach can be easily adapted to other statistically two-dimensional separated flows.

7.6 Acknowledgments

The authors wish to thank the DGA (Direction Générale de l'Armement) and CNRS (Centre National de la Recherche Scientifique) for their financial support.

Bibliography

J.-L. Aider, A. Danet, and M. Lesieur. Large-eddy simulation applied to study the influence of upstream conditions on the time-dependant and averaged characteristics of a backward-facing step flow. *Journal of Turbulence*, 8, 2007.

J-F Beaudoin, O. Cadot, J-L. Aider, and J. Wesfreid. Drag reduction of a bluff body using adaptive control methods. *Phys. Fluids.*, 18:085107, 2006.

R. Becker, M. Garwon, C. Gutknecht, G. Barwolff, and R. King. Robust control of separated shear flows in simulation and experiment. *Journal of Process Control*, 15:691–700, 2005.

B.A. Belson, O. Semeraro, C.W. Rowley, and D.S. Henningson. Feedback control of instabilities in the two-dimensional blasius boundary layer: The role of sensors and actuators. *Phys. Fluids.*, 25, 2013.

G. Le Besnerais and F. Champagnat. Dense optical flow by iterative local window registration. *ICIP (1)*, 2005.

S. Bhattacharjee, B. Scheelke, and T.R. Troutt. Modifications of vortex interactions in a reattaching separated flow. *AIAA J.*, 24(4):623–629, 1986.

P. Bradshaw and F.Y.F. Wong. The reattachment and relaxation of a turbulent shear layer. *J. Fluid Mech.*, (52):113–135, 1972.

T. Cambonie and J.-L. Aider. Transition scenario of the round jet in crossflow topology at low velocity ratios. *Physics of Fluids (1994-present)*, 26(8):084101, 2014.

T. Cambonie, N. Gautier, and J.-L. Aider. Experimental study of counter-rotating vortex pair trajectories induced by a round jet in cross-flow at low velocity ratios. *Exp. Fluids, post-print available on the arXiv*, 54(3):1–13, 2013.

P. Chakraborty, S. Balachandar, and R.J. Adrian. On the relationships between local vortex identification schemes. *J. Fluid Mech.*, 535:189–214, July 2005.

P. Chakraborty, S. Balachandar, and R.J. Adrian. Kinematics of local vortex identification criteria. *J. Vis.*, 10(2):137–140, April 2007.

F. Champagnat, A. Plyer, G. Le Besnerais, B. Leclaire, S. Davoust, and Y. Le Sant. Fast and accurate piv computation using highly parallel iterative correlation maximization. *Exp. Fluids.*, 50:1169–1182, 2011. ISSN 0723-4864.

M.S. Chong, A.E. Perry, and B.J. Cantwell. A general classification of 3-dimensional flow fields. *Phys. Fluids.*, 2:765–777, 1990.

K. B. Chun and H. J. Sung. Control of turbulent separated flow over a backward-facing step by local forcing. *Exp. Fluids.*, 21:417–426, 1996.

J.A. Dahan, A.S. Morgans, and S. Lardeau. Feedback control for form-drag reduction on a bluff body with a blunt trailing edge. *J. Fluid Mech.*, 704:360–387, 2012.

S. Davoust, L. Jacquin, and B. Leclaire. Dynamics of m = 0 and m = 1 modes and of streamwise vortices in a turbulent axisymmetric mixing layer. *J. Fluid Mech.*, 709:408–444, 2012.

N. Gautier and J.-L. Aider. Real time, high frequency planar flow velocity measurements. *Journal of Visualization, post-print available on the arXiv.*, 2013a.

N. Gautier and J.-L. Aider. Control of the separated flow downstream of a backward-facing step using visual feedback. *Royal Society Proceedings A, post-print available on the arXiv.*, 469, 2013b.

N. Gautier and J.-L. Aider. Effects of pulsed actuation upstream a backward-facing step. *to be published in the Compte-Rendu de l'Académie des Sciences - Mécanique (CRAS II B). Post-print available on the arXiv.*, 2014.

L. Henning and R. King. Robust multivariable closed-loop control of a turbulent backward-facing step flow. *Journal of Aircraft*, 44, 2007.

A. Hervé, D. Sipp, P. Schmid, and M. Samuelides. A physics-based approach to flow control using system identification. *J. Fluid Mech.*, 702:26–58, 2012.

S.-C. Huang and J. Kim. Control and system identification of a separated flow. *Phys. Fluids.*, 2008.

M. Kreizer, D. Ratner, and A. Liberzon. Real-time image processing for particle tracking velocimetry. *Exp. in Fluids.*, (52):1187–1200, 2009.

J. Neumann and H. Wengle. Dns and les of passively controlled turbulent backward-facing step flow. *Flow Turbul. Combust.*, (71):297–310, 2003.

M. Pastoor, R. King, B. R. Noack, A. Dillmann, and Tadmor G. Model-based coherent-structure control of turbulent shear flows using low-dimensional vortex models. *American Institute of Aeronautics and Astronautics*, 2003.

J. Roberts. *Control of underactuated fluid-body systems with real-time image velocimetry.* Phd, MIT, 2012.

F.W. Roos and J.T. Kegelman. Control of coherent structures in reattaching laminar and turbulent shear layers. *AIAA J.*, 24(12):1956–1963, 1986.

F. Sartor, G. Losfeld, and R. Bur. Piv study on a shock-induced transition in subsonic flow. *Exp. Fluids.*, 53:815–827, 2012.

P.G. Spazzini, G. Luso, M. Onorato, N. Zurlo, and G.M. Di Cicca. Unsteady behavior of back-facing step flow. *Exp. Fluids.*, 30:551–561, 2001.

C. Willert, M. Munson, and M. Gharib. Real-time particle image velocimetry for closed-loop flow control applications. *15th international Symposium on Applications of laser techniques to fluid mechanics, 05-08 Jul. 2010. Lisbon Portugal*, 2010.

J. Zhou, R.J. Adrian, S. Balachandar, and T.M. Kendall. Mechanisms for generating coherent packets of hairpin vortices in channel flow. *J. Fluid Mech.*, 387:353–396, 1999.

Chapter 8

Feed-Forward Control of a Backward-Facing Step Flow

This chapter features an experimental implementation of a feed-forward control algorithm based on an Auto-Regressive Moving Average Exogenous (ARMAX) model. The goal is to determine how an approach, which has seen great success in numerical simulations, fares in an experimental setting. Real-time velocimetry was very useful. It greatly accelerated the work as there was no need to introduce physical wall bounded sensors into the experimental apparatus.
A challenging aspect of this work was ensuring the linear nature of the flow. Actuation and perturbation amplitudes must be kept to a minimum, which can be difficult given the hardware. Furthermore sensors and actuators being bi-dimensional, perturbations were required to be so as well. Calibration and validation data sets were used to create and calibrate the model. In addition to being used to compute actuation, the model itself is very useful and allows us to determine to what extent the flow can be controlled. Unlike numerical simulations impulse responses for the model show no amount of actuation can fully negate incoming perturbations. Nevertheless a control action was able to effectively suppress a portion of the incoming perturbation. This resulted in decreased downstream fluctuations. For cases where the flow behaves linearly this is a valid approach, further work should consider three-dimensional sensors and actuators.

8.1 Abstract

Closed-loop control of an amplifier flow is experimentally investigated. A feed-forward algorithm is implemented to control the flow downstream a backward-facing step perturbed by upstream perturbations. Upstream and downstream data are extracted from real-time velocity fields to compute an ARMAX model used to effect actuation. This work, done at Reynolds number 430, investigates the practical feasibility of this approach which has shown great promise in a recent numerical study by Hervé et al. (2012). The linear nature of the regime is checked, 2D upstream perturbations are introduced, and the degree to which the flow can be controlled is quantified. The resulting actuation is able to effectively reduce

downstream energy levels and fluctuations. The limitations and difficulties of applying such an approach to an experiment are also emphasized.

8.2 Introduction

Closed-loop flow control is of major academic and industrial interest. At the interface of control theory and fluid mechanics it is pertinent to many engineering domains, such as aeronautics and combustion. It can be used to reduce aerodynamic drag of an automobile or an airplane, increase combustion efficiency, or enhance mixing. Control of amplifier flows like boundary layers, mixing layers, jets or separated flows is particularly relevant and challenging. Indeed, amplifier flows are globally stable, however convective instabilities will amplify disturbances while being advected downstream (Marquet et al. (2008), Brandt et al. (2011)). Incoming perturbations are likely to be amplified to the point where they disrupt the entire flow. Nullifying these disturbances before they can be amplified by the flow is a great challenge for the flow control community (Schmid and Henningson (2001)). Typically when considering a laminar amplifier flow, the control objective can be to inhibit the transition to turbulence. Examples of such flows abound, a much-studied amplifier flow being that over a backward-facing step (BFS) (Barkley et al. (2002), H. M. Blackburn (2008)) which presents an unsteady region of convective instability. Another example is that of the flow over a cavity, used for studying the control of global instabilities (Rowley and Williams (2006)).
Control of amplifier flows has been the subject of much research (Hervé et al. (2012), Belson et al. (2013)). A control law can be computed using one of two ways. One possibility is to compute the model using beforehand knowledge of the physics of the flow (Sipp et al. (2010)). When derived directly from the Navier-Stokes equations these models are of very high order and require reduction before they can be used in a realistic setting. Model reduction is still a rich and very active research field, see Efe and Ozbay (2003), Rowley et al. (2004), Akervik et al. (2007). In some cases a physical analysis of the flow can yield simple models leading to efficient control laws as shown in Pastoor et al. (2008), Gautier and Aider (2013c). The second option is system identification as suggested by Ljung (1999). In this case, the flow is probed until a model can be derived from its responses. This approach is data based: it seeks to build an input-output model for the flow from empirical observations. Such an approach has been applied with success to the control of the recirculation bubble behind a BFS, see Becker et al. (2005), Henning and King (2007).

The BFS is considered as a benchmark geometry for the study of amplifier flows: separation is imposed by a sharp edge creating a strong shear layer susceptible to Kelvin-Helmholtz instability. Upstream perturbations are amplified in the shear layer leading to significant downstream disturbances. This flow has been extensively studied both numerically and experimentally (Armaly et al. (1983), Hung et al. (1997), Beaudoin et al. (2004), Aider et al. (2007)).

The principle of feed-forward control is to act on the flow upon detection of an event as opposed to the more common feed-back control where one reacts to an event. Feed-forward algorithms have been successfully used in flow control in numerical simulations (Belson et al. (2013)). Recently Hervé et al. (2012) have shown the effectiveness of a feed-forward algo-

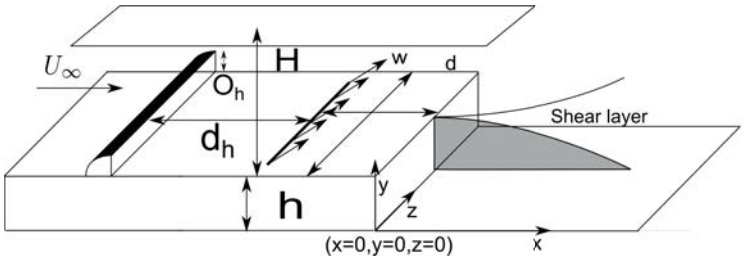

Figure 8.1: Sketch of the BFS geometry and definition of the main parameters.

rithm computed using an Auto-Regressive Moving-Average Exogenous model (ARMAX) to capture the relevant dynamics of the flow. The resulting control law leads to reduced energy levels and fluctuations. The aim of this work is to determine the feasibility and robustness of this approach in an experimental setting, a perturbed backward facing step flow.

8.3 Experimental Setup

8.3.1 Water tunnel

Experiments were carried out in a hydrodynamic channel in which the flow is driven by gravity. The flow is stabilized by divergent and convergent sections separated by honeycombs. The quality of the main stream can be quantified in terms of flow uniformity and turbulence intensity. The standard deviation σ is computed for the highest free stream velocity featured in our experimental set-up. We obtain $\sigma = 0.059$ cm.s^{-1} which corresponds to turbulence levels of $\frac{\sigma}{U_\infty} = 0.0023$. For the present experiment the flow velocity is $U_\infty = 2.1$ cm.s^{-1} giving a Reynolds number based on step height $Re_h = \frac{U_\infty h}{\nu} = 430$. Following the assumptions of Hervé et al. (2012) Reynolds number was chosen to ensure a sub-critical linear 2D flow.

8.3.2 Backward-Facing Step geometry and upstream perturbation

The BFS geometry and the main geometric parameters are shown in figure 9.1. BFS height is $h = 1.5$ cm. Channel height is $H = 7$ cm for a channel width $w = 15$ cm. The vertical expansion ratio is $A_y = \frac{H}{h+H} = 0.82$ and the span-wise aspect ratio is $A_z = \frac{w}{h+H} = 1.76$. The injection slot is located $d/h = 2$ upstream of the step edge.
The principle of the method described in Hervé et al. (2012) is to devise an input-output model for the flow based on experimental data. This model is used to compute actuation aimed at negating incoming upstream noise, thereby preventing its amplification. Because our sensor is 2D in the symmetry plane and our actuator can only deliver span-wise homogeneous actuation, a 2D upstream perturbation is required for effective control. As shown in figure 9.1 a 2D obstacle with a rounded leading edge of height $O_h = 0.8$ cm has been placed at $d_h = 15$ cm upstream from jet injection (12 h from the step edge) to perturb the flow. Because of the low Reynolds number the flow stays 2D.

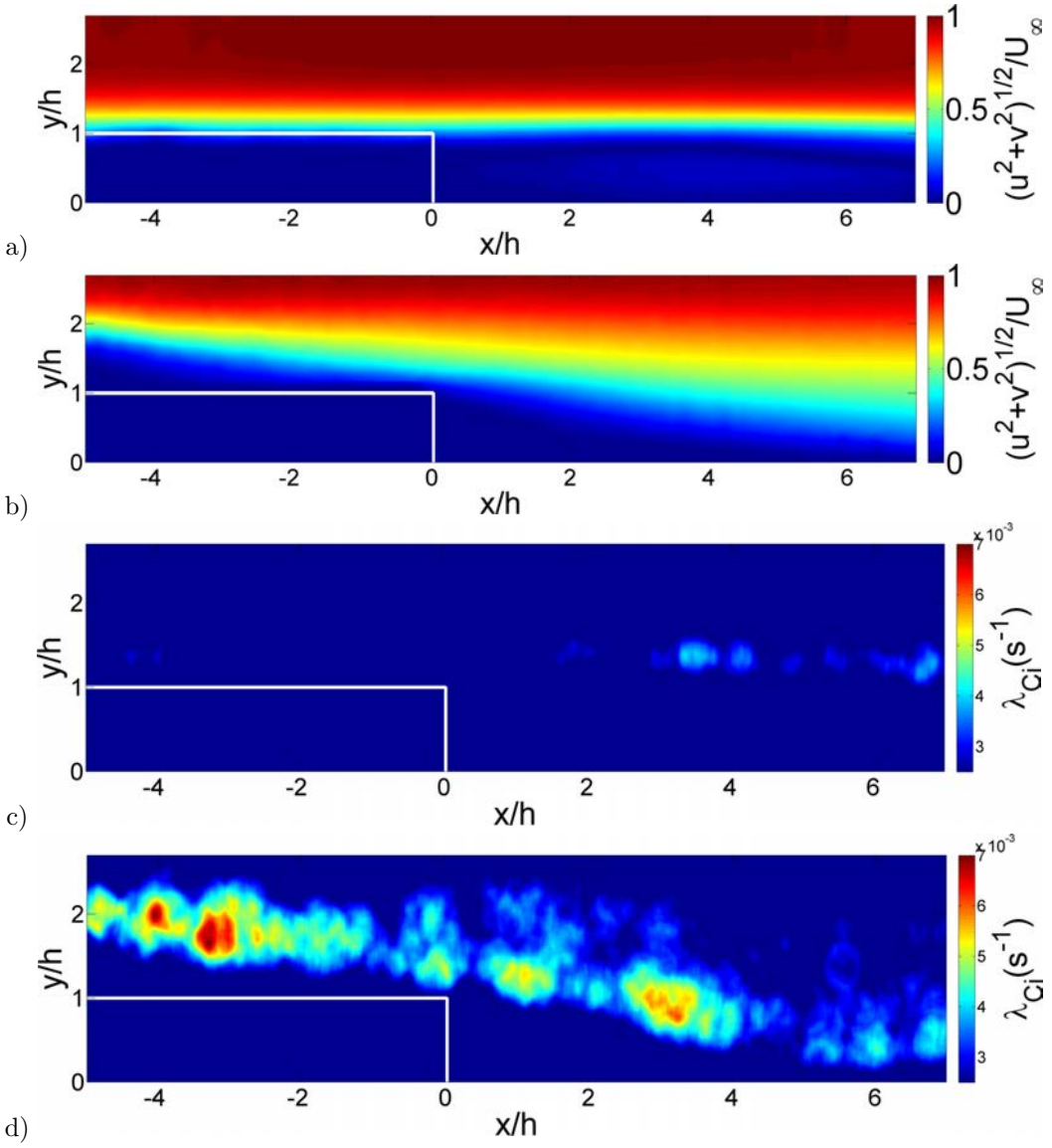

Figure 8.2: Mean velocity magnitude contour fields for the perturbed (b) and unperturbed (a) flow. Instantaneous snapshots showing contours of λ_{Ci} for the flow perturbed (d) and unperturbed (c) flow.

8.3.3 Sensor: 2D real-time velocity fields computations

The sensors used as inputs for the closed-loop experiments are visual sensors, i.e. regions of the 2D PIV (Particle Image Velocimetry) velocity fields measured jn the symmetry plane as shown in figure 8.4. The flow is seeded with 20 μm neutrally buoyant polyamid seeding particles. They are illuminated by a laser sheet created by a 2W continuous laser beam operating at $\lambda = 532$ nm. Images of the vertical symmetry plane are recorded using a Basler acA 2000-340km 8bit CMOS camera. Velocity field computations are run on a Gforce GTX 580 graphics card. The algorithm used to compute the velocity fields is based on a Lukas-Kanade optical flow algorithm called FOLKI developed by Besnerais and Champagnat (2005). Its offline and online accuracy has been demonstrated and detailed by Champagnat et al. (2011), Gautier and Aider (2013a). Furthermore this acquisition method was successfully used in Davoust et al. (2012), Gautier and Aider (2013b). The size of the velocity fields is 17.2×4.6 cm^2. They are computed every $\delta_t = 40ms$, for a sampling frequency $F_s = 25Hz$.

8.3.4 Uncontrolled flow

The swirling strength criterion λ_{Ci} is an effective way of detecting vortices in 2D velocity fields introduced and improved by Chong et al. (1990), Zhou et al. (1999). For 2D data the swirling criterion is defined as $\lambda_{Ci} = \frac{1}{2}\sqrt{4\det(\nabla \mathbf{u}) - \mathrm{tr}(\nabla \mathbf{u})^{\mathbf{2}}}$ (when this quantity is real). Figures 8.2 a) and b) show the mean velocity amplitude fields for the perturbed (with obstacle) and unperturbed (without obstacle) flows. Figures 8.2 c) and d) show corresponding λ_{Ci} snapshots, highlighting the perturbations caused by the upstream obstacle. Figure 8.2 d) shows the steady stream of vortices created by the obstacle interacting with the recirculation. Quantitatively, λ_{Ci} in the perturbed flow is an order of magnitude higher than for the flow unperturbed flow. Boundary layer thickness at the step edge for the flow with and without obstacles are $\delta = 1.34$h and $\delta = 1.73$h respectively.
Turbulent kinetic energy (TKE) is defined as $k(x,y,t) = \frac{1}{2}(u'(x,y,t)^2 + v'(x,y,t)^2)$, where u', v' are longitudinal and vertical velocity fluctuations. Figure 8.3(a) shows the time-averaged TKE field $< k(x,y) >_t$ downstream of the step for the unperturbed case, while figure 8.3(b) shows the perturbed case. The field exhibits two regions of high TKE. The lower region corresponds to the perturbation induced recirculation bubble. The upper region corresponding to perturbations induced by vortices shed by the upstream obstacle.

8.3.5 Actuation

In Hervé et al. (2012) actuation is a gaussian flow sink/source placed above the step, which is not physically feasible. In our case, actuation is provided by a flush slot jet, 0.1 cm long and 9 cm wide. This actuation has been chose to obtain a perturbation as homogeneous along the span-wise direction as possible. The jet angle to the wall is 45^o. The slot is located 3 cm (2h) upstream the step edge (figure 9.1). Jet flow is induced using water from a pressurized tank. It enters a plenum and goes through a volume of glass beads designed to homogenize the incoming flow. Jet amplitude is controlled by changing tank pressure. Because channel pressure is higher than atmospheric pressure this allows us to provide both blowing and suction. The convection time from jet injection to measurement area is 2 s ($< 0.5Hz$). The maximum actuation frequency f_a is about 1Hz which is sufficient for these experiments.

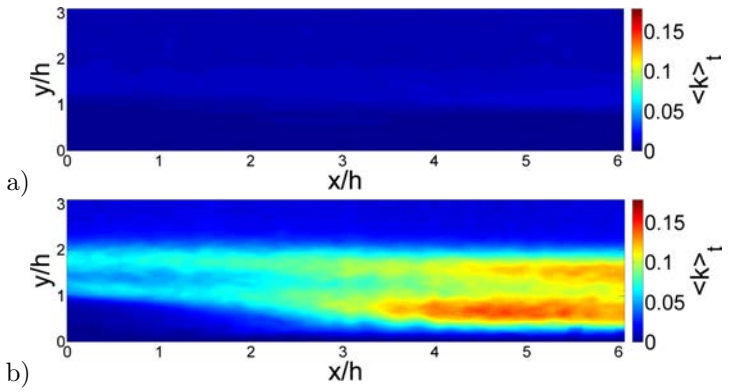

Figure 8.3: TKE field $< k(x,y) >_t$ downstream the BFS unperturbed (a) perturbed (b).

The control law output velocities, these are converted into pressure commands using a pre-calibrated transfer function.

8.4 ARMAX model

8.4.1 Introduction

An ARMAX model is used because it can be derived from experimental data, P. Pamart et al. (2010). Furthermore it has been shown by Hervé et al. (2012) that it is particularly well adapted at modeling the BFS flow when in the linear regime.

Two exogenous inputs $s(t), u(t)$ and one output $m(t)$ are used. The first exogenous input $s(t)$ measures fluctuations of spatially averaged λ_{Ci} (small grey area on figure 8.4). Such a sensor is well suited to the detection of upstream vortices created by the obstacle. The second exogenous input is jet to cross-flow velocity ratio $u(t)$.
Output $m(t)$ is a measure of TKE fluctuations in the recirculation region. The control objective is to negate the incoming perturbations created by the obstacle in order to reduce overall downstream TKE fluctuations. TKE is averaged over the whole downstream velocity field (large grey area on figure 8.4):

$$m(t) = \frac{\int k(x,y,t)dxdy}{\int dxdy} \tag{8.1}$$

Following Hervé et al. (2012) the equation for the model is defined in eq 8.2:

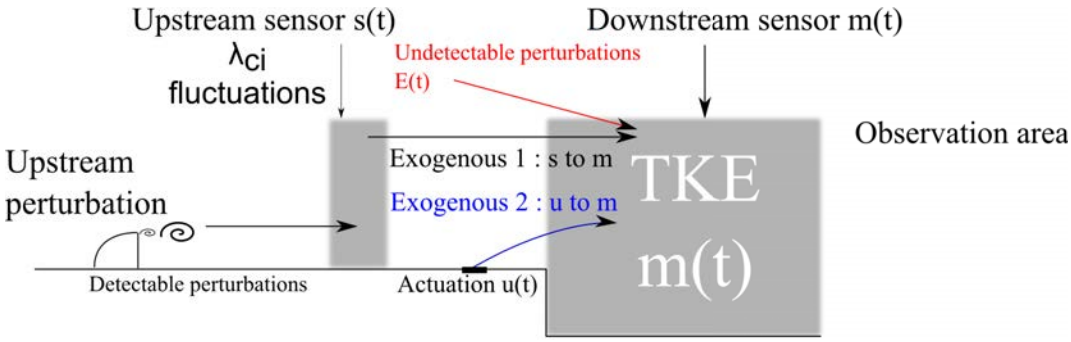

Figure 8.4: Schematic description of the main terms used in the ARMAX model.

$$\underbrace{m(t)+\sum_{k=1}^{n_a} a_k m(t-k)}_{auto-regressive} = \underbrace{\sum_{k=n_{du}}^{n_{du}+n_{bu}} b_k^u u(t-k)}_{exogenous\ 1} + \underbrace{\sum_{k=n_{ds}}^{n_{ds}+n_{bs}} b_k^s s(t-k)}_{exogenous\ 2} + E(t) \tag{8.2}$$

$$E(t) = \underbrace{\sum_{k=n_1}^{n_c} c_k e(t-k)}_{moving\ average} + e(t)$$

To achieve feed-forward control, the effects of upstream sensing $s(t)$ and actuation $u(t)$ on the output $m(t)$ must be quantified. For a pure feed-forward control, upstream estimation should be independent of actuation, see Semeraro (2013). During control, $u(t)$ is a function of $s(t)$. For our experimental setup we found that interference between actuation and the upstream sensor caused the control to saturate actuation. To avoid this effect, an inclined jet has been used instead of a wall normal jet. Moreover since $s(t)$ only measures the presence of vortices it is weakly affected by downstream actuation compared to vertical velocity for example. Special care must be given to lower actuation amplitude as much as possible so that it does not affect the upstream sensor. Figure 8.5 shows the cross correlation function between $s(t)$ and $u(t)$ for two cases: the calibration case and a case where there is interference (jet amplitude is too high) between the upstream sensor and the actuator. Interference results in high correlation between s and u whereas in our calibration case correlation is negligible.

Coefficients (a_k, b_k^u, b_k^s) are computed to minimize error $e(t)$ at all times. To calibrate the model the user must provide time series for both inputs and outputs, the longer the better. Values for $n_a, n_{du}, n_{bu}, n_{ds}, n_{bs}$ are tied to the physics of the flow and are determined by the user. These coefficients are linked to time delays in the flow system. The flow time history required for the model to work properly is given by $n_a.\delta_t$ (auto-regressive part). $n_{du}.\delta_t$ and $n_{ds}.\delta_t$ are the times required for the respective inputs to affect the output; they are linked to flow convective velocity. $n_{bu}.\delta_t$ and $n_{bs}.\delta_t$ represent input time scales. They correspond to the time during which upstream effects impact the output signal. Finally n_c is used to model noise and ensures robustness (Hervé et al. (2012)). This value is chosen iteratively,

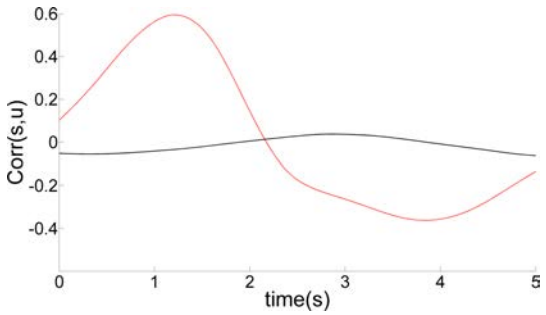

Figure 8.5: Cross correlation functions between $s(t)$ and $u(t)$ for the calibration case (black) and a case with interference between the upstream sensor and the actuator (dotted red).

once all other coefficients have been fixed, to get the best possible fit between experimental data and model output.

8.4.2 Model Computation

Figure 8.6 shows a small segment of the calibration time series. The forcing law $u(t)$ used in these series is one of pseudo random pulses. Pulses are made to occur at random intervals, long enough for the effects of the previous pulse to have subsided before the next pulse. During these intervals the only input to the system is $s(t)$. This allows the effects of actuation and upstream perturbations to be computed using a single time series. Impulse amplitude for actuation $u(t)$ should be chosen such that it is high enough to affect the output $m(t)$ but low enough to avoid perturbations of the upstream output $s(t)$. The mean value was removed for $m(t)$ because the focus is on suppressing fluctuations in the output. Calibration data were acquired over 25 minutes. Figure 8.7 shows the auto correlation function for $m(t)$. A quasi-oscillatory behavior can be observed. It can be used to choose n_a which is such that $n_a.\delta_t$ equals half the oscillatory period, as recommended by Hervé et al. (2012).

Figure 8.8 shows the response to an impulse, which can be used to evaluate the coefficients $n_{du}, n_{bu}, n_{ds}, n_{bs}$. The time delay t_{du}=2.5s between the beginning of the actuation and the response gives $t_{du} = n_{du}.\delta_t$. The upstream sensor is located 3.5 cm upstream the jet injection. Assuming perturbations travel at channel velocity, this implies a time delay of $t_{ds} \approx 1.7$ s for an upstream disturbance to affect the output, thus $n_{ds}.\delta_t = t_{du} + t_{ds}$.
Let t_{bu} be the time during which an impulse in u affects the output, as shown in figure 8.8, then $n_{bu}.\delta_t = t_{bu}$. Because the response to an impulse in s is more difficult to distinguish we assume $n_{bs} = n_{bu}$. Finally n_c is chosen after the other coefficients have been fixed in order to get the best possible agreement between model and real outputs. Table 8.1 summarizes the final coefficients used in the computation of the ARMAX model using the Matlab *armax* function (Ljung (1999)), it also shows the corresponding time delays and averages in seconds.

Figure 8.9a compares ARMAX output to the source signal for the calibration series. Agreement is good at 96 %. Figure 8.9b compares ARMAX output to the source signal for the validation series; agreement is slightly lower at 94 %. s, u, m are initialized at zero, which explains the poorer agreement at the start.

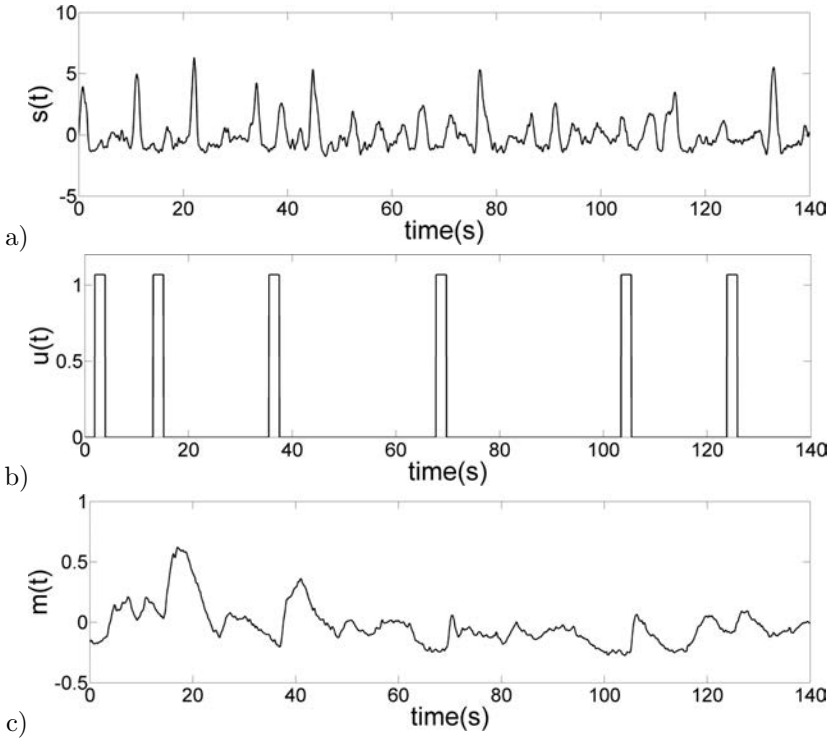

Figure 8.6: Calibration time series. a) $s(t)$ captures the influence of upstream disturbances; b) $u(t)$ pseudo-random control law; c) $m(t)$ spatially averaged downstream TKE, mean value has been removed.

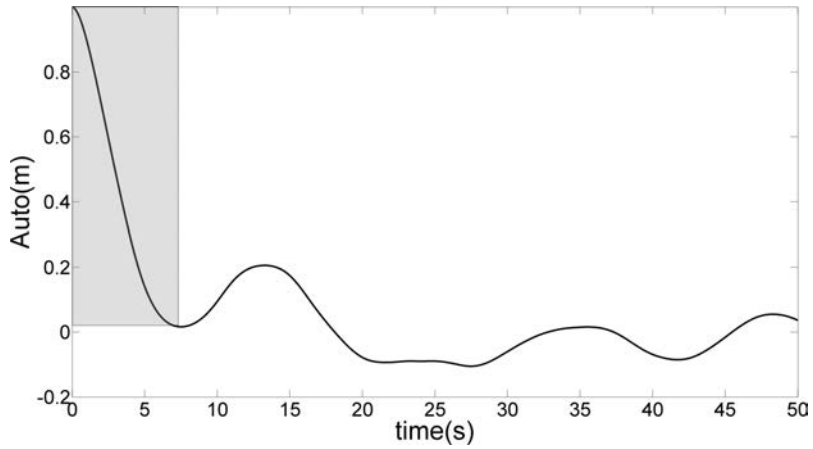

Figure 8.7: Auto correlation function for $m(t)$.

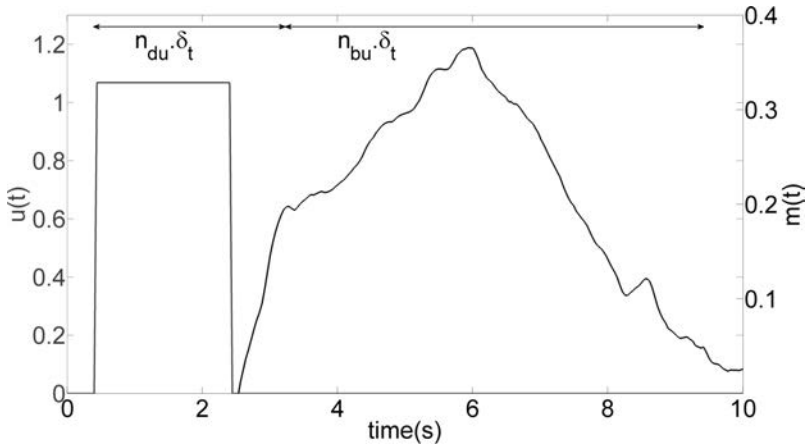

Figure 8.8: Output impulse response

n_a	n_{du}	n_{bu}	n_{ds}	n_{bs}	n_c
175	63	125	105	125	5
7.0 s	2.5 s	5 s	4.2 s	5 s	0.2 s

Table 8.1: ARMAX coefficients

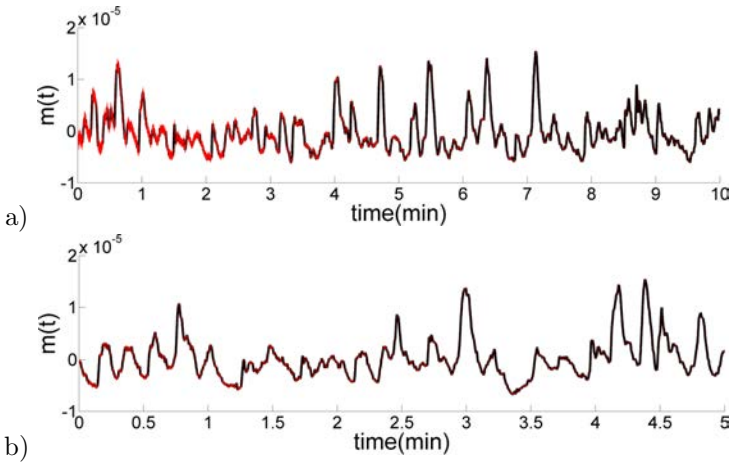

Figure 8.9: a) Calibration data set, model performance (dotted red) compared to experimental results (in black). b) Validation data set, model performance (dotted red) compared to experimental results (in black).

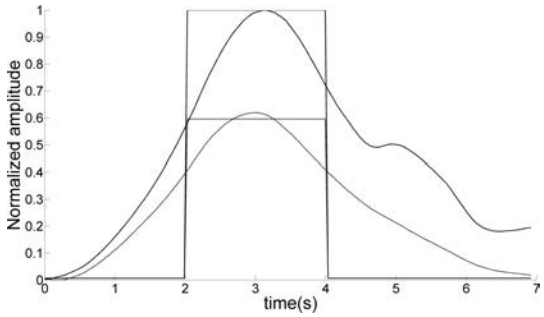

Figure 8.10: Time evolution of the $m(t)$ in response to a short impulse of different amplitudes (solid and dotted lines). The signals have been shifted in time to better highlight the linear nature of the response.

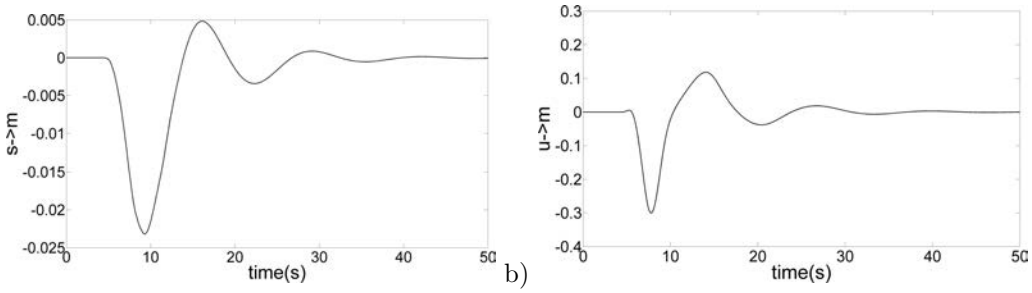

a) b)

Figure 8.11: a) ARMAX impulse response for exogenous input s(t). b) ARMAX impulse response for exogenous input u(t).

8.4.3 Linearity

A major underlying assumption of this approach is the linearity of the system. In our setup this was checked by imposing periodic pulsed forcing, for two different amplitudes. For both amplitudes, the response in $m(t)$ was averaged over each impulses. This phase-averaged response is shown in figure 8.10. Impulse amplitude ratio is also given for comparison. The signals were shifted in time to facilitate comparison. Figure 8.10 shows how a change in impulse amplitude leads to a proportional change in response amplitudes, confirming the linear behavior of the flow. Linearity was also checked when varying the size of the window where TKE is computed. Averaging over smaller windows, closer to the step, where non-linearities are weaker, did not improve system linearity.

8.5 Results

8.5.1 Control law

Figures 8.11a and 8.11b show the impulse response for both exogenous inputs. These figures show impulse responses are qualitatively similar, however they differ in amplitude.

Impulses responses can help determine if a model is "controllable" and whether or not the objective (negating TKE fluctuations) is *a priori* attainable, which makes them an invaluable diagnostics tool. To achieve fluctuation suppression the control law suggested by Hervé et al. (2012) was computed.
Only perturbations detected in $s(t)$ can potentially be canceled out. Other sources of disturbance are not modeled and are ignored by the control law. Equation 8.3 illustrates how the output signal can be written as a combination of the input signals.

$$m(t) = \sum_{k=0}^{\infty} h_k^s s(t-k) + h_k^u u(t-k) \tag{8.3}$$

The coefficients h_k^s, h_k^u are obtained by computing the impulse response of the ARMAX model as described in equation 4.2 and 8.5 for an impulse response $s(t=0) = 1, u(t=0) = 1$.

$$\forall k \; m_{impulse\; s}(t=k) = h_k^s \; s(0) \tag{8.4}$$
$$\forall k \; m_{impulse\; u}(t=k) = h_k^u \; u(0) \tag{8.5}$$

These coefficients can be used to express $m(t)$ as a function of $s(t), u(t)$ as shown in equation 8.6. Previously $s(t)$ was used to compute the model, here it is used as an input which allows us to compute $u(t)$. This is done over $Nt = 2000$ time steps (T = 80 s).

$$M_{Nt} = H_u U^f + G_u U^P + G_s S^P \tag{8.6}$$

with

$$M_{Nt} = \begin{pmatrix} m_t \\ m_{t+1} \\ \vdots \\ m_{t+Nt} \end{pmatrix}, U^f = \begin{pmatrix} u_t \\ u_{t+1} \\ \vdots \\ u_{t+Nt} \end{pmatrix}, U^P = \begin{pmatrix} u_{t-1} \\ u_{t-2} \\ \vdots \\ u_{t-Nt} \end{pmatrix}, S^P = \begin{pmatrix} s_t \\ s_{t-1} \\ \vdots \\ s_{t-Nt} \end{pmatrix}$$

$$H_u = \begin{pmatrix} h_0^u & & & \\ h_1^u & h_0^u & & \\ \cdots & \cdots & \ddots & \\ h_{Nt}^u & \cdots & \cdots & h_0^u \end{pmatrix}, G_u = \begin{pmatrix} h_1^u & \cdots & \cdots & h_{Nt}^u \\ h_2^u & \cdots & h_{Nt}^u & 0 \\ \cdots & \iddots & & 0 \\ h_{Nt}^u & \cdots & \cdots & 0 \\ 0 & 0 & 0 & 0 \end{pmatrix}, G_s = \begin{pmatrix} h_0^s & \cdots & \cdots & h_{Nt}^s \\ h_1^u & \cdots & h_{Nt}^s & 0 \\ \cdots & \iddots & & 0 \\ h_{Nt}^s & \cdots & \cdots & 0 \end{pmatrix}$$

Our goal is to find U^f such that $M_{Nt} = 0$ thus $U^f = (-H_u^+ G_u)U^P + (-H_u^+)S^P$. Because our interest is in actuation at time t, we have $u(t) = U^f(1)$. This is computed at every time step. One should note the similarities with model predictive control (MPC), where the model is iteratively updated in conjunction with a cost minimizing control law at each time step, see Camacho and Bordons (2013). Here control is computed over a finite time horizon, and past control moves are taken into account when computing future control. However this approach differs from MPC because no cost function is minimized over that time horizon.
H_u^+ denotes the pseudo-inverse (Penrose (1955)). A simple inverse amplifies high frequencies, yielding an impractical control law. Using a pseudo-inverse with non zero tolerance dampens

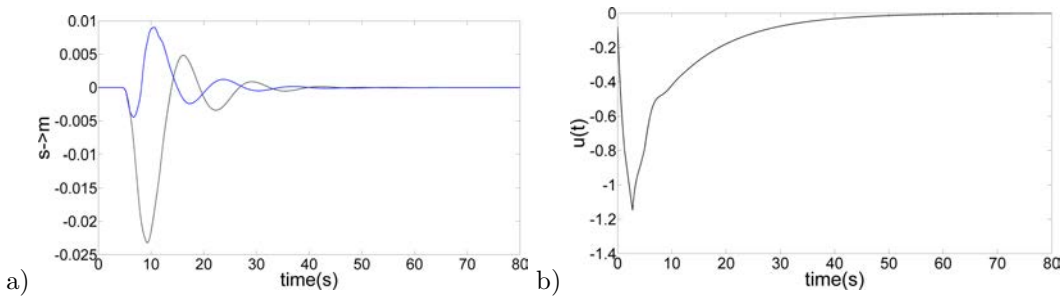

Figure 8.12: a) Controlled (blue) and uncontrolled (dotted black) response to an impulse in $s(t)$. b) Resulting control law $u(t)$.

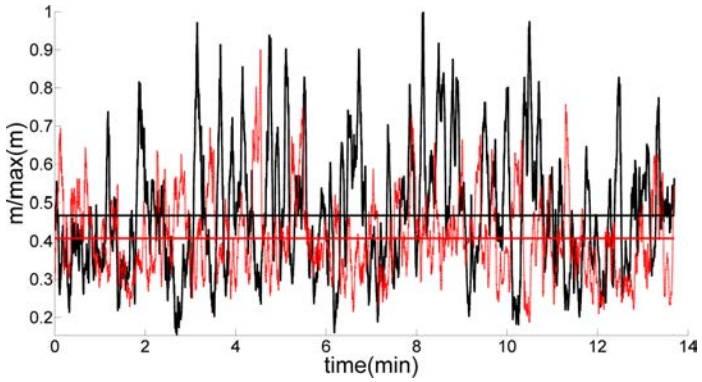

Figure 8.13: Controlled (dotted red) and uncontrolled flow (thick black) outputs. Mean values are also displayed.

high frequencies. Setting this tolerance level is equivalent to applying a filter and enables an effective compensator design. In practice the tolerance level must be chosen such that actuation can follow the control law. Since actuator cannot achieve changes faster than 1 Hz, the tolerance level was chosen such that the impulse response control law did not exhibit fluctuations above 1 Hz, leading to a value of 2.5.

Figure 8.12a compares the controlled and uncontrolled response of $m(t)$ to an impulse in $s(t)$. Figure 8.12b shows the corresponding non dimensional control law. These figures show that while complete fluctuation negation is impossible, fluctuation damping is achievable. Such a control law will negate a portion of upstream disturbances. Furthermore since part of the perturbation will not have the chance to be further amplified in the shear layer this should result in noteworthy reduction in downstream TKE fluctuations. Hervé et al. (2012) found a far greater reduction for the impulse responses. One of the reasons for this is the location of the actuator, at the wall in our experiment, instead of in the bulk above the wall in the numerical simulation. The vortices created by the obstacle travel too far from the wall (approximately one step height) to be as successfully suppressed.

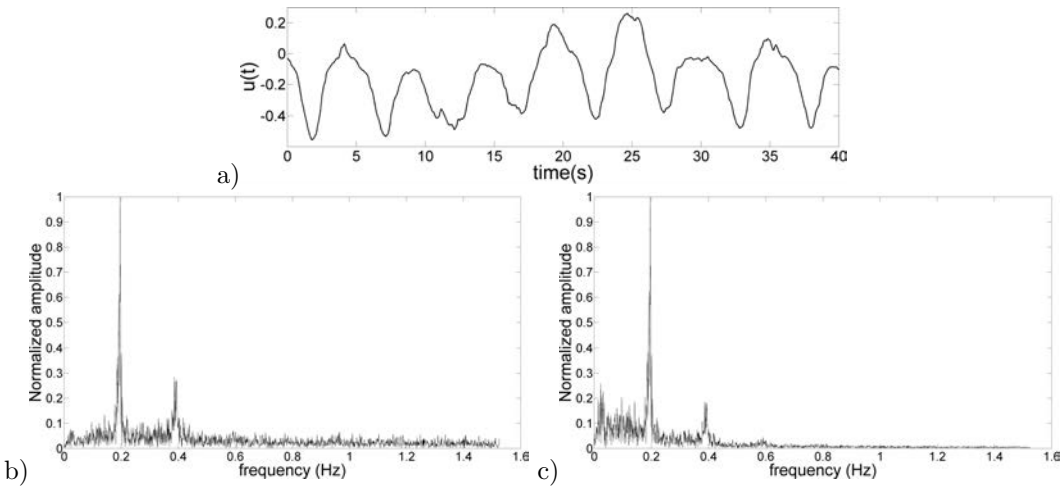

Figure 8.14: a) Control law output $u(t)$ over one minute. b) Normalized frequency spectrum for $s(t)$. c) Normalized frequency spectrum for $u(t)$.

8.5.2 Control results

Figure 8.13 shows a comparison between outputs for the controlled and uncontrolled flow. Comparison was done over 14 minutes (21000 iterations). The results clearly show a reduction in fluctuations for the controlled flow (-35 %). Moreover a reduction in mean value is also observed (-15 %). The mean value reduction is an added benefit of fluctuation reduction. Better performances could be expected when considering the impulse responses. Additional noise sources not accounted for by the upstream sensor are likely to be present in an experimental flow, contributing to degraded performance.
Figure 8.15 shows the mean TKE field for the controlled and uncontrolled flows in the region of interest. The reduction in mean TKE is clear, as is a slight augmentation in recirculation size. Furthermore the effects of control are heterogeneous: while the TKE in the recirculation region seems mainly unaffected, the region of high TKE induced by the obstacle is successfully suppressed.

Figures 8.16 shows the ratio of negative to positive longitudinal velocity (χ) for the perturbed unperturbed (a), perturbed (b) and controlled (b) flows. This is an effective measure measure of recirculation. This result highlights the effect of the control action on recirculation.

Figure 8.14a shows the non-dimensional control output sampled over one minute. One can see that the control signal is one of periodic suction. Figures 8.14b and 8.14c show the frequency spectra for $s(t)$ and $u(t)$. A double peak is present in both spectra for the same frequency. This explains the physical processes involved during control. An incoming vortex is detected as a spike in $s(t)$. The response is a sharp aspiration as shown by figure 8.12. Thus, the control is operating in opposition.

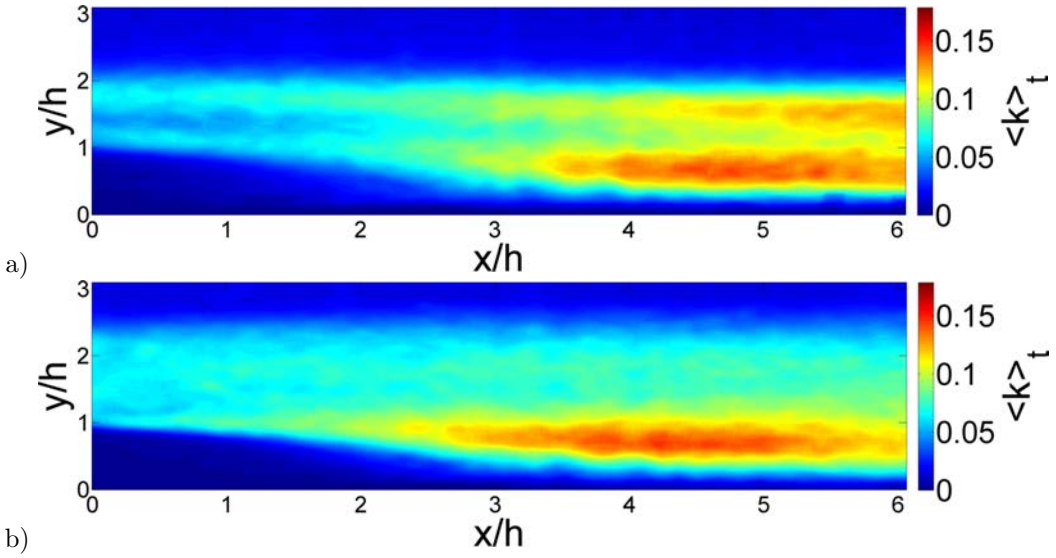

Figure 8.15: Comparison of the time-averaged 2D TKE field obtained for the perturbed, uncontrolled (a) and controlled (b) flows.

8.6 Conclusion

For the first time, an experimental implementation of a feed-forward control algorithm based on a ARMAX model was conducted on a backward-facing step flow. Results show the validity of such an approach. Nevertheless, to ensure successful implementation special care should be given to actuation, in particular to prevent contamination of the upstream sensor. Moreover, this approach is limited to the linear regime of the flow.
Analyzing impulse responses gives valuable insight into the flows controllability as well as the potential for success of the method. While these responses tell us full negation of upstream disturbances is impossible, the computed model was able to reliably predict flow responses and yield a control law able to reduce energy levels and fluctuations. Future work should involve span-wise sensors and actuators thus allowing span-wise heterogeneous disturbances to be controlled as proposed and evaluated numerically by Semeraro et al. (2011).

8.7 Acknowledgments

The authors gratefully acknowledge the support of the DGA (Direction Générale de l'Armement).

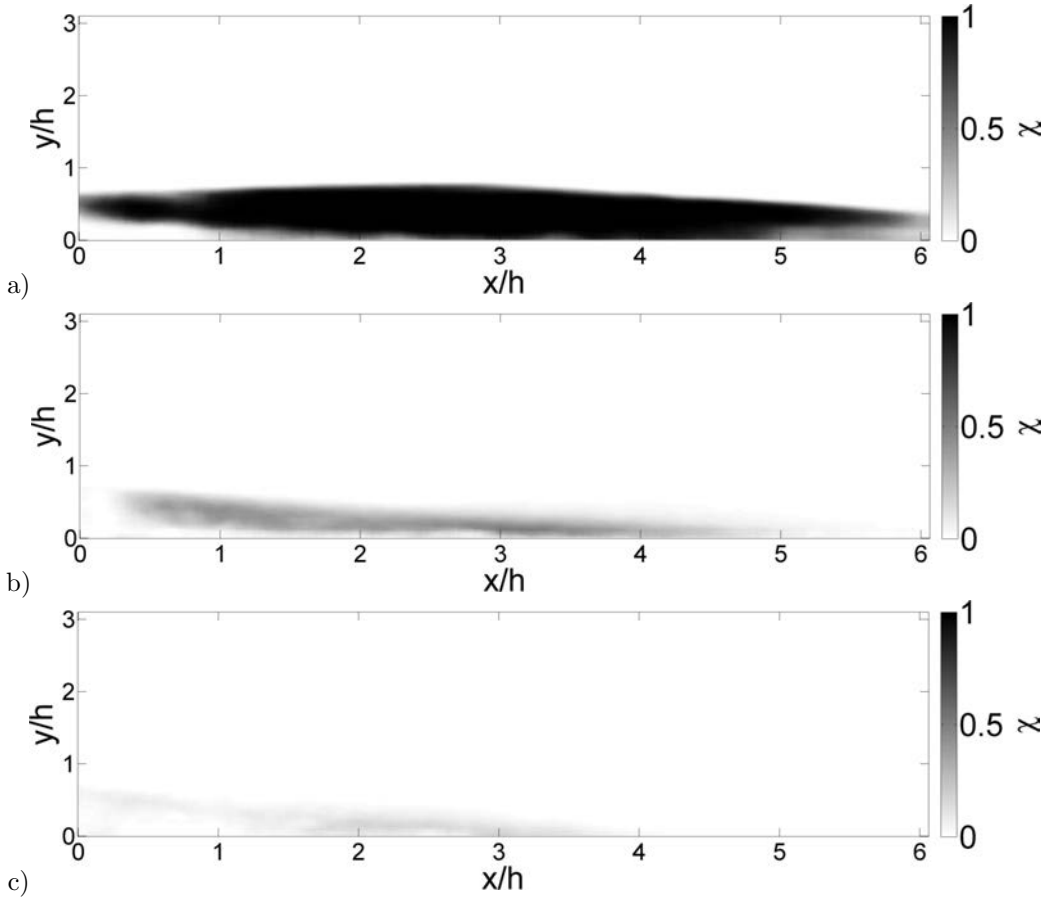

Figure 8.16: Ratio of negative to positive longitudinal velocity χ for the unperturbed (a), perturbed (b) and controlled (c) flows.

Bibliography

J-L. Aider, A. Danet, and M. Lesieur. Large-eddy simulation applied to study the influence of upstream conditions on the time-dependant and averaged characteristics of a backward-facing step flow. *Journal of Turbulence*, 8, 2007.

R. Akervik, J. Hoepffner, U. Ehrenstein, and D.S. Henningson. Optimal growth, model reduction and control in a separated boundary-layer flow using global eigenmodes. *J. Fluid Mech.*, 579:305–314, 2007.

B. F. Armaly, F. Durst, J. C. F. Pereira, and B. Schonung. Experimental and theoretical investigation of backward-facing step flow. *J. Fluid Mech.*, 127:473–496, 1983.

D. Barkley, M.G.M Gomes, and R.D. Anderson. Three-dimensional instability in flow over a backward facing step. *J. Fluid Mech.*, 473:167–190, 2002.

J-F. Beaudoin, O. Cadot, J-L. Aider, and J.E. Wesfreid. Three-dimensional stationary flow over a backwards-facing step. *European Journal of Mechanics.*, 38:147–155, 2004.

R. Becker, M. Garwon, C. Gutknecht, G. Barwolff, and R. King. Robust control of separated shear flows in simulation and experiment. *Journal of Process Control.*, 15:691–700, 2005.

B.A. Belson, O. Semeraro, C.W. Rowley, and D.S. Hennginson. Feedback control of instabilities in the two-dimensional blasius boundary layer: The role of sensors and actuators. *Phys. Fluids.*, 25, 2013.

Guy Le Besnerais and Frederic Champagnat. Dense optical flow by iterative local window registration. In *ICIP (1)*, pages 137–140, 2005.

L. Brandt, D. Sipp, J. Pralits, and O. Marquet. Effect of base flow variation in noise amplifiers: the flat-plate boundary layer. *J. Fluid Mech.*, 687:503–528, 2011.

E.F. Camacho and C. Bordons. *Model predictive control*. Springer, 2013.

F. Champagnat, A. Plyer, G. Le Besnerais, B. Leclaire, S. Davoust, and Y. Le Sant. Fast and accurate piv computation using highly parallel iterative correlation maximization. *Exp. Fluids.*, 50:1169–1182, 2011. ISSN 0723-4864.

M.S. Chong, A.E. Perry, and B.J. Cantwell. A general classification of 3-dimensional flow fields. *Phys. Fluids.*, 2:765–777, 1990.

S. Davoust, L. Jacquin, and B. Leclaire. Dynamics of m = 0 and m = 1 modes and of streamwise vortices in a turbulent axisymmetric mixing layer. *J. Fluid Mech.*, 709:408–444, 2012.

M.O. Efe and H. Ozbay. Proper orthogonal decomposition for reduced order modeling: 2d heat flow. *Proceedings of 2003 IEEE Conference on Control Applications*, 2:1273–1277, 2003.

N. Gautier and J-L. Aider. Real time, high frequency planar flow velocity measurements. *under consideration for publication in Journal of Visualization, avalaible on the arXiv under Real-time planar flow velocity measurements using an optical flow algorithm implemented on GPU*, 2013a.

N. Gautier and J-L. Aider. Control of the flow behind a backwards facing step with visual feedback. *Royal Society Proceedings A.*, 469, 2013b.

N. Gautier and J.L. Aider. Frequency lock closed-loop control of a separated flow using visual feedback. *Submitted to Exp. Fluids., available on the arXiv*, 2013c.

S. J. Sherwin H. M. Blackburn, D. Barkley. Convective instability and transient growth in flow over a backward-facing step. *J. Fluid Mech.*, 603:271–304, 2008. doi: 10.1017/S0022112008001109. URL `http://dx.doi.org/10.1017/S0022112008001109`.

L. Henning and R. King. Robust multivariable closed-loop control of a turbulent backward-facing step flow. *Journal of Aircraft*, 44, 2007.

A. Hervé, D. Sipp, P. Schmid, and M. Samuelides. A physics-based approach to flow control using system identification. *J. Fluid Mech.*, 702:26–58, 2012.

L. Hung, M. Parviz, and K. John. Direct numerical simulation of turbulent flow over a backward-facing step. *J. Fluid Mech.*, 330:349–374, 1997.

L. Ljung. *System Identification : Theory for the User, 2nd ed.* Prentice Hall, 1999.

O. Marquet, D. Sipp, D. Chomaz, and J.M. Jacquin. Amplifier and resonator dynamics of a low-reynolds number recirculation bubble in a global framework. *J. Fluid Mech.*, 605: 429–443, 2008.

and J. Dandois P. Pamart, E. Garnier, and P. Sagaut. Narx modeling and adaptive closed-loop control of a separation by synthetic jet in unsteady rans computations. *5th AIAA Flow Control Conference*, 2010.

Mark Pastoor, Lars Henning, Bernd R. Noack, Rudibert King, and Gilead Tadmor. Feedback shear layer control for bluff body drag reduction. *J. Fluid Mech.*, 608:161–196, 2008.

R. Penrose. A generalized inverse for matrices. *Proc. Camb. Phil. Soc.*, 51:406–413, 1955.

C.W. Rowley and D.R. Williams. Dynamics and control of high-reynolds-number flow over open cavities. *Annual Review of Fluid Mechanics.*, 38:251–276, 2006.

C.W. Rowley, T. Colonius, and R.M. Murray. Model reduction for compressible flows using pod and galerkin project. *Physica D.*, 189:115–129, 2004.

P.J. Schmid and D.S. Henningson. Stability and transition in shear flows. *Applied Mathematical Sciences.*, 142, 2001.

O. Semeraro. *Active control and modal structures in transitional shear flows*. PhD thesis, KTH, 2013.

O. Semeraro, S. Bagheri, L. Brandt, and D.S. Henningson. Transition delay in a boundary layer flow using active control. *J. Fluid Mech.*, 677:63–102, 2011.

D. Sipp, O. Marquet, P. Meliga, and A. Barbagallo. Dynamics and control of global instabilities in open flows: a linearized approach. *Applied. Mech. Review.*, 63, 2010.

J. Zhou, R.J. Adrian, S. Balachandar, and T.M. Kendall. Mechanisms for generating coherent packets of hairpin vortices. *J. Fluid Mech.*, 387:535–396, 1999.

Chapter 9

Closed-loop control of a wall-bounded separation experiment using machine learning

This chapter features the first experimental implementation of machine learning control on a separated flow. The novelty comes from using genetic programming, inspired by evolution and natural selection, to generate a control law able to efficiently achieve a user defined objective. The principle is as follows: control laws are randomly generated making up a generation, they are evaluated with respect to a user-defined cost function, the best performing laws are copied, crossed and mutated to produce a new, better faring generation. This process is iterated until a suitable control law is found. What is suitable is up to the user as there are no strict convergence criteria. The only major downside of this approach is the constraints it places on the experimental setup as it must be operated continuously over several days at fixed operating conditions.
The most important parameter is the cost function. It was chosen such that low recirculation area was rewarded and high actuation cost penalized. Running the experiment 24/7 over a 5 days yielded an effective and novel control law. Traditionally periodic forcing is used to reduce recirculation (see chapter 7) however this control law achieves remarkable results playing on the physics of the recirculation bubble. Although very different from periodic forcing this approach is as effective and naturally adapts to changes in operating conditions (such as a change in free-stream velocity). Furthermore the low frequency nature of this actuation makes it easier to implement. Furthermore this control law could easily be implemented using parietal sensors to compute recirculation length, which we have shown to be equivalent to recirculation area in chapter 5.
It should be noted that running a genetic approach in wind tunnels should prove less cumbersome. Indeed evaluating individuals is quicker as the time scales involved are usually shorter.

9.1 Abstract

A novel, model free, approach to experimental closed-loop flow control is implemented on a separated flow. Feedback control laws are generated using genetic programming where they are optimized using replication, mutation and cross-over of best performing laws to produce a new generation of candidate control laws. This optimization process is applied automatically to a backward-facing step flow at $Re_h = 1350$, controlled by a slotted jet, yielding an effective control law. Convergence criterion are suggested. The law is able to produce effective action even with major changes in the flow state, demonstrating its robustness. The underlying physical mechanisms leveraged by the law are analyzed and discussed. Contrary to traditional periodic forcing of the shear layer, this new control law plays on the physics of the recirculation area downstream the step. While both control actions are fundamentally different they still achieve the same level of effectiveness. Furthermore the new law is also potentially easier and cheaper to implement actuator wise.

9.2 Introduction

Flow control is a rapidly evolving interdisciplinary field comprising many disciplines, like fluid mechanics, technological innovations for sensors and actuators, control theory, optimization and machine learning. Its potential engineering applications have an epic proportion, including aerodynamic of cars, trucks, trains, wind-turbines or gas-turbines, as well as medical equipments or chemical plants, just to name a few. Flow control is employed to reduce aerodynamic drag for cars (Beaudoin and Aider, 2008, Gillieron and Kourta, 2010, Joseph et al., 2013), to find alternative lift-off and take-off configurations for aircraft and or to improve mixing efficiency (M'Closkey et al., 2002).

There have been many successful implementations of passive and active open-loop flow control (Fourrié et al., 2010, Joseph et al., 2012, Gautier and Aider, 2013b). Closed-loop control offers great potential for increased robustness and efficiency and is currently the subject of an increasing ongoing research efforts (Henning and King, 2007, Tadmor et al., 2010, Beaudoin et al., 2006, Pastoor et al., 2008, Brandt et al., 2011, Semeraro et al., 2011, Gautier and Aider, 2013a). In experiments, most closed-loop controls are adaptive (Henning and King, 2007, Beaudoin et al., 2006, Gautier and Aider, 2013a) and based on slowly varying periodic forcing. In-time control remains very challenging because of the non-linear nature of fluid phenomena. Most model-based control designs are based on a (locally) linear reduced-order model and ignore frequency cross-talk. The low-dimensionality of the model is key for robustness and online capability in experiments (Noack et al., 2011, Bergmann and Cordier, 2008, Hervé et al., 2012). Only a few control-oriented reduced-order models address frequency cross-talk (Luchtenburg et al., 2009, Luchtenburg, 2010).

The challenges of model-based control design have led us to search for model-free control laws using machine learning methods such as evolutionary algorithms (Wahde, 2008) or artificial neural networks (Lee et al., 1997). These have been successfully used in many disciplines such as bio-informatics, medicine and computer science (Harik, 1997, Ferreira, 2001, Shah-Hosseini, 2009).

The relevant techniques to achieve such a goal are genetic algorithms (GA), artificial neural networks (ANN) and genetic programming (GP). GAs where first suggested for flow

control by (Rechenberg, 1994). They have been used in fluid mechanics for shape optimization (Toivanen et al., 1999, Gardner and Selig, 2003), to optimize feedback control schemes for wall Turbulence (Morimoto et al., 2002), to find optimal wing configurations in insect flight (Berman and Wang, 2007), to minimize drag on a cylinder in numerical simulations (Milano and Koumoutsakos, 2002a) or to fine tune a control law to minimize drag in a experimental turbulent channel flow (Milano and Koumoutsakos, 2002b). It should be noted that in these examples featuring GA the goal is optimizing tuning parameters. The algorithm is used to search for the best parameters of a given, set control law. As GA can tunes parameters, it can only be employed to optimize given designs of control laws. Model-free control using machine learning methods has been pioneered by Lee et al. (1997) using ANN (Kim, 2003). While ANN can approach solutions by a complex combination (described by the network structure) of sigmoids functions, the performance of such an algorithm depends on the learning scheme implemented. If the classical errors back-propagation learning scheme is implemented, then the search algorithm is gradient based and thus sensitive to local minima. Genetic algorithms can be used to avoid this problem.

The third technique (GP) is used to find a control law optimizing a cost function. As with GA, an exploration of the search space is achieved alongside cost functional minimization. The main difference and advantage compared to GA is that GP is optimizing arbitrary functions, allowing for use in a model-free manner and thus explore a larger search space. When comparing GP to ANN the advantage lies in the output of the GP, which is the expression of the function. This allows the study of the control law and the gain of knowledge on the flow physics.

These algorithms are commonly used in many logistic and pattern recognition tasks. However GP-based control laws are rare in experimental closed-loop flow control. One of the obstacles to application of GP to experimental flow control is that a large number of experiments is required to fulfill the criterion for statistical convergence. Recently, Duriez et al. (2014) used GP to find closed-loop control laws in flow control problems. This approach proved surprisingly effective when applied on complex dynamical systems to closed-loop turbulence control in an experiment (Parezanovic et al., 2014).

The objective of the present study is to use GP to control a separated flow for the first time. The control objective is chosen to be the reduction of recirculation bubble area downstream a backward-facing step (BFS). In Sect. 9.3, the experiment is described. The machine learning approach is presented in Sect. 9.4. The closed-loop control results are discussed and benchmarked against periodic forcing in Sect. 9.5. Sect. 9.6 summarizes the main finding and provides future directions.

9.3 Experimental Setup

9.3.1 Water tunnel

Experiments were carried out in a hydrodynamic channel in which the flow is driven by gravity. The flow is stabilized by divergent and convergent sections separated by honeycombs. The quality of the main stream can be quantified in terms of flow uniformity and turbulence intensity. The standard deviation σ is computed for the highest free stream velocity featured in our experimental set-up. We obtain $\sigma = 5.9 \times 10^{-4}\,\mathrm{m.s^{-1}}$ which corresponds to turbulence

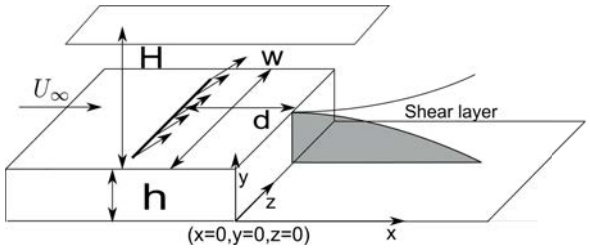

Figure 9.1: Sketch of the BFS geometry, position of the slotted jet and definition of the main parameters.

levels of $\sigma/U_\infty = 2.3 \times 10^{-3}$. For the present experiment the flow velocity is $U_\infty = 7.3 \times 10^{-2}\,\mathrm{m.s}^{-1}$ giving a Reynolds number based on step height $Re_h = U_\infty h/\nu = 1350$. This Reynolds number was chosen because of the limitations of the injection system.

9.3.2 Backward-Facing Step geometry

The BFS is considered a benchmark geometry for the study of separated flows: separation is imposed by a sharp edge creating a strong shear layer susceptible to Kelvin-Helmholtz instability. Upstream perturbations are amplified in the shear layer leading to significant downstream disturbances. This flow has been extensively studied both numerically and experimentally (Armaly et al., 1983, Hung et al., 1997, Beaudoin et al., 2004). The BFS geometry and the main geometric parameters are shown in figure 9.1. BFS height is $h = 1.5 \times 10^{-2}\,\mathrm{m}$. Channel height is $H = 7 \times 10^{-2}\,\mathrm{m}$ for a channel width $w = 15 \times 10^{-2}\,\mathrm{m}$. The vertical expansion ratio is $A_y = \frac{H}{h+H} = 0.82$ and the spanwise aspect ratio is $A_z = \frac{w}{h+H} = 1.76$. The injection slot is located $d/h = 2$ upstream of the step edge. The boundary layer thickness at the step edge is $\delta = 1.3h$.

9.3.3 Sensor: 2D real-time velocity fields computations

The sensor is built on a real-time computation of the vector fields. The velocity fields are computed based on snapshots from the seeded flow. The seeding particles are 20 μm neutrally buoyant polyamid particles. They are illuminated by a laser sheet created by a 2W continuous laser beam operating at $\lambda = 532$ nm. Images of the vertical symmetry plane are recorded using a Basler acA 2000-340km 8bit CMOS camera. Velocity fields are computed in real-time on a Gforce GTX 580 graphics card. The algorithm used to compute the velocity fields is based on a Lukas-Kanade optical flow algorithm called FOLKI developed by (Le Besnerais and Champagnat, 2005). Its offline and online accuracy has been demonstrated and detailed by (Champagnat et al., 2011, Gautier and Aider, 2014a). Furthermore this acquisition method was successfully used in (Gautier and Aider, 2013a, Davoust et al., 2012, Gautier and Aider, 2014b). Velocity fields are computed over an area of $(17.2 \times 4.6) \times 10^{-4}\,\mathrm{m}^2$ which translates into a $9 \times 3\,h^2$ area. The time between two snapshots yielding one velocity field is $\delta t = 10 \times 10^{-3}\,\mathrm{s}$. 42 image pairs are processed per second. Figure 9.2 a) shows a typical example of the instantaneous velocity magnitude field downstream the step for the uncontrolled flow.

Recirculation plays a major role in the BFS flow and is overwhelmingly used for flow assessment as well as an objective for the control of flow separation (Henning and King, 2007, Chun and Sung, 1996). It has also been shown that the recirculation bubble can be linked to drag (although the relationship is far from trivial) (Dahan et al., 2012). We choose to evaluate the state of the flow through the instantaneous recirculation area, computed from instantaneous velocity fields, as our input. It is a 2D extension of the more common recirculation length evaluated using wall measurements. The recirculation area and recirculation length have been shown to behave the same way by Gautier & Aider (Gautier and Aider, 2013a). The normalized instantaneous recirculation area $s(t)$ is computed using equation (9.1),

$$\begin{aligned} s(t) &= \frac{\int H(-u(x,y,t))\ \mathrm{d}x\mathrm{d}y}{A_0} \\ A_0 &= 1/T \int_0^T A_{uncont}(t)\mathrm{d}t, \end{aligned} \tag{9.1}$$

where H is the Heaviside function , $u(x, y, t)$is streamwise velocity and A_0 is the time-averaged recirculation area for the uncontrolled flow.See figure 9.1 for x, y, z directions. The figure 9.2 b) shows the instantaneous recirculation area corresponding to the instantaneous velocity field shown on figure 9.2 b) and computed using equation (9.1).

9.3.4 Actuator

Actuation is provided using upstream injection through a spanwise slotted jet as shown in figure 9.1. The angle between the jet axis and the wall is 45^o. The jet flow is induced using a pressurized water tank. It enters a plenum and goes through a volume of glass beads designed to homogenize the incoming flow. The jet amplitude U_j is controlled by changing tank pressure. Because channel pressure is higher than atmospheric pressure this allows us to provide both blowing and suction. Maximum actuation frequency f_a is about 2Hz. To achieve closed-loop control, the control value $b = U_j/U_{max}$ (U_{max} being the maximum jet velocity) is computed as a function of the sensor value s inside a Labview project. The specific control laws are derived using machine learning control.

9.4 Machine Learning Control

MLC is a generic, model free, approach to control of non-linear systems. Control laws are optimized with regard to a problem specific objective function using genetic programming (Koza et al., 1999). A first generation of control laws candidates $b_i^1(s)$, called individuals ($b_i^1(s)$ is the i^{th} individual of the 1^{st} generation), is randomly generated by combining user defined functions, constants and the sensor value s (see appendix 9.8). Each individual is evaluated yielding a value for the cost function J. A new population b_i^2 is then generated by evolving the first generation. The procedure is iterated until either a known global minimum of J is reached or the evolution is stalled. This process is resumed in figure 9.3.

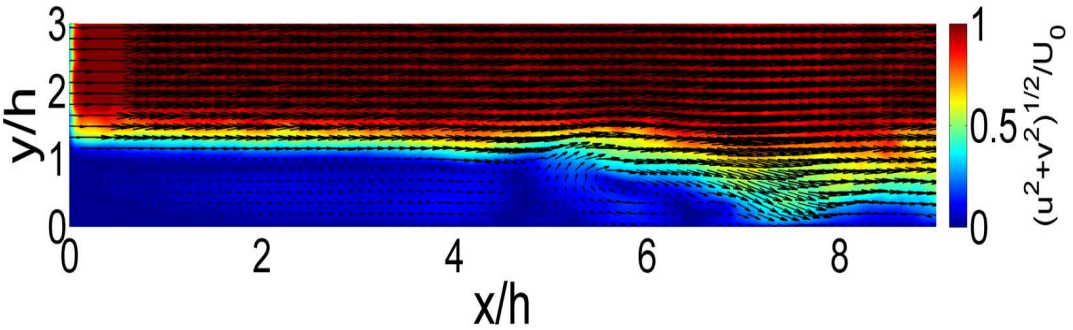

(a)

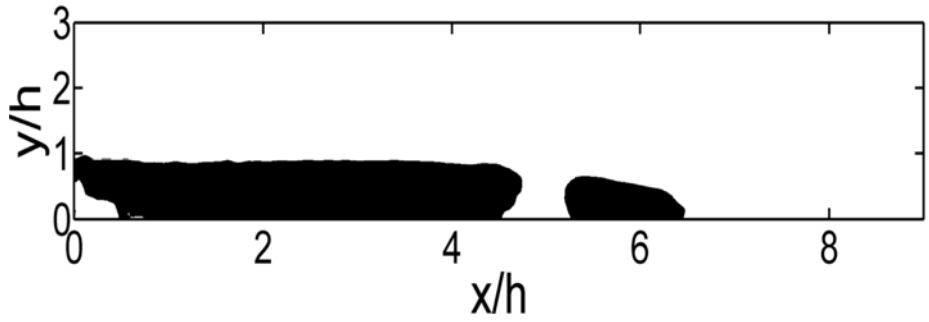

(b)

Figure 9.2: (a) Instantaneous velocity snapshot. Arrows show the instantaneous velocity field while the background color indicates the magnitude of the instantaneous velocity. The edge of the backward facing step is at $x = 0$ and $y = 1$. (b) Corresponding instantaneous mapping of the recirculation area. A black dot indicates a velocity vector with negative streamwise velocity.

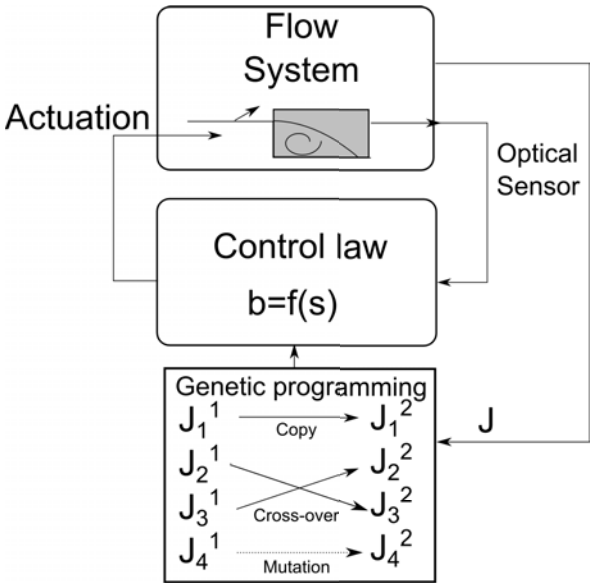

Figure 9.3: Control loop featuring genetic programming. Control laws $b(s)$ are evaluated by the flow system. This is done over several generations of individuals. New generations are generated by replication, cross-over and mutation J_i^n refers to the i^{th} individual of generation n.

9.4.1 Population generation

The number of individuals inside a generation has a strong influence on the process. While a large number of individuals will certainly lengthen the total time of the experiment, it will also ensure a higher diversity which is known to be a key parameter of all evolutive algorithms. In the present study, each generation is made of 500 individuals. This number of individuals is a good compromise between performance and testing time. It has proven to be enough to converge on most single input/single output problem, and is still manageable in terms of total experimental time.

The first individuals $b_i^1, 1 \leq i \leq 500$ are generated as expression trees made of user-defined nodes (see Appendix 9.8). These nodes are functions (sin, cos, exp, log, tanh), basic operations $(+, -, \times, /)$, constants and the sensor input $s(t)$. The root of the expression tree, i.e. the value returned by the function it defines, is the control value. To build the expression tree, a recursive algorithm is used: a first node is chosen, then for each argument this node can accept, new nodes are added randomly until all terminal nodes do not accept any arguments (constants or sensor). The algorithm is made so that the first generation contains expression trees of different depth and density to ensure diversity in the population. Furthermore all individuals are different.

9.4.2 Evaluation

Expression trees can be easily written as LISP expressions. The evaluation is done by translating the LISP expression (for example $(+(\sin s)(/\ 2.343\ s))$) into a control law inside the software responsible for the real-time closed-loop control ($b = \sin(s) + (2.343/s)$). The numerical value used to grade each individual is the cost function J linked to the control problem. In our case the goal is to reduce the recirculation area over the evaluation time with a penalization by the energy used for the actuation:

$$J = \langle s \rangle_T + w \langle |b| \rangle_T^2 > 0, \tag{9.2}$$

where T is the evaluation time ($T = 60\,\mathrm{s}$). The first component, quantifies the state of the flow and integrates the sensor $s(t)$ during the evaluation time. $s(t)$ is normalized by the time-averaged uncontrolled recirculation area $A_0 =< s >_T$. Normalization is important as it allows corrections taking into account variations in the flow conditions (i.e. temperature variations, flow rate drifts). A_0 is recomputed every 250 individuals to compensate for any drifts. The second component, weighted by w, is tied to actuation energy and is normalized by the maximum jet velocity U_{max}. In the following, we choose $w = 3/2$, to strongly penalize high actuation costs. Although the choice for w is arbitrary, the value represents a trade-off between the gain on area reduction and actuation cost. Setting a low (respectively high) value of w means that the performance of the system is much more (respectively less) important than the cost of the control. A balanced value can be derived by evaluating how much one is ready to spend in energy to achieve a given performance. The ratio between performance gain and actuation cost of the most effective open-loop control (see section 9.5.3) suggests a value close to $w = 3/2$. This value was found to strike a good balance between recirculation reduction and actuation cost. It should be noted J could be appended to further constrain the control laws, for example it could be modified to penalize non zero-net mass

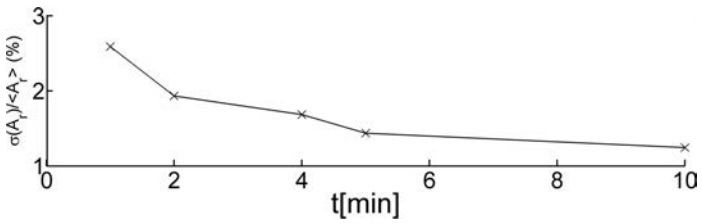

Figure 9.4: Standard deviation of mean recirculation area in percentage over ten evaluations for different evaluation periods.

flux actuation (by penalizing the difference between blowing and suction fluxes) or strong variations in actuation intensity (by penalizing the derivative of the control signal).

The evaluation time is also a key parameter as it will determine how long the whole experiment will last. Figure 9.4 shows that a one minute evaluation is enough to get significant statistics for an evaluation of J good enough to discriminate individuals by performance. As time is spent refilling the jet supply tank, the time between two evaluations varies and can reach two minutes. Approximately 1000 individuals, i.e. two generations, are evaluated over 24 hours.

Because control laws can be constants (e.g. $b = 0.2 + 0.17$) or be outside the actuator's operating range (e.g. $b = \exp(9.87) + (s \times s)$), each control law is pre-evaluated before it is applied to the flow. If it is found to saturate the actuator, it is assigned a very high cost. This step takes a few milliseconds and is done to ensure faster convergence by discarding uninteresting functions. Because of the random nature of the first generation most individuals saturate the actuator.

9.4.3 Breeding of subsequent generations and stop criteria

Once every individual of the current generation has been evaluated, they are sorted by their cost function value J. The five best individuals are evaluated again, the cost values are averaged and the population is sorted again. This re-evaluation procedure is repeated five times to ensure that the value of the best individuals is reliable. The individuals of the next generation are then produced through 3 different processes. Mechanisms are based on a tournament process: 7 individuals are randomly chosen, the individual elected to enter a breeding process is the one with the lowest cost function value. This ensures that the best individuals inside a generation will be used a lot, while less performing individuals still have a chance to be part of the next generation. Individuals selected this way will then be either replicated, mutated or crossed to generate the individuals of the next generation. The probabilities of replication, mutation and crossover are respectively 10%, 20% and 70%. This new generation is then evaluated and the whole process is iterated. The process can stop for two reasons. The first one is when J reaches 0 which in general does not occur. Most of the time, the process is stopped when the best values of J over the population stop improving over several generations.

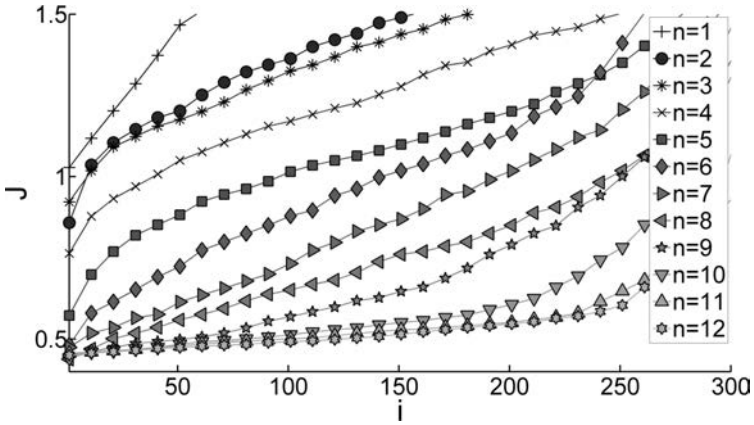

Figure 9.5: Cost functions of the first 300 individuals in all twelve generations.

9.5 Results

Machine learning control asdescribed in § 9.4 has been applied to the backward-facing step plant presented in §9.3. Generation convergence is analyzed in § 9.5.1. The best control law of the final generation is presented in § 9.5.2. This control law is compared with open-loop forcing (§ 9.5.3) and tested for robustness with respect to the Reynolds number in §9.5.4.

9.5.1 Convergence of machine learning control

The evolution of the cost function with increasing number of individuals is shown in Figure 9.5 for all twelve generations. All random control laws of the first generation are seen to be ineffective, i.e. produce only cost functions which are worse than the uncontrolled flow ($J_i^1 > 1$ for all i). Considering the large search space created by the many ways one can arrange the node functions, sensor and constants, it is not surprising that a Monte-Carlo process with 500 individuals is ineffective. A few effective control laws can be seen as soon as the second generation. The slope of the cost function J_i as a function of the index i is improved. This clearly shows that the search algorithm is effective in exploring and exploiting the search-space defined by the cost function. All subsequent generations perform better than the previous one, i.e. $J_i^{n+1} < J_i^n$. After the 9^{th} generation, the performance of the best individuals appear to converge.

The average of the best five control laws $J^n_{[1..5]} := (J_1^n + J_2^n + J_3^n + J_4^n + J_5^n)/5$ is shown in figure 9.6 for each generation. Convergence is reached after the 8^{th} generation. A good termination criterion appears to be to stop the iteration once the average of the cost function for the first 5 individuals no longer improves. In our case the experiment was stopped after no substancial enhancement was obtained in 5 generations from the 8^{th} to 12^{th} generation. As the number of generations increases the first 5 control laws become very similar and averaging over them is a more robust measure than taking just the best one.

The evaluation of the 12 generations translates into a week of continuous automatized experiments. At the end of the week, the training phase is finished and an effective, closed-

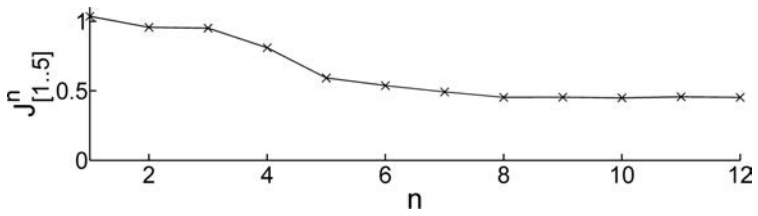

Figure 9.6: Cost functions averaged over the five best individuals for each generation

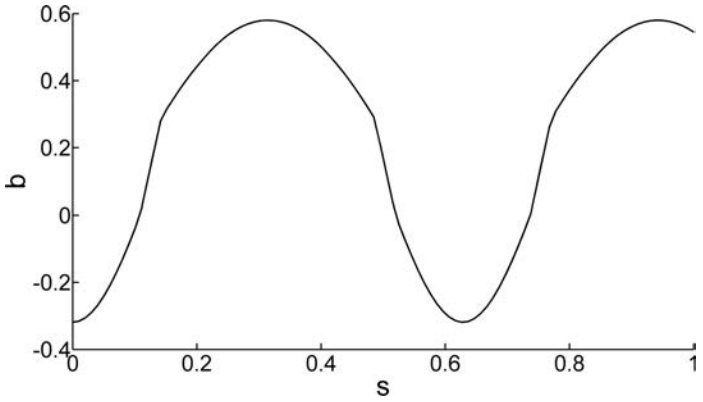

Figure 9.7: Graph of the best control law $b = K(s)$ ((9.3)) obtained after 12 generations.

loop control law has been obtained. While a week of experiment is an investment, it has to be compared with the time needed by other methods to obtain a viable real-time closed-loop control, which usually is accounted in months. This places this approach in the category of control algorithm that can be used to obtain a controller in a comparatively small amount of time.

9.5.2 Analysis of the best control law obtained through genetic programming

The control law $b = K(s)$ has a complex mathematical expression, given in equation (9.3).

$$b = \exp -0.1138 \times \log(\cos(\log(s)) - \sin(\cos(\tanh(\sin(s))))). \tag{9.3}$$

Yet, the graph of the best control law for the final generation has a simple structure as shown on figure 9.7 for $0 \leq s \leq 1$. Indeed, the controlled normalized recirculation area is by definition positive, $s \geq 0$. Experimentally, the instantaneous recirculation area associated with the best law is found to be always smaller than the averaged uncontrolled region resulting in $s \leq 1$. Note that the control law leads to a combination of blowing and suction as a function of s.

The actuation command b has an interesting non-proportional and non-monotonous dependency on s with two similar maxima $b \approx 0.6$ (injection) and two similar minima $b \approx 0.3$

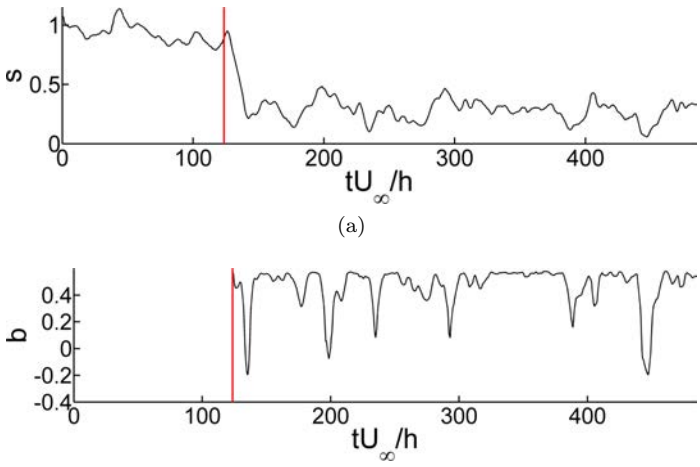

Figure 9.8: (a) System response s to the control law, the vertical line shows when control starts at $t = 120\,\mathrm{s}$. (b) Corresponding actuation b.

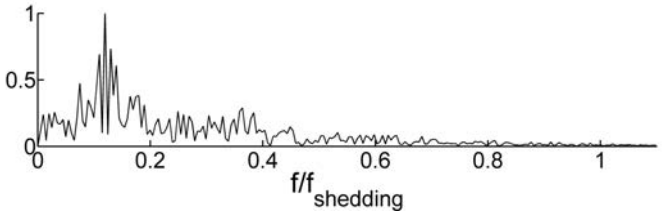

Figure 9.9: Normalized frequency spectrum obtained by Fourier transform of the actuation signal, frequency is normalized by vortex shedding frequency

(suction) which shows that it could not be obtained through a linear process. Near uncontrolled values for the recirculation zone ($s \sim 1$), large jet injection reduces the area. This injection decreases with s until suction sets in at intermediate values ($s \sim 0.73$). In the post-transient regime ($0.12 < s < 0.32$), injection increases with recirculation area. For $s < 0.12$, suction sets in. Most of the time, injection $b \approx 0.5$ occurs. During short periods with low recirculation zones, suction sets in or, at minimum, injection is significantly reduced.

It is interesting to look at the time-series of $s(t)$ (figure 9.8a) and the corresponding actuation amplitude $b(t)$ (figure 9.8b) for the best closed-loop control law. Once the control starts at time $t = 25$ s (vertical red line) the recirculation area is quickly and strongly decreased down to 20 %, corresponding to a 80% reduction on average. For $0 < s < 0.3$, actuation b is roughly an affine function of s (see figure 9.7). The figure 9.8b shows that the actuation is indeed a succession of short period of suction followed by a longer period of blowing ($b \approx 0.45$).

This feedback loop creates oscillations at 0.1 Hz, as observed in figures 9.8a, 9.8b and confirmed by the frequency analysis for the actuation signal shown in figure 9.9. We conjecture

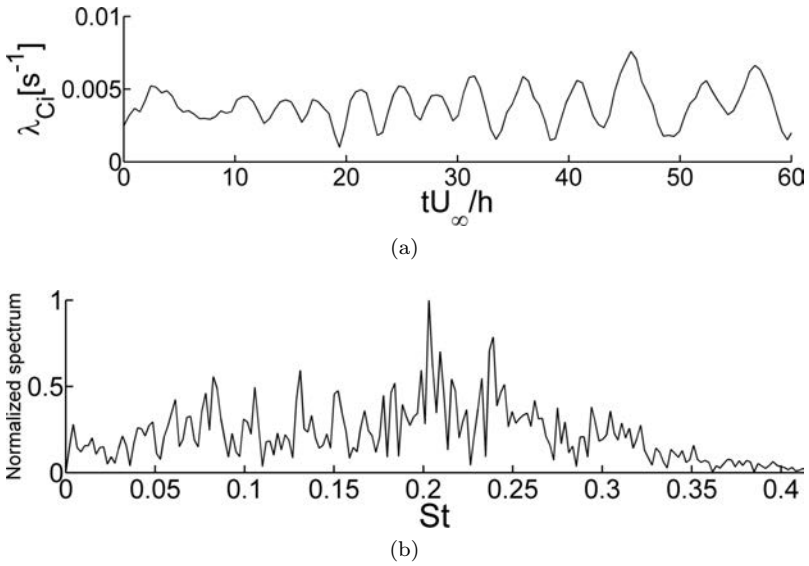

Figure 9.10: $\lambda_{Ci}(t)$ signal over 60 non-dimensionalized time units, uncontrolled flow, (b) Normalized frequency spectrum showing a peak at 0.97 Hz.

that this frequency is the flapping frequency of the recirculation bubble which is typically an order of magnitude lower than the shear layer shedding frequency (Spazzini et al., 2001) (shown in figure 9.10b), as illustrated by figure 9.9.

The 0.1 Hz feedback dynamics is probably triggered by the choice of our input, the instantaneous recirculation area, and the natural flapping frequency. The periodic events of reduced injection or low suction are awarded by the cost function which penalizes the actuation.

It is important to notice that the low frequency nature of this actuation enables "slow" actuators to positively affect high Reynolds number flows. It may remove strong constraints on the actuator in industrial settings which usually deal with high frequency vortex sheddings (typically a few hundreds Hz for full-scale automotive aerodynamics). In addition, it has been shown that recirculation area and recirculation length behave in the same way (Gautier and Aider, 2013a). Wall pressure sensors could be used to evaluate recirculation length in real-time (Henning and King, 2007) which could be used as an input to this new control law, making realistic applications viable .

9.5.3 Comparison to periodic forcing

Pulsing jet injection at the natural shedding frequency is an effective way of reducing recirculation area (Chun and Sung, 1996, Pastoor et al., 2008, Gautier and Aider, 2013b) making it a natural benchmark for this approach. We choose a periodic forcing at the Kelvin-Helmholtz frequency with a duty cycle of 50%, which means the jets are turned on half the time. An effective way of computing the natural shedding frequency is to compute the swirling strength criterion $\lambda_{ci}(s^{-1})$. This criterion was first introduced and subsequently improved by (Chong

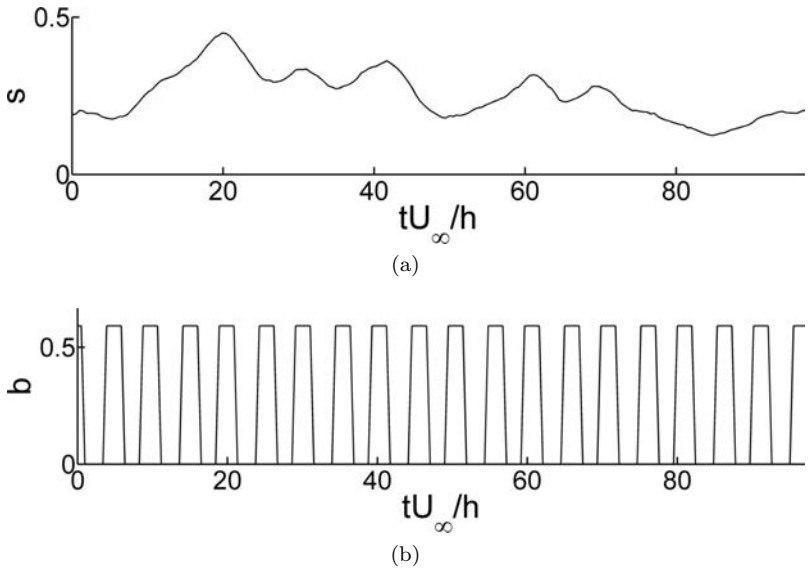

Figure 9.11: (a) System response to periodic forcing over 20 seconds. (b) Corresponding actuation.

et al., 1990, Zhou et al., 1999). It was also recently used as an input in closed-loop flow control experiments (Gautier and Aider, 2013a). For 2D data λ_{Ci} can be computed quickly and efficiently following equation (9.4),

$$\lambda_{Ci} = \frac{1}{2}\sqrt{4\det(\nabla \mathbf{u}) - \mathrm{tr}(\nabla \mathbf{u})^{\mathbf{2}}}, \tag{9.4}$$

when such a quantity is real, else $\lambda_{Ci} = 0$. The shedding frequency is obtained by spatially averaging λ_{Ci} in the vertical direction at $x = 5h$. The sampling frequency is $f_s = 10$Hz. This is equivalent to counting vortices as they pass through an imaginary vertical line at $x = 5h$. Figure 9.10a shows the corresponding scalar over 60 seconds. Figure 9.10b shows the frequency spectrum obtained by Fourier transform. The natural shedding frequency is well defined and close to 1 Hz. This gives us the frequency for periodic forcing.

Figure 9.11a shows the reduction of the recirculation area using periodic forcing (figure 9.11b). Control is effective in reducing the recirculation. The cost function for this control law is $J_{periodic} = 0.423$ which is quite similar to the one found through genetic programming ($J_{genetic} = 0.419$). The MLC law still performs slightly better. Intriguingly, similar performances are achieved but with quite different dynamics and frequencies. The periodic forcing excites the Kelvin-Helmholtz frequencies at 1 Hz while the MLC law exploits the flapping frequency around 0.1 Hz.

Re_h	900	1350	1800
$J_{closed-loop}$	0.33	0.42	0.59
$J_{open-loop}$	0.75	0.42	0.76

Table 9.1: Cost function at different Reynolds numbers.

9.5.4 Robustness

The control law was tested for various Reynolds numbers in order to test its robustness. Table 9.1 shows the resulting cost functions. The cost function does not increase by more than 20% while Reynolds number changes by a factor 2. The cost function for the open-loop forcing is also shown. This open-loop forcing is done at the optimal shedding frequency at $Re_h = 1350$ and is not changed with Reynolds number. Because it is tied to the recirculation area MLC control law adapts to changes in operating conditions, ensuring consistent, reliable performances. Because natural frequency changes with free-stream velocity, the open-loop control shows poor performance at different Reynolds numbers. Performance variations for the MLC law are due to changes in jet to cross-flow momentum ratio. To further improve robustness the control law could be amended in the following way: $b = f(Re_h)K(s)$ where f is a function to be determined. *

9.6 Conclusion

Machine learning control has been used to determine a cost effective control law minimizing recirculation on a backward-facing step flow. During the twelve generations needed to converge towards the control law, the population has evolved toward solutions better fitting the problem, which is translated in lower cost function values. The process is stopped when no amelioration can be foreseen, judging by the statistical values returned by the algorithm. As no convergence can be proven, there is no guarantee this control is optimal. However the nature of the cost function allows to judge the performance of the solution and whether actuation can be rated as effective.

Without deriving a model for the input-output system, the genetic programming approach is able to converge on an efficient and robust control law linking a real-time measure of recirculation area to actuation value. Though the design of the experiment is kept at its simplest, an 80% reduction of the recirculation area has been achieved. Moreover, the control law obtained highlight a mechanism which is not based on the exploitation of the Kelvin-Helmholtz instability as for the open-loop control, but rather on lower frequencies which are likely related with frequencies of the recirculation region.

Robustness can be increased by closed-loop laws. It is demonstrated that the control law designed by genetic programming for a given Reynolds number stays efficient in other operative conditions as compared to open-loop designed control with rapidly deterioring performance. Robustness would be reinforced by integrating a condition change during evaluation, though it would lengthen overall evaluation time.

Genetic programming has proven to be efficient at resolving multi-input/multi-output problems. Thus adding more freedom to the algorithm, by adding control outputs and sensors inputs, will increase the number of mechanisms the control laws can access in order

to reduce the cost function. For instance adding time delays or derivative of the sensor would allow an embedding of the dynamical system and thus allow the control law to access more information on the state of the system.

This novel approach of experimental flow control competes with other approaches in terms of efficiency and robustness. Being model-free and capable of producing virtually any kind of control law (linear, non-linear, with history of sensors and actuators) it can be used in a systematic fashion, with a known time consumption on the plant. This enables the method to be used on flows with a specific geometry which has not been thoroughly investigated, such as a detailed vehicle model or a turbine geometry.

9.7 Acknowledgements

NG and JLA wish to thank the DGA for their support, TD and BN acknowledge funding by the French ANR (Chaire d'Excellence TUCOROM and SEPACODE), MS and MA acknowledge the support of the LINC project (no. 289447) funded by ECs Marie-Curie ITN program (FP7-PEOPLE-2011-ITN).

Bibliography

B.F. Armaly, F. Durst, J.C. Pereira, and B. Schönung. Experimental and theoretical investigation of backward-facing step flow. *J. Fluid Mech.*, 127:473–496, 1983.

J.-F. Beaudoin and J.-L. Aider. Drag and lift reduction of a 3D bluff body using flaps. *Exp. Fluids.*, 44(4):491–501, APR 2008. doi: 10.1007/s00348-007-0392-1.

J-F. Beaudoin, O. Cadot, J-L. Aider, and J.E. Wesfreid. Three-dimensional stationary flow over a backwards-facing step. *Eur. J. Mech. B-Fluid*, 38:147–155, 2004.

J-F. Beaudoin, O. Cadot, J.-L. Aider, and J.E. Wesfreid. Drag reduction of a bluff body using adaptive control methods. *Phys. Fluids.*, 18:085107, 2006.

M. Bergmann and L. Cordier. Optimal control of the cylinder wake in the laminar regime by trust-region methods and pod reduced-order models. *J. Comput. Phys.*, 227:7813–7840, 2008.

G. Berman and Z. Wang. Energy-minimizing kinematics in hovering insect flight. *J. Fluid Mech.*, 582:153–168, 2007.

L. Brandt, D. Sipp, J. Pralits, and O. Marquet. Effect of base flow variation in noise amplifiers: the flat-plate boundary layer. *J. Fluid Mech.*, 687:503–528, 2011.

F. Champagnat, A. Plyer, G. Le Besnerais, B. Leclaire, S. Davoust, and Y. Le Sant. Fast and accurate piv computation using highly parallel iterative correlation maximization. *Exp. Fluids.*, 50:1169–1182, 2011. ISSN 0723-4864.

M.S. Chong, A.E. Perry, and B.J. Cantwell. A general classification of 3-dimensional flow fields. *Phys. Fluids.*, 2:765–777, 1990.

K. B. Chun and H. J. Sung. Control of turbulent separated flow over a backward-facing step by local forcing. *Exp. Fluids.*, 21:417–426, 1996.

J.A. Dahan, A.S. Morgans, and S. Lardeau. Feedback control for form-drag reduction on a bluff body with a blunt trailing edge. *J. Fluid Mech.*, 704:360–387, 2012.

S. Davoust, L. Jacquin, and B. Leclaire. Dynamics of m = 0 and m = 1 modes and of streamwise vortices in a turbulent axisymmetric mixing layer. *J. Fluid Mech.*, 709:408–444, 2012.

T. Duriez, V. Parezanović, J.-C. Laurentie, C. Fourment, J. Delville, J.-P. Bonnet, L. Cordier, B. R. Noack, M. Segond, M. W. Abel, N. Gautier, J.-L. Aider, C. Raibaudo, C. Cuvier, M. Stanislas, and S. Brunton. Closed-loop control of experimental shear layers using machine learning (invited). In *7th AIAA Flow Control Conference*, pages 1–16, Atlanta, Georgia, USA, 2014.

C. Ferreira. Gene expression programming: A new adaptive algorithm for solving problems. *Complex Systems.*, 13:87–129, 2001.

G. Fourrié, L. Keirsulck, L. Labraga, and P. Gillieron. Bluff-body drag reduction using a deflector. *Exp. Fluids.*, 50:385–395, 2010.

B. Gardner and M. Selig. Airfoil design using a genetic algorithm and an inverse method. *41st Aerospace Sciences Meeting and Exhibit*, 2003.

N. Gautier and J-L. Aider. Control of the separated flow downstream a backward-facing step using real-time visual feedback. *P. R. Soc. A*, 469, 2013a.

N. Gautier and J-L. Aider. Effects of pulsed actuation upstream a backward-facing step. *Proceedings GDR2502 Controle Des Decollements.*, 2013b.

N. Gautier and J-L. Aider. Real time, high frequency planar flow velocity measurements. *To be published in Journal of Visualization, avalaible on arXiv under "Real-time planar flow velocity measurements using an optical flow algorithm implemented on GPU"*, 2014a.

N. Gautier and J-L. Aider. Experimental feed-forward control of the backwards-facing step flow. *under consideration for publication at J. Fluid Mech. Preprint available at arXiv*, 2014b.

P. Gillieron and A. Kourta. Aerodynamic drag reduction by vertical splitter plates. *Exp. Fluids.*, 48:1–16, 2010.

G.R. Harik. *Learning gene linkage to efficiently solve problems of bounded difficulty using genetic algorithms*. PhD thesis, University of Michigan, 1997.

L. Henning and R. King. Robust multivariable closed-loop control of a turbulent backward-facing step flow. *J. Aircraft*, 44, 2007.

A. Hervé, D. Sipp, P. Schmid, and M. Samuelides. A physics-based approach to flow control usingsystem identification. *J. Fluid Mech.*, 702:26–58, 2012.

L. Hung, M. Parviz, and K. John. Direct numerical simulation of turbulent flow over a backward-facing step. *J. Fluid Mech.*, 330:349–374, 1997.

P. Joseph, X. Amandolese, and J. L. Aider. Drag reduction on the 25 degrees slant angle ahmed reference body using pulsed jets. *Exp. Fluids.*, 52(5):1169–1185, May 2012.

P. Joseph, X. Amandolese, C. Edouard, and J.-L. Aider. Flow control using mems pulsed micro-jets on the ahmed body. *Exp. Fluids.*, 54(1):1–12, 2013.

J. Kim. Control of turbulent boundary layers. *Phys. Fluids*, 15(5):1093–1105, 2003.

J.R. Koza, F.H. Bennett III, and O. Stiffelman. *Genetic Programming as a Darwinian Invention Machine*, volume 1598 of *Lect. Notes Comput. Sc.* Springer, 1999.

G. Le Besnerais and F. Champagnat. Dense optical flow by iterative local window registration. In *IEEE Image Proc.*, pages 137–140, 2005.

C. Lee, J. Kim, D. Babcock, and R. Goodman. Application of neural networks to turbulence control for drag reduction. *Phys. Fluids*, 9(6):1740–1747, 1997.

D.M. Luchtenburg. *Low-dimensional modelling and control of separated shear flows*. PhD thesis, Berlin Institute of Technology, 2010.

D.M. Luchtenburg, G. Dirk, M. Gunther, B. Noack, K. Rudibert, and T. Gilead. A generalized mean-field model of the natural and high-frequency actuated flow around a high-lift configuration. *J. Fluid Mech.*, 623:283–316, 2009. doi: 10.1017/S0022112008004965. URL `http://dx.doi.org/10.1017/S0022112008004965`.

R.T. M'Closkey, J.M. King, L. Cortelezzi, and A.R. Karagozian. The actively controlled jet in cross-flow. *J. Fluid Mech.*, 452:325–335, 2002.

M. Milano and P. Koumoutsakos. A clustering genetic algorithm for cylinder drag optimization. *J. Comput. Phys.*, 175:79–107, 2002a.

M. Milano and P. Koumoutsakos. A clustering genetic algorithm for cylinder drag optimization. *Proc. 3rd Symp. Smart Control of Turbulence, Tokyo*, pages 107–113, 2002b.

Kenichi Morimoto, Kaoru Iwamoto, Yuji Suzuki, and Nobuhide Kasagi. Genetic algorithm-based optimization of feedback control scheme for wall turbulence. In *Proc. 3rd Symp. Smart Control of Turbulence*, pages 107–113, 2002.

B. R. Noack, M. Morzyński, and G. Tadmor. *Reduced-Order Modelling for Flow Control*. Number 528 in CISM Courses and Lectures. Springer-Verlag, Vienna, 2011.

V. Parezanovic, J.-C. Laurentie, T. Duriez, C. Fourment, J. Delville, J.-P. Bonnet, L. Cordier, B. R. Noack, M. Segond, M. Abel, T. Shaqarin, and S. L. Brunton. Mixing layer manipulation experiment – from periodic forcing to machine learning closed-loop control. *Flow Turbul. Combust.*, In press, 2014.

M. Pastoor, L. Henning, B.R. Noack, R. King, and G. Tadmor. Feedback shear layer control for bluff body drag reduction. *J. Fluid Mech.*, 608:161–196, 2008.

I. Rechenberg. Evolution strategy. *Frommann-Holzboog, Stuttgart*, 1994.

O. Semeraro, S. Bagheri, L. Brandt, and D.S. Henningson. Transition delay in a boundary layer flow using active control. *J. Fluid Mech.*, 677:63–102, 2011.

H. Shah-Hosseini. The intelligent water drops algorithm: a nature-inspired swarm-based optimization algorithm. *Int. J. Bio-inspired Comp.*, 1, 2009.

P.G. Spazzini, G. Luso, M. Onorato, N. Zurlo, and G.M. Di Cicca. Unsteady behavior of a back-facing flow. *Exp. Fluids.*, 30:551–561, 2001.

G. Tadmor, O. Lehmann, B. R. Noack, L. Cordier, J. Delville, J.-P. Bonnet, and M. Morzyński. Reduced order models for closed-loop wake control. *Philos. T. Roy. Soc. A*, 369(1940):1513–1524, 2010.

Raino AE Mäkinen Jari Toivanen, Jacques Périaux, and France Cloud Cedex. Multidisciplinary shape optimization in aerodynamics and electromagnetics using genetic algorithms. *Int. J. Numer. Meth. Fluids*, 30:149–159, 1999.

M. Wahde. *Biologically Inspired Optimization Methods: An Introduction*. WIT Press, 2008.

J. Zhou, R.J. Adrian, S. Balachandar, and T.M. Kendall. Mechanisms for generating coherent packets of hairpin vortices. *J. Fluid Mech.*, 387:535–396, 1999.

9.8 Appendix

In this appendix we provide further explanations about how control laws are translated from expression trees (§ 9.8.1) and how the mutation and crossover operations are performed (§ 9.8.2).

9.8.1 Control laws and expression trees.

An expression-tree can be viewed in a graphical way as a tree-like representation of the function under consideration as in figure 9.12 with nodes (round shapes) representing user-defined functions and leaves (square shapes) representing the constants and inputs of the function. The root of the tree (the top node) is the function output. This tree can also be described by a LISP expression. A LISP expression is easily generated and manipulated from a computational point of view. For instance the function $b(s) = \exp(-2s + sin(3.56 * s))$ which is represented by the tree in figure 9.12 is represented by the LISP expression $(\exp(+(* - 2s)(\sin(*3.56s)))$. The fact that the operator comes first allows to generate, evaluate and manipulate the individual with recursive functions.

9.8.2 Genetic programming operations on expression trees.

The figure 9.13 illustrates how the operations of mutation and crossover are performed.

The mutation operations (left) are performed by selecting a node, erasing the node and its subtree and growing a new subtree randomly. Part of the information contained in the individual is kept while new information is allowed to enter the population. The mutation operation increases the diversity and is responsible for exploring the search space with larger steps. The crossover operation (right) consists in selecting one node in each of the two individuals under consideration. The nodes and their subtrees are then exchanged. No new content is brought in but combinations of operations from good individuals (they both won a 7 contestants tournament) are tested together. The crossover is responsible for exploring the search space around individuals that are performing correctly. By adjusting the crossover and mutation probabilities, it is possible to adjust the genetic programming way of converging. A high rate of mutation will explore more of the search space while a high rate of crossover will converge faster around detected minima, whether global or local.

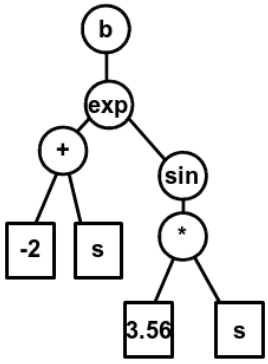

Figure 9.12: A typical expression tree.

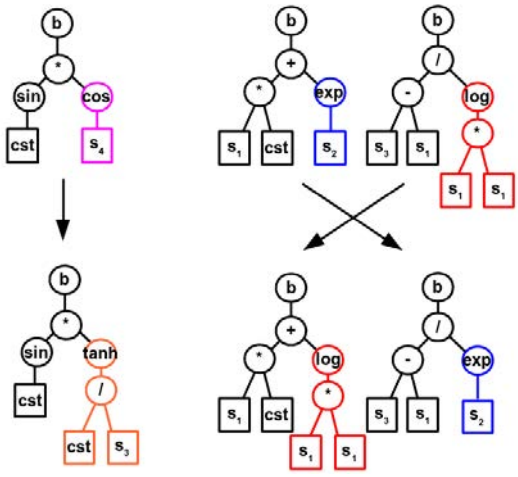

Figure 9.13: Left: a possible mutation of an individual. Right: a possible crossover between two individuals

Chapter 10

Conclusions & Perspectives

10.1 Conclusion

A method for real-time high frequency computations of experimental flow velocity fields is devised and implemented. It presents significant advantages in terms of flow measurements, with the potential to greatly accelerate parametric studies, allow on the fly tuning and prototype control algorithms.
This approach was leveraged for the purposes on controlling the separated flow past a backward-facing step in a hydrodynamic channel. The viability of closed-loop control using optical sensors was demonstrated through PID and gradient descent recirculation area control. Subsequently a parametric study was conducted to better qualify actuation. Optimal injection parameters were determined enabling more sophisticated control.
A novel approach dubbed frequency lock control was successfully implemented. Image processing was used to determine vortex shedding frequency, thus the shear layer could be excited in an optimal manner whatever the operating conditions greatly reducing recirculation. In addition the applicability of model-based and machine learning control paradigms was investigated. An ARMAX reduced order model for a low Reynolds number perturbed flow was obtained using empirical data. Using this model a control action was devised able to significantly reduced the effects of incoming perturbations. Machine learning control yielded an original robust feedback control law able reduce recirculation behind a step while operating at very low frequencies, drastically lowering engineering constraints on the actuator, making it attractive for real world applications.
These control schemes are general and can be extended to a wide range of situations. Optical sensors applied to flow control provide a wealth of information, determining what is relevant is an ongoing effort. The work featured here has barely scratched the surface and much remains to be done ! However the ease with which control algorithms can be implemented using these methods bodes well for the future of flow control.

10.2 Perspectives and considerations

Real-time velocimetry can and should be improved ! It would speed-up progress in fluid mechanics, allowing experimentalists to perform quicker, better targeted studies where results are streamed instantly to the observer without the burdensome bother of lengthy processing. If greater precision is required, real-time method can be used to determine optimal operating conditions paving the way for more slower, more precise algorithms.

10.2.1 Application to drag measurements

Bi-dimensional velocity fields can be used to estimate the drag experienced by a body. An experimental demonstration of this approach can be found in Ger (2000), where momentum balance is used to estimate drag. Unfortunately no comparison is made to direct, more reliable means of drag determination such as weight beams, strain gauges or piezo-electric sensors. In Noca et al. (1997, 1999) several methods for drag determination from velocity fields are detailed and thoroughly investigated. Again however no comparison can be made to data obtained through non-visual means. In the experimental study by Granta et al. (2005) velocity fields are used to compute and compare drag and lift for two separate airfoils.
It would be interesting to apply these methods on an experimental setup featuring both direct drag measurements and real-time velocity field computations. In some cases it might be possible to effect real-time optical drag estimations. The applications are boundless : shape optimizations, better costs functions for flow control, more relevant parametric studies etc...

10.2.2 Real-time stereoscopic velocity field computations

Conceptually there is but a small step between real-time computation of two and three component two-dimensional velocity fields. In practice however the hardware constraints are stringent. To effect real-time computations of stereoscopic fields the setup must be doubled: two cameras and two acquisition boards. Luckily it is simpler to use a single GPU to limit memory transfers. Such a setup would be capable of producing stereoscopic velocity fields at high rates in real-time.

10.2.3 Real-time computation of three-dimensional velocity fields

The Grail of flow velocimetry. This could be achieved by using a real-time stereoscopic setup and a moving laser plane. Another way of going about it is leveraging the computing power of the GPU to speed up existing 3D PTV algorithms, such as the one used in appendix A. Alternatively work is ongoing on novel GPU algorithms for 3D PIV (Cheminet et al. (2014)). A combination of GPU processing and high speed smart camera pre-processing such as featured in Kreizer et al. (2010) could be very effective, with the added benefit of lowering constraints on camera to computer transfer bandwidth.
Such a method could be used, among other things for reliable drag measurements in three-dimensional flows. Completely determining the entire flow state would allow for better control design and validation, leading to increased performance.

Bibliography

Drag reduction of motor vehicles by active flow control using the coanda effect. *Exp. in Fluids*, 28:74–85, 2000.

A. Cheminet, B. Leclaire, F. Champagnat, A. Plyer, R. Yegavian, and G. Le Besnerais. Accuracy assessment of a lucas-kanade based correlation method for 3d piv. *17th International Symposium on Applications of Laser Techniques to Fluid Mechanics Lisbon, Portugal, 07-10 July, 2014*, 2014.

I. Granta, G. McCutcheona, A.H. McColgana, and D. Hurstb. Optical-velocimetry, wake measurements of lift and induced drag on a wing. *Optics and Lasers in Engineering*, 44: 282–303, 2005.

M. Kreizer, D. Ratner, and A. Liberzon. Real-time image processing for particle tracking velocimetry. *Exp. Fluids*, 48:105–110, 2010.

F. Noca, D. Shiels, and D. Jeon. Measuring instantaneous fluid dynamic forces on bodies, using only velocity fields and their derivatives. *J. Fluids Struc*, 89:49–60, 1997.

F. Noca, D. Shiels, and D. Jeon. A comparison of methods for evaluating time-dependant fluid dynamic forces on bodies, using only velocity fields and their derivatives. *J. Fluids Struc*, 11:345–350, 1999.

Appendix A

Experimental study of counter-rotating vortex pair trajectories induced by a round jet in cross-flow at low velocity ratios

T. CAMBONIE, N. GAUTIER, J.-L. AIDER
Published online 28 February 2013

A.1 Abstract

Circular flush Jets In Cross-Flow were experimentally studied in a water tunnel using Volumetric Particle Tracking Velocimetry, for a range of jet to cross-flow velocity ratios, r, from 0.5 to 3, jet exit diameters d from 0.8 cm to 1 cm and cross-flow boundary layer thickness δ from 1 to 2.5 cm. The analysis of the 3D mean velocity fields allows for the definition, computation and study of Counter-rotating Vortex Pair trajectories. The influences of r, d and δ were investigated. A new scaling based on momentum ratio r_m taking into account jet and cross-flow momentum distributions is introduced based on the analysis of jet trajectories published in the literature. Using a rigorous scaling quality factor Q to quantify how well a given scaling successfully collapses trajectories, we show that the proposed scaling also improves the collapse of CVP trajectories, leading to a final scaling law for these trajectories.

A.2 Introduction

Jets In Cross-Flows (JICF) are complex three-dimensional flows which can be found in many engineering applications such as film cooling of turbines and combustors or the control of

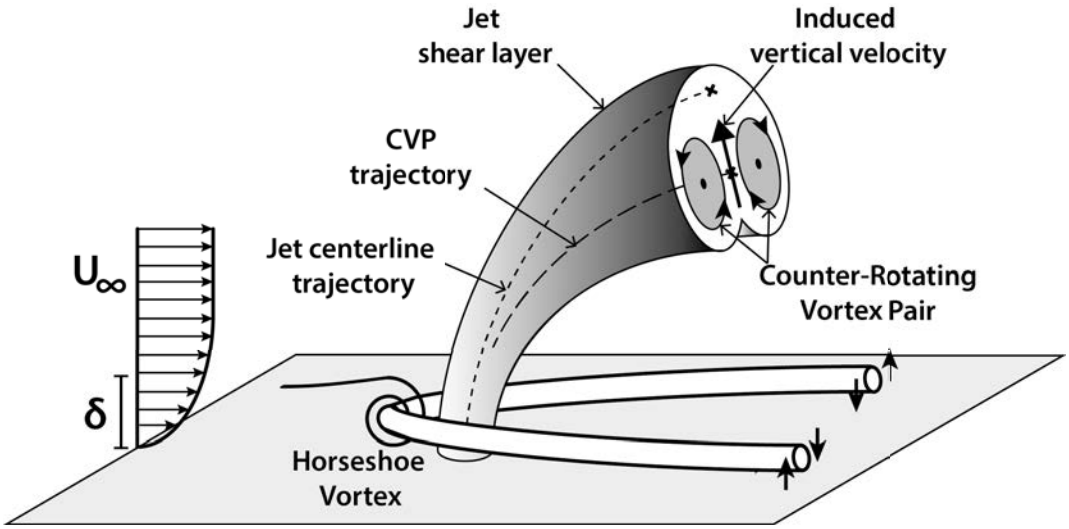

Figure A.1: Sketch of jet in cross-flow: the CVP and the Horseshoe vortex are the main swirling structures observed in the mean velocity field.

separated flows over airfoils and ground vehicles (Margarson (1993), Godard and Stanislas (2006), Joseph et al. (2012)). The control and understanding of JICF's is of great industrial interest. Its complexity also makes it a great challenge for academic research. Thus, it has been the subject of many experimental, numerical and theoretical studies over the past fifty years which are well summarized in the recent review by Karagozian (2010).

When studying a JICF, many parameters can be considered, such as the Reynolds numbers of both jet and cross-flow, the diameter of the jet or the velocity ratio. The latter is considered as the key parameter and is defined as $r = \sqrt{\rho_j \overline{V_j}^2 / \rho_\infty U_\infty^2}$ where ρ_j,V_j are the jet density and mean exit velocity and ρ_∞, U_∞ are the free stream density and velocity. When jet and free stream fluid densities are equal, the momentum ratio becomes $r = \overline{V_j}/U_\infty$.

The main feature of the mean flow observed in previous studies is the counter-rotating vortex pair (CVP), sketched on Fig. A.1. CVP are, to our knowledge, always present in time-averaged velocity fields. Moreover, the CVP is the only structure remaining far from the injection site, sometimes persisting as far as a thousand jet diameters as shown by Baines and Keffer (1963). The CVP has been investigated in detail by Chassaing et al. (1974), Blanchard et al. (1999), Cortelezzi and Karagozian (2001) and Marzouk and Ghoniem (2007). Characterization of its location through the study of its trajectory is therefore of great interest.

We consider low velocity ratios ($r < 3$). Most previous studies focused on higher velocity ratios ($r > 2 - 3$). Low velocity ratios JICF's were investigated by Camussi et al. (2002) and Gopalan et al. (2004). A significant difference between high and low velocity ratios is the interaction with the boundary layer: at low r the jet interacts with the boundary layer leading to a profound modification of the flow structure. Transition between globally unstable and convectively unstable flow has been shown to exist at $r = 3$ by Megerian et al.

(2007). A transition at very low velocity ratios ($r = 0.3$) has been observed by Cambonie and Aider (2012). It is a transition from a *blown* jet topology to a *classical* jet topology. These transitions could impact the CVP. Our range of velocity ratios is $0.5 < r < 3$, above the transition from blown jet to classical jet.
To our knowledge there are no parametric studies focusing on CVP trajectory, although they are mentioned as vortex curves and studied by Fearn and Weston (1974) and Karagozian (1986). The objective of this paper is to define the CVP trajectories in such a way that it can be computed for any velocity ratio and to propose a scaling for these trajectories which takes into account jet and boundary layer momentum distributions, cross-flow boundary layer thickness and jet diameter for low velocity ratios.

A.3 Experimental setup

Water tunnel, jet supply system and geometries

Experiments were conducted in a hydrodynamic channel in which the flow is driven by gravity. The walls are made of Altuglas for easy optical access from any direction. Upstream of the test section the flow is stabilized by divergent and convergent sections separated by honeycombs. The test section is 80 cm long with a rectangular cross section 15 cm wide and 20 cm high as described in Fig. A.2.
The mean free stream velocity U_∞ ranges between 0.9 to 8.37 $cm.s^{-1}$ corresponding to $Re_\infty = \frac{U_\infty d}{\nu}$ ranging between 220 and 660. The quality of the main stream can be quantified in terms of flow uniformity and turbulence intensity. The spatial σ_s and temporal σ_t standard deviations are computed using a sample of 600 velocity fields. The values are, for the highest free stream velocity featured in our data, $\sigma_s = 0.038$ $cm.s^{-1}$ and $\sigma_t = 0.059$ $cm.s^{-1}$ which corresponds to turbulence levels $\frac{\sigma_s}{U_\infty} = 0.15$ % and $\frac{\sigma_t}{U_\infty} = 0.23$ %, respectively.
A custom made plate with a specific leading-edge profile is used to start the cross-flow boundary layer. The boundary layer over the plate is laminar and stationary according to $Re_x = \frac{U_\infty x}{\nu} < 2100$, where x is the distance to the leading edge of the plate, for the highest free stream velocity case, which is considerably less than the critical value for this profile. The boundary layer characteristics were investigated using 600 instantaneous 3D velocity fields without a jet present for all cross-flow velocities. The average field allows us to compute the boundary layer velocity profiles. The boundary layer thickness δ varies from 2.5 cm to 1 cm for increasing cross-flow velocity.
These unperturbed fields were used to compute cross flow velocity by averaging longitudinal velocity in the volume field, excluding the boundary layer.

The jet supply system was custom made. Water enters a plenum and goes through a volume of glass beads designed to homogenize the incoming flow. The flow then goes through a cylindrical nozzle which exits flush into the cross-flow. In the following, we focus on nozzles with different diameters d and different injection lengths l_n (Fig. A.3, and table A.1). The jet axis is normal to the flow. The mean vertical jet velocity $\overline{V_j}$ ranges between 1.9 and 8 $cm.s^{-1}$, leading to velocity ratios $r = \overline{V_j}/U_\infty$ ranging between 0.5 to 3. The dimensions of the jet nozzle and flow characteristics for the 22 configurations presented in this study are summarized in table A.1.

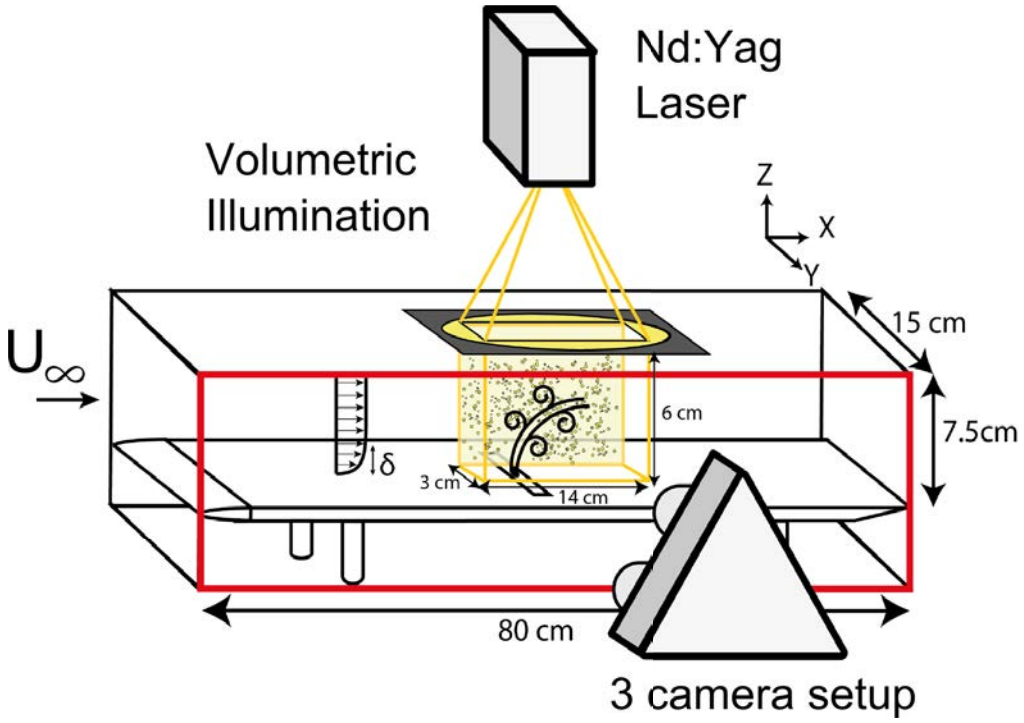

Figure A.2: Definition of the experimental test section. The flow goes from left to right and develops over a raised plate with NACA leading edge. The measurement volume is lit through the upper plate. The three cameras of the V3V system are tracking particles through the side-wall of the channel. The jet nozzle is located 42*cm* downstream of the leading edge.

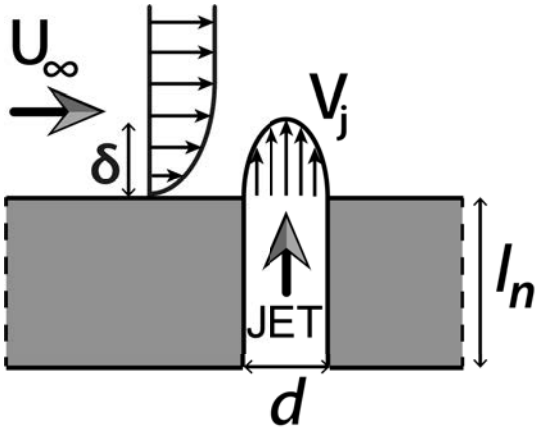

Figure A.3: 2D sketch of the injection site with definitions of the main geometric and physical parameters.

Configuration Number	1	2	3	4	5	6	7	8	9	10	11
$d(cm)$	0.8	0.8	0.8	0.8	0.8	0.8	0.8	0.8	0.8	1	1
$l_n(cm)$	1	1	1	1	1	1	1	1	1	1	1
$U_\infty(cm.s^{-1})$	5.58	4.13	2.66	1.87	6.53	6.51	6.54	6.39	4.01	2.57	1.70
$\overline{V_j}(cm.s^{-1})$	3.04	3.04	3.04	3.04	3.31	5.40	7.00	7.95	6.25	3.87	2.85
δ/d	1.83	1.96	2.31	2.7	1.78	1.78	1.78	1.78	1.59	1.87	2.25
Re_∞	450	330	210	150	520	520	520	510	400	260	170
r	0.54	0.74	1.14	1.62	0.51	0.83	1.07	1.24	1.56	1.51	1.67
r_m	0.75	1.01	1.58	2.23	0.70	1.13	1.45	1.68	2.11	2.105	2.29
Markers	-●	−×	−•	−+	-▼	-▲	−−	· · ·	− · −	–	-◆

Configuration Number	12	13	14	15	16	17	18	19	20	21	22
$d(cm)$	1	1	1	1	1	1	1	1	1	1	1
$l_n(cm)$	1	1	0.5	0.5	0.5	2	2	2	3	3	3
$U_\infty(cm.s^{-1})$	1.23	1.07	6.58	3.20	2.06	6.55	3.24	2.09	6.55	3.25	2.17
$\overline{V_j}(cm.s^{-1})$	2.02	1.71	6.30	6.30	6.30	6.30	6.30	6.30	6.30	6.30	6.30
δ/d	2.59	2.72	1.41	1.71	2.06	1.42	1.70	2.05	1.42	1.70	2.02
Re_∞	120	110	660	320	210	650	320	210	660	330	220
r	1.64	1.59	0.96	1.97	3.05	0.96	1.94	3.01	0.96	1.94	2.9
r_m	2.27	2.20	1.29	2.65	4.10	1.32	2.66	4.12	1.32	2.67	4.00
Markers	-●	−×	−•	−+	-▼	-▲	−−	· · ·	− · −	–	-◆

Table A.1: The 22 configurations are defined by a set of eight parameters: jet diameter, injection length, free stream velocity, jet velocity, boundary layer thickness, Reynolds number and momentum ratios. The markers associated to each configuration, and used in the following figures, are also defined.

3D Particle Tracking Velocimetry measurements

To analyze the mean-flow characteristics of the JICF, we use volumetric particle tracking velocimetry (3DPTV). The method was pioneered by Willert and Gharib (1992) and further developed by Pereira and Gharib (2002). The set-up was designed and the physical parameters were chosen to optimize the quality of the instantaneous velocity fields, using the methodology of Cambonie and Aider (2013). We used $50\mu m$ polyamide particles (PSP) for seeding, with a concentration of 5.10^{-2} particles per pixel. The flow is illuminated through the upper wall and the particles are tracked using three cameras facing the side wall (Fig. A.2). The three double-frame cameras are 4 MP with a 12 bit output. Volumetric illumination is generated using a 200 mJ pulsed YaG laser and two perpendicular cylindrical lenses. Synchronization is ensured by a TSI synchronizer. The measurement volume (l_x, l_y, l_z) is $14 \times 6 \times 3\ cm^3$. The spatial resolution is one velocity vector per millimeter for both the instantaneous and mean three-components velocity field . This resolution might not always allow for the detection of the smallest structures in the flow, especially for higher velocity ratios. Nevertheless the jet diameter has been chosen to ensure a good spatial resolution of the main vortices ($8\ mm < d < 10\ mm$). The characteristic width of a vortex is the an order of magnitude higher than the spatial resolution allowing us to clearly detect the CVP. The acquisition frequency is $7.5Hz$. 1000 instantaneous velocity fields are recorded for each configuration to ensure statistical convergence of the mean velocity field.

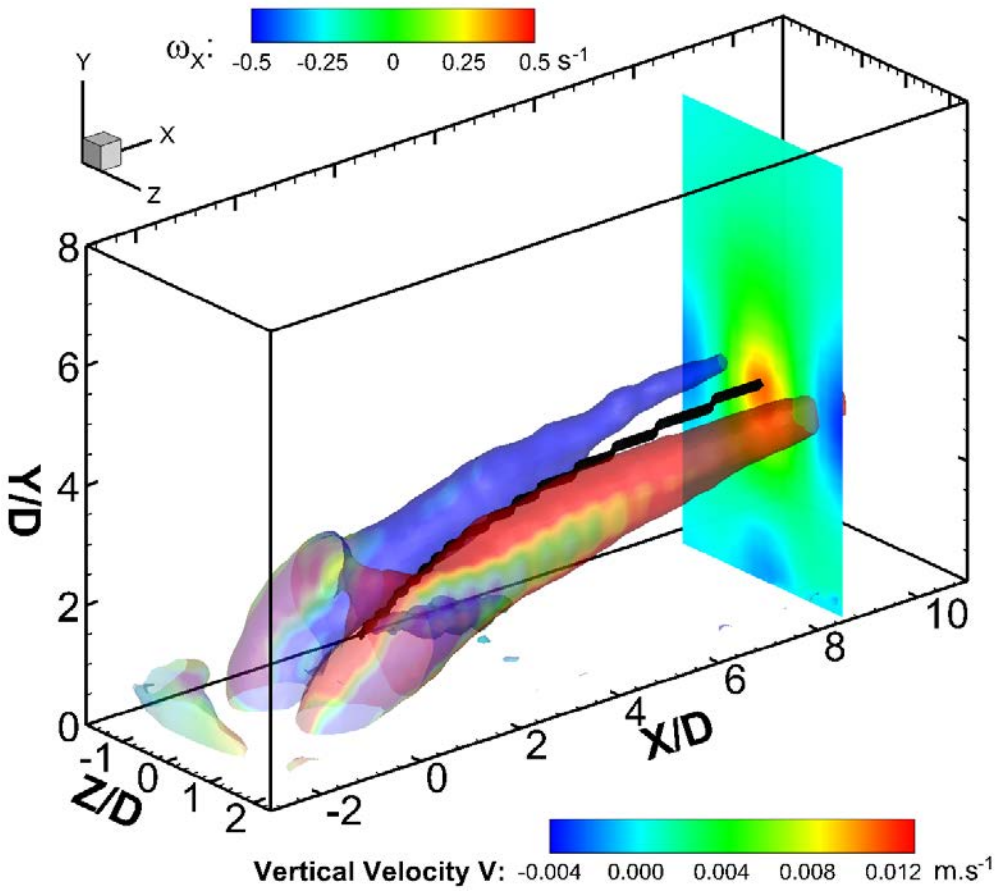

Figure A.4: Mean iso-surface of λ_{ci} colored by longitudinal vorticity for configuration 7 (velocity ratio $r = 1.07$, together with a contour of vertical velocity at $X = 10d$. The computed CVP trajectory is shown as a thick black line.

A.4 Trajectory computation

Visualization of the CVP

To analyze the complex three-dimensional flow, we use the swirling strength criterion λ_{ci}. It was first introduced by Chong et al. (1990) who analyzed the velocity gradient tensor and proposed that the vortex core be defined as a region where ∇u has complex eigenvalues. It was later improved and used for the identification of vortices in three-dimensional flows by Zhou et al. (1999). This criterion allows for an effective detection of vortices even in the presence of shear. It is calculated for the entire 3D velocity fields. Fig. A.4 shows a typical example of the main vortical structures present in the mean velocity field using isosurfaces of $1.5 \cdot \sigma(\lambda_{Ci})$ (where σ is the spatial standard deviation) colored by the longitudinal vorticity.

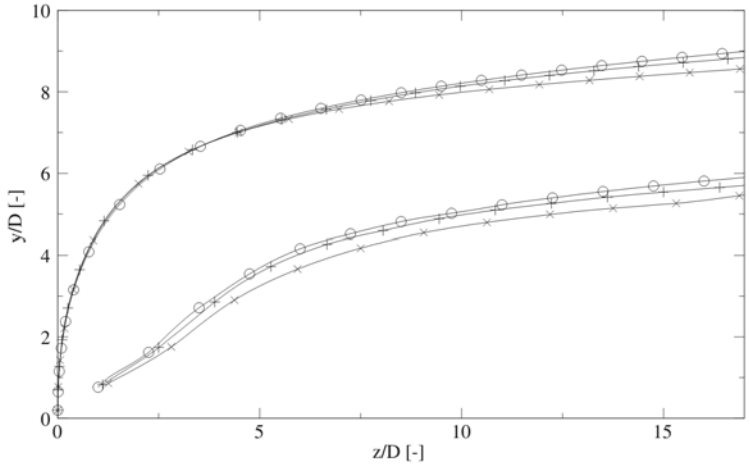

Figure A.5: Jet centerline trajectories (higher curves), CVP trajectories (lower curves) computed in the numerical simulations of Salewski et al. (2007). To the different trajectories correspond different number of cells for the numerical simulations: 3.8 million cells (-●), 3.2 million cells (+) and 2.4 million cells (×).

One can clearly see the two counter-rotating vortices growing downstream of the injection site. The vertical velocity field is also visualized in the $X/d = 10$ cross-section showing the strong outflow region induced by the CVP. The CVP creates a well-defined outflow region in its center. Thus a practical way of computing the CVP trajectory is to look for the locus of maximal vertical velocity.

Jet and CVP trajectory

It is important to stress that CVP trajectory and jet trajectory are distinct entities. Muppidi and Mahesh (2007), Salewski et al. (2007), as well as Hasselbrink and Mungal (2001) show that the CVP trajectory lies under the jet trajectory.
There are several ways of defining the jet trajectory: the jet centerline (for circular jets it is the streamline starting at the center of the injection nozzle), the locus of maximum velocity or the locus of maximum concentration. Yuan and Street (1998) compare these methods and show that although the computed trajectories vary, they show the same behavior.
Fig. A.5 (Salewski et al. (2007)) features numerical data showing the jet centerline trajectory and the location of the CVP. The CVP does not start at origin ($x = 0, y = 0$) and is clearly lower than the jet centerline. However both trajectories are parallel for $z/d > 8$. This is because the CVP is a structure of the mean flow field, a time average of transient structures in the instantaneous flow as shown by Fric and Roshko (1994).

When the velocity ratio r is high enough, the difference between jet and CVP trajectories can be observed in our data, as shown by Fig. A.6 a. To compute these trajectories we locate the two vertical velocity maxima in every cross sections. This gives the (y-z)-coordinates of the CVP and jet trajectory for the given abscissa. This computation method is straight-

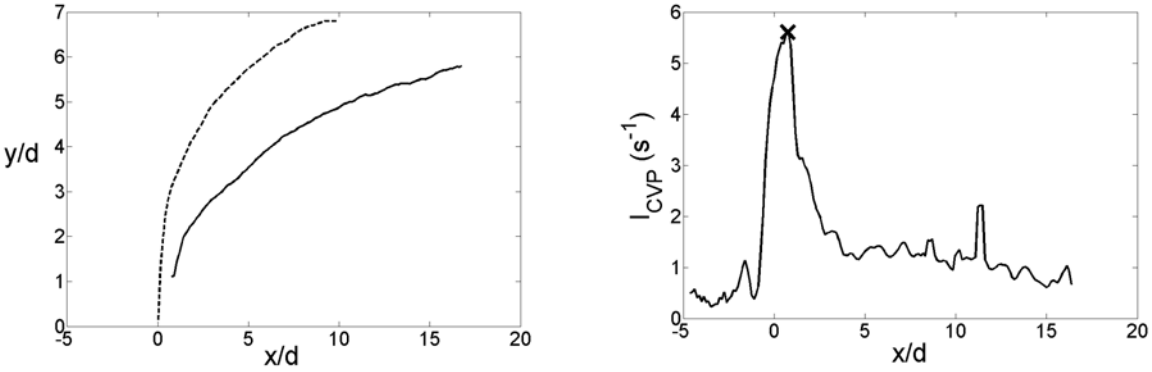

Figure A.6: a) Jet (- -) and CVP(-) trajectories for configuration 10 ($r = 1.51$). b) Swirling strength of the strongest vortex for configuration 10. Maximum is indicated by a cross.

forward, easy to implement and applicable at any velocity ratio. It allows us to distinguish vertical velocity created by the CVP and vertical velocity from the jet itself.

Computing CVP trajectories

The method for CVP trajectory computation featured above is not self-sufficient as it does not yield the start of the trajectory. To determine where to start the trajectory we track the vortex pair, by computing the two maxima of swirling strength λ_{ci} in every constant cross section. This allows us to compute the intensity of the vortex pair I_{CVP} along the trajectory of its cores. Fig. A.6 b shows the intensity of the strongest core for configuration 10. We define the start of the CVP trajectory as the abscissa of the maximum of swirling strength of the strongest vortex core which corresponds to lateral shear on the side on the jet.
It might seem unduly complicated to track the outflow instead of the vortex cores themselves. Indeed another way of defining the CVP trajectory is by computing the mean trajectory of both streamwise vortex cores, however it is not as practical. Fig. A.7 a and A.7 b show CVP trajectories for configuration 10 computed by both methods. Fig. A.7 a shows that CVP trajectories computed using vertical velocity and λ_{ci} are in good agreement.This demonstrates the relevance of detecting the CVP using the outflow. Fig. A.7 b shows the (more common) case where difference in the strength of the vortex cores induces large fluctuations in computed trajectory using swirling strength. Similarly, tracking only one vortex core is much less reliable. Trajectories extracted with λ_{ci} are less reliable, specifically when the intensity of the vortices differs. For our experimental data we obtain considerably better results when considering the locus of vertical velocity maxima than for the locus of λ_{Ci} maxima.

Trajectories were computed in a volume, but they are very close to the symmetry plane. Therefore only the y-component of the trajectory will be analyzed hereafter. We show on Fig. A.8 a and b all 22 computed trajectories using non-dimensional coordinates (y/δ, x/d).

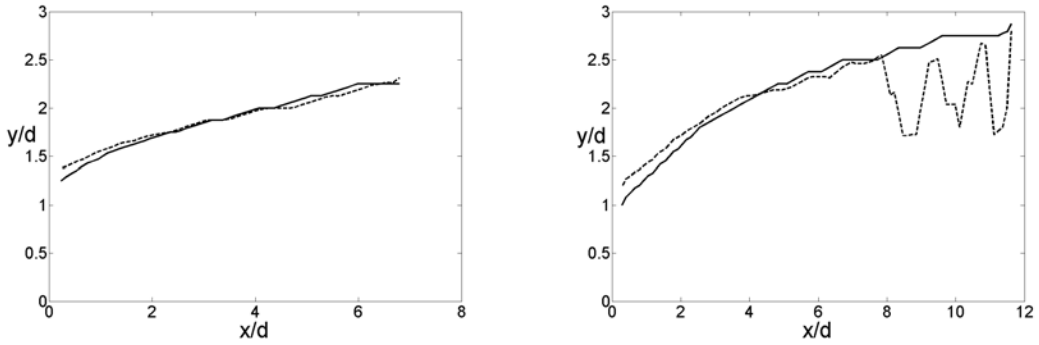

Figure A.7: a) CVP trajectories computed using vertical velocity (-) and λ_{ci} (- -) for configuration 3. b) CVP trajectories computed using vertical velocity (-) and λ_{ci} (- -) for configuration 2.

Trajectories are widely distributed inside and outside the boundary layer (between 0.5 to 3.5 δ).

A.5 Definition and relevance of the momentum ratio r_m

In most of the previous studies of JICF, the velocity ratio r is considered as the key parameter despite its limitations: it does not take into account some important features such as the boundary layers of the jet and the cross-flow. Indeed, Muppidi and Mahesh (2005) have shown that the classic rd scaling was not sufficient to collapse all jet trajectories published in the literature onto a single curve. They suggest that the jet exit velocity profile as well as the cross-flow boundary layer thickness influence the jet. This is supported by the analysis of the influence of jet exit velocity profile on jet trajectories conducted by New et al. (2006). To account for momentum distribution in the jet and boundary layer we introduce a momentum ratio r_m integrating the momentum distribution of the jet and cross-flow boundary layer (also mentioned in Muppidi and Mahesh (2005)), equation A.1:

$$r_m^2 = \frac{\frac{1}{S}\int_S V_j^2 dS}{\frac{1}{\delta}\int_0^\delta U_{cf}^2 dy} \tag{A.1}$$

where $U_{cf}(y)$ is the cross-flow velocity at y and S is the jet nozzle exit section. To highlight the difference with the velocity ratio r, r_m can be decomposed in three parts:

$$r_m = (\sqrt{r_{m,jet}} \cdot \frac{1}{\sqrt{r_{m,cf}}}) \cdot r \tag{A.2}$$

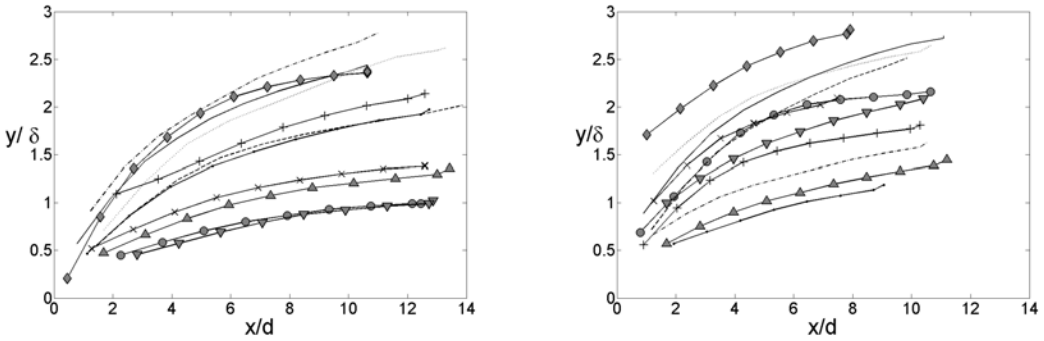

a) b)

Figure A.8: a) Trajectories for configurations 1 to 11. b) Trajectories for configurations 12 to 22. Markers are detailed in table A.1.

with

$$r_{m,jet} = \frac{S\int_S V_j^2 dS}{(\int_S V_j dS)^2} = \frac{\overline{V_j^2}}{\overline{V_j}^2}, \qquad r_{m,cf} = \frac{\int_0^\delta U_{cf}^2 dy}{\delta U_\infty^2} = \int_0^1 (\frac{U_{cf}}{U_\infty})^2 (\frac{a}{\delta}) da \tag{A.3}$$

This decomposition involves two non-dimensional shape factors: $r_{m,cf}$ and $r_{m,jet}$. $r_{m,cf}$ accounts for the momentum distribution in the cross-flow boundary layer ($0 < r_{m,cf} < 1$, by definition), while $r_{m,jet}$ accounts for the momentum distribution in the jet.
To quantify the influence of the velocity profiles on these two new shape factors, we use the boundary layer velocity profiles shown on Fig. A.9 a for the cross-flow and the velocity profiles shown on Fig. A.9 b for the jet. Typical values obtained for $r_{m,cf}$ with the Blasius ($r_{m,cf} = 0.52$) or experimental ($r_{m,cf} = 0.57$) boundary layer profiles are shown on table A.2. $r_{m,cf} \approx 1$ corresponds to a plug profile. This is coherent with the fact a boundary layer with much momentum near the wall leads to a lower trajectory. In the following, the value of $r_{m,cf}$ is computed using experimental velocity data.

profiles	Blasius	Experimental
$r_{m,cf}$	0.52	0.57

profiles	Plug / Tophat	Parabolic
$r_{m,jet}$	1	1.33

Table A.2: Significant values for $r_{m,cf}$ and $r_{m,jet}$ for typical velocity profiles.

Our measurement method does not allow for a sufficient resolution of the velocity profiles at the exit of the jet nozzle to satisfactorily compute the value of $r_{m,jet}$ with experimental data. Consequently $r_{m,jet}$ is estimated using the expression for boundary layer thickness in a smooth pipe proposed by Mohanty and Asthana (1978). Knowing the jet velocity and the nozzle injection length we compute the analytical jet exit velocity profiles shown in Fig. A.9 b, before computing the associated values for $r_{m,jet}$. Values for $r_{m,jet}$ vary between 1 (for

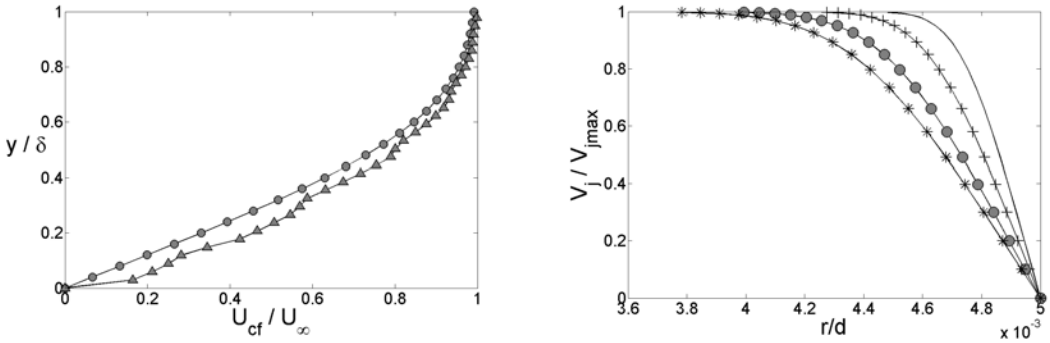

a) b)

Figure A.9: (a) ▲: Experimental boundary layer velocity profile for configuration 13, ●: theoretical Blasius boundary layer profile. b) Theoretical jet velocity profiles as a function of injection length. $l_n = 0.5cm, r_{m,jet} = 1.04$ ($-$); $l_n = 1cm, r_{m,jet} = 1.05$ ($+$); $l_n = 2cm, r_{m,jet} = 1.07$ (●); $l_n = 3cm, r_{m,jet} = 1.09$ ($-+$)

a top-hat profile) and 1.33 (for a parabolic profile). Muppidi and Mahesh (2005) show that a parabolic JICF achieves higher penetration than a top-hat JICF. This is corroborated by experimental work by New et al. (2006). Their interpretation is that the thicker shear layers associated with parabolic JICF delay the formation of leading-edge and lee-side vortices. Therefore possible values taken by $r_{m,jet}$ are coherent with the effect of jet velocity profile on jet trajectory. Consider two jet trajectories with identical velocity ratios, boundary layer profiles and jet exit diameter but with different exit velocity profiles: one with a parabolic profile, one with a top-hat velocity profile. The parabolic jet penetrates deeper resulting in a higher overall trajectory. For both cases, values of r are identical. Values of r_m are different, making r_m the more relevant parameter.
As shown in table A.1, we obtain $0.75 < r_m < 4.10$ corresponding to $0.55 < r_{m,cf} < 0.67$ and $1.05 < r_{m,jet} < 1.13$ for our configurations.

A.6 Influence of experimental parameters on CVP trajectories

Influence of velocity ratio and boundary layer thickness

Fig. A.10 a and b show the influence of velocity ratio. The x and y coordinates are scaled by d.
In Fig. A.10 a the velocity ratio ranges from $r = 0.54$ to $r = 1.62$, while jet exit velocity and profile are kept constant. Cross-flow velocity changes and therefore boundary layer thickness changes also.
In Fig. A.10 b velocity ratio ranges from $r = 0.51$ to $r = 0.84$, while cross-flow velocity, boundary layer thickness and profile are kept constant. Jet exit velocity and profile change.

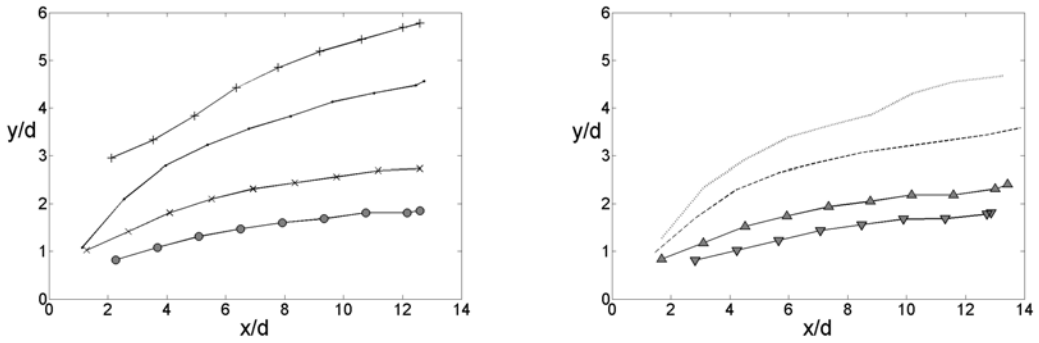

a) b)

Figure A.10: a) Influence of the velocity ratio on the CVP trajectories with constant jet exit velocity for $r = 0.54$ (-●), $r = 0.74$ ($-\times$), $r = 1.14$ ($-\bullet$), $r = 1.62$ ($-+$). b) Influence of the velocity ratio on the CVP trajectories with constant boundary layer thickness and profile for $r = 0.51$ (-▼), $r = 0.83$ (-▲), $r = 1.07$ ($--$), $r = 1.24$ ($\cdots$).

It should be noted that with a constant injection length it is experimentally impossible to vary jet velocity ratio while keeping jet exit velocity profile and boundary layer thickness constant. In all cases the trajectory of the CVP rises with an increase in velocity ratio.
Fig. A.11 compares CVP trajectories for different values of the boundary layer thickness. All other parameters being equal CVP trajectories penetrate deeper when the cross-flow boundary layer is thicker. The same result has been obtained numerically for jet trajectories by Muppidi and Mahesh (2005) and observed by Cortelezzi and Karagozian (2001). This is explained by the fact a thinner boundary layer has more momentum close to the jet exit. Jet trajectories bend earlier and the resulting CVP is created closer to the wall, thus resulting in an overall lower CVP trajectory.

Influence of jet exit velocity profile through variation of injection length

For a constant jet flowrate, changing the injection length modifies the jet exit velocity profile. Fig. A.12 shows CVP trajectories for different nozzle injection lengths, while cross-flow velocity and mean jet velocity are kept constant for two different velocity ratios. An increase in injection length leads to more parabolic jet exit velocity profiles as illustrated in Fig. A.9 b. Fig. A.12 shows that the more parabolic the velocity profile, the higher the CVP trajectory. Although nozzle lengths do not come close to what one would need to ensure a full parabolic profile ($l_n > 60d$) the effect on CVP trajectory is significant. This is an important result: even a small modification of the exit velocity profile can change the height of the CVP trajectories significantly. This sensitivity could be due to the low velocity ratios featured for this data. This issue is investigated in section A.7. Apart from the discussion on trajectory scaling, this data clearly illustrates how it is possible to obtain higher trajectories without spending more energy, only by modifying the design of the injection.

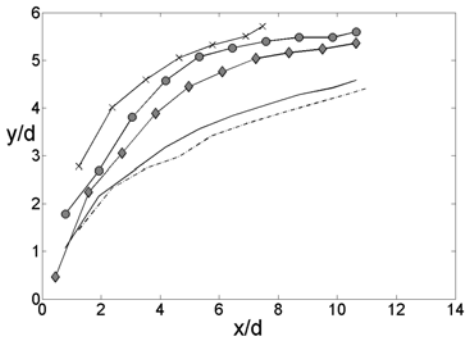

Figure A.11: Influence of boundary layer thickness on CVP trajectories: $\delta = 1.59d$ $(-\cdot)$, $\delta = 1.87d$ $(-)$, $\delta = 2.25d$ (-◆), $\delta = 2.59d$ (-●), $\delta = 2.79d$ $(-\times)$.

A.7 Trajectory Scaling

Scaling quality factor

In order to quantitatively compare how well different scalings collapse trajectories we define a non-dimensional scaling quality factor Q. A perfect scaling would collapse all trajectories onto a single curve, in other words the scattering would be null. This can be characterized by a quantitative criterium.

For a given abscissa $\tilde{x}$ we define $Y(\tilde{x})$ the set of values taken by the trajectories at this abscissa. We define $[\tilde{x}_{start}, \tilde{x}_{end}]$ the range where trajectories exist. $\tilde{x}_{start}$ is then the first abscissa where an outflow region can be identified, i.e where the first trajectory starts, while $\tilde{x}_{end}$ corresponds to where the longest trajectory ends. This range may change depending on how the abscissa is scaled.

For our trajectories, the case arises where not all of them are defined for a given $\tilde{x}$. In order to take this into account we introduce $N(\tilde{x})$ and N_{curves}, respectively the number of curves defined at abscissa $\tilde{x}$ and the total number of curves considered for scaling. The scaling quality factor is defined as the integral of trajectory scatter relative to the mean over the range where these trajectories exist.

$$Q = \int_{\tilde{x}_{start}}^{\tilde{x}_{end}} \frac{\sigma(Y)}{\overline{Y}}(\tilde{x}).\frac{N(\tilde{x})}{N_{curves}} d\tilde{x} \tag{A.4}$$

where $\sigma(Y)$ is the standard deviation of Y and $\overline{Y}$ is the mean of Y for a given abscissa $\tilde{x}$. $Q = 0$ corresponds to a perfect scaling.

To take into account the fact that trajectories are not defined over the same spatial range, this relative scatter is weighted by the ratio, $\frac{N(\tilde{x})}{N_{curves}}$. This is done to give more meaning to the collapse of many trajectories than to the collapse of a few. For a set of trajectories defined over the same domain the weight is one, and the definition for Q can be simplified to the expression shown in equation A.5:

$$Q = \int_{\tilde{x}_{start}}^{\tilde{x}_{end}} \frac{\sigma(Y)}{\overline{Y}}(\tilde{x}).d\tilde{x} \tag{A.5}$$

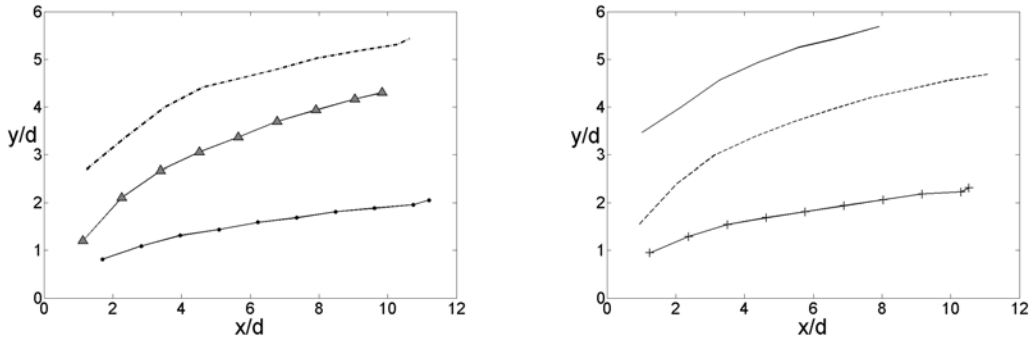

Figure A.12: a) Influence of injection length l_n on CVP trajectories for $r = 0.96$ and constant boundary layer thickness and profile: $l_n = 0.5cm$ $(-\bullet)$, $l_n = 2cm$ $(\text{-}\blacktriangledown)$, $l_n = 3cm$ $(\cdots)$. b) Influence of injection length l_n on CVP trajectories for $r = 1.9$ and constant boundary layer thickness and profile: $l_n = 0.5cm$ $(-+)$, $l_n = 2cm$ $(--)$, $l_n = 3cm$ $(-\cdot-)$.

Normalizing by the mean is necessary to ensure that multiplication of all trajectories by any constant does not change the value of Q.
This method is applicable to any collection of 2D curves, for any scaling of the x-coordinate. Particularly Q can be used to gauge the efficacy of a given scaling of CVP or jet trajectories. For clarity, Q is normalized by its value Q_0 taken when the data is not scaled, both in x and in y.

Reflexions on previously published jet trajectories

To the best of the authors knowledge there are no CVP trajectory data for which jet exit velocity profile, boundary layer thickness and profile are available. However since CVP trajectories follow the same trends as jet trajectories (e.g. deeper penetration with increase in momentum ratio) we will begin our discussion using jet trajectory data published in Muppidi and Mahesh (2005). These results were chosen because the varying parameters were boundary layer thickness and jet exit velocity profile for two different velocity ratios. Table A.3 summarizes the different parameters used by Muppidi and Mahesh (2005) for their study. The corresponding values of $r_{m,jet}, r_{m,cf}$ and r_m were computed using the data presented in their paper.
The objective is to derive an approach to the scaling of these jet trajectories which can be applied to CVP trajectories. Muppidi and Mahesh (2005) present a scaling that successfully collapses their trajectories. This scaling uses a parameter h extracted from the data as the y-coordinate at a distance $x = 0.05d$. Because CVP trajectories do not start at $x = 0$, h is not defined and cannot be used for scaling purposes. Moreover our objective was to validate a more general scaling based on experimental parameters. Thus an alternate scaling was sought.

Fig. A.13 shows the influence of jet velocity profile and boundary layer thickness for different velocity ratios on jet trajectories. Tophat and parabolic jet exit velocity profiles are used. As shown in table A.3 values of r_m are higher for the parabolic profile. For the CVP, jet penetration is higher for parabolic velocity profiles and for thicker boundary layers.

case	I	II	III	IV	V	VI	VII	VIII	IX
Velocity ratio r	1.52	1.52	1.52	1.52	5.7	5.7	5.7	5.7	5.7
$\delta_{80\%}$	1.32d	1.32d	0.44d	0.44d	1.32d	1.32d	0.44d	0.44d	6.4d
$r_{m,jet}$	1.33	1.185	1.33	1.185	1.185	1.33	1.185	1.33	1.33
$r_{m,cf}$	0.52	0.52	0.52	0.52	0.52	0.52	0.52	0.52	0.52
r_m	2.44	2.29	2.44	2.29	9.16	8.60	9.16	8.60	9.16
Markers	-●	$-\times$	$-*$	$-\cdot$	-▼	▲	$-\vert$	$--$	$-$

Table A.3: Parameters for jet trajectories from Muppidi and Mahesh (2005), and corresponding values for $r_{m,jet}, r_{m,cf}$ and r_m obtained using their parameters.

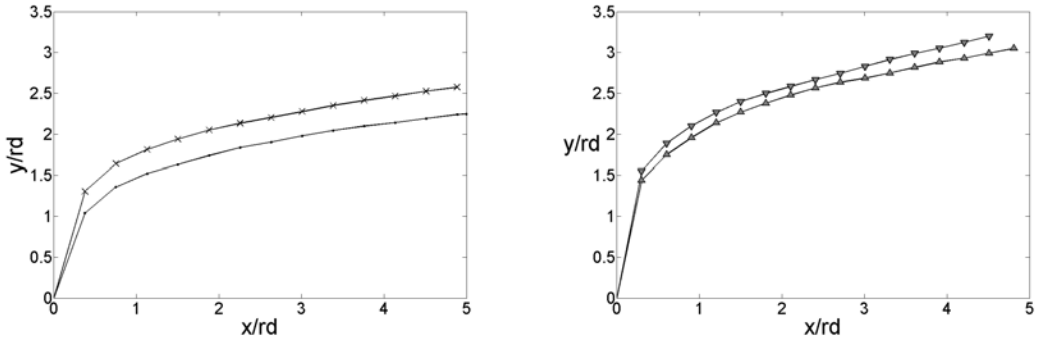

a) b)

Figure A.13: a) Jet trajectories for constant jet exit velocity profile and velocity ratio but varying boundary layer thickness$-\bullet$, $\delta = 0.44d$, $-\times$, $\delta = 1.32d$. b) Trajectories for constant velocity ratio, boundary layer thickness. Jet exit velocity profile varies between tophat and parabolic. Parabolic : -▲,$r_m = 8.6$. Top-hat : -▼,$r_m = 9.16$. From Muppidi and Mahesh (2005) data.

Scaling of jet trajectory

Trajectory scaling of a circular jet in cross-flow has been the subject of much research (Pratte and Baines (1967), Smith and Mungal (1998), Yuan and Street (1998), Hasselbrink and Mungal (2001), Muppidi and Mahesh (2005), Gutmark et al. (2008)), however no scaling is fully satisfactory. Among the most successful scalings, the rd scaling by Pratte and Baines (1967) has proven to collapse most experimental trajectories. For $5 < r < 35$, they show the

collapse of the centerline trajectory with the rd length scale defined as follows:

$$\frac{y}{rd} = A(\frac{x}{rd})^b \tag{A.6}$$

where $A = 2.05$ and $b = 0.28$. However more recent works by Muppidi and Mahesh (2005) and New et al. (2006) show that this scaling is not satisfactory for flows where boundary layer thickness and jet exit velocity profile vary. Several attempts were made to scale jet trajectories while accounting for these factors (Muppidi and Mahesh (2005), Gutmark et al. (2008)).

A scaling using r^α was introduced by Karagozian (1986) for high velocity ratios. Similarly we choose to consider a scaling using r_m^α to account for jet exit velocity profile, where α quantifies the influence of momentum ratio r_m and is unknown *a priori*. To account for the influence of the boundary layer thickness we introduce, in a manner analogous to Muppidi and Mahesh (2005) who use $(\frac{h}{d})^C$, the non-dimensional parameter $(\frac{\delta}{d})^\beta$, where β quantifies the influence of δ on trajectory. This leads to the new scaling described in equation A.7:

$$\frac{y}{{r_m}^\alpha d(\frac{\delta}{d})^\beta} \tag{A.7}$$

Reasoning on the physics of the flow and empirical data, it is possible to define upper and lower bounds for β and α.
To $\alpha = 1,\ \beta = 0$ corresponds the scaling $\frac{y}{r_m d}$. Having $\beta < 0$ would mean the jet penetrates deeper with a decreasing boundary layer thickness, therefore $\beta > 0$. Moreover for high velocity ratios where the jet exit profile is usually a plug profile with a fixed boundary layer profile which gives $r_m \propto r$ thus making this scaling equivalent to the rd scaling.
To $\alpha = 1,\ \beta = 1$ corresponds the scaling $\frac{y}{r_m \delta}$. Having $\beta > 1$ would mean deeper jet penetration with decrease in jet diameter, therefore $\beta > 1$. Similarly the data shows how trajectories rise with d, therefore $\beta < 1$.
Using the same reasoning we obtain $\alpha > 0$, since trajectories rise with r_m. There is however no upper bound on α.
Fig. A.14 c, d shows scaled trajectories using equation A.7 compared to the classic rd scaling (Fig. A.14 a,b). For a given set of jet trajectories we search for α, β to obtain the best possible collapse. This is equivalent to minimizing the quality factor Q, here used in its simplified form defined in equation A.5.
Note that jet exit velocity profile and boundary layer thickness do not affect trajectories in the same way for different velocity ratios.

For $r = 5.7$ (Fig. A.14 a,c), we have $y/(r_m^{1.5} d(\frac{\delta}{d})^{0.05})$ whereas for $r = 1.5$ (Fig. A.14 b,d) we obtain $y/(r_m^{2.3} d(\frac{\delta}{d})^{0.16})$. Indeed two different sets of exponents are found depending on r, i.e $\alpha(r)$ and $\beta(r)$. The exponents for r_m and $(\frac{\delta}{d})$ give us insight into how jet trajectory is influenced by jet exit velocity profile and boundary layer thickness. These results indicate that for low velocity ratios, jet trajectory will be more sensitive to variations of the incoming cross flow boundary layer thickness. While for high velocity ratios boundary layer thickness is less of an issue and the trajectory is mainly influenced by the momentum ratio. The proposed scalings achieve significant collapse as shown in Fig. A.14. It also shows how the

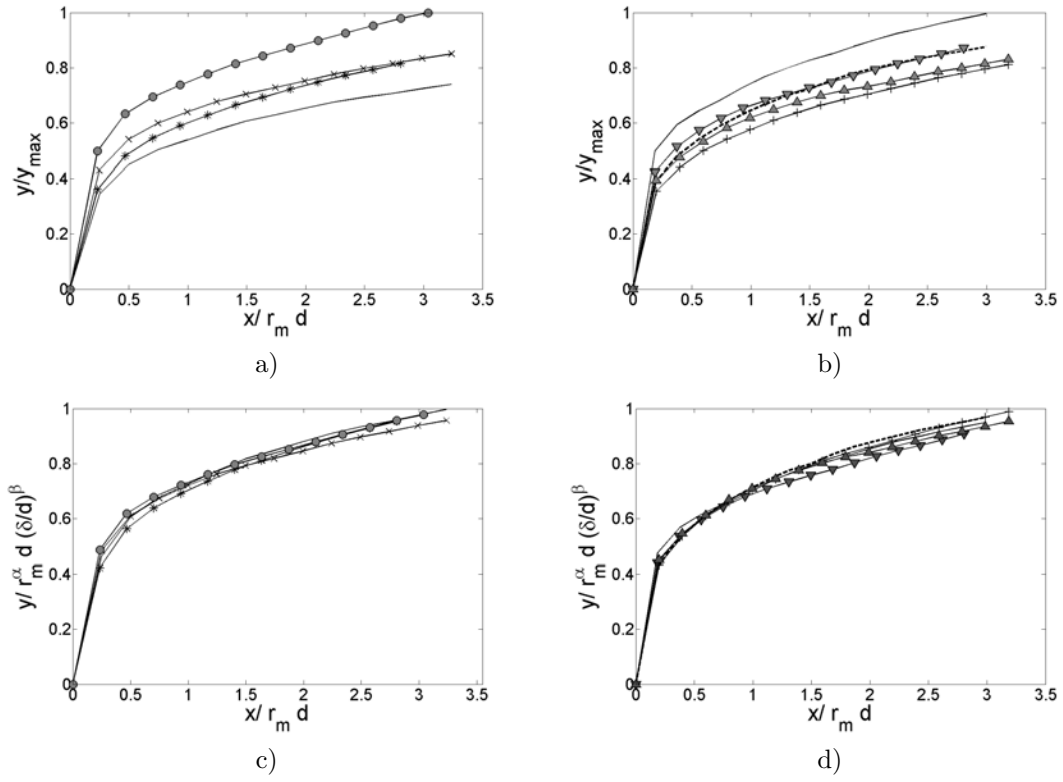

Figure A.14: a) Jet trajectories without scaling in y for case I (-●), case II (−×), case III (−∗), case IV (−•). b) Jet trajectories without scaling for case V (-▼), case VI (-▲), case VII (−|), case VIII (−−), case IX (−). c) Jet trajectories from a) with scaling for $r_m^{2.23}$ and $(\frac{\delta}{d})^{0.16}$ leading to $Q = 20\%$. d) Jet trajectories from b) with scaling for $r_m^{1.55}$ and $(\frac{\delta}{d})^{0.06}$ leading to $Q = 26\%$. Each set of trajectories is normalized to make the original and scaled trajectory set comparable.

scaling differs whether high or low velocity ratios are considered.

Table A.4 summarizes the different scalings and how successfully they collapse the data. The proposed scaling achieves similar or better collapse than the scaling proposed by Muppidi and Mahesh (2005). It requires the determination of two parameters, whereas the $rd(\frac{h}{d})^C$ scaling requires only one. On the other hand h has to be extracted from the data independently for each trajectory, whereas r_m and δ are experimental parameters known *a priori*. For this data, the scaling suggested in Gutmark et al. (2008) does not result in trajectory collapse, on the contrary it increases the dispersion of the curves. It is most likely due to a typographic mistake in the printed scaling formula. For instance, the $\frac{d}{\delta}$ factor has to be inverted to make physical sense.

Scalings	No scaling	y/rd	y/$r_m d$
cases I to IV ($r = 1.5$)	$Q = 67.8\%$	$Q = 67.8\%$	$Q = 60.8\%$
cases V to IX ($r = 5.7$)	$Q = 46.0\%$	$Q = 46.0\%$	$Q = 36.6\%$
cases I to IX	$Q = 100.0\%$	$Q = 78.4\%$	$Q = 73.3\%$

Scalings	Muppidi y/$(rd(\frac{h}{d})^C)$	Gutmark $y/rd/(r_b \cdot (r^2 \frac{d}{\delta})^{0.45})$ $\Leftrightarrow y/(rd \cdot (r_b(r^2 \frac{d}{\delta})^{0.45}))$	y/$r_m^\alpha d(\frac{\delta}{d})^\beta$
cases I to IV ($r = 1.5$)	$Q = 41.6\%$	$Q = 220.0\%$	$Q = 13.5\%$, ($\alpha = 2.23, \beta = 0.16$)
cases V to IX ($r = 5.7$)	$Q = 32.3\%$	$Q = 393.3\%$	$Q = 12.0\%$, ($\alpha = 1.55, \beta = 0.05$)
cases I to IX	$Q = 36.3\%$	$Q = 336.9\%$	$Q = 28.0\%$, ($\alpha = 1.14, \beta = 0.08$)

Table A.4: Comparison of quality factors obtained for different scalings.

Scaling of CVP trajectories

Experimental CVP trajectory data analyzed in section A.6 and jet trajectory data discussed in section A.7 show that both types of trajectories behave in the same manner when parameters vary. This is to be expected since the CVP is a structure created by the jet and it seems CVP trajectory follows jet centerline trajectory.

Nevertheless there are differences between CVP and jet trajectories. CVP trajectories do not start at the jet exit ($x = 0, y = 0$) and are lower than jet trajectories. Moreover, since jet trajectories (Salewski et al. (2007)) and CVP trajectories are parallel in the far field, it is impossible for both types of trajectories to assume a power law and retain that parallelism. Nevertheless a power law will be used to scale CVP trajectories, keeping in mind that the starting point abscissa for CVP trajectories vary ($x_{start} \simeq 1.5d$ for most trajectories).

Since the trajectories of the CVP are influenced by momentum ratio r_m, diameter d and boundary layer thickness δ, the scaling described in equation A.7 is applied to our data.

Determination of the optimal scaling for CVP trajectories

To determine the influence of boundary layer thickness on CVP trajectories we consider configurations 9 to 13. In these cases, boundary layer thickness varies from $1.36d$ to $2.26d$ while $r_m = 2.2 \pm 5\%$. Best collapse is obtained for $\beta = 0.91$, thus for these cases boundary

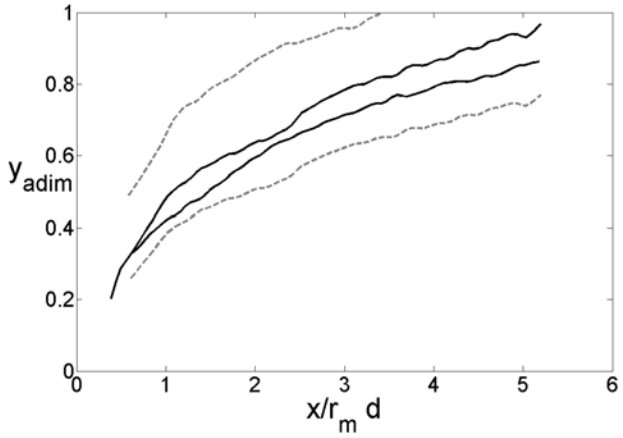

Figure A.15: Highest and lowest trajectories for configurations 9 to 13, before (grey, dotted line) and after (black, solide line) scaling by $d(\delta/d)^{\beta}$ ($Q = 28.3\%$). y axis is normalized to help comparison.

layer thickness has a significant relative influence on CVP trajectory.

Fig. A.15 shows the highest and lowest of the trajectories before and after scaling by $d(\frac{\delta}{d})^{\beta}$. Collapse is significant ($Q = 28.3\%$). $\beta = 0.91$ is much higher than the value found in section A.7 although the velocity ratios are comparable ($r = 1.5$ and $r = 1.6$). CVP trajectories being lower, interaction with boundary layer would be stronger for this velocity ratio, resulting in a higher value for β.

To go further, a simplifying assumption is made: β is assumed to be constant. In other words, the way the boundary layer thickness affects trajectory is considered independent of other parameters such as r, $r_{m,jet}$ or $r_{m,cf}$. Of course, this is not strictly true as shown in section A.7. Furthermore since some of these trajectories are close or even inside the boundary layer (see Fig. A.10) it stands to reason β would change with momentum ratio. However data are insufficient for a more thorough analysis of this issue, another extensive parametric study would be required. Nevertheless, based on the data from Muppidi and Mahesh (2005) analyzed in the previous section, we can expect β to be a decreasing function of r_m.

To determine the influence of r_m we consider configurations 1 to 8 and 14 to 22. All these configurations feature variations in r_m. However these variations are brought about in different ways: variations in r ($0.51 < r < 3.05$) by changing jet velocity and cross flow velocity and variations in $r_{m,jet}$ by changing jet velocity profile. We find $\alpha = 1.23$ ($Q = 13.1\%$). Fig. A.16 shows the highest and lowest trajectories before and after scaling by $r_m^{\alpha} d(\frac{\delta}{d})^{\beta}$.

For all 22 configurations the scaling mentioned gives $Q = 13.14\%$. This relatively high value is most likely due to the fact that α and β are considered constant when they have been shown to depend on r. Furthermore the underlying assumption of a power law scaling, i.e that there exists a scaling such that trajectories can be expressed as $y = Ax^b$ where A and

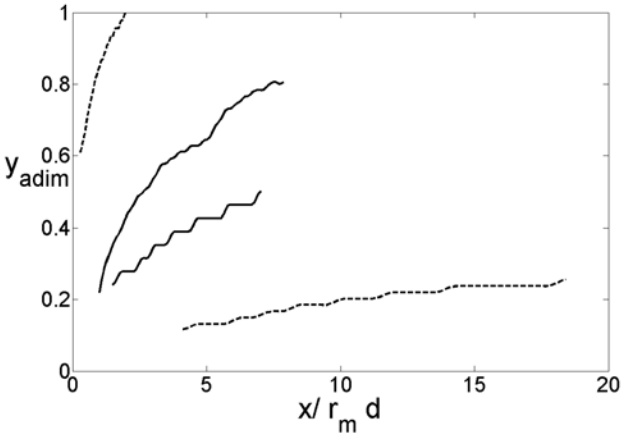

Figure A.16: Lowest and highest CVP trajectories for configurations 1 to 8 and 14 to 22. No scaling (- -) and after scaling (-) leading to $Q = 13.1\%$. y axis is normalized to allow visual comparison.

b are constant, is erroneous as shown by New et al. (2006). However the proposed scaling does allow for significant collapse with a 43% improvement over the rd scaling.

Using the computed values for α and β, the scaled data are well fitted with a power law as described in equation A.8:

$$\frac{y}{{r_m}^{\alpha} d(\frac{\delta}{d})^{\beta}} = A(\frac{x}{r_m d})^b \tag{A.8}$$

with $A = 0.48$, $b = 0.42$. Commonly rd scalings of the jet trajectory yield $1.2 < A < 2.6$ and $0.28 < b < 0.34$. For CVP trajectories A is lower because the trajectory lies under the jet centerline. Possible uses of this equation are many-fold. For example when devising an experiment involving jets in cross-flow it could be helpful to choose the proper geometrical and physical parameters for a given objective.

Finally, we summarize on Fig. A.17 how the main scalings discussed previously collapse all CVP trajectories. The improvements in collapse brought about by each scalings are clear and quantified by the decrease of the quality factor which is minimum for the scaling based on momentum ratio proposed in this study (Fig. A.17d). For the range of parameters considered here, equation A.8 allows for a decent approximation of the CVP's position in space as illustrated on Fig. A.17 d.

A.8 Conclusions

An experimental study of the CVP trajectories created by a round JICF has been carried out in an hydrodynamic tunnel. 3D3C velocity fields were used to identify the CVP's and their corresponding outflow regions. The outflow region is used to define and compute CVP

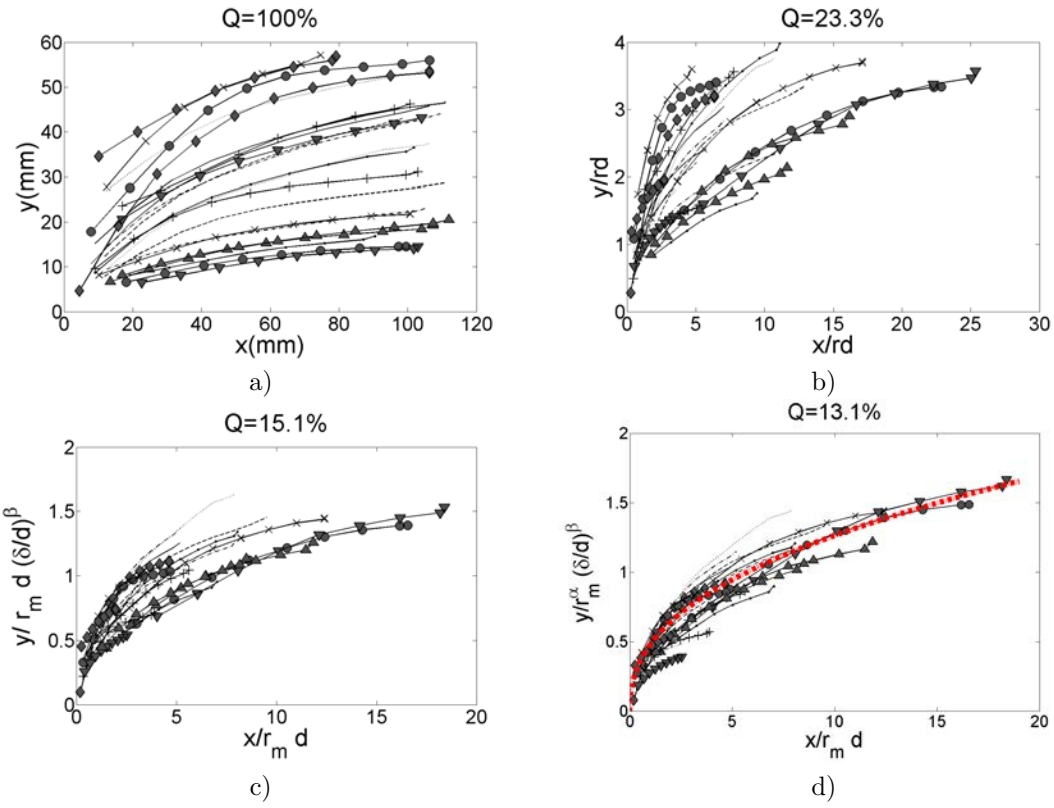

Figure A.17: Whole set of trajectories scaled with different scalings. y axis is normalized to help comparison. a) Trajectories without scaling, b) Trajectories with rd scaling, c) Trajectories with $(\delta/d)^{\beta}$ scaling, d) final scaling together with the trajectory described in equation A.8 (red dotted line).

trajectories for 22 JICF configurations, including those with a low velocity ratio r. The influence of jet velocity and profile as well as cross flow velocity and boundary layer thickness on CVP trajectories is investigated. Parallels are drawn between the behavior of jet and CVP trajectories.

A more general momentum ratio r_m is introduced as an improvement of the velocity ratio r to take into account the boundary layer and jet exit momentum distributions. The relevance of r_m for jet and CVP trajectories is demonstrated for numerical and experimental data.
Experimental CVP trajectories and jet trajectories from the literature are scaled and analyzed. The quality of a given scaling is defined and allows for the determination of the relative significance of each parameter (momentum ratio, boundary layer thickness) on trajectories. A new scaling taking into account jet exit momentum distributions, velocity ratio and boundary layer thickness is proposed.
Finally, a unique trajectory taking into account all relevant parameters is suggested for CVP trajectories.

A.9 Acknowledgments

The authors gratefully acknowledge the ADEME (Agence De l'Environnement et la Maitrise de l'Energie) for its financial support, as well the reviewers for their helpful comments.

Bibliography

W.D. Baines and J.F. Keffer. The round turbulent jet in cross wind. *J Fluid Mech*, 15: 481–488, 1963.

J.N. Blanchard, Y. Brunet, and A. Merlen. Influence of a counter rotating vortex pair on the stability of a jet in a cross flow: an experimental study by flow visualizations. *Experiments in fluids*, 26(1-2):63–74, JAN 1999. ISSN 0723-4864.

T. Cambonie and J.L. Aider. Optimal seeding for high spatial resolution instantaneous volumetric measurements. application to low velocity ratios jets in cross-flow. *16th Int Symp on Applications of Laser Techniques to Fluid Mechanics, Lisbon, Portugal*, 2012.

T. Cambonie and J.L. Aider. Seeding optimization for instantaneous volumetric velocimetry. application to a jet in cross-flow. *submitted to Exp. in Fluids*, 2013.

R. Camussi, G. Guj, and A.Stella. Experimental study of a jet in a crossflow at very low Reynolds number. *J Fluid Mech*, 454:113–144, MAR 10 2002. ISSN 0022-1120.

P. Chassaing, J. George, A. Claria, and F. Sananes. Physical characteristics of subsonic jets in a cross-stream. *J. Fluid Mech*, 62:41–64, 1974.

M.S. Chong, A.E. Perry, and B.J. Cantwell. A general classification of 3-dimensional flow fields. *Physics of Fluids*, 2:765–777, 1990.

L. Cortelezzi and A.R. Karagozian. On the formation of the counter-rotating vortex pair in transverse jets. *J. Fluid Mech*, 446:347–373, NOV 10 2001. ISSN 0022-1120.

R. Fearn and R.P. Weston. Vortictiry assosciated with a jet in a cross flow. *AIAA Journal*, 12:1666–1671, 1974.

T.F. Fric and A. Roshko. Vortical structure in the wake of a transverse jet. *J Fluid Mech*, 279:1–47, NOV 25 1994. ISSN 0022-1120.

G. Godard and M. Stanislas. Control of a decelerating boundarylayer. part 3: Optimization of round jets vortex generators. *Aerospace Science and Technology*, 10:455–464, 2006.

S. Gopalan, B. M. Abraham, and J. Katz. The structure of a jet in cross flow at low velocity ratios. *Physics of fluids*, 16:2067–2087, June 2004.

E.J. Gutmark, I.M. Ibrahim, and S. Murugappan. Circular and noncircular subsonic jets in cross flow. *Physics of Fluid*, 20(7), JUL 2008. ISSN 1070-6631.

E.F. Hasselbrink and M.G. Mungal. Transverse jets and jet flames. part 1. scaling laws for strong transverse jets. *J. Fluid Mech*, 443, 2001.

P. Joseph, X. Amandolese, and J-L. Aider. Drag reduction on the 25 degres slant angle ahmed reference body using pulsed jets. *To be published in Exp. in Fluids*, 2012.

Ann R. Karagozian. Transverse jets and their control. *Progress in Energy and Combustion Science*, 36(5):531 – 553, 2010. ISSN 0360-1285.

A.R. Karagozian. An analytical model for the vorticity associated with a transverse jet. *AIAA Journal*, 4:429–436, mar 1986.

R.J. Margarson. Fifty years of jet in cross flow research. *AGARD*, pages 1–141, 1993.

Y. Marzouk and A. Ghoniem. Vorticity structure and evolution in a transverse jet. *J. Fluid Mech*, 575:267–305, MAR 25 2007. ISSN 0022-1120.

S. Megerian, J. Davitian, L.S. Alves, and A.R. Karagozian. Transverse-jet shear-layer instabilities. Part 1. Experimental studies. *J. Fluid Mech*, 593:93–129, DEC 25 2007. ISSN 0022-1120.

A.K. Mohanty and S.B.L. Asthana. Laminar flow in the entrance region of a smooth pipe. *J Fluid Mech*, 90:433–447, 1978.

S. Muppidi and K. Mahesh. Study of trajectories of jets in crossflow using direct numerical simulations. *J Fluid Mech*, 530:81–100, MAY 10 2005. ISSN 0022-1120.

S. Muppidi and K. Mahesh. Direct numerical simulation of round turbulent jets in crossflow. *J Fluid Mech*, 574:59–84, MAR 10 2007. ISSN 0022-1120.

T.H. New, T.T. Lim, and S.C. Luo. Effects of jet velocity profiles on a round jet in cross-flow. *Experiments in Fluids*, 40:859–875, 2006.

F. Pereira and M. Gharib. Defocusing digital particle image velocimetry and the three-dimensional characterization of two-phase flows. *Measurement Science & Technology*, 13 (5):683–694, MAY 2002. ISSN 0957-0233.

B.D. Pratte and W.D. Baines. Profiles of round turbulent jet in cross flow. *J. Hydr . Div*, 92:53, 1967.

M. Salewski, D. Stankovic, and L. Fuchs. Mixing in circular and non-circular jets in crossflow. *Flow Turbulence Combust*, pages 255–283, 2007.

S.H. Smith and M.G. Mungal. Mixing, structure and scaling of the jet in crossflow. *J Fluid Mech*, 357:83–122, FEB 25 1998. ISSN 0022-1120.

C.E. Willert and M. Gharib. 3-Dimensional particle imaging with a single camera. *Experiments in Fluids*, 12(6):353–358, APR 1992. ISSN 0723-4864.

L.L. Yuan and R.L. Street. Trajectory and entrainment of a round jet in crossflow. *Physics of fluids*, 10(9):2323–2335, SEP 1998. ISSN 1070-6631.

J. Zhou, R.J. Adrian, S. Balachandar, and T.M. Kendall. Mechanisms for generating coherent packets of hairpin vortices. *J Fluid Mech*, 387:535–396, 1999.

Appendix B

The Reynolds number

There are a many dimensionless numbers in fluid dynamics, but none more common than the Reynolds number. Common flows can be accurately modeled by the Navier-Stokes equation (B.1).

$$\frac{\partial \rho \mathbf{u}}{\partial t} + \nabla \cdot (\rho \mathbf{u} \otimes \mathbf{u}) = -\nabla p + \nabla \cdot \overline{\overline{\tau}} \tag{B.1}$$

where $\overline{\overline{\tau}}$ is the viscous stress tensor, and ρ local fluid density. Let us suppose the fluid is newtonian (air, water) this means the viscous stress tensor $\overline{\overline{\tau}}$ is proportional to the local strain rate: the rate of change of its deformation over time. The proportionality factor is called the cinematic viscosityμ, kinematic viscosity is $\nu = \mu/\rho$. We will also suppose fluid density ρ remains constant. This results in equation (B.2).

$$\frac{\partial \mathbf{u}}{\partial t} + \nabla \cdot (\mathbf{u} \otimes \mathbf{u}) = -\frac{1}{\rho}\nabla p + \nu \Delta \mathbf{u} \tag{B.2}$$

Now let us call d and U a characteristic length and velocity of the flow system. We will also set $\tilde{u} = \frac{u}{U}$, $\tilde{x} = \frac{x}{d}$ and $\tilde{p} = \frac{p}{\rho}$. Equation B.2 becomes equation (B.3).

$$\frac{\partial \tilde{\mathbf{u}}}{\partial t} + \nabla \cdot (\tilde{\mathbf{u}} \otimes \tilde{\mathbf{u}}) = -\nabla \tilde{p} + \frac{1}{Re_d}\Delta \tilde{\mathbf{u}} \tag{B.3}$$

With $Re_d = \frac{dU}{\nu}$ the Reynolds number based on d. Equation B.3 shows how the Reynolds number determines the importance of viscous effects in the flow. There are several other interpretations for this number, however what one must remember is that it is an important parameter for many flows, including the backward facing step flow and the flow over a flat plate. In the case of the backward-facing step flow Reynolds number is computed using the step height as characteristic length scale and free-stream velocity as characteristic flow velocity, $Re_h = U_\infty h/\nu$.

Appendix C

Recirculation, fields

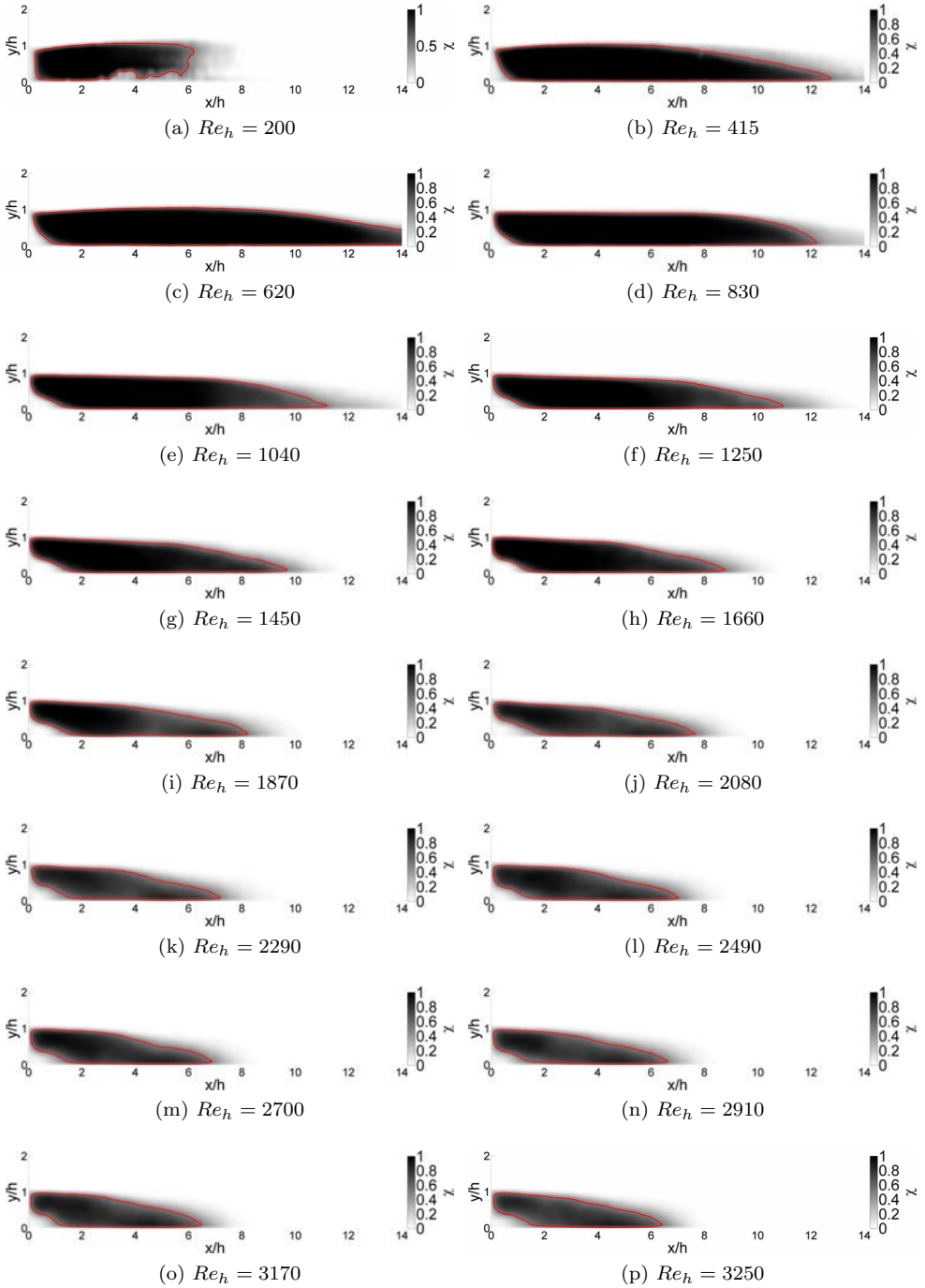

(a) $Re_h = 200$ (b) $Re_h = 415$

(c) $Re_h = 620$ (d) $Re_h = 830$

(e) $Re_h = 1040$ (f) $Re_h = 1250$

(g) $Re_h = 1450$ (h) $Re_h = 1660$

(i) $Re_h = 1870$ (j) $Re_h = 2080$

(k) $Re_h = 2290$ (l) $Re_h = 2490$

(m) $Re_h = 2700$ (n) $Re_h = 2910$

(o) $Re_h = 3170$ (p) $Re_h = 3250$

Figure C.1: Recirculation time fractions for multiple Reynolds numbers, middle vertical plane

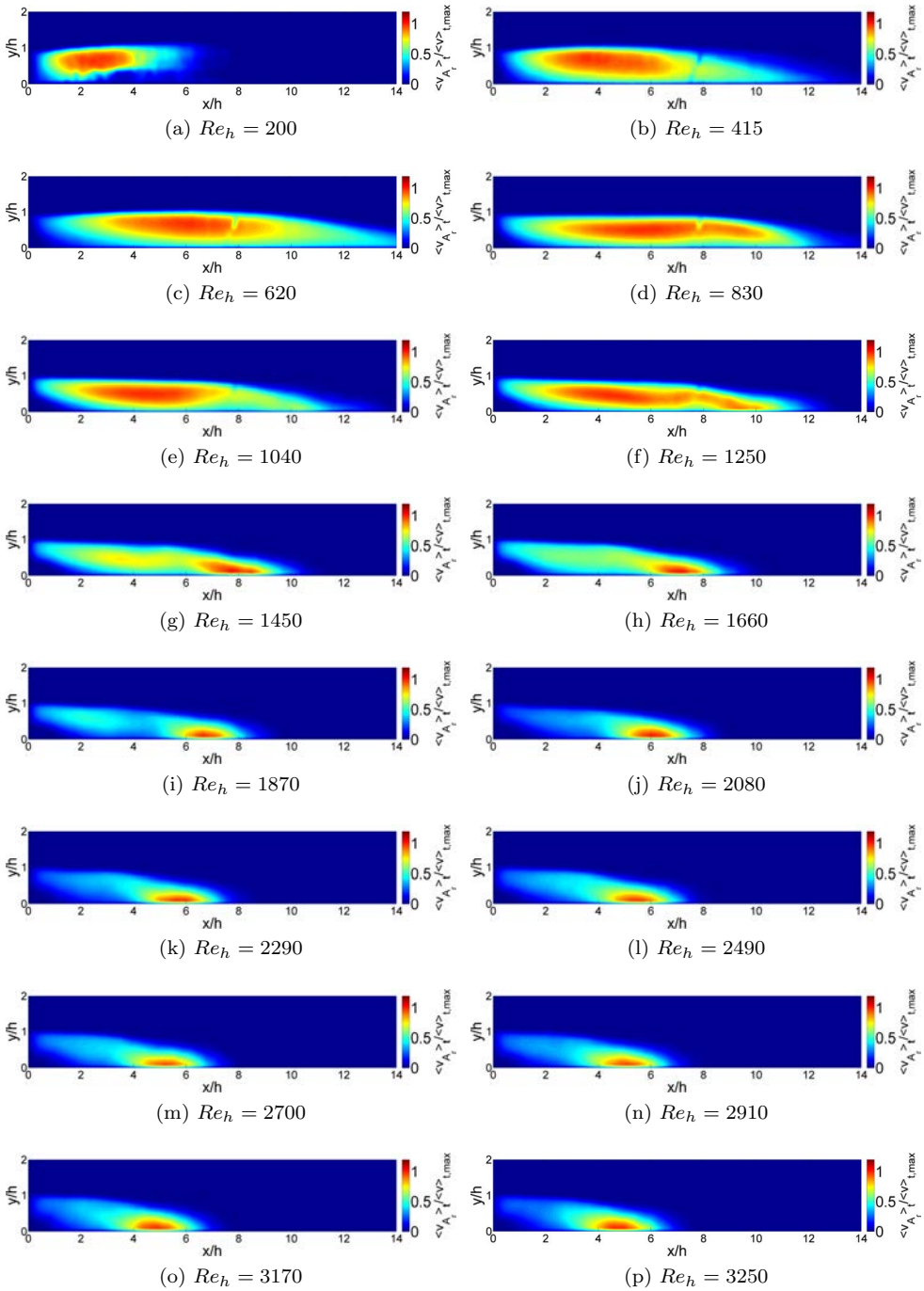

(a) $Re_h = 200$ (b) $Re_h = 415$

(c) $Re_h = 620$ (d) $Re_h = 830$

(e) $Re_h = 1040$ (f) $Re_h = 1250$

(g) $Re_h = 1450$ (h) $Re_h = 1660$

(i) $Re_h = 1870$ (j) $Re_h = 2080$

(k) $Re_h = 2290$ (l) $Re_h = 2490$

(m) $Re_h = 2700$ (n) $Re_h = 2910$

(o) $Re_h = 3170$ (p) $Re_h = 3250$

Figure C.2: Recirculation intensity for multiple Reynolds numbers, middle vertical plane

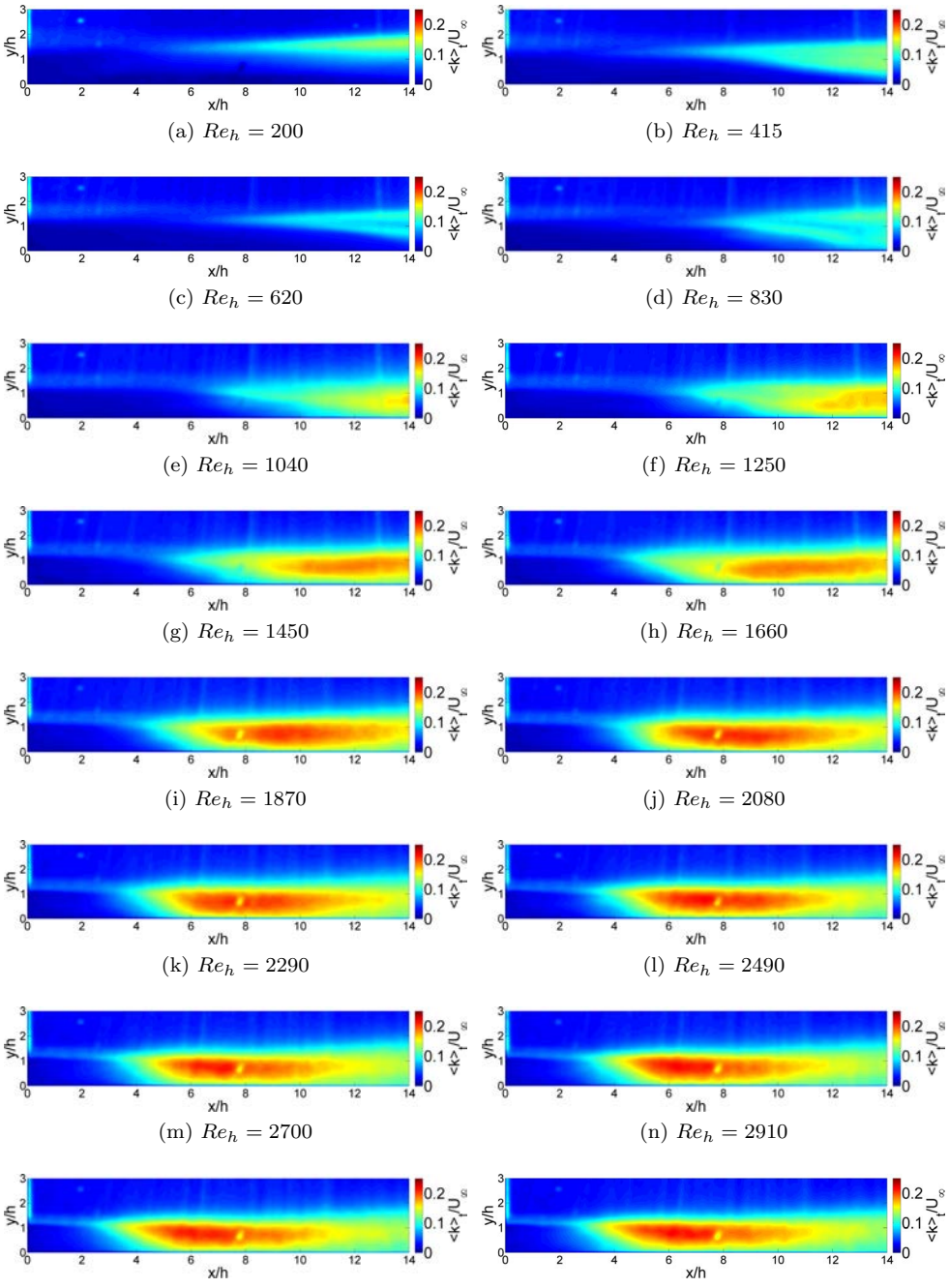

(a) $Re_h = 200$ (b) $Re_h = 415$

(c) $Re_h = 620$ (d) $Re_h = 830$

(e) $Re_h = 1040$ (f) $Re_h = 1250$

(g) $Re_h = 1450$ (h) $Re_h = 1660$

(i) $Re_h = 1870$ (j) $Re_h = 2080$

(k) $Re_h = 2290$ (l) $Re_h = 2490$

(m) $Re_h = 2700$ (n) $Re_h = 2910$

(o) $Re_h = 3170$ (p) $Re_h = 3250$

Figure C.3: Time averaged turbulent kinetic energy field for multiple Reynolds numbers, middle vertical plane

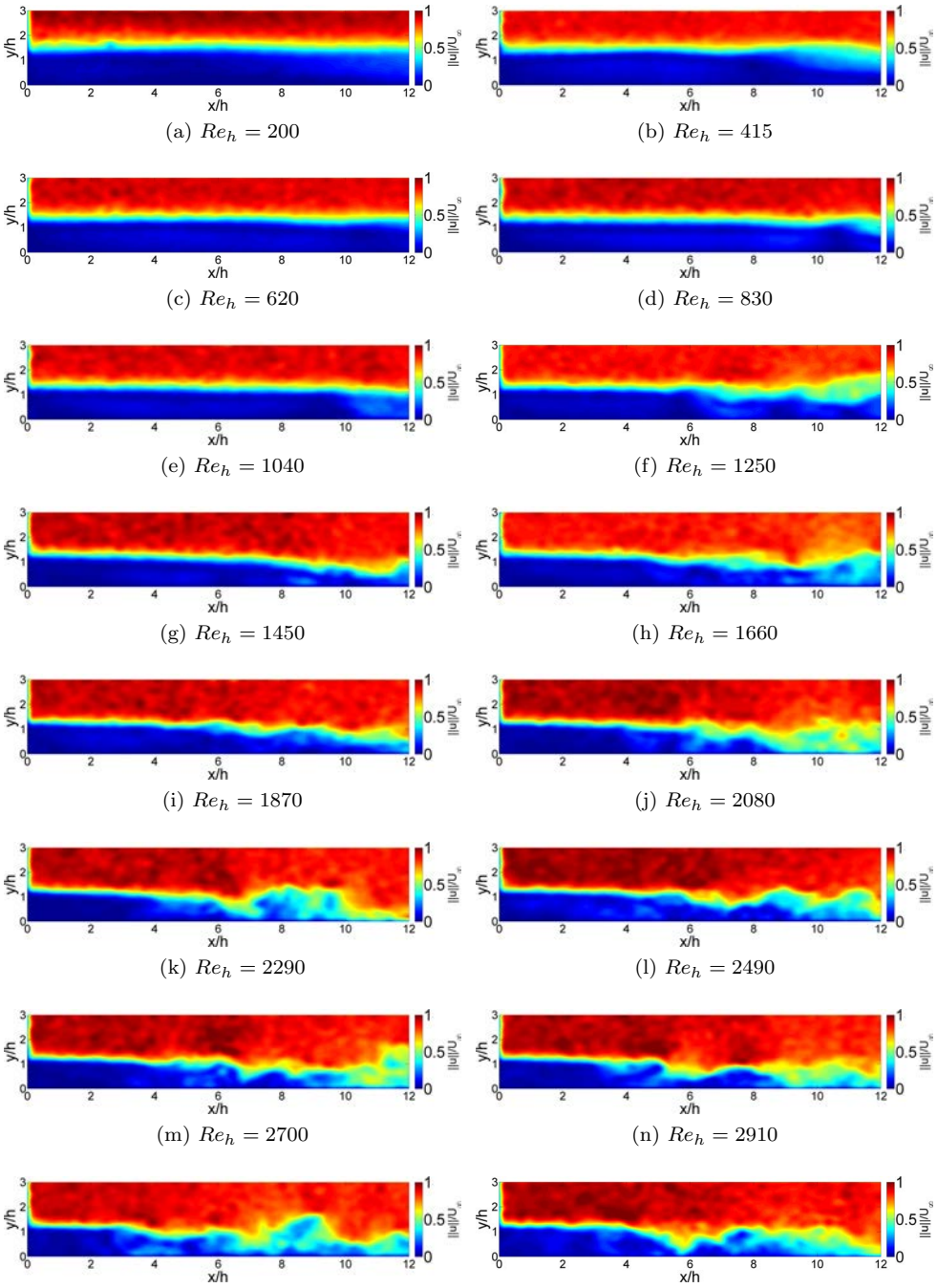

(a) $Re_h = 200$ (b) $Re_h = 415$

(c) $Re_h = 620$ (d) $Re_h = 830$

(e) $Re_h = 1040$ (f) $Re_h = 1250$

(g) $Re_h = 1450$ (h) $Re_h = 1660$

(i) $Re_h = 1870$ (j) $Re_h = 2080$

(k) $Re_h = 2290$ (l) $Re_h = 2490$

(m) $Re_h = 2700$ (n) $Re_h = 2910$

(o) $Re_h = 3170$ (p) $Re_h = 3250$

Figure C.4: Instantaneous velocity amplitude snapshots for multiple Reynolds numbers, middle vertical plane

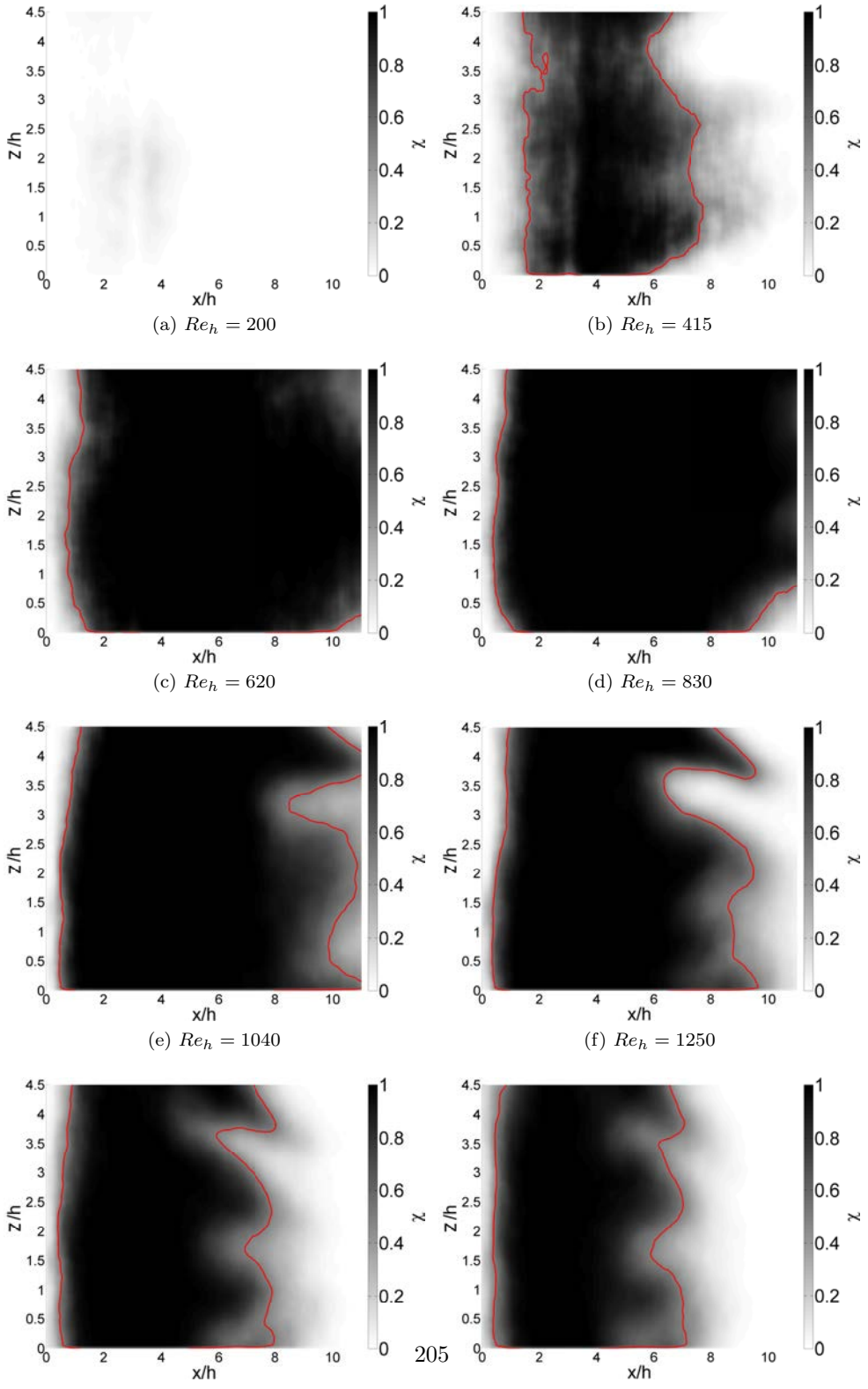

(a) $Re_h = 200$ (b) $Re_h = 415$

(c) $Re_h = 620$ (d) $Re_h = 830$

(e) $Re_h = 1040$ (f) $Re_h = 1250$

(g) $Re_h = 1450$ (h) $Re_h = 1660$

Figure C.5: Recirculation time fractions for multiple Reynolds numbers, middle horizontal plane

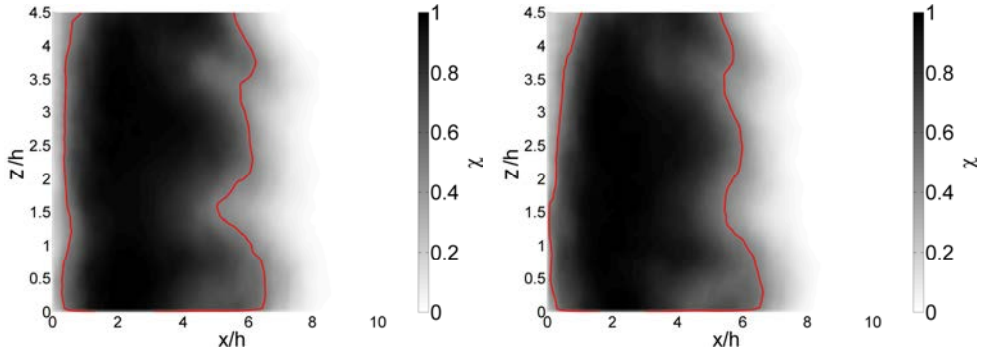

(i) $Re_h = 1870$ (j) $Re_h = 2080$

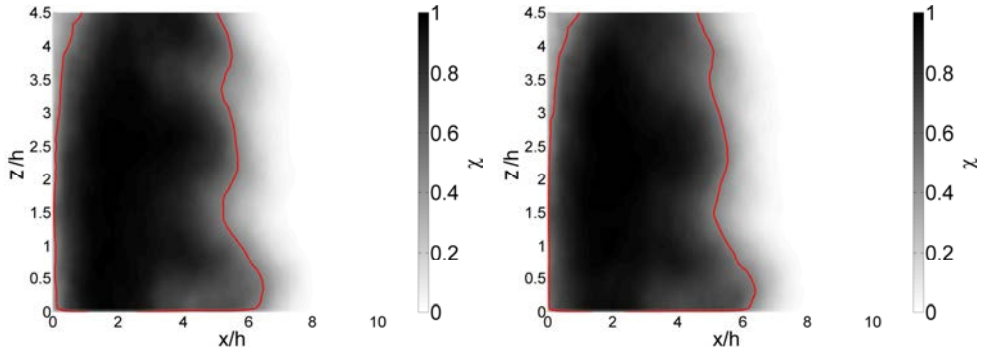

(k) $Re_h = 2290$ (l) $Re_h = 2490$

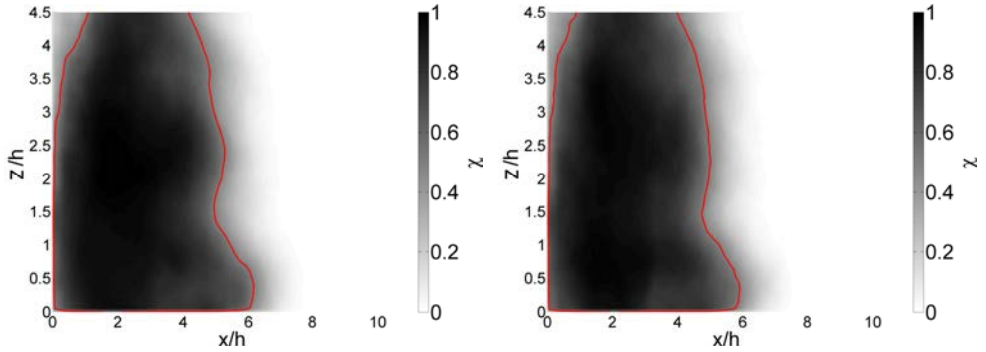

(m) $Re_h = 2700$ (n) $Re_h = 2910$

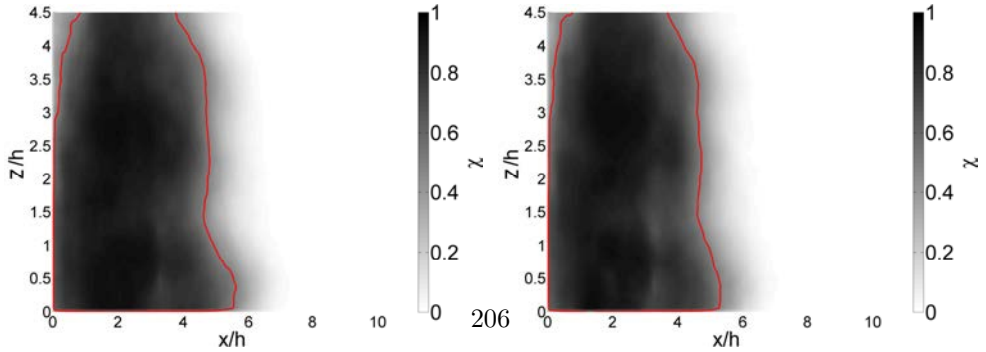

(o) $Re_h = 3170$ (p) $Re_h = 3250$

Figure C.5: Recirculation time fractions for multiple Reynolds numbers, middle horizontal plane

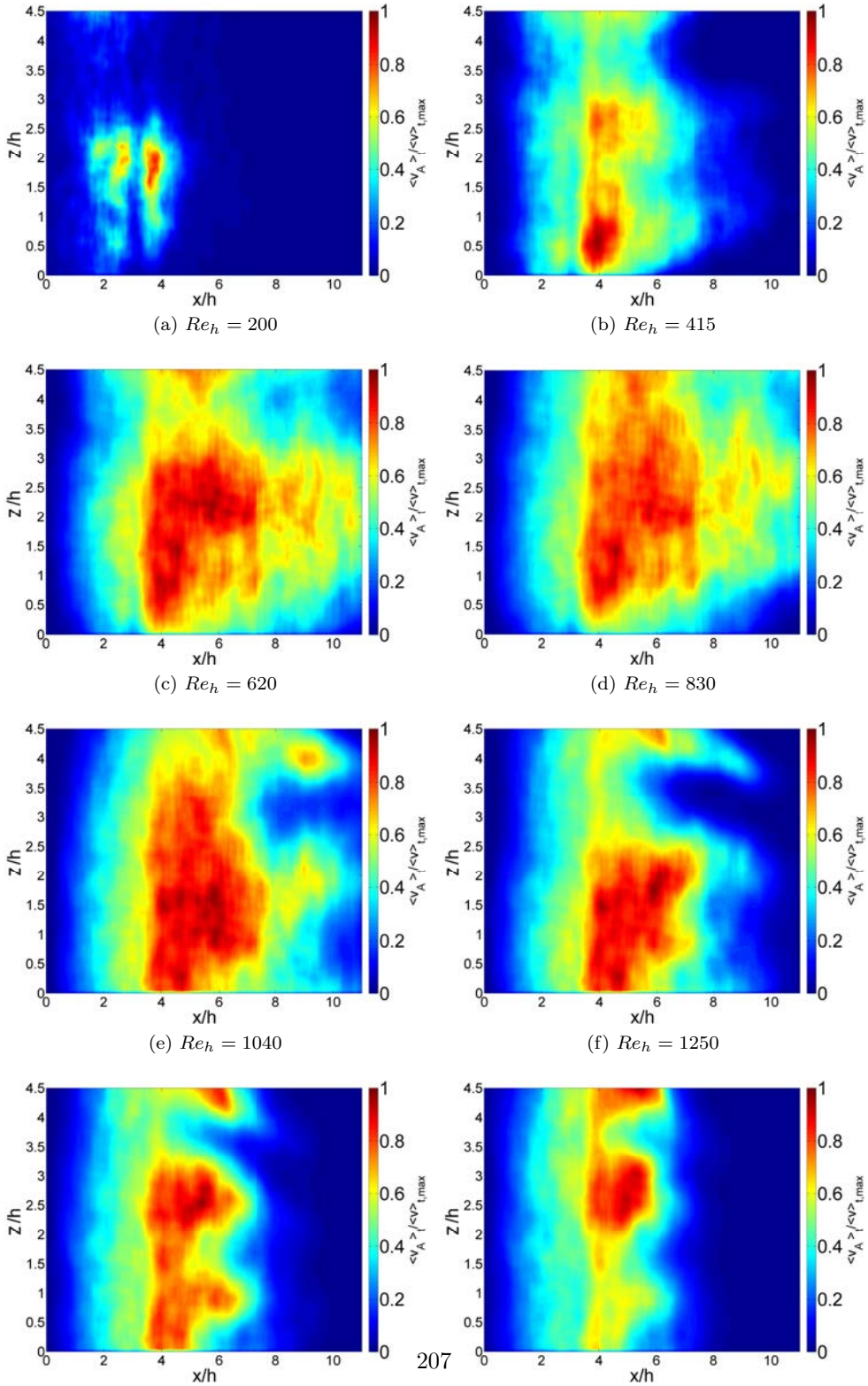

(a) $Re_h = 200$ (b) $Re_h = 415$

(c) $Re_h = 620$ (d) $Re_h = 830$

(e) $Re_h = 1040$ (f) $Re_h = 1250$

(g) $Re_h = 1450$ (h) $Re_h = 1660$

Figure C.6: Recirculation intensity for multiple Reynolds numbers, middle horizontal plane

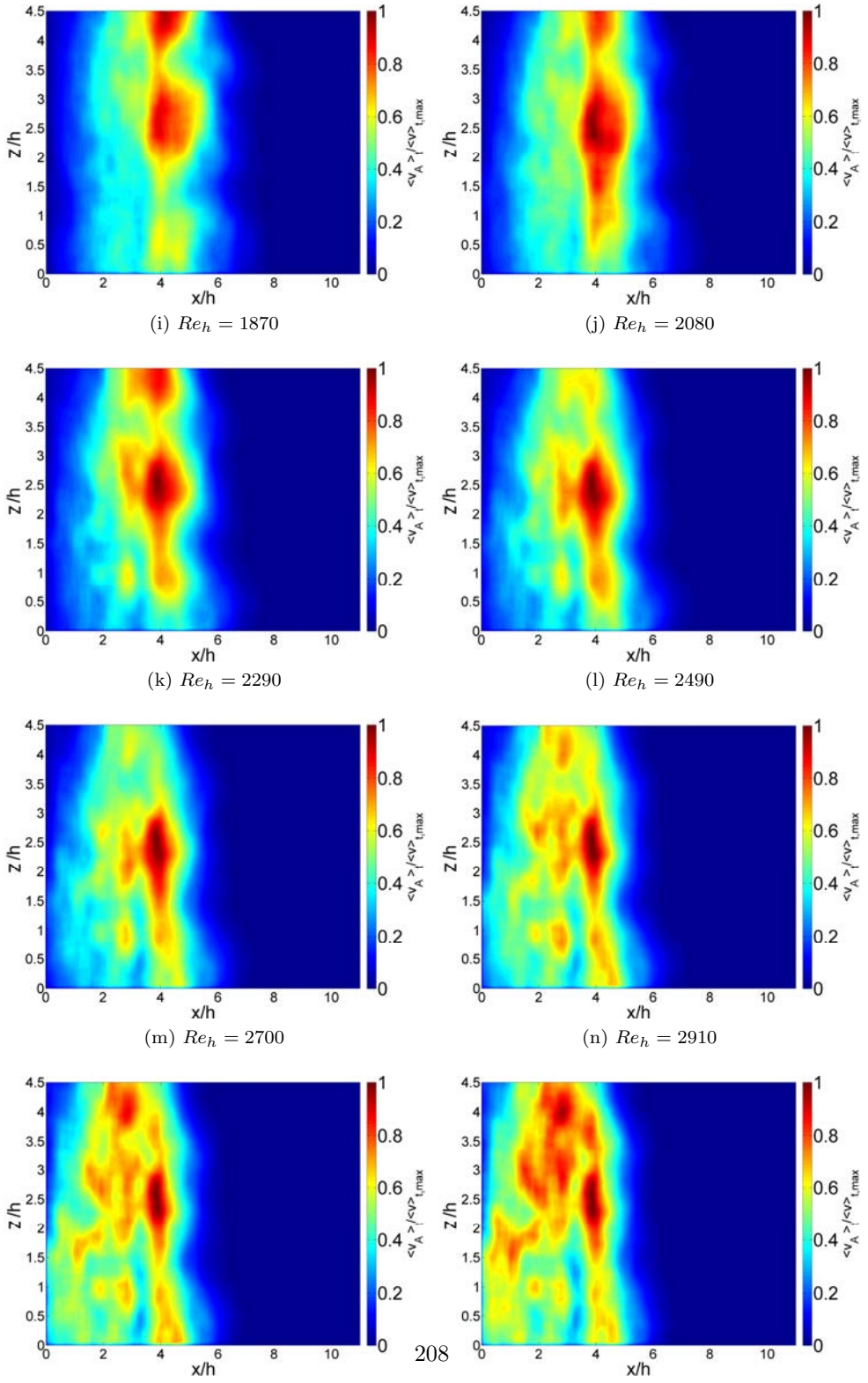

(i) $Re_h = 1870$ (j) $Re_h = 2080$

(k) $Re_h = 2290$ (l) $Re_h = 2490$

(m) $Re_h = 2700$ (n) $Re_h = 2910$

(o) $Re_h = 3170$ (p) $Re_h = 3250$

Figure C.6: Recirculation intensity for multiple Reynolds numbers, middle horizontal plane

Appendix D

Boundary layer profiles

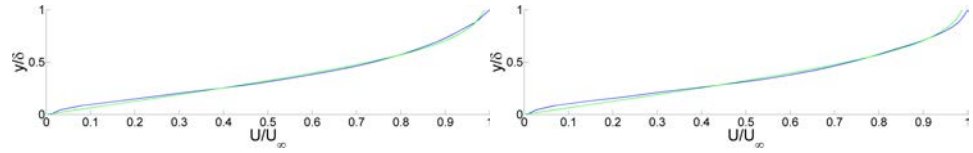

(a) $Re_h = 250$

(b) $Re_h = 470$

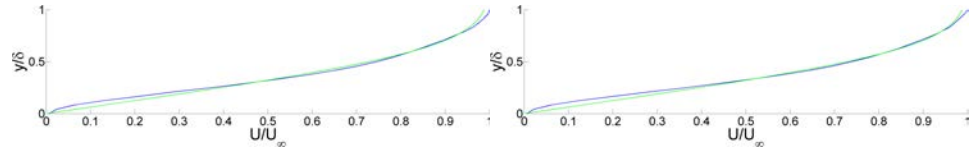

(c) $Re_h = 700$

(d) $Re_h = 900$

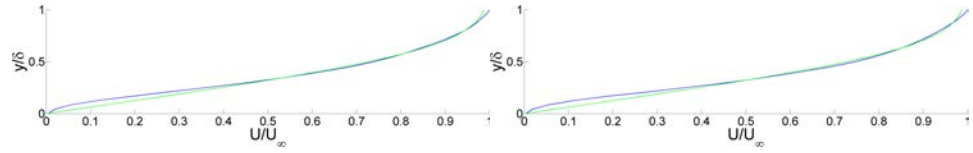

(e) $Re_h = 1130$

(f) $Re_h = 1350$

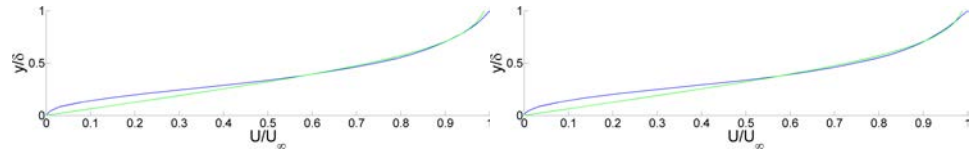

(g) $Re_h = 1550$

(h) $Re_h = 1780$

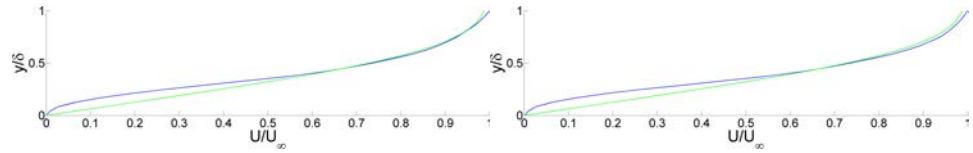

(i) $Re_h = 1960$

(j) $Re_h = 2170$

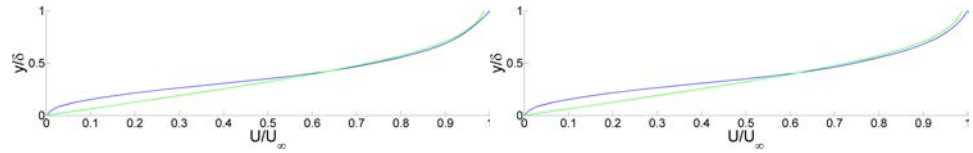

(k) $Re_h = 2350$

(l) $Re_h = 2570$

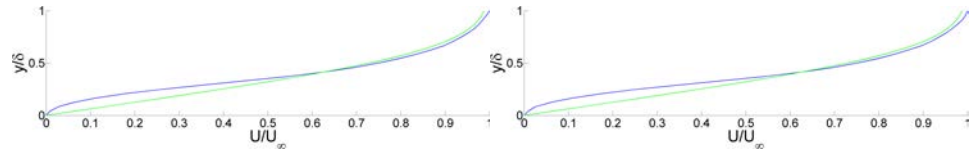

(m) $Re_h = 2780$

(n) $Re_h = 2960$

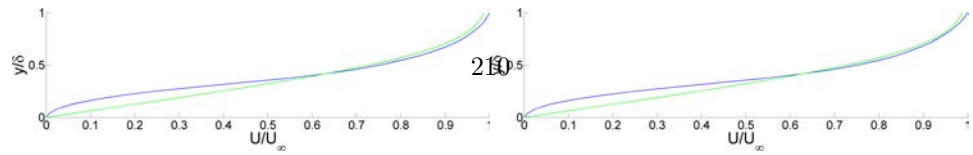

(o) $Re_h = 3200$

(p) $Re_h = 3380$

Figure D.1: Experimental velocity profiles at the step edge (blue) and Blasius velocity profiles (green) as a function of Reynolds numbers